A MODELING STUDY OF ION IMPLANTATION IN CRYSTALLINE SILICON INVOLVING MONTE CARLO AND MOLECULAR DYNAMICS METHODS

CHAN HAY YEE, SERENE

NATIONAL UNIVERSITY OF SINGAPORE
2006

A MODELING STUDY OF ION IMPLANTATION IN CRYSTALLINE SILICON INVOLVING MONTE CARLO AND MOLECULAR DYNAMICS METHODS

CHAN HAY YEE, SERENE
{B. Eng (Hons.), NUS}

A THESIS SUBMITTED

FOR THE DEGREE OF DOCTOR OF PHILOSOPHY

DEPARTMENT OF CHEMICAL AND BIOMOLECULAR

ENGINEERING

NATIONAL UNIVERSITY OF SINGAPORE

2006

ACKNOWLEDGEMENT

I wish to thank my main supervisor, Associate Professor Srinivasan M.P for his patience and guidance in my doctoral work at the National University of Singapore. Without him and the support of the Chemical and Biomolecular Engineering department, this work would not have progressed as smoothly as it had. I would also like to thank my past and present co-supervisors, Dr Ida Ma Nga Ling and Dr Jin Hongmei from the Institute of High Performance Computing for all resources, encouragement and invaluable discussions. I would also like to express heartfelt gratitude to my mentors at Chartered Semiconductor, Dr Lap Chan, Dr Ng Chee Mang and Dr Francis Benistant for all computational and fab equipment resources and for imparting their vast knowledge in all aspects. Their constant support and enthusiasm provided light at the tunnel's end in an otherwise dreary path.

This work would not have possible without the support from a few research institutes and organizations, namely Axcelis Technologies (U.S), Cascade Scientific (U.K), Integrated Systems Engineering (ISE, Zurich), Institute of Materials Research and Engineering (IMRE, Singapore), Institute of High Performance Computing (IHPC, Singapore) and the department of Physics (NUS, Singapore). My scholarship from the Agency of Science, Technology and Research (A*STAR, Singapore) is also gratefully acknowledged.

I wish to express my appreciation to my fellow friends in NUS and colleagues in Chartered Special Projects group for all fun and laughter, peace and joy. Lastly, I would like to express my love and gratitude to my parents who have been standing beside me all these years, and my brother who never thought I would come this far. And of course to the special person in my life, John, for holding my hand through the trials and tribulations.

TABLE OF CONTENTS

Contents Page

SUMMARY

The modeling of ion implantation profiles has been a longstanding problem. From the initial use of analytical functions based on empirical parameters to the use of atomistic methods to predict the dopant distributions, countless problems have been faced and addressed. Each passing generation in the growth of the integrated-circuit chip demands smaller feature dimensions and shallower source drain junctions. Modeling techniques based on continuum methods are no longer sufficient to address problems based on an atomistic scale.

In this dissertation, the limitations faced by common analytical models of ion implantation are addressed. Atomistic methods are deemed to replace such statistically-based methods. Monte Carlo and molecular dynamics are the two main techniques used. Such methods are physically realistic and the implementation of these methods is no longer hindered by long computational times and insufficient memory space with the advent of supercomputers. A new ion implantation model is proposed in this thesis that not only combines the simplicity of analytical techniques, but also the accuracy of atomistic methods. It can also be easily assimilated in commercial process simulators for two/three-dimensional simulation and diffusion studies. Based on this new model and extensive Monte Carlo simulations, implantation tables are set up and presented. However, typical Monte Carlo methods are based on the binary collision approximation (BCA) which becomes inaccurate at low implant energies. The exact breakdown energies have never been clearly defined; this work attempts to estimate these energies for different dopants from first-principles calculations.

Molecular dynamics is proposed to replace Monte Carlo methods in the low energy regime. Not only are multiple interactions accounted for, the molecular dynamics code used in this work allows for the use of accurate interatomic potentials calculated specifically for each ion-target pair. The potentials are calculated from density functional theory and found to give substantially improved results over commonly used repulsive potentials. The electronic losses associated with each collision are also accurately predicted by the use of a robust local electronic stopping model based on phase shift factors. The phase shifts are calculated from first-principles scattering theory and found to give accurate range profiles even in channeling directions. A low energy database consisting of a large number of experimentally measured profiles have been set up not only to verify the models in the codes, but also to identify and eliminate common experimental artifacts associated with ultra-shallow depth profiling. Different SIMS (Secondary Ion Mass Spectrometry) instruments have been used at optimized analyzing conditions in the setting up of this database. By comparing simulation and experiments, the capabilities and limitations of different mass analyzers have been ascertained. A technique has also been proposed to utilize the ranges of coincidences between simulated and experimental profiles to calibrate the full low energy profile. The comparisons also show that the BCA breakdown limits are reasonable approximations to the true limits.

This work yields not only a reproducible method to model ion implantation profiles; in addition, well-calibrated simulated and experimental ultra-shallow profiles have been obtained which serve to provide a good foundation for future diffusion studies. Not only does this work have an important impact on future device modeling, it possesses useful applications in the semiconductor industry, especially since feature miniaturization demands accurate modeling of implantation profiles. This work answers the necessary call for the scaling of technology nodes and provides a good foundation for advances in TCAD simulation.

LIST OF TABLES

LIST OF FIGURES

LIST OF SYMBOLS

$C(z)$	Number of ions per unit volume (concentration)
z	Implanted depth taken in the vertical direction
D_T	Number of ions per unit area impacting on the wafer surface (dose)
R_p	Mean projected range
s_z	Projected range straggling (vertical standard deviation)
s_{LAT}	Projected range straggling (lateral standard deviation)
γ	Skewness, third moment of Pearson IV distribution, accounts for asymmetry
β	Kurtosis, fourth moment of Pearson IV distribution, accounts for flatness of profile
V(r)	Interatomic potential between atoms/potential energy of system
a_0	Bohr radius (0.529Å)
a	Screening parameter
r	Interatomic distance between atoms
r_C	Cut-off radius, maximum distance where surrounding atom affects the central atom
Δr	Infinitesimal displacement of atoms
t_0	Initial time
t	Instantaneous time
Δt	Infinitesimal time step
Z_1	Atomic number of projectile (implanted ion)
E_0	Initial energy of incident ion
M_1	Atomic mass of projectile (implanted ion)
V_0	Incident velocity of projectile ion
V_1	Projectile ion's final velocity
Z_2	Atomic number of target (substrate atom)
M_2	Atomic mass of target atom (substrate atom)

V_2	Target atom's final velocity
E_C	Total energy of system in center-of-mass (CM) coordinates
M_C	Mass of projectile ion in center-of-mass (CM) coordinates
V_C	Velocity of projectile ion in center-of-mass (CM) coordinates
ϕ	Angle of recoil after impact in laboratory coordinates
Φ	Angle of recoil after impact in center-of-mass (CM) coordinates
Θ	Final angle of scatter after impact in center-of-mass (CM) coordinates
J_C	Angular momentum in center-of-mass (CM) coordinates
P	Impact parameter
T	Energy transferred in the collision from incident projectile to target projectile
ε	Reduced energy
S	Stopping energy in units of $eV/atom/cm^2$
Z_{eff}	Effective charge of projectile ion
γ	Correction factor relating effective charge to Z_1
ν	Instantaneous velocity of projectile ion
ν_r	Instantaneous velocity of the ion relative to the electrons
ν_F	Fermi velocity of target electrons
y_r	Reduced relative velocity of projectile ion
ρ	Electron density
r_s	One-electron radius of a centrosymmetric electron charge distribution
Λ	Screening length which describes how electrons screen the nucleus
N	Number of electrons bound to the ion
q	Charge fraction
R_0	Distance of closest approach in a binary collision
C_{el}	Parameters for local electronic energy loss in modified Oen-Robinson model
P_d	Probability that in a certain depth interval of the target a pseudo-projectile is moving in a damaged region

P_s	Saturation level of sub-linear growth or critical value for onset of super-linear increase of the damage.
f_d	Damage accumulation function (dependent on defect types present)
E_n^A	Nuclear energy deposition per target atom
N_d^A	Number of displacements per target atom
E_d	Displacement energy of silicon (~15eV)
L_i	Legendre polynomials of degree i
z_{min}	Minimum depth between which the impurity/damage concentration falls within the range of interest
z_{max}	Maximum depth between which the impurity/damage concentration falls within the range of interest
Tdepth	Depth in μm where concentration is 1×10^{15} atoms/cm^3 (used in SCALP model)
Cx%	Concentration at x% of *Tdepth* (used in SCALP model)
$\nabla_{x,y,z}$	Gradient (del) in x-, y- and z- dimensions
F	Interatomic force between atoms
k_B	Boltzmann constant 1.38066×10^{-23} J/K
ψ	Electron wavefunction
f	Molecular orbitals
c	Atomic orbitals
k_F	Fermi momentum of target electrons
d_l	Phaseshift for the scattering of an electron
E_F	Fermi energy

CHAPTER 1 INTRODUCTION

1.1 Motivation

The main driving force for performance in the semiconductor industry lies in the need to increase both the speed and the density of silicon transistors with decreasing size. Down-scaling of transistor chip dimensions equates to larger numbers of devices per wafer, which leads to higher performance, as smaller channel lengths result in faster transistors. Hence, for similar processing costs, manufacturers can produce larger numbers of dies from the wafer or improve the functionality of the chips by placing more transistors in the same die area. At present, the semiconductor industry faces tough challenges in meeting its goal. The 2004 International Technology Roadmap for Semiconductors (ITRS) has highlighted the need for characterization methodologies for ultra-shallow geometries, source-drain junctions and low dopant levels. The main goal is to meet vertical junction depth prediction accuracy of 10% (of the physical gate length) which falls approximately in the range of 2 to 4 nm. A schematic of the Metal-Oxide Semiconductor (MOS) is given in Fig. 1.1 (Wolf, 1990).

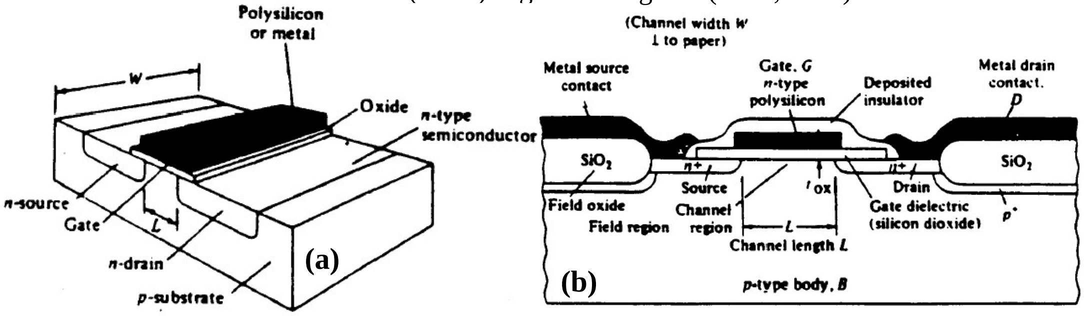

Fig. 1.1 (a) Structure of an Metal-Oxide Semiconductor (MOS) device (b) Cross-sectional view of MOS device

Typical silicon processing techniques include diffusion, ion implantation, oxidation, thin film deposition, chemical or plasma etching, and metallization etc. Among all these processes, ion implantation and dopant diffusion are particularly strongly affected by device miniaturization and remains an active area of study. Ion implantation has been a dominant tool for introducing dopants into the silicon crystal. A typical Complementary-MOS (CMOS) process employs approximately a dozen ion implantation steps to form isolation wells, source/drain junctions, channel-stops, threshold voltage adjusts, punchthrough stoppers and other doped areas of the p- and n-channel MOS transistors. Understanding key thermodynamic and transport phenomena in the implant and diffusion steps with size shrinkage becomes increasingly important, but increasingly difficult to study by experimental techniques alone. Moreover, the cost of fabrication for test lots increases with each technology generation making characterization of material parameters by the usual trial and error method extremely expensive. These factors make simulation of front-end processes a critical component in today's integrated-circuit (IC) technology development. With the advent of faster and cheaper supercomputers, simulation is not only an effective and affordable tool for exploring the vertical and lateral profiles of a modern transistor; it aims to replace physical optimization experiments with virtual ones.

The importance of predictive and computationally efficient implant and diffusion models for the IC fabrication process is evident. As the ion enters the crystal, it gives up its kinetic energy to the lattice atoms by means of nuclear stopping and electronic stopping and finally comes to rest at some depth in the crystal. In order to accurately model the ion implantation process, physically realistic models for both key stopping processes are essential. In addition, implantation produces damage in the form of lattice point defects like interstitials and vacancies, as well as non-substitutional dopants which destroys the pristine condition of crystalline silicon. The induced damage causes dechanneling of the dopant and affects the overall shape of the doping distribution, so an accurate impurity profile cannot be obtained without correctly accounting for dechanneling effect of the damage. Moreover, most of the as-implanted impurities are in interstitial sites and are thus electrically inactive. This necessitates a high-temperature anneal step to activate the dopants atoms and repair the damaged silicon crystal to maintain good electrical properties. Since dopant diffusion is mediated by point defects and the number of such defects increases significantly after ion implantation, post implant annealing is characterized by anomalous diffusion of dopants. This phenomenon, known as Transient Enhanced Diffusion (TED), results in junction depth changes and degradation in the performance of advanced generation transistors. Right after the implantation step, before the high temperature annealing, dopant atoms are already believed to interact with point defects, forming mobile dopant-defect pairs, immobile complexes, and precipitates at room temperature. At the same time, they may also undergo clustering, recombination and diffusion processes. The final dopant distribution is thus a complex combination of a wide range of atomic-scale interaction. Since TED is directly correlated with the implantation impurity and damage distributions, accurate profiles are needed from the ion implantation simulation to be the inputs for the diffusion simulations.

Ion implantation simulations can be broadly classified into three categories: one uses phenomenological models, such as SUPREM IV (Law et al., 1988); the second one is based on the binary collision approximation (BCA) such as in UT-MARLOWE (Tasch et al., 1989) and Crystal-TRIM (Posselt et al., 1994), which are often referred to as Monte Carlo (MC) simulators due to the use of random numbers; the final category is molecular dynamics (MD) (Nordlund 1995). The last two categories are physically based methods, because the motion of the particles is calculated using physical principles. Compared with the semi-empirical phenomenological models, physically based models are rather computationally intensive, however they compensate by their better predictive power. Under the binary collision approximation, the motion of randomly generated energetic particles is described by sequences of binary collisions with target atoms, and the energy loss and direction change at every collision event are tracked. MD, on the other hand, describe the motion of all the atoms concerned in the collision process, by establishing and solving numerically Newton’s equation of motion for all the atoms in the system. The concept of MD is simple but requires longer computational time and larger memory resources compared to MC methods based on BCA. However, MD simulations can provide atomic and structural information which is not possible by other methods, such as channeling effect, and time and space evolution of atomic coordinates, which resemble real-time observations. In summary of what has been discussed so far, ion implantation profiles have a profound effect on device performances, and the final profiles depend on both the as-implanted impurity profiles and the implantation-induced damage. The modeling of ion implantation is thus motivated by three objectives: one is to obtain a computationally efficient and robust technique to model the ion implantation process so that simulation and experiment are complementary; experimental uncertainties and limitations under difficult implant conditions can be identified and surmounted. The second is to achieve accurate nuclear and electronic stopping models so that the scattering phenomenon of impurity profiles for any species can be well described at any implant energy. The final and most important motivation is the need to obtain predictive initial ion implantation profiles which serve to initiate further diffusion studies, hence elucidating the mechanisms of complex dopant-defect interactions and their effect on TED.

1.2 Dissertation Objectives

In this dissertation, the three main techniques of simulating ion implantation, namely phenomenological modeling involving statistical distributions, Monte Carlo methods and Molecular Dynamics methods will be employed to meet the following objectives:

1. Proposal of a robust and predictive ion implantation model that can be easily assimilated in commercial process simulators, and that counters the limitations and combines the merits of the above-stated techniques.
2. Calibration of low and intermediate energy ion implantation profiles for modeling of ultra-shallow junction formation. This requires the following information.
    a. Accurate nuclear and electronic stopping models applicable for a wide variety of industrially important dopants in the low and intermediate energy regime at different crystal orientations.
    b. Reliable and well-calibrated experimental ion implantation profile data for a wide variety of industrially important dopants in the low and intermediate

energy regime at different crystal orientations.

3. TED studies with well-calibrated initial ion implantation profiles, which aim to predict post-implant-pre-anneal impurity and damage distributions taking into account microscopic interactions between point defects and dopant atoms.

To meet the above-mentioned objectives, both continuum and atomistic modeling are utilized, with model parameters obtained from first-principles calculation.

1.3 Dissertation Overview

The remainder of this thesis is organized as follows. Chapter 2 will outline the background on previous work which includes a review of phenomenological models used before physically-based methods became popular, their deficiencies and advent of Monte Carlo (MC) and Molecular Dynamics (MD) atomistic methods. The history and physics underlying some of the more popular nuclear and electronic stopping models will also be described. Chapter 3 will focus on MC methods utilizing the Binary Collision Approximation, and a new model based on MC-BCA simulations will be proposed to replace ion implantation tables in Chapter 4. Chapter 5 describes a MD technique to replace MC-BCA in the low energy regime. This chapter consists of two main sections: firstly, the treatment of nuclear effects by pair potentials calculated from first-principles and secondly, the use of a non-local electronic stopping model that requires calculations of explicit phase shift factors. The estimation of the breakdown limits of BCA by ab-initio calculations will be shown in Chapter 6, together with a qualitative comparison of different potentials and electronic stopping models that are used in the MD code. Chapter 7 will describe the experimental technique used to calibrate the simulated profiles, Secondary Ion Mass Spectrometry (SIMS) and the setting up of the low energy database that covers a wide range of dopants at various implant tilts and rotations. Discrepancies between simulated and experimental profiles in terms of equipment capability and modeling limitations will also be discussed. Chapter 8 will summarize the major contributions of this study with recommendations for future work. Chapter 9 concludes this work.

CHAPTER 2 BACKGROUND LITERATURE

2.1 Modeling Ion Implantation

Ion implantation has been the principal means of introducing dopant impurities into semiconductors during the device manufacturing process. This technique allows precise control over the amount of dopant deposited into the material, usually crystalline silicon. From the process modeling viewpoint, ion implantation provides the initial condition for subsequent diffusion modeling, hence it is imperative to ensure that the initial profile resulting from ion implantation is modeled accurately.

Computer-Aided Design (CAD) models for ion implantation fall into three main categories. Phenomenological models are based on analytical distribution functions, and are statistical in nature, relying upon fits to experimental data to reproduce the observed profiles of dopant ions. It is computationally inexpensive and works well for simple geometries in one dimension. On the other hand, physically-based models like the Monte Carlo (MC) and Molecular Dynamics (MD) methods attempt first-principles calculations based either upon two-body scattering theory termed Binary Collision Approximation (BCA) or solution of the equations of motion for the entire system of atoms. Although computationally intensive, these methods can easily handle the most complicated structures and play an increasingly dominant role in the modeling of ion implantation especially with device miniaturization.

2.1.1 Analytical Distribution Functions

Analytical distribution function models for ion implantation profiles are the simplest and fastest models to execute. These methods based on statistical distributions together with spatial moments have now been used for more than 20 years. The principle of these methods is to assume an analytical type for the function and to calculate its free parameters from its spatial moments. These moments can either be obtained by experiments or theory. When used in conjunction with accurate experimental data for a particular implant condition, analytical methods can be quite an effective means of modeling profiles in the vertical direction, normal to the wafer surface. This technique is based on distribution functions which represent the concentration of the implanted impurity as a function of the vertical distance into the wafer. The particular distribution function chosen should have the following properties:

1. It has a unique maximum.
2. The integral of the distribution from the surface of the wafer to the back of the wafer should equate to the total implanted dose, that is, the total number of ions implanted per unit area.

These properties are satisfied by several distribution functions; the Gaussian, Pearson Type IV and the double Pearson Type IV are most commonly used.

Possibly the simplest distribution to describe the concentration of implanted impurities as a function of depth, the Gaussian distribution, given by Eq. (2.1) has only two moments, i.e. the mean projected range, R_p and the projected range straggling σ_z (the vertical standard deviation).

$$C(z) = \frac{D_T}{\sqrt{2\pi}\,\sigma_z} \exp\left[\frac{-(z - R_p)^2}{2\sigma_z^2}\right] \qquad (2.1)$$

C is the number of ions per unit volume (concentration) and D_T is the number of ions per unit area impacting on the wafer surface (dose). Tables of the Gaussian distribution function parameters for common ion-target combinations have been calculated based upon the Lindhard stopping theory (Lindhard et al., 1963) and are tabulated in literature (Gibbons et al., 1975 and Smith, 1977). However, the symmetric Gaussian distribution cannot accurately describe actual concentration profiles because of several factors. Among these are backscattering of ions lighter than the target atoms, forward scattering of ions much heavier than target atoms, and especially channeling which steers the ion into crystal channels, resulting in deep-ranged profiles with tails. Gibbons et al. (1973) improvised by using two jointed half-Gaussian distributions with three moments to take into account the asymmetry of the profiles. Two different standard deviations are used to the left and to the right of the implant profile peak, as shown in Eq. (2.2).

$$\begin{aligned} C(z) &= \frac{2D_T}{\sqrt{2\pi}\,(\sigma_{z1}+\sigma_{z2})}\exp\left[\frac{-(z-R_p)^2}{2\sigma_{z1}^2}\right] \quad \text{for } z \langle R_p \\ &= \frac{2D_T}{\sqrt{2\pi}\,(\sigma_{z1}+\sigma_{z2})}\exp\left[\frac{-(z-R_p)^2}{2\sigma_{z2}^2}\right] \quad \text{for } z \rangle R_p \end{aligned} \tag{2.2}$$

However, these first-generation models are used only for the sake of simplicity or for a lack of higher moments since it is recognized that for a realistic description of one-dimensional (1D) profiles, at least four moments must be taken into account. For this purpose, the Pearson IV distribution introduced by Hofker et al. (1975) is commonly used.

The Pearson IV distribution uses four parameters to model the implant profile and is defined as

$$C(z) = D_T f(z) \tag{2.3}$$

where f(z) is given by

$$f(z) = K\left|b_2 z'^2 + b_2 z' + b_0\right|^{\frac{1}{2b_2}} \exp\left\{-\frac{b_1/b_2 + 2b_1}{\sqrt{4b_2 b_0 - b_1^2}}\arctan\left[\frac{2b_2 z' + b_1}{\sqrt{4b_2 b_0 - b_1^2}}\right]\right\} \tag{2.4}$$

z’ is given by (z-R_p) and K is a normalization factor, chosen such that

$$\int_{-\infty}^{+\infty} f(z)\,dz = 1 \tag{2.5}$$

and the constants b_0, b_1 and b_2 are given by

$$b_0 = -\frac{\sigma_z^2\left(4\beta - 3\gamma^2\right)}{10\beta - 12\gamma^2 - 18} \tag{2.6}$$

$$b_1 = -\frac{\sigma_z \gamma(\beta + 3)}{10\beta - 12\gamma^2 - 18} \tag{2.7}$$

$$b_2 = -\frac{2\beta - 3\gamma^2 - 6}{10\beta - 12\gamma^2 - 18} \tag{2.8}$$

Besides the mean projected range R_p and the standard deviation, σ_z, the additional two moments γ and β account for the non-idealities of actual concentration profiles. Backscattering of light ions like boron in silicon results in asymmetry, or skewness. The *coefficient of skewness* γ or third moment of the distribution is negative for light dopants and positive for heavy dopants, which means that a dopant like arsenic penetrates deeper into the substrate while carbon or boron concentrates near the surface. The fourth moment of the distribution function β is the degree of flattening near the mean, called the *coefficient of excess or kurtosis*. Positive values suggest that the function is more sharply peaked than the normal distribution; negative values suggest a flattened distribution near the mean value. While Pearson IV distributions are found to be especially well suited to match boron profiles in silicon (Hofker et al., 1975), Ryssel et al. (1980) found that this is also true for boron in SiO_2 and Si_3N_4, for arsenic in silicon, SiO_2 and Si_3N_4, and all other combinations that were investigated. For all the cases, a proper tilting angle during implantation had to be used to avoid channeling. The residual amount of channeling, which is difficult to suppress completely, was incorporated into the moments of the Pearson distribution. Comparisons with experimental range profiles obtained using the $^{10}B(n,\alpha)^{7}Li$ nuclear reaction and activation analysis (Jahnel et al., 1981) also showed that Pearson IV distributions are well-suited to describe implantation profiles of arsenic and boron in crystalline silicon, SiO_2 and Si_3N_4 for energies from 30 to 400 keV. Due to the nature of the measurement technique, the experimentally determined values for the third and fourth moment scatter over a relatively large range. In later years, Hobler et al. (1987) presented a two-dimensional model of ion implantation, which allows for position-dependent lateral moments based on the Pearson IV distribution. The moments were calculated by fitting the Pearson IV distribution to Monte Carlo simulations obtained by a modified version of the code TRIM (Biersack et al., 1980) and expressed in simple analytical formulae for four elements boron, phosphorous, arsenic and antimony in *amorphous* silicon. His data applied well to heavy ions where no channeling occurs, but deviations are expected for light ions like boron. In later chapters, a similar study will be described based on Hobler's model, but in crystalline silicon instead. In general, the Pearson IV distribution is still popular especially where the material is non-crystalline and ion channeling effects are not significant.

For implantations into crystalline materials, it is common to take ion channeling into account by using the sum of two Pearson IV distributions, the first profile representing the profile of ions which do not channel ("amorphous" profile) and the second representing the channeled ions which form the characteristic tail in the distribution ("channeling" profile). Besides the eight parameters (four for each Pearson) describing the dual-Pearson function, a ninth parameter is needed to determine the fraction of ions channeling. The dual-Pearson approach was first implemented in ion implantation modeling by Tasch et al. (1989) and has demonstrated successful ability to accurately model boron, BF_2 and arsenic implants in crystalline silicon (Yang et al., 1994 and Morris et al., 1995). Morris et al. (1995) used an automatic parameter extraction program to extract the nine moments from a combination of experimental and Monte Carlo simulated profiles. These parameters are arranged in a lookup table in which each set of nine parameters corresponds to the profile for a particular combination of implant dose, energy, tilt angle, rotation angle and oxide thickness. For the implant conditions for which no parameters are available, a linear 5-phase interpolation algorithm was developed. This algorithm interpolates in the five-dimensional parameter space of energy, dose, tilt angle, rotation angle and oxide thickness. The lookup tables are implemented in the process simulators SUPREM-III, SUPREM-IV (Law et al., 1988), FLOOPS (Law, 1993) and provide a fast, efficient way of obtaining range profiles for any user-specified implant condition in crystalline silicon at minimal computational time.

Other analytical models include the Edgeworth distribution (Gibbons et al., 1973) and Legendre polynomials (Li et al., 2002) which have found relative success. However, with the advent of supercomputers, savings on computational time has been compromised with better physically-based methods. Commercial process simulators usually come with both phenomenological and atomistic model options.

2.1.2 Atomistic Models: Monte Carlo and Molecular Dynamics methods

The atoms set in motion by interactions with incident ions dissipate their initial kinetic energies in a series of inelastic encounters with other atoms of the solid. The resulting cascade of displaced atoms and the accompanying damage are eventually responsible for the changes that occur in the irradiated solid. A good understanding of such atomic-displacement effects requires a detailed analysis to the problem of statistical thermodynamics namely, explaining the macroscopic properties of matter resulting from the interplay of a large number of atoms, a job unachievable by phenomenological modeling. Atomistic techniques such as Monte Carlo (MC) and molecular dynamics (MD) methods are important in computer simulation of statistical physics and are recognized tools in science, complementing theory and experiment.

The central idea of Monte Carlo (MC) methods is to represent the solution of a mathematical or physical problem by a parameter of a true or hypothetical distribution and to estimate the value of this parameter by sampling from this distribution. It aims at a probabilitistic description from the outset, relying on the use of random numbers. One can generate a stochastic trajectory through the phase space of the model considered and averages of calculated properties. Molecular dynamics (MD), on the other hand, amounts to numerically solving Newton's equations of the interacting many-body system, and one can obtain static properties by taking averages along the resulting deterministic trajectory in phase space. MD has been a useful methodology for a very long time but its use for the N-body system problem remained unsolvable for three or more bodies until the appearance of digital computers. Theoretical studies on systems in equilibrium have met with much success; statistical mechanics based on the partition function provides a formal description of equilibrium systems, but once out of equilibrium, MD helps in bridging the gaps (Rapaport, 1995). It is crucial to recognize the difference between these two methods. The sequence of events in MC methods does not correspond to a sequence in real time, as opposed to the role of time as an explicit variable in MD methods. As such, MC algorithms are fundamentally unable to describe nonequilibrium processes, unlike MD. Despite this, MC methods overcome one of the most severe problems of simulations methods, namely exhaustive sampling of the relevant configuration space. In MD, the local configuration updates imposed by the small time step in the discretized versions of the equations of motion allow only slow exploration of configuration space through a sequence of many small steps. MC methods do not have the equivalent of a time step error; the target distribution is sampled exactly with only statistical errors. Hence, MC methods are still widely used in describing physical phenomena.

MC techniques were first utilized in ion implantation modeling by Robinson et al. (1963) and Oen et al. (1963) to predict the slowing down of 1-10keV copper atoms in copper substrate. Their model assumed that the moving atom loses all of its energy through binary elastic collisions with the atoms of the solid. In addition, the ion is assumed to move through a collection of atoms which are arranged such that the directional properties of the physical lattice are neglected while the lattice density is preserved. Following their work, Beeler et al. (1963) studied the range and damage effects of channeling trajectories in a Wurtzite structure. The primary knock-on atoms (PKA) collision cascade is also described by a branching sequence of binary collision events between the moving atom and the stationary target atom. In this case, the crystalline structure of the target is taken into account. Robinson et al. (1974) expanded the calculations to other simple metals like iron and gold, and discussed the limitations of the binary-collision-approximation (BCA). The computational code used, named MARLOWE, assumed that the particles move only along straight-line segments, these being the asymptotes of their paths. The inelastic atomic collisions are considered to be composed of a quasi-elastic part and a separate electron excitation part. The separation is permissible partly because the low mass of electrons prevents them from carrying significant momentum and also because the inelastic energy loss in individual collisions is small. The quasi-elastic atomic scattering is described by classical mechanics. MARLOWE was subsequently modified by the Technology Computer Aided Design (TCAD) group at The University of Texas at Austin, led by Tasch et al. (1989). The first version of the modified code, UT-MARLOWE was an ion-implantation simulator capable of modeling the implantation of boron into single-crystalline silicon with a bare surface or with a thin oxide layer (Klein et al., 1992). Subsequent versions extended the model capability to other atomic species like arsenic and incorporated a more sophisticated damage model with amorphous pocket formation (Yang et al., 1992). Later versions include models for molecular implants of BF_2, multiple or staged implants, enhanced damage models, and a reduction scheme to reduce computational time (Yang et al., 1996). Subsequent revisions and improvements to this code include a new electronic stopping model which is valid for energies ranging from a few keV to several MeV (Morris, 1997) and a damage accumulation model which allows detailed calculations of interstitial and vacancy concentrations, cluster sizes and amorphous regions (Tian, 1997).

Another widely popular Monte Carlo code which assumes the particles to move in binary nuclear collisions and straight free-flight-paths between collisions is the TRIM code (Biersack et al., 1980). TRIM was developed for determining ion ranges and damage distributions as well as angular and energy distributions of backscattered and transmitted ions in *amorphous* targets. The nuclear and electronic energy losses or stopping powers are assumed to be independent. Thus, particles lose energy in discrete amounts in nuclear collisions and lose energy continuously from electron interactions. Based on the work of MARLOWE and TRIM, a string of MC codes was developed aimed at predicting 1D implantation profiles and their dependence on process parameters like ion species, implantation energy, wafer tilt and rotation, and the thickness of a overlying oxide layer in *crystalline* silicon. These include COSIPO (Hautala 1986), ACOCT (Yamamura et al., 1987), PEPPER (Mulvaney et al., 1989), Crystal-TRIM (Posselt et al., 1992, 1994, 2000) and other various codes which attempt to improvise the original MC codes either by accounting for simultaneous interactions by simultaneous scattering vector summation, based on momentum scaling (Hane et al., 1990) or by introduction of a electronic energy loss model taking into account the silicon electron density distribution effects obtained by X-ray data (Murthy et al., 1992). While the range profiles obtained from these codes showed good agreement with experimental data, they could only describe 1D implantation profiles in the vertical direction. Hobler (1995) developed the code IMSIL with the aim of implementing verified and efficient models, enabling 2D simulations of profiles over a larger concentration range. The 2D dopant distributions are calculated by randomly selecting the starting points of the ions between two positions defining a mask opening. He concluded that a Gaussian function, which is typically used to describe lateral profiles due to the lack of experimental data, is inappropriate to describe the lateral distribution. In the same year, Lorenz et al. (1995) calculated the 3D distribution of implanted dopant atoms using a convolution between an advanced multilayer model for the vertical distribution and a lateral distribution which involves both a depth-dependent lateral range straggling and a depth-dependent lateral kurtosis.

The MC-BCA technique has been relatively successful in analyzing the impact of a single atom at intermediate to high energies. However, this method is limited when implant of clusters or large molecular species is performed. The binary collision approximation also becomes inaccurate at low energies. There are two main reasons for the failure of BCA in the low energy regime. The first is the fact that the BCA assumes that the potential energy of the ion at the start of the collision is negligible compared to its kinetic energy. Thus, BCA can be expected to fail when the kinetic energy of the ion becomes comparable to the interatomic potential energy of the ion and target atom. Secondly, multi-body interactions are neglected. These interactions become important when the interatomic potentials of not only the nearest target, but also more distant ones, are non-negligible compared to the kinetic energy. Both deficiencies occur at low implant energies, and also in crystal channels at high energies. At low energies however, the effects of multi-body interactions are very pronounced. These limitations of BCA have been addressed by several workers. Gartner et al. (1993) performed a systematic computer simulation study of boron distributions in crystalline and amorphous Si for implantation energies between 0.2-5keV using the codes TRIM, MARLOWE and BCCRYS, a code developed by the authors to account for multiple interactions. An interaction sphere with a critical radius was defined. The ion motion within the interaction spheres was described by binary collisions while outside the interaction spheres, ion motion was determined by multiple interactions. Better agreement with experiments was obtained with BCCRYS code; however, the remaining disagreement suggested that a further improvement of the approximate inclusion of multiple interactions in the binary collision model was necessary. The authors proposed a check of the validity of the different multi-body models with corresponding results obtained using MD codes, because they provide an exact description of the multiple interactions. Arias et al. (1995) also concluded that the binary collision models based on asymptotic trajectories were not accurate enough to reproduce the experimental low energy implantation profiles. A more accurate BCA model was proposed which is based on the detailed pre-calculation of the path of the particles for a set of collision events, using a numeric method similar to MD calculations, together with the use of an interpolation procedure in order to reduce the computation time. A comparison between BCA and MD simulations was made by Posselt et al. (1995) at low implants energies of 250eV, 500eV and 1keV for silicon implantation into crystalline silicon. The results demonstrated that at least half of the differences between BCA and full MD simulations can be attributed to target-target interactions while the remainder is due to the approximation of binary collisions. In the case of silicon implantation into single-crystalline silicon, it was shown that below 500eV BCA results become inaccurate, both for channeling and random directions of ion incidence. Instead of time-consuming full MD calculations, MD simulations without accounting for target-target interactions were suggested by the authors to obtain an improvement in accuracy compared to BCA simulations.

The major advantage in using MD arises from its ability to provide atomic and structural information, such as channeling effect, and time and space evolution of atomic coordinates in the order of picoseconds, which are closer to real time observations. While the concept of MD is simple, longer computational time and larger memory resources are required than for MC methods. The large computational burden restricts the applicable time scale of full MD calculations to nanoseconds. However, drawbacks such as high computational cost and lack of realistic models are gradually overcome by the increase in computational power, development of efficient algorithms and accurate calibration of empirical potentials. MD, like MC techniques, was initially applied to the study of the dynamics of radiation damage for pure metals like copper. The original Brookhaven National Laboratory investigation of radiation-damage events by computer simulation (Gibson et al., 1960) has remained possibly the only complete discussion of the criteria that must be satisfied for the simulation of complex many-body or N-body problem. Based on a simple model of face-centered cubic copper, the authors presented a detailed study on the orbits of knock-on atoms and configurations of various static defects consisting of interstitials and vacancies. Following their work, many workers have employed similar iteration techniques and Newton's equations of motions to solve the N-body system. Erginsoy et al. (1964) applied the simulation method to α iron and presented the differences in the damage configurations between the body-centered cubic lattice of iron and the face-centered cubic lattice of copper. Gay et al. (1964) also used an approach similar to Gibson's model but used a different method of calculation for metallic copper. They concluded that differences between BCA and N-body models will be particularly apparent in calculations of range distributions where large relative changes in small scattering angles and energy transfers are particularly significant. Their investigation also suggested the necessity for more complex models other than BCA models for all theoretical research below approximately 500eV. Similarly, investigations by Harrison et al. (1969) of radiation-damage events by computer simulation were very much initiated by Gibson's work. Instead of the central-difference (CD) method of integration used by the aforementioned authors, Harrison's group employed the average-force (AF) method, and concluded that the rationale and implications of this concept has theoretical and practical advantages over the CD algorithm. Subsequent work by this group focused much on the elucidation of sputtering mechanisms mainly for the Cu/Ar+ system by MD simulations using different potential functions (Harrison et al., 1976, 1978, 1982). More sputtering studies were conducted on Cu(100) and Cu(111) surfaces with normally incident Ar+ ions by Shapiro et al. (1985) using the multiple interaction code SPUT1 which employed the predictor-corrector method to integrate simultaneously the classical equations of motion for the incident ion (Ar+) and for atoms (Cu) located at the lattice sides of an ideal crystallite. The code was improvised later (Shapiro et al., 1988) to SPUT2 which used the same integration method but a more efficient neighbor-list logic for force computations compared to SPUT1. The net force on the incident ion was obtained from the superposition of two-body forces between the atom and its neighbors. The study was later extended to the sputtering of Cu dimers (Shapiro et al., 1994). Pair potentials were gradually replaced with the many-body, embedded-atom-method (EAM) potentials to describe the interactions between target-atoms. Such potentials can fit both the bulk properties of the target material and the properties of the free dimer with reasonable accuracy. The EAM potential is an empirical potential fitted to the cohesive energy, lattice constant, bulk modulus, and average shear modulus and has been shown to give good agreement with measured surface properties, like the surface relaxation, and describes atomic emission phenomena in the eV regime in good agreement with other many-body potentials (Gades et al., 1992). Much of the initial simulation studies based on MD focused on metallic systems, especially Cu, which typically employed many-body potentials like the EAM potential to describe the low-energy dynamic properties (Karetta et al., 1992) and also multi-component systems like Ni/Al, which was described by Kornich et al. (1998) using many-body tight-binding potentials to elucidate the role of atomic mass and interatomic potential in low energy ion induced elementary mass and energy transport processes like sputtering and relocations as well as in the connected processes of defect production.

With growing focus on the prediction and manufacturing of ultra-shallow source and drain junctions in transistor fabrication, such atomistic simulation studies gradually shifted from metallic to semiconductor systems. A first-principles simulation study of collision cascades was conducted in bulk alkali halides KCl and NaCl to test various interatomic potentials for Cl-Cl, Cl-K and Cl-Na by Keinonen et al. (1991). Theoretical interatomic potentials were tested at energies 5 to 350eV against experimental data of the intrinsic collision cascades obtained from γ-ray-induced Doppler-broadening (GRID) method. The full MD code used, MOLDY, solved the equations of motion of both the recoiling and target atoms by numerical integration with a time step of 0.5fs. For computational efficiency, only a small simulation cell was used for the range calculations. The same group later tested interatomic potentials for Si-Si interactions at energies 10eV to 5keV for silicon ions in ion-beam amorphized silicon by simulating range distribution data with the MD method (Keinonen et al., 1994). Comparisons of simulated profiles obtained with three different potentials with experimental range profiles measured using a nuclear reaction technique showed that an ab-initio potential based on the density-functional formalism (Jones et al., 1989) yielded better agreement compared to the universal ZBL potential (Ziegler et al., 1985) and Molière potential (Eckstein, 1991). The single most time-consuming function in a full MD simulation is the calculation of the forces on each atom, and considerable effort has been expended in trying to increase the efficiency of this part of MD codes. Verlet (1967) devised a book-keeping method, called neighbor-list, which reduces the CPU time needed for locating the neighbors that is required for the force calculation. If the number of atoms, N, is larger than 2000, however, the CPU time for calculating neighbor-list is still very large since this time is proportional to N^2. To circumvent this problem, the linkcell method was proposed, where the time to locate neighbors and the need for memory increase only linearly with N (Allen et al., 1987). Other time-saving methods include the multiple time-step (MTS) method first proposed by Street et al. (1978) for Lennard-Jones systems, in which two or more timesteps of different lengths are used to calculate the time evolution of rapidly and slowly varying forces in a MD simulation. The authors had shown that the dynamic behavior of the simulated system was dominated by short-ranged forces which vary rapidly in time. This allowed the reduction of the frequency of the evaluation of the secondary long-ranged forces. Use of this method had shown an increase in computation speeds by factors of 3 to 8. Based on the MTS method, Nakano et al. (1993) implemented a parallel MD algorithm, extending it for three-body potentials on the SiO_2 system. On the other hand, Smith et al. (1989) carried out MD simulations of keV argon bombardment of silicon using the moving atom approximation. In that scheme, applicable at 0K, the equations of motion of only the atoms that are moving or have a significant force exerted on them are integrated in time. This approach reduced the computer time by about a factor of 3 while maintaining the integrity of the calculated properties. Zhu et al., (1993) employed a hybrid neighbor-list and linkcell method which was incorporated in the full MD code DYNAMO developed for simulating a large number of pure metal and alloy systems. Their method consisted of the force evaluation on only those atoms that change in a given quantity their position, their acceleration or their acceleration integral. Similarly, Marques et al. (1995) presented a scheme that reduced the simulation time of ion bombardment processes by integrating the motion of particles depending on its energy: the more energetic particles are integrated more frequently than the less energetic ones. Two kinds of particles were distinguished: the incident ion, which has the highest energy, and the target atoms, which have lower energies associated to the thermal vibrations within the solid. In this way, the ion energy established the magnitude of the basic timestep, and the ratio between its energy and the thermal vibrational energy of the target atoms determined the integration frequency.

Despite the many time-saving techniques proposed over the years, full MD simulations were confined to studies of low energy bombardment because entire domain coverage of the large collision cascades that result from high energy range calculations still proved too exhaustive. To counter this problem, Nordlund (1995) employed the Recoil Ion Approximation (RIA) in his code MDRANGE to calculate ion ranges at high energies (>1keV). This assumption was based on the fact that the interactions between the recoil ion and its nearest neighbors are much stronger than the interactions between lattice atoms at high energies. Based on the aforementioned code MOLDY (Keinonen et al., 1994), a cell-translation MD-RIA method was proposed for calculating ion ranges and deposited energies in the recoil energy range 100eV to 100keV. Only the interactions that are involved in the slowing down process were accounted for, which then allowed range and energy distributions at higher energies to be calculated. Use of RIA omitted many redundant features in conventional full MD codes and hence, reduced computational overhead. Besides RIA, two other features differentiated Nordlund's scheme from typical MD simulations: the selection process of the time step and the treatment of the simulation cell boundaries. This scheme was compared to results obtained from the BCA code TRIM (Biersack et al., 1980) and the full MD code MOLDY; results showed that the RIA method improved efficiency by at least 15 times. Much of the work in this dissertation is based on the code MDRANGE. A detailed description of the models and features used in the code will be given in subsequent sections. A MD-RIA scheme based on Nordlund's cell-translation technique was later proposed by Beardmore et al. (1998) for calculating the concentration-depth profile of dopants in ion-irradiated materials. Besides the RIA assumption, several methods of reducing computational time were also used in their code REED (Rare Event Enhanced Domain Following) like Verlet's variable time step algorithm (Verlet, 1967), Smith's moving atom approximation (Smith et al., 1989), pair potential approximation and the domain following method. In particular, a novel rare-event algorithm was proposed that allowed statistically reliable results to be obtained over a range of several orders of magnitude in the dopant concentration. This algorithm was later modified and incorporated in MDRANGE (Sillanpaa et al., 1999) for modeling channeling effects in crystalline silicon and producing sharper end-of-range junctions.

The two techniques discussed, Monte Carlo methods utilizing the binary collision approximation (BCA) and molecular dynamics (MD) methods, broadly encompass all the ion implantation computer simulation codes available. Round robin studies have been conducted by many workers to investigate and compare the predictive capability of such codes. Sigmund et al. (1989) studied the ejection of a copper atom through a planar copper surface as a function of recoil velocity and depth of origin. Results were obtained from six MD codes, four binary collision lattice simulation codes, and eight MC codes. Large differences were found between the predictions of the various codes, but the cause of these differences could be accounted for in most cases, in terms of the potential, electronic stopping and other factors involved. The authors were able to obtain a fairly clear picture from all three types of codes for the depth range and the angular range for ejection at energies relevant to sputter ejection, although a quantitative discussion would have to include an analysis of replacement collision events which has been omitted in this study. On ion implantation, a detailed round robin study was also initiated to study the transmission of ions through crystalline layers (Gartner et al., 1995). Computer simulations were performed by eleven groups using six different MD codes and six different BCA codes which have been mentioned earlier. The process simulated was the transmission of 0.2keV, 0.5keV, and 1.0keV boron atoms through nine monolayers of Si(100) and the transmission of 1.0keV Ar atoms through 5 monolayers of Cu(100). In all cases the energy distribution and the angular distribution of the transmitted atoms had been calculated with and without taking into account the interactions between the target atoms (i.e. with and without the RIA assumption). Results showed that the MD codes considered provided reliable results. Small deviations of the MD results from the different groups were seen to be partly due to the different energy cutoff procedures and the different methods for sampling impact locations that were used. The study also concluded that the binary collision concept can be used in principle even for the low energies considered. This conclusion was also reached by Hobler et al. (2001) who found that the BCA assumption did not introduce significant errors in the case of channeling simulations even at very low energies. An upper limit to the breakdown energy of BCA in crystalline silicon was proposed under non-channeling conditions, taking 5% deviation in the mean projected range as the criterion. The authors also addressed the validity of the RIA assumption in ion-solid interactions at low energies by comparisons with full MD simulations, and found the validity of RIA to extend to energies well below 100eV. A lower energy limit that is dependent on the dopant species for the use of MD-RIA had also been proposed; however it should be noted that the limits given for both BCA and RIA are not sharp but depend on the level of accuracy used. Given the range of validity of both assumptions and the fact that MD preserves the correct treatment of simultaneous interactions of the projectiles with the target atoms which BC fails to do, the authors proposed use of either an acceleration technique for full MD calculations or a sophisticated electronic stopping model in MD-RIA in order to predict range profiles accurately in the low energy regime. In the following section, a discussion of the nuclear and electronic stopping models commonly used in MC-BCA and MD codes will be given. Accurate treatment of nuclear effects involves an adequate choice of potentials, while electronic effects depend significantly on the local electron density.

2.2 Energy loss mechanisms in solids

As a charged energetic particle enters a solid target, it loses energy by two basic mechanisms. The first is nuclear scattering, in which the nucleus of the ion elastically collides with the nucleus of an atom in the target. Each scattering event causes the ion to lose energy, and also to change direction. The second mechanism is electron energy loss, which occurs when an ion interacts with the electrons of the target atoms and slows in a manner analogous to frictional drag. This mechanism is inelastic and does not alter the direction of the ion’s trajectory, only its energy. The development of the theory of an ion slowing down in a solid had been difficult because the problem of describing both the ion and target is complex. Once the ion penetrates the solid, it is quickly stripped of some of its electrons and its charge state becomes a function of the target. The electrons of the target then polarize around the moving ion causing a modification of the charge state of the ion, which further affects the target. Some of the target atoms penetrate through the ion’s electron cloud causing quantum excitation of available states.

Complicating matters further, all these effects depend on the changing ion's velocity. This study of the penetration of a particle into matter could well have begun 400 years ago with the study of projectile ballistics. Since then, scientific progress has led to breakthrough stopping theories applied in all aspects like the development of quantal scattering in the 1920's, the study of nuclear fission in 30's and 40's, the study of nuclear physics in the 50's, the technological applications of ion implantation for material modification in the 60's, and the use of ion beams in material analysis in the 70's.

The evolution of stopping theories started with early studies on radioactive particles. The first step in unraveling the mystery of the atom was taken in the groundbreaking work of Curie et al. (1898) who found that particles could penetrate thin films. However, early attempts to create a particle energy loss theory were inconclusive for there was yet an accurate model of the atom. A unified theory of stopping was finally proposed for the first time by Bohr (1913a, 1913b) after Rutherford (1911) gave a theory of the structure of atoms. According to the Rutherford theory, the atoms consisted of a positively charged nucleus surrounded by a system of electrons kept together by attractive forces from the nucleus with the total negative charge of the electrons equivalent to the positive charge of the nucleus. Much of Bohr's ideas were based on Rutherford's model. The separation of the energy loss of ions passing through matter into two components, nuclear and electronic stopping, was one of Bohr's original conclusions. He concluded that the particle's velocity was more important than its energy and also correctly deduced that the electronic stopping would be far greater than the nuclear stopping for energetic light ions. A breakthrough in understanding stopping powers came 20 years later when Bethe (1928, 1930) and Bloch (1928, 1933) approached the problem from the perspective of quantum mechanics and derived in the Born approximation the fundamental equations for the stopping of very fast particles in quantized electron plasma. This theoretical approach remained the basic method for evaluating the energy loss of light particles with velocities 10MeV/amu to 2GeV/amu because the ion projectile may not be fully stripped of its electrons below these velocities and above that, there may be additional relativistic corrections. Bohr (1940, 1941) later suggested that the ion be considered to be stripped of all electrons with velocities lower than the ion velocity, and using the Thomas Fermi atom, he presented a relationship between the effective charge in energy loss to the target electrons, Z_1*, the atomic number Z_1, the ion velocity V and the Bohr velocity V_0 ($\approx 2\times10^8$ cm/sec), shown in Eq. (2.9).

$$Z_1^* = Z_1^{1/3}\, V / V_0 \tag{2.9}$$

The Thomas Fermi model is a self-consistent theory averaged over microscopic shell effects introduced first by Thomas (1927) and then independently, by Fermi (1927) shortly after Schrodinger invented his famous quantum-mechanical wave equation in 1926. It is a statistical theory to approximately describe the electron density and the ground state energy for a large atom or molecule with a large number, N, of electrons. Schrodinger's equation, which would give the exact density and energy, cannot be easily handled for large N. Much of the work cited from here on is based on the Thomas Fermi atom. Following Bohr's work, Lamb (1940) calculated the ranges and rates of energy loss of the fission fragments of uranium on the basis of a model in which the charge of the fragment is obtained from its energy and its successive ionization potentials. He suggested that the stopping of the fission fragment would be significantly altered by the target electron velocity distribution. Fermi (1940) followed the same train of thought as Bohr and Lamb, but focused his study on how the polarization of the medium affected the field of the charged particle moving through it. Using a theory based on classical electrodynamics, he concluded that the loss of energy of a fast charged particle due to the ionization of the material through which it is passing is considerably affected by the density of the material. He attributed the effect to the alteration of the electric field of the passing particle by the electric polarization of the medium. Knipp et al. (1941) successfully used the concepts of Bohr and Lamb to scale H stopping values to equivalent He ion stopping powers. The energy loss of heavy ions due to collisions with electrons was determined by the ionic charge, which in turn depended on the ratio of the velocities of the most loosely bound electron within the ion, and of the ion. All these theoretical studies, though fragmentary, provided scaling relationships for the heavy ion stopping and ranges which allowed for prediction from existing data to systems with different ions, targets and energies.

2.2.1 Nuclear Energy Loss

For the ion-target atom interaction with a sufficiently large minimum distance, the interatomic potential V(r) is influenced by the presence of the electrons, so that a screened Coulomb potential has to be employed. The energy loss to target nuclei is thus essentially the study of screened Coulomb collisions between two colliding atoms. Naturally, the development of proper interatomic potentials V(r) is closely related to the choice of the atomic potentials of the collision partners. Statistical models of interatomic potentials had been widely used in calculating nuclear stopping powers because of their universal applicability. The most widely used is the Sommerfeld approximation to the Thomas Fermi potential (Sommerfeld, 1932), the Moliere approximation (Moliere, 1947), the Lenz-Jensen (Lenz, 1932 and Jensen, 1932) and the Bohr potential (Bohr, 1948). Much of the earlier work which used the Thomas Fermi model to estimate the screened Coulomb potential V(r) between atoms had been summarized in the classical review by Bohr (1948).

$$V(r) = \frac{Z_1 Z_2}{r} \exp\left(-{}^{r}\!/_{a}\right) \tag{2.10}$$

Z_1 and Z_2 are the atomic numbers, r is the interatomic separation and a is a screening parameter. These potentials may be considered to consist of two parts: a Coulombic term (1/r) arising from the positive point nucleus and a screening function due to the surrounding electron cloud. The screening function can be defined as the ratio of the atomic potential at some radius to the potential caused by an unscreened nucleus. With specification of the screening parameter, the classical scattering and energy transfer can be calculated. Bohr argued that the screening parameter could be approximated by the expression shown in Eq. (2.11) while Firsov (1953) used numerical techniques to derive the interatomic potentials of two colliding Thomas Fermi atoms. After calculating the numerical values of the potentials as a function of the interatomic separation, Firsov found that the best fit to the screening function was obtained by using a screening length given by Eq. (2.12).

$$a_{Bohr} = \frac{a_0}{\left(Z_1^{2/3} + Z_2^{2/3}\right)^{1/2}} \tag{2.11}$$

$$a_{Firsov} = \frac{a_0}{\left(Z_1^{1/2} + Z_2^{1/2}\right)^{2/3}} \tag{2.12}$$

There is general agreement that the Thomas Fermi screening function overestimates the potential at large distances and hence the stopping cross-sections at low energies, and that the opposite is the case for the Bohr screening function. The difference between Lenz-Jensen and Moliere, although noticeable only in the low-energy range, reflects the inherent uncertainty of this type of statistical potentials (Sigmund, 2004).

The first unified theory to stopping and range theory was made by Lindhard et al. (1963) and their approach is commonly called LSS-theory. In their work, a theoretical discussion was given of ranges of heavy ions passing through matter with moderate velocities, based on a simple scaling theory of ion-atom collisions. Probability distributions in total range and various averages were studied, as well as ranges projected on initial direction of motion. Cited in over 2,240 publications since 1963, this work was revolutionary in bringing together all the bridging approximations so that stopping and range distribution calculations could be performed simultaneously within the same model based on statistical atoms. The study of ranges of heavy ions passing through matter, and probability distributions of ranges required a detailed investigation of integro-differential equations related to evolution of probabilities. The comprehensive solutions were meant to represent an average behavior, disregarding individual deviations due to quantal shell resonances in ions or atoms. With the LSS-theory, it was possible to predict the range of ions in solids within a factor of two, which is remarkable considering the fact that it was applicable for the entire range of atomic species and energies up to the stopping power maximum. The LSS-theory was the last of the comprehensive theories based on statistical models of atom-atom collisions. Improvements in range and stopping calculations over the next two decades were made by the application of numerical techniques to traditional theoretical approaches and removal of some of the approximations of Bohr, Firsov and Lindhard. The incorporation of more realistic Hartree-Fock atoms into the theory gave significant improvements to the prediction of electronic (Rousseau et al., 1971) and nuclear (Wilson et al., 1977) stopping, permitted by the advent of computers.

Since the appearance of the LSS-theory, heavy-ion stopping had been typically categorized into three regimes (a) a low-speed regime where the electronic stopping force is taken to be proportional to the projectile velocity and approximately given by the estimates of Lindhard et al. (1961) or Firsov (1959) (b) a high-speed regime characterized by the Bethe (1930) formula, and (c) an intermediate regime around and above the stopping maximum which had most often been characterized by a Bethe-type formula in conjunction with some effective ion charge (Northcliffe, 1963). While this characterization had been useful in the scaling of experimental data, the process of theoretical understanding and quantitative description of the intermediate regime had been slow. This was largely attributed to the complexity of understanding the connection between ion charge and energy loss in connection with the so-called density effect, i.e., the distinct difference in measured equilibrium charge states between gaseous and solid media and lack of knowledge about the contribution of charge exchange and projectile excitation at intermediate velocities. Brandt et al. (1982) took an important step when they established an explicit connection between ion charge and stopping force. The effective charge of energetic ions was calculated in a dielectric-response approximation. The central feature of Brandt’s theory, i.e. the entrance of the ion charge via a partially screened Coulomb potential as suggested originally by Bohr (1948) in his famous review of particle penetration, had been susceptible to subsequent theoretical attacks. In the quoted paper, Bohr stated that the regimes of validity of classical-orbit models and of quantal perturbation theory were roughly complementary: The stopping of low-charge particles like electrons and protons at high speed could be accurately described by the Bethe theory which treated projectile-target interaction by quantal perturbation theory to lowest order. It seemed appropriate in an alternative approach to start at the opposite end, i.e. the classical limit, in an attempt to find a comprehensive theory of heavy-ion stopping when the accuracy of this scheme deteriorated with increasing projectile charge and decreasing speed.

Stopping theory for heavy ions had been quite fragmentary until around 1995. Theoretical predictions were available for slow ions (Firsov, 1959) (Lindhard et al., 1961) but not for heavy ions at high speeds. Stopping parameters had to be extracted from empirical inter- and extrapolations (Steward et al, 1966) (Northcliffe et al., 1970) (Ziegler et al., 1980, 1985) (Hubert et al., 1980, 1990). The situation changed rapidly after 1995. The theory by Bohr (1913a, 1913b), which had been considered to be mainly of historic interest until then, was rediscovered as a valuable tool in the description of heavy ion stopping. A new derivation by Lindhard et al. (1996) reestablished the stopping formula of Bloch (1928, 1933) and demonstrated its superiority over the famous stopping formula of Bethe (1928, 1930) for the case of heavy ions. The stopping powers were calculated by a simple method; its starting point rose from the deviation of the precise theory from first-order quantum perturbation. It was shown that this deviation can be expressed in terms of the transport cross section, σ_{TR} for scattering of a free electron by the ion. In the non-relativistic case the deviation is precisely the Bloch correction to Bethe’s formula. The corresponding relativistic correction is obtained from σ_{TR} for scattering of an electron in the ion potential. Hence, the scattering distribution need not be found; only a single quantity, σ_{TR} determined by differences of successive phase shifts was needed. The authors established a major improvement of the relativistic theory for stopping of heavy ions. Several independent schemes were developed to non-perturbatively describe the stopping of ions carrying electrons. Sigmund et al. (2000, 2002) developed a binary stopping model based on Bohr's theory and incorporated screening, higher order shell corrections, high-speed quantum and relativity corrections as well as projectile excitation and ionization to characterize the electronic stopping of swift heavy ions in matter. Grande et al. (1998, 2002) reviewed the convolution approximation for the impact-parameter dependent energy loss on the determination of the stopping force for heavy projectiles. It was found that the convolution approximation, in the perturbative mode, yielded remarkable agreement with full semi-classical approximation (SCA) results for bare as well as screened ions at all impact parameters. Maynard et al. (2001, 2002) determined the charge dependent stopping cross-section of partially ionized heavy ions in a carbon target in the energy range of a few MeV by calculating the classical evolution of the Wigner function of the target electrons during collision. Arista (2002) proposed a self-consistent non-linear approach based on the σ_{TR} approach to calculate the energy loss of heavy ions on a wide range of velocities. The purpose was to develop a non-linear stopping power evaluation method that could be applied at finite ion velocities, bridging the current gap between the low and high energy models. Such developments allowed the prediction of stopping forces without the use of fitting parameters.

2.2.2 Electronic Energy Loss

The separation of energy loss of the ion into nuclear and electronic losses was first proposed by Bohr (1913a, 1913b). This assumption ignored the possible correlation between hard nuclear collisions and large inelastic losses due to electronic excitation; the correlation was deemed insignificant when many collisions are averaged over, as when an ion penetrates a solid but was of importance for single scattering studies and for very thin targets. Bohr based his study of electronic stopping cross-sections on a model which considered the target a collection of harmonic oscillators whose frequency was determined by optical absorption data. Unfortunately, quantum-mechanics stipulates that electrons have strong wave characteristics and cannot be localized. Therefore, electrons, unlike nuclei, cannot be treated as point masses and an accurate description of electronic stopping is a much harder process. Several attempts were made to introduce quantum-mechanics into the problem, and it was finally done by Bethe (1930). This work was further expanded to relativistic particles by Bethe and Bloch. The Bethe-Bloch theory considered a particle interacting with an isolated atom of harmonic oscillators. This approach solved the charged-particle/atom energy loss problem quantum mechanically in the first Born approximation. It was initiated when the results of the earlier Bohr work differed significantly from the results of Bethe. Bloch (1933a, 1933b) found that the Bohr distant collision theory was quantum-mechanically correct as the mean energy loss averaged over all electronic transitions but his solution for the close collision energy loss differed from that of Bohr and Bethe. Bohr had assumed for close collisions that the atomic electron was free while Bethe had represented such collisions with plane waves. Bloch showed that the Bohr classical solution was valid for hard close collisions while the Bethe solution was valid for weak scattering. Bloch then provided a solution which reduced to the Bohr solution for hard collisions and almost reduced to the Bethe solution for weak collisions.

The next advancement in electronic stopping theory was the consideration of the target as a collection of interacting electrons, i.e. a plasma and to consider the energy loss to collective effects such as dynamic polarization and energy loss to plasmons. Fermi (1940) and Fermi and Teller (1947) were the first to treat the target electrons as plasma. Beginning with the Maxwell equations, the problems of binding energies, dispersion of the electron oscillators and damping constants on collective motion were considered. In the following decade, electronic interactions of a particle with plasma were then extensively treated. Lindhard (1954) presented generalized methods to self-consistently treat the response of a free electron gas to a perturbation and he derived an explicit function for the interaction. It included the polarization of the electrons by the charged particle, the resultant charge-screening and the plasma density fluctuations. Neufeld et al. (1955) treated the plasma as a homogeneous dispersive medium characterized by a dielectric constant which was a function of both the frequency of the applied field and also its wave number. Based also on Maxwell’s equations, an expression was derived for the distribution of the polarization density in the space surrounding a moving particle. Fano (1956) developed a quantum analog of the classical electron oscillator model. This theory argued that the Hamiltonian of long-wave excitations of matter is equivalent to that of an assembly of oscillators. These oscillators were then coupled with the electromagnetic field oscillators and the normal modes of the coupled systems were analyzed. The first attempt to evaluate electronic stopping cross sections for protons in solids was by Bonderup (1967) who used the Lindhard stopping formalism and Lenz-Jensen atoms to represent the atoms in a solid. This work was extended to Hartree-Fock atoms by Rousseau et al. (1971) and to actual solid-state charge distributions by Ziegler (1978).

To calculate the stopping of protons in solids rather than in a gas of electrostatic particles, the effective charge of these ions in solids need to be evaluated. This was a problem because no one could propose a way to measure the charge state of protons in solids. Brandt (1975) investigated this problem from both theoretical and experimental aspects but found no evidence that hydrogen ions would have bound electrons in their passage through solids. Ferrell et al. (1977) calculated the charge state of slow light ions in free electron gases using a self-consistent potential approach. They also compared the stopping power obtained from linear-response theory with that found from numerically computed phase shifts for electron scattering on the screened potential of an ion. They found that He ions might bind an electron in a metal, and protons could do so in a dilute free electron gas. Echenique et al. (1981) calculated the stopping power of an electron gas for slow ions using the density functional formalism. They evaluated the non-linear self-consistent potential around the ion and determined the energy loss from scattering theory directly. It was found that their calculations differed from those obtained from linear-response theory in that the atomic character of the projectile was fully accounted for. A breakthrough was finally achieved when Brandt and Kitagawa (1982) concluded after a long series of experimental and theoretical work that hydrogen ions were always protons with an effective charge of one. Their work formed the basis of many modern electronic stopping parameterizations.

Based on the spirit of the Brandt-Kitagawa (BK) effective charge theory, the non-local electronic stopping power consists of two parts: one is the globally average effective charge taking into account the ionization of the moving particles and screening effect, and another is the stopping power of a proton. In order to calculate the stopping power for a heavier particle, the proton stopping power should be multiplied by the square of the effective charge, which is calculated by taking into account the ionization of the moving particle and screening effects. It was found that for the ionization, the velocity stripping of the BK formulism worked well at lower velocities, while at high velocities, it was necessary to use an energy stripping criteria such as that proposed by Mathar (1995). The BK theory makes simplifying assumptions about the shape of the ions' electron clouds and does not directly account for the quantum-mechanical stopping cross section between an ion and the target atom electrons. As such, all stopping models based on the BK theory are more or less phenomenological in nature. Ziegler et al. (1985) developed a non-local stopping model, the so-called ZBL stopping based on the BK model. Fermi velocity was treated as a constant depending on the target material and may have an empirical correction factor. The stopping of protons was obtained from a fit of eight parameters that have different values in each elemental target material. The ZBL stopping is still widely used, mainly because it is easy to calculate for any material and is included in the popular simulation program TRIM (Biersack et al., 1980). It is reasonably accurate due to the use of numerous free parameters but it becomes inaccurate when channeling is significant because it is a non-local parameterization where the stopping is the same everywhere in the crystal. The accuracy of the ZBL stopping powers can be improved by using range measurements to determine a correlation factor (Sillanpaa, 2000). Azziz et al. (1985) also developed a non-local model named ABS model after the respective authors which treated the Fermi velocity as a free parameter. Although it was not a very successful nor physically well-motivated theory, it inspired other more successful models. Azziz et al. (1987) later developed a local electronic stopping model which was not based on the BK theory, but it was not too well-received. Local electronic stopping is dependent on the position in the crystal and assumed not to be a polarization effect but primarily a direct exchange of electrons between the two colliding atoms.

Klein et al. (1990) developed a local model based on the effective charge theory of the BK model and proton stopping power of Echenique et al. (1981). He used the same expressions for charge fraction and stopping of protons as the ABS model, but calculated the stopping from a spherically symmetric charge distribution (Ziegler et al., 1985). The model was developed for low energy implanted ions and accounted for the effect of the local variation of the electron density between the lattice atoms in the silicon crystal target material on the amount and rate of energy loss due to electronic processes. It was subsequently incorporated into the Monte Carlo code MARLOWE (Robinson et al., 1974) and achieved success in the simulation of boron implants into single-crystal silicon over a wide range of energies and incident angles but could not give accurate results for arsenic. The improved version of the code containing the local electron concentration-dependent electronic stopping model was renamed UT-MARLOWE (Klein et al., 1992). Cai et al. (1996, 1998) and Beardmore et al. (1998) eventually developed a local stopping model, which calculated the stopping of protons from a spherically symmetric charge distribution similar to Klein et al. (1990) but the Fermi velocity of the target was treated as a free parameter, just as in the ABS model. This parameter had a different value for each ion-target combination and was meant to take into account the Z_1 dependence of the electronic stopping cross section, i.e. the oscillations observed for the stopping powers of different ions in the same material. Their model therefore combined features from the ABS and Klein's models and contained a version of the Firsov model (Firsov, 1959) to describe the loss of kinetic energy due to the momentum transfer between the electrons of the ion and those of the target atoms. While it had achieved remarkable accuracy, it contained a free parameter and therefore unsatisfactory from a physical point of view. In summary, the Bethe-Bloch theory provided the foundation to solve the charged ion electronic energy loss problem. Most of the non-local electronic stopping models used today are modifications to the BK non-local model or Lindhard's model, while local models are typically based on the work of Robinson et al. (1974) and Firsov (1959). In this dissertation, a local electronic stopping model will be presented which is based on the BK theory but contains no free parameters, and hence no additional adjustments for every ion-target combination.

2.3 Experimental Techniques for Range Profiling

Accurate experimental data are necessary for any physically-based model calibration. Direct comparison of experimental and simulated data not only allows the refinement of experimental conditions, hence reducing the contribution of experimental artifacts, it also permits calibration and validation of the models in the simulation code. Model parameters are usually fine-tuned in order to obtain the best overall fits to the experimental data, and the success of the model is gauged by the degree an extent to which the model agrees with experimental data. In this section, the experimental techniques commonly used to describe ion implantation profiles are described. It is not intended to give a comprehensive, full description of the experimental details, but rather the basic concepts, which will aid in the interpretation and analysis of the data to be shown in later chapters.

2.3.1 Ion Implantation

In the olden days, enhancement of the metallic properties of semiconductors was achieved by deposition of dopants on the wafer surface which are subsequently driven into the wafer by diffusion. This obsolete technology has almost been completely replaced by ion implantation. Ion implantation is the near-room temperature process in which energetic, charged atoms or molecules are directly introduced into a substrate to make the semiconductor silicon electrically active. Desired dopants are accelerated to energies in the keV-MeV range and they penetrate the surface of the wafer with energies that are a million or more times higher than thermal energies. The crystalline structure of implant-damaged silicon can be recovered through subsequent annealing cycles. Ion implanters are the most complex systems used in the fabrication of transistors. Fig. 2.1 shows the schematic drawing of a commercial ion implanter. For most ion implanters, they contain the following sub-systems (Wolf et al., 2000):

- A *feed source* of material which contains the species to be implanted. Commonly used dopants, such as B, P and As are not gaseous at room temperature; they must be supplied to the ion source as part of a molecular compound that is gaseous at 300K.
- An *ion source*, provided with its own power supply and vacuum pump which ionizes the feed gas. Plasma is produced at pressures approximately 10^{-3} Torr.
- An *ion extraction and analyzing device* which selects only the ion species of interest according to their mass and rejects all others.
- An *acceleration tube* (and its power supplies) which creates the acceleration field needed to increase the ion energy to the desired level or decelerate the ions if an energy less than that caused by the extraction voltage is required.
- A *scanning system* which is used to distribute the ions uniformly over the target.
- A *system end station* which includes a Faraday cup, a current integrator which directly measures the implant dose by collecting the beam current and integrating it over the implant time, and a sub-system that loads, holds and positions the wafers.
- A *high-vacuum pumping system* which serves to evacuate the magnetic analysis area, the acceleration column, and the end station to a background pressure of $< 10^{-6}$ Torr.
- Finally, a *computer and control system* which provides recipe-driven operation of the implanter and some degree of automation in the operation.

Ion beam current is important because it dictates the overall throughput of the implanter. The ion beam current in implanters ranges from about 10 μA to 30 mA, depending on the implant species, energy and model of the implanter. As integrated circuit fabrication design transcends to deep-sub-micron feature sizes, the design for implanters were driven to divide functionality in a different way. Ion implanters are categorized depending on their useful energy range.

- *Low-energy implanters*: High-current tools capable of operating with a maximum beam current of 1 to 20mA, over energy range of 0.2-80 keV.
- *High-energy implanters*: Maximum beam energy as high as 400 keV to several MeV with beam current ranging from 5 µA to 50 µA.

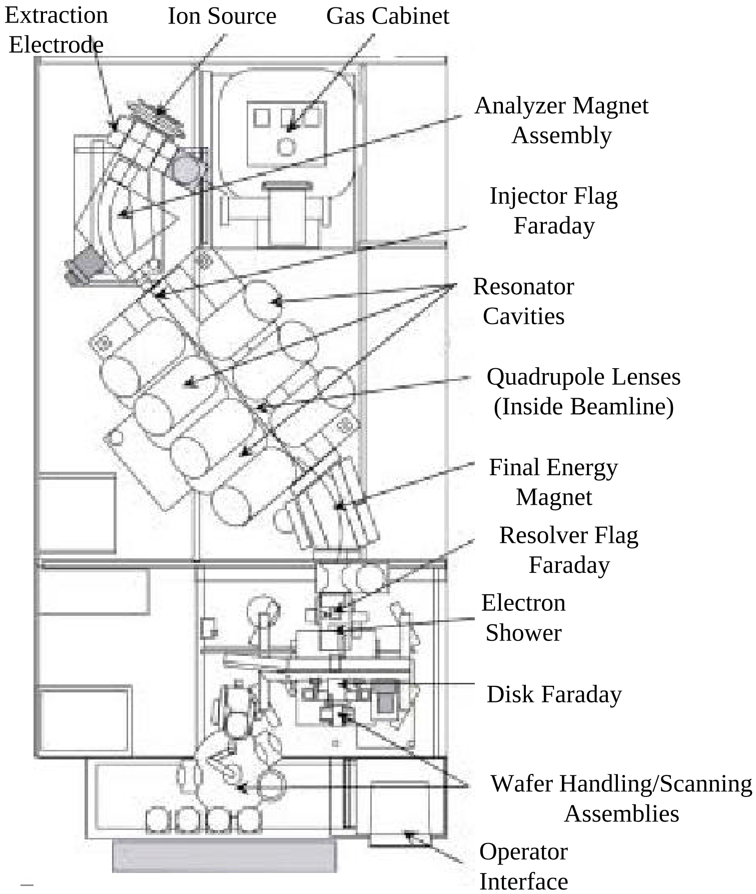

Fig. 2.1 Schematic of a commercial ion implanter. Courtesy of Axcelis Technologies.

Some of the terms in ion implantation terminology which will be frequently encountered in the following chapters are discussed here. **Dose** is the number of implanted ions per unit area. Typical doses range from 10^{11} to 10^{16} atoms/cm^2. After implantation, the implanted ions are measured in units of concentration (atoms/cm^3). **Tilt and rotation** (also called twist) are two angles that define the direction at which the ion beam impinges on the wafer. The tilt angle is measured relative to the <100> direction perpendicular to the surface of a (100) silicon wafer.

The angle results from tilting the wafer about an axis located at and parallel to the <110> wafer flat. Rotation angle measures the rotation of the wafer about an axis perpendicular to the centre of the wafer. **Range** is the total distance that an ion travels in the target and this trajectory is not a straight line due to collisions between an ion and the target nuclei. The projection of this range in the direction parallel with the incident beam represents the penetration depth of the implanted ions along the implantation direction and is known as the **projected range**.

Process non-uniformities and limitations of the implant equipment can limit device yield. Some limitations include elemental and particulate contamination, dose monitoring inaccuracies due to beam charge state change effects, implantation mask issues, wafer charging during ion implantation, poor dose matching from machine-to-machine in production implanters, tilt-angle and "scan lock-up" non-uniformities in electrostatically scanned machines and dose variations on the scale of die sizes (Wolf et al., 2000). In this study, all sources of errors were carefully controlled so that any possible inaccuracies during implantation were kept to a minimum.

2.3.2 Impurity Depth Profiling

Amongst the many methods available for measuring the range distributions, namely ERDA (Elastic Recoil Detection Analysis), NRB (Nuclear Resonance Broadening), RBS (Rutherford Backscattering Spectrometry) and C-V (capacitance-voltage) profiling, SIMS (Secondary Ion Mass Spectrometry) is one of the most popular analytical techniques because it is an extremely sensitive method and has a detection limit of less than a ppm. Additionally, one does not need to know any stopping mechanisms to interpret the measurements. Today, SIMS is widely used for analysis of trace elements in solid materials, especially semiconductors and thin films. During SIMS analysis, the sample surface is slowly sputtered away. Continuous analysis while sputtering produces information as a function of depth, called a depth profile. When the sputtering rate is extremely slow, the entire analysis can be performed while consuming less than a tenth of an atomic monolayer. This slow sputtering mode is called *static* SIMS in contrast to *dynamic* SIMS used for depth profiles. Considering the merits of SIMS and the limitations of the other techniques in measuring ultra-shallow profiles, SIMS will be the primary technique used in this work. Both static and dynamic SIMS have been employed for range profiling. A brief description of the three main instruments used, namely time-of-flight (ToF), quadrupole (Q) and magnetic-sector (MS), as well as the basic principle behind this technique will be described shortly.

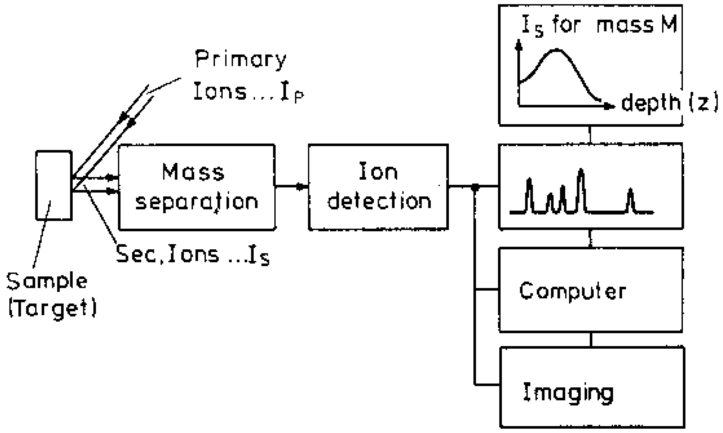

Fig. 2.2 Principles of Secondary Ion Mass Spectrometry (Benninghoven et al., 1987).

Fig. 2.2 shows the principle behind the ion-bombardment-induced-emission process. SIMS utilizes a beam of energetic ions to sputter away a solid surface producing ionized sputtered particles which can be mass spectrometrically detected. In *static* SIMS, a pulsed primary ion beam sputters material from the top monolayer of a sample. Secondary ions are collected and focused into a reflectron **time-of-flight (ToF)** mass spectrometer, where they are separated according to mass. Mass separation is performed by measuring the length of time it takes secondary ions to reach the detector; the lighter the ion, the less time it takes to reach the detector. Highest mass resolution is achieved by using the shortest primary ion pulses; the shorter the pulse, the more precise the determination of the time it takes ions to reach the detector. With *dynamic* SIMS, the surface of a sample is bombarded with a continuous, focused beam of primary ions. The impact of the ions sputters atoms from the surface of the material, producing secondary ions in the process. The secondary ions are then extracted into a mass spectrometer. *Dynamic* SIMS instruments use two kinds of mass analyzers, magnetic sector (MS) and quadrupole (Q). **Magnetic sector (MS)** instruments are most common. Electrostatic and magnetic fields are used to separate the ions according to their mass-to-charge ratio. Ions of different mass-to-charge ratios are measured by changing the strength of the magnetic field. As the ion beam passes through the magnetic field, the particles are acted on by a force at right angles, both to the direction of motion and to the direction of the magnetic field. **Quadrupole (Q)** mass analyzers are shown in Fig. 2.3. Ideally, the rods have hyperbolic shapes, but this geometry can be approximated with closely spaced circular rods. Alternating and direct voltages on the rods cause the ions to oscillate after entering the quadrupole. For a given set of voltages, ions with a single mass-to-charge ratio undergo stable oscillation and traverse through the rods. All other ions have unstable oscillations and strike the rods. The alternating frequency and the ratio between the alternating and direct voltages remain constant. Scanning the voltages scans the mass spectrum.

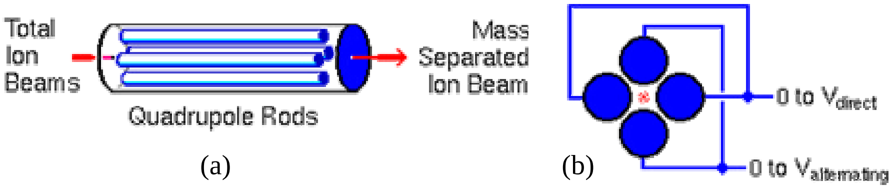

Fig. 2.3 Quadrupole mass analyzer consisting of four circular rods (a) Front view (b) Cross sectional view. Courtesy of Charles Evans Analytical Group.

Depth information on the impurity atoms is provided by recording the intensity of the selected mass as the sputtering process erodes the sample, thus producing the detected signal from increasingly greater depths beneath the original sample surface. The crater thus formed as a result of sputtering is typically a square with sides of a few hundred micrometers. The depth of the crater is measured using a surface profilometer. The intensity of the sputtered ions is monitored by mass spectrometry. Conversion of ion counts to atomic concentration is achieved by using the relative sensitivity factor (RSF). The RSF is a conversion factor dependent on the primary beam species and its energy, as well as the impurity and target species. The RSF is obtained by analyzing a sample from a calibration standard with an accurately known dose.

Besides determination of the elemental composition and the trace levels of impurities and dopants in solid materials, *dynamic* SIMS with a focused scanning ion beam also allows a 3D analysis of the sample (imaging SIMS). Dynamic and imaging SIMS have been and still are applied successfully in semiconductor and integrated circuit analysis. Some of the more important parameters in SIMS analysis include primary ion species, primary ion energy and primary ion beam incident angle. The choice of primary beam species is dictated by the effects of the ion on the SIMS analysis parameters such as the secondary ion yield, detection limit, depth resolution, surface topology formation and sputter rate etc. O_2^+ and Cs^+ are the most frequently used species because of their well-known secondary ion yield enhancement effects. When used as a primary beam, O_2^+ enhances the yield of electropositive secondary ions by several orders of magnitude while Cs^+ increases the yield of electronegative ions. Due to this effect, O_2^+ has become a common choice for electropositive ion species like B, and Cs^+ for electronegative species like P and As. The primary beam energy is also an important parameter. High primary beam energy results in higher primary beam current, better beam focusing as well as greater secondary ion and sputtering yields. However, high energy results in loss of depth resolution due to the atomic mixing caused by the knock-on of target matrix atoms and impurity atoms deeper into the substrate. Therefore, the primary beam energy needs to be optimized by balancing profile broadening, ion yields and ion beam focusing.

In this chapter, typical analytical and atomistic models used for modeling of ion implantation have been reviewed. The physics underlying Monte Carlo and Molecular Dynamics methods were also described. The historical theories leading to present energy loss mechanisms in terms of nuclear and electronic scattering were then explained. The theory and implementation of the main experimental technique used in this work for characterizing of range profiles, SIMS, is next described. In the next chapter, the factors affecting SIMS measurement accuracy, the typical sources of errors and the capabilities and limitations of different mass analyzers used in this work will be discussed in detail.

CHAPTER 3 METHODOLOGY I: MONTE CARLO METHODS

3.1 Theory of Binary Collision Approximation (BCA)

The history of Monte Carlo (MC) methods using the Binary Collision Approximation (BCA) in simulating ion implantation had been described in the previous chapter. MC methods are stochastic techniques, meaning they are based on the use of random numbers and probability statistics to investigate problems. Solving equations, which describe the interactions between two atoms, is fairly simple but solving the same equations for hundreds or thousands of atoms would prove too exhaustive. With MC methods, a large system can be sampled in a number of random configurations, and the data can be used to describe the system as a whole. The essence of MC techniques in the context of modeling ion implantation is to use random methods to locate target atoms as well as random values to obtain collision parameters. The first BCA simulations were reported by Robinson (1963) and Oen et al. (1963) to predict the slowing down of low energy copper atoms in copper substrate. MARLOWE, subsequently developed by Robinson et al. (1974) was one of the very first BCA code developed which employed a crystalline target with all the atoms having well-defined initial positions. The other popular code, TRIM (Biersack et al., 1980) was developed for determining ion ranges and damage distributions as well as angular and energy distributions of backscattered and transmitted ions in *amorphous* targets. It was and still is a very popular code among experimentalists and in the modeling arena. Crystal-TRIM (Posselt et al, 1992, 1994, 1995, 2000) is the main BCA code used in this dissertation. Based on the TRIM code, Crystal-TRIM is able to determine the range of impurities and damage in both amorphous and crystalline substrates and incorporates many new features such as a phenomenological model which treats the enhanced dechanneling of the ions due to damage buildup during implantation and semi-phenomenological models to treat electronic energy loss. The fundamentals of the code will be briefly outlined in the next section after a mathematical representation of the binary collision approximation is presented in this section (Ziegler et al., 1985).

The basic assumption in modeling energy loss due to nuclear collision is that the ion will interact with only one target atom at a time. This simplification allows the use of the binary scattering theory from classical mechanics. The following assumptions are also made in BCA:

1. Prior to a collision with a projectile, target atoms are at rest.
2. The projectiles move in straight lines between binary collisions with target atoms.
3. The motion of recoiled target atoms is not followed (unless in full cascade simulations)

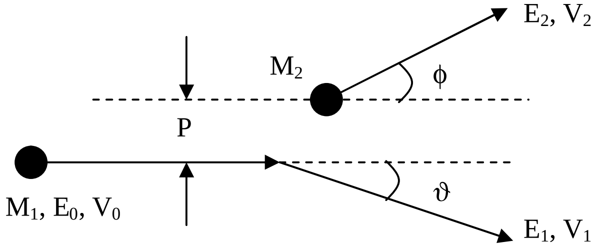

Fig. 3.1 Schematic drawing of two-body scattering theory in laboratory coordinates

Consider Fig. 3.1 where particle 1 (ion) has mass M_1 and initial kinetic energy E_0 and approaches particle 2 (target), an initially stationary particle with mass M_2. The distance, P is called the impact parameter. After collision, the ion will deviate from its original path by an angle ϑ and ϕ is the recoil angle of the target ion. In classical non-relativistic elastic collisions, the following laws of conservation hold for laboratory coordinates:

Conservation of energy (laboratory coordinates):

$$E_0 = \frac{1}{2} M_1 V_0^2 = \frac{1}{2} M_1 V_1^2 + \frac{1}{2} M_2 V_2^2 \tag{3.1}$$

V_0 is the incident velocity of the ion with mass M_1 and V_1 is the ion's final velocity after striking the target atom of mass M_2, which recoils with velocity V_2.

Conservation of momentum (laboratory coordinates):

Longitudinal: $M_1 V_0 = M_1 V_1 \cos\vartheta + M_2 V_2 \cos\phi$ (3.2)

Lateral: $0 = M_1 V_1 \sin\vartheta + M_2 V_2 \sin\phi$ (3.3)

Suppose the problem is restated in centre-of-mass (CM) coordinates rather than laboratory coordinates. This transformation allows the reduction of the relative motion of two particles to that of a single particle moving in a central potential centered at the origin of the CM coordinates, provided the force acts only along the line joining them (no transverse forces). The main advantage of the CM system lies in its ability to describe the mutual interaction of the two colliding particles by a force-field V(r) which only depends on the absolute value of the interatomic separation, r. Hence, there is only one equation of motion, which has r as the independent variable and describes a particle moving in a central force field V(r). Fig. 3.2 shows the same scattering event in CM coordinates in which the total momentum of the system is zero. The coordinate system moves with velocity V_C relative to the laboratory coordinates, and the new angles of scatter and recoil are Θ and Φ respectively.

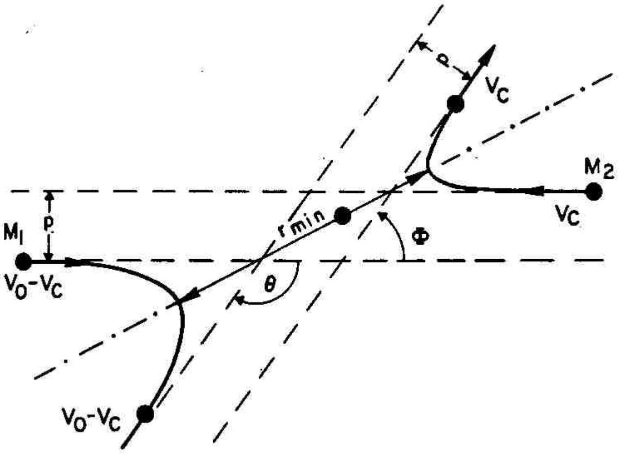

Fig. 3.2 Schematic drawing of two-body scattering theory in center-of-mass coordinates

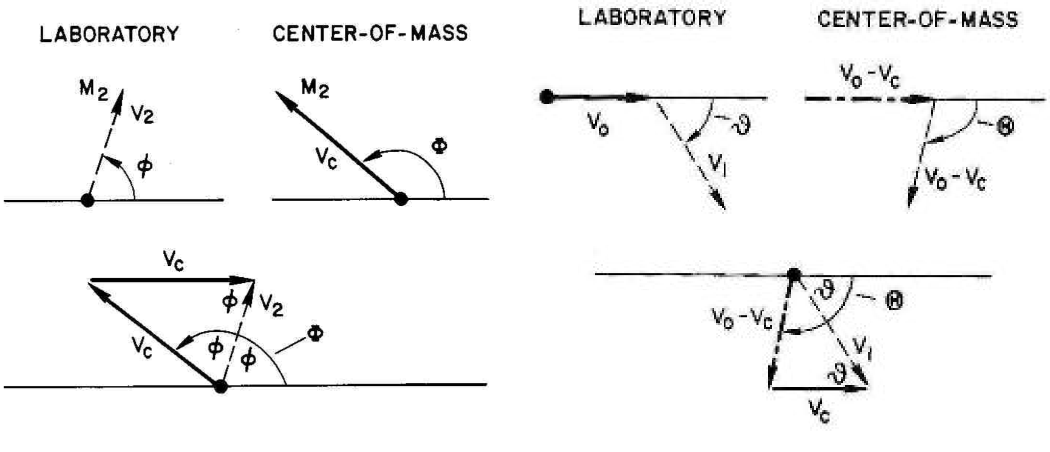

(a) (b)

Fig. 3.3 Angular conversion of center-of-mass coordinates to laboratory coordinates for the (a) target particle and (b) projectile particle (Ziegler et al., 1985)

For CM coordinates, the system velocity, V_C is defined such that there is zero net momentum in the system. A reduced mass, M_C is also defined as in Eq. (3.5)

$$M_1 V_0 = (M_1 + M_2) V_C \tag{3.4}$$

$$\frac{1}{M_C} = \frac{1}{M_1} + \frac{1}{M_2} \text{ or } M_C = \frac{M_1 M_2}{M_1 + M_2} \tag{3.5}$$

Simultaneous solution of Eqs (3.4) and (3.5) yields the CM velocity, V_C.

$$V_C = \frac{M_1 V_0}{M_1 + M_2} = \frac{M_C V_0}{M_2} \tag{3.6}$$

The ion and target velocities are thus given by (see Fig. 3.3)

$$V_{t\arg et} = V_C = \frac{M_C V_0}{M_2} \tag{3.7}$$

$$V_{ion} = V_0 - V_C = \frac{(M_1 + M_2) V_C}{M_1} - V_C$$

$$= \frac{(M_1 + M_2) V_C - M_1 V_C}{M_1} = \frac{M_2 V_C}{M_1} = \frac{M_2 M_C V_0}{M_1 M_2} = \frac{M_C V_0}{M_1} \tag{3.8}$$

Eqs. (3.7) and (3.8) show that the system velocity remains constant and is independent of the final angle of scatter between the two particles. Hence the total linear momentum of the system is always zero and the particle velocities are inversely proportional to their masses.

$$\frac{V_{ion}}{V_{t\arg et}} = \frac{V_0 - V_C}{V_c} = \frac{M_2}{M_1} \tag{3.9}$$

The total CM energy, E_C is equivalent to the initial CM kinetic energy, as in Eq. (3.10)

$$E_C = \frac{1}{2} M_C V_0^2 \tag{3.10}$$

Also shown in Fig. 3.2, the angular momentum, J_C is identical in both systems and is simply related to the impact parameter, P by Eq. (3.11).

$$J_C = M_C V_0 P \tag{3.11}$$

The conversion of scattering angles from CM system to laboratory system, as shown in Fig. 3.3, is straightforward for target-atom recoil because its initial laboratory velocity is zero. Hence, its laboratory final velocity vector, V_2 is related to its CM velocity vector, V_C by the translation vector between the two systems, V_C as defined in Eq. (3.4) to make the total momentum of the system zero. As shown in Fig. 3.3a, the vector triangle is isosceles with two sides equal to V_C, so the two recoil angles can be related as shown in Eq. (3.12) where Φ is the CM analog of the laboratory angle ϕ.

$$F = 2f \tag{3.12}$$

From Fig. 3.2, the projectile CM angle can be related by

$$F = (p - Q) = 2f \tag{3.13}$$

By applying the cosine law, another useful relation can be derived.

$$V_2^2 = V_C^2 + V_C^2 - 2V_C^2\cos(p - 2f) = 2V_C^2[1 - \cos(p - F)] = 2V_C^2(1 - \cos Q) \tag{3.14}$$

Since $\cos(p - 2f) = -\cos(2f)$ and $\cos(2f) = 2\cos^2 f - 1$

$$V_2^2 = 2V_C^2(1 - \cos Q) = 2V_C^2[1 - \cos(p - F)] = 2V_C^2[1 - \cos(p - 2f)] = 2V_C^2\{1 - [-\cos(2f)]\}$$

$$= 2V_C^2[1 + \cos(2f)] = 2V_C^2\left[1 + \left(2\cos^2 f - 1\right)\right] = 4V_C^2\cos^2 f$$

$$\therefore V_2 = 2V_C\cos f = \frac{2V_0M_C\cos f}{M_2} \tag{3.15}$$

Eq. (3.15) relates the final recoil velocity to the laboratory angle of recoil. The energy transferred in the collision from the incident projectile to the target projectile, T can thus be given by Eq. (3.16).

$$T = \frac{1}{2}M_2V_2^2 = \frac{1}{2}M_2\left(\frac{2V_0M_C\cos f}{M_2}\right)^2 = \frac{2}{M_2}\left(V_0M_C\cos f\right)^2 \tag{3.16}$$

Relating Eq. (3.16) back to the angle of scatter of the projectile by using Eq. (3.13) gives

$$T = \frac{2}{M_2}\left(V_0M_C\cos f\right)^2 = \frac{2}{M_2}\left[V_0M_C\cos\frac{(p - Q)}{2}\right]^2 = \frac{2}{M_2}\left(V_0M_C\sin\frac{Q}{2}\right)^2$$

$$= \frac{2V_0^2M_C^2}{M_2}\sin^2\frac{Q}{2} = \frac{4E_CM_C}{M_2}\sin^2\frac{Q}{2} = \frac{4}{M_2}\sin^2\frac{Q}{2}\left(\frac{1}{2}M_CV_0^2\right)\left(\frac{M_1M_2}{M_1 + M_2}\right)$$

$$= \frac{4\sin^2 Q/2}{M_2}\left[\frac{1}{2}V_0^2\left(\frac{M_1M_2}{M_1 + M_2}\right)^2\right] = \frac{4M_1M_2\sin^2 Q/2}{(M_1 + M_2)^2}\left(\frac{1}{2}M_1V_0^2\right) = \frac{4E_0M_1M_2}{(M_1 + M_2)^2}\sin^2\frac{Q}{2} \tag{3.17}$$

Eq. (3.17) gives the energy lost by the projectile (ion) to the target particle during a scattering event. To eventually obtain the stopping cross section for the energy transferred the probability for each final scattering angle must be known and this can be obtained by evaluating the details of the scattering trajectory and hence the probability of scatter into each scattering angle. Because the total linear momentum in the CM system is zero, the two-body problem is reduced to a one-body problem centered at the origin of the CM coordinates (Fig. 3.2) and the evaluation of one particle's path gives the path of the other particle. Hence, an important assumption is that the force between the two particles acts only along the line joining them, and there are no transverse forces. The derivation of the complete particle scattering will be shown here in polar coordinates for the vector connecting the projectile and the target atom. The azimuthal polar coordinate will be given by Θ and the radial coordinate by r. The time derivatives of motion in polar coordinates will be given by $\dot{r} = dr/dt$ and $\dot{Q} = dQ/dt$.

Conservation of energy (CM coordinates):

$$E_C = \frac{1}{2} M_C \left(\dot{r}^2 + r^2 \dot{Q}^2 \right) + V(r) \tag{3.18}$$

E_C is the same CM energy shown in Eq. (3.10) given in polar coordinates.

Conservation of angular momentum (CM coordinates):

$$J_C = M_C r^2 \dot{Q} \tag{3.19}$$

The laboratory analog of the constant of angular momentum had been given in Eq. (3.11). Elimination of J_C by combining Eqs. (3.11) and (3.19) gives

$$J_C = M_C r^2 \dot{Q} = M_C V_0 P \Rightarrow \dot{Q} = \frac{V_0 P}{r^2} \tag{3.20}$$

Substituting Eq. (3.20) into Eq. (3.18) gives us an expression for the radial equation of motion.

$$E_C = \frac{1}{2} M_C \left(\dot{r}^2 + r^2 \dot{Q}^2 \right) + V(r) = \frac{1}{2} M_C \left[\dot{r}^2 + r^2 \left(\frac{V_0 P}{r^2} \right)^2 \right] + V(r) = \frac{1}{2} M_C \left[\dot{r}^2 + \left(\frac{V_0 P}{r} \right)^2 \right] + V(r)$$

$$\dot{r}^2 = \frac{2E_C - 2V(r)}{M_C} - \left(\frac{V_0 P}{r} \right)^2 = \frac{2\left(1/2\, M_C V_0^2\right) - 2V(r)}{M_C} - \left(\frac{V_0 P}{r} \right)^2 = \frac{M_C V_0^2 - 2V(r)}{M_C} - \left(\frac{V_0 P}{r} \right)^2$$

$$= V_0^2 \left[\frac{M_C - 2V(r)/V_0^2}{M_C} - \left(\frac{P}{r} \right)^2 \right] = V_0^2 \left[1 - \frac{V(r)}{\frac{1}{2} M_C V_0^2} - \left(\frac{P}{r} \right)^2 \right] = V_0^2 \left[1 - \frac{V(r)}{E_c} - \left(\frac{P}{r} \right)^2 \right]$$

$$\therefore \dot{r} = \frac{dr}{dt} = V_0 \left[1 - \frac{V(r)}{E_c} - \left(\frac{P}{r} \right)^2 \right]^{1/2} \tag{3.21}$$

Combining Eqs (3.20) and (3.21) gives

$$\frac{dQ}{dr} = \frac{dQ}{dt}\frac{dt}{dr} = \frac{\dot{Q}}{\dot{r}} = \frac{P}{r^2 \left[1 - \frac{V(r)}{E_C} - \left(\frac{P}{r} \right)^2 \right]^{1/2}} \tag{3.22}$$

Integration of Eq. (3.22) over the entire collision path, and taking into account the initial value Θ = π, the final expression can be found to be

$$Q = p - \int_{-\infty}^{\infty} \frac{Pdr}{r^2 \left[1 - \frac{V(r)}{E_C} - \left(\frac{P}{r} \right)^2 \right]^{1/2}} \tag{3.23}$$

This equation allows the evaluation of the final angle of scatter, Θ in terms of the initial CM energy, E_C, the potential, V(r) and the impact parameter, P. Eq. (3.23) is also called the *general orbit equation for two-body central force scattering*, or sometimes the *classical scattering integral*. There are two conditions for its use:

1. The central force potentials of each particle must not vary with time, nor depend on the particle's motion. Hence, the potential must be spherically symmetric.
2. The laws of conservation of energy and momentum must hold for the system as a whole.

3.2 Monte Carlo BCA code Crystal-TRIM

The Monte Carlo BCA code, Crystal-TRIM (Posselt et al, 2000) is the main BCA code used in this dissertation. It allows the atomistic simulation of ion implantation by describing the motion of randomly generated energetic pseudo-particles by sequences of binary collisions with target atoms in the closest environment. At each collision, the momentum of the projectile is changed due to elastic nuclear scattering and inelastic electronic energy loss. Of the three basic assumptions given in Sec. 3.1, the first two assumptions are made in the treatment of binary collisions in Crystal-TRIM; it is also assumed that the change in target composition during implantation is neglected. For all the simulations done in this work, full cascade simulations were performed. This means that not only the motion of the incident ions is followed but also the trajectories of energetic target atoms in collision cascades. Though computationally more demanding, full cascade simulations yield physically correct profiles of ballistically produced vacancies and displaced atoms. It should also be noted that two coordinate systems are used in the algorithm, the crystal system and the target system. The motion of projectiles is described within the crystal system while the target system is employed to register physical quantities of interest like the number of stopped projectiles, the nuclear and electronic energy deposition and the number of displaced atoms in a certain volume element of the target. Ion incidence, backscattering and transmission are also described within the target system. The fundamentals of the code will be outlined in the following subsections, particularly the treatment of nuclear effects with the use of a “universal” repulsive potential, semi-phenomenological models for treatment of electronic stopping, the phenomenological model which treats the enhanced dechanneling of the ions due to damage buildup during implantation, the trajectory split algorithm and the lateral duplication method developed to increase the efficiency of the BCA simulation, as well as the integration of the Crystal-TRIM code into a multi-dimensional process simulator for the silicon technology. Its capabilities and limitations in predicting the depth profiles of ions in amorphous and single-crystalline silicon in different energy regimes and beam orientations will also be investigated by comparisons with available experimental data, particularly its ability to describe the dose dependence of the shape of dopant depth distributions, the formation of amorphous layers, and the influence of the level of pre-damage on the 1D profiles of subsequently implanted ions which affects the channeling of the incident projectiles.

3.2.1 Nuclear energy loss: ZBL universal potential

From the mathematical treatment of binary collisions using classical mechanics shown in the previous section, Eq. (3.17) shows that the energy loss during the scattering event is not only a function of the initial kinetic energy, the masses of the two particles, but also of the scattering angle, Θ which is in turn a function of a central force potential V(r). The elastic interaction between the projectile and the target atom is described by the solely repulsive “universal” ZBL potential (Ziegler et al., 1985) in Crystal-TRIM.

$$V_{ZBL}(r) = \frac{Z_1 Z_2 e^2}{r} \boldsymbol{F}\left(\frac{r}{a}\right) \tag{3.24}$$

Z_1 and Z_2 are the atomic numbers, r is the interatomic separation and a is a screening parameter. The ZBL potential, named after Ziegler, Biersack and Littmark, consisted of a Coulombic term (1/r) arising from the positive point nucleus and a screening function Φ due to the surrounding electron cloud. The screening function can be defined as the ratio of the atomic potential at some radius to the potential caused by an unscreened nucleus. The calculation of the screening function (and hence the interatomic potential) had been done by Ziegler et al. (1985) using a simplified quantum mechanical approach. This method begins with two atomic charge distributions of two Hartree-Fock atoms and as the two atoms approach, the total interaction potential energy can be calculated based on self-consistent-field methods.

$$V = V_{NN} + V_{EN} + V_{EE} + V_K + V_A \tag{3.25}$$

V_{NN} = Electrostatic potential energy between the nuclei

V_{EN} = Interaction energy between each nucleus and the other electron distribution

V_{EE} = Pure electrostatic interaction energy between the two electron distributions

V_K = Increase in kinetic energy of the electrons in the overlap region due to Pauli excitation

V_A = Increase in exchange energy of these electrons

The advantage of this procedure lies in its application to any two atoms as long as the two charge distributions are given. The aim was to find a single analytical screening function which can accurately predict the interatomic potential between any two atoms. Since the study of *all* atom-atom combinations was too exhaustive, 261 atoms pairs were randomly selected from all stable atomic numbers to form a representative group of interatomic potentials. Each of the interatomic screening functions was then fit with a series of three exponentials.

$$F(\mathrm{x}) = \sum_{\mathrm{i}=1}^{3} \mathrm{A_i} \exp(-\mathrm{B_i x}) \tag{3.26}$$

where x = r/a, A_i and B_i are the fitting coefficients. The summation of the A_i coefficients must equate to one so that for x= 0, the screening function Φ = 1.

$$\sum_{\mathrm{i}=1}^{3} \mathrm{A_i} = 1 \tag{3.27}$$

The final universal screening function obtained after fitting the screening functions for the 261 atom pairs is given in Eq. (3.28); x= r/a.

$$F(\mathrm{x}) = 0.1818\mathrm{e}^{-3.2\mathrm{x}} + 0.5099\mathrm{e}^{-0.9423\mathrm{x}} + 0.2802\mathrm{e}^{-0.4028\mathrm{x}} + 0.02817\mathrm{e}^{-0.2016\mathrm{x}} \tag{3.28}$$

The universal screening parameter, a, given by Eq. (3.29) where a_0 is the Bohr radius was found to give a tighter grouping, compared to the screening lengths given by Bohr (1948) or Firsov (1953) which had been shown previously in Eqs. (2.10) and (2.11).

$$\mathrm{a_{ZBL}} = \frac{0.8854\mathrm{a_0}}{\mathrm{Z_1^{0.23} + Z_2^{0.23}}} \tag{3.29}$$

The universal ZBL potential, described by a single analytical function can be easily calculated for various ion-target pairs and this has been done for nine industrially common dopants (B, C, N, F, P, Ge, As, In and Sb) with silicon as the target atom, as shown in Fig. 3.4. $V_{ZBL}(r)$ have been calculated from r=0Å to r=10Å at regular intervals of 0.1Å. However, only values up to r=4Å are displayed since the potential approaches zero as r approaches infinity. Mathematically, this is depicted in the decaying exponential terms in the screening function as r goes to infinity. Physically, we know that as the two atoms move away from each other, the field effect of one atom on the other diminishes until the total energy of the two atoms approaches that of two isolated atoms, i.e. zero. On the other hand, as r approaches zero, the screening function approaches one, and the force field governing the two atoms is a pure Coulombic interaction, increasing to infinite values as the electron clouds of the two atoms overlap. The large positive values represent strong repulsive forces between the two atoms, and it is this highly repulsive region that governs the trajectories of ions at high velocities. On the other hand, the absence of attractive forces (negative energies) while inconsequential at high velocities, play a significant role at low velocities, especially for heavy ions. This effect of the ZBL repulsive potential on the range profiles for different elements with different energies will be investigated and compared against *ab-initio* potentials calculated from density functional theory in the next chapter. From Fig. 3.4, it is also shown that with increasing atomic mass, the absolute potential energies increases. For example, at an interatomic separation of 1Å from the target atom Si, a light ion like B (atomic mass 10.81) possesses a repulsive force (24eV) 5 times weaker than the force between the heavier Sb (atomic mass 121.75) and Si (117eV). This can be largely explained by their electronic configurations. B [$1s^2$ $2s^2$ $2p^1$] is much less shielded from the silicon atom compared to a heavier atom like Sb [$1s^2$ $2s^2$ $2p^6$ $3s^2$ $3p^6$ $3d^{10}$ $4s^2$ $4p^6$ $4d^{10}$ $5s^2$ $5p^3$] whose d electrons provide stronger screening and hence a greater repulsive force from the approaching silicon. The ZBL potential had been further reviewed by comparisons with 106 experimentally determined potentials (Ziegler et al, 1985) and a maximum deviation of 5% could be achieved.

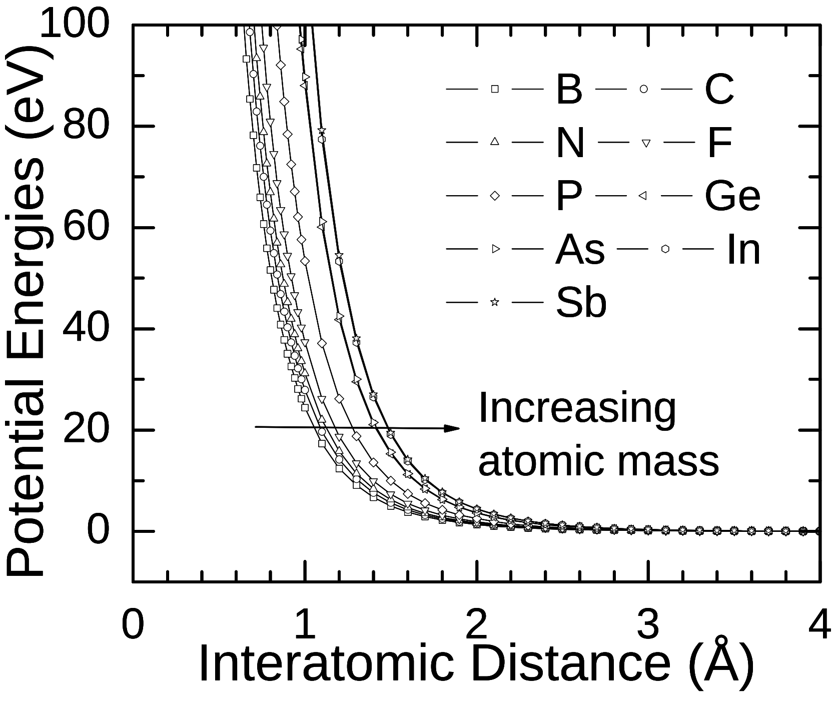

Fig. 3.4 Energies (in eV) obtained from the ZBL universal potential function for nine dopants (B, C, N, F, P, Ge, As, In and Sb)

Based on the energy loss and classical scattering integral derived in Sec. 3.1, the average energy transferred when summed over all impact parameters had also been derived by Ziegler et al. (1985) and the universal nuclear stopping power can be given analytically as

$$S_n(E_0) = \frac{8.462\times10^{-15} Z_1 Z_2 M_1 S_n(e)}{(M_1 + M_2)(Z_1^{0.23} + Z_2^{0.23})} \tag{3.30}$$

The reduced energy, ε is given by

$$e = \frac{32.53 M_2 E_0}{Z_1 Z_2 (M_1 + M_2)(Z_1^{0.23} + Z_2^{0.23})} \tag{3.31}$$

The reduced nuclear stopping, $S_n(\varepsilon)$ is given by the following formulae.

For ε≤30keV: $$S_n(e) = \frac{\mathrm{In}(1 + 1.1383e)}{2(e + 0.01321e^{0.21226} + 0.19593e^{0.5})} \tag{3.32}$$

For ε>30keV: $$S_n(e) = \frac{\ln(e)}{2e} \tag{3.33}$$

Fig. 3.5 shows the universal nuclear stopping in eV/atom/cm^2 for the same nine elements calculated over the energy range 10^{-8} to 10^8 eV.

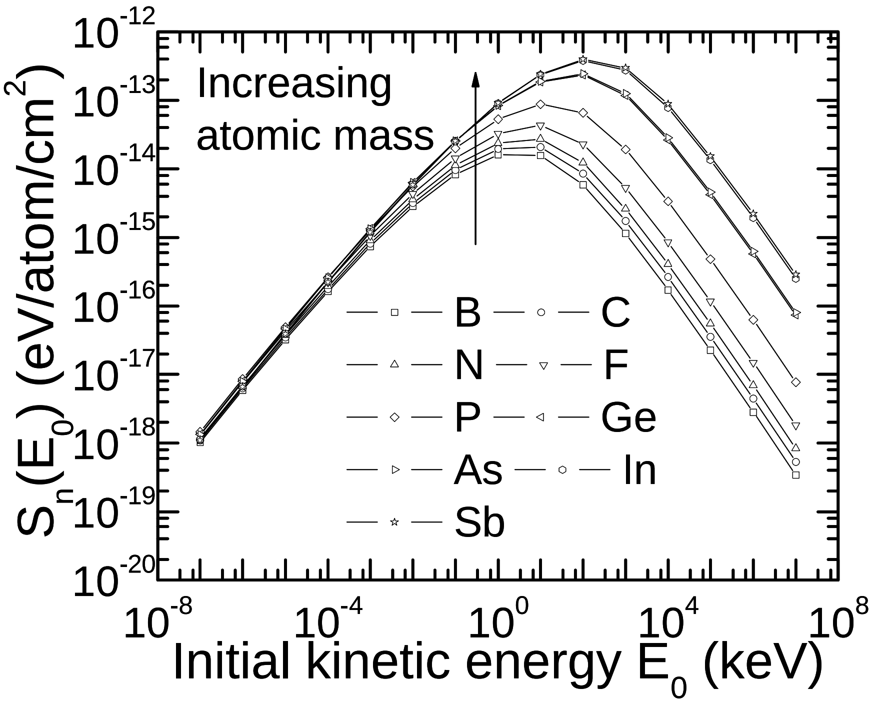

Fig. 3.5 Universal nuclear stopping in eV/atom/cm^2 for nine dopants (B, C, N, F, P, Ge, As, In and Sb)

The stopping power due to nuclear effects increases with atomic mass; the difference being greater as initial kinetic energy increases. This is reflected in Eq. (3.30) where $S_n(E_0)$ is largely a function of the masses and the initial kinetic energy. It is also understandable in view of the energy and momentum transferred during the collision process. High mass ions like In and Sb approaches the target with greater momentum as compared to light ions and hence the nuclear energy deposited to the primary knock-on atom by the incident ion is larger. This also implies that the amount of post-implantation damage created in the initially pristine silicon is larger for heavier ions than light ions. Fig. 3.5 also shows that for all the elements there is an optimum energy beyond which nuclear stopping decreases as energy increases. As the ion approaches with higher velocities, nuclear stopping is no longer the dominant mode of energy transfer. Electrons from the target atoms penetrate the ion’s electronic shells and electronic energy loss increases because there is less shielding of the nucleus. The electronic energy stopping model used in Crystal-TRIM will be described in the next section.

3.2.2 Electronic energy loss: ZBL and Oen-Robinson model

Electronic excitations at a binary collision and between two collisions are described by the inelastic electronic energy loss of the projectile. Two semi-phenomenological models are used to treat this effect. In the simulation of ion implantation into amorphous targets the spatial variation of the electron density in the target is generally not relevant. Hence, the so-called non-local approach is employed using the ZBL formula (Ziegler et al, 1985) which uses an average density of the electrons. Like many other non-local models, the ZBL model is based on the Brandt-Kitagawa (BK) (Brandt et al., 1982) theory. Because it does not directly account for the quantum mechanical stopping cross section between an ion and the target atom electrons and makes simplifying assumptions of the shape of the electron clouds, all models based on the BK theory are more or less phenomenological in nature. The electronic stopping of a heavy ion is factorized into two components, the effective charge Z_{eff} and the electronic stopping of a proton S_p, as shown in Eq. (3.34).

$$S_{el}^{BK} = Z_{eff}^{2} S_{p}\left(\rho, \nu\right) \tag{3.34}$$

The local electron density is given by ρ and ν is the velocity of the ion. According to the BK theory, the Fermi velocity of the target electrons is determined by Eq. (3.35) where r_s, given by Eq. (3.36) is the one-electron radius of the centrosymmetric charge distribution of density ρ given by Eq. (3.37) and α is a constant given by Eq. (3.38). Λ is the screening length which describes how electrons screen the nucleus while N is the number of electrons bound to the ion.

$$\nu_{F} = \frac{1}{\alpha r_{s}} \tag{3.35}$$

$$r_{s} = \left(\frac{3}{4\pi\rho}\right)^{1/3} \tag{3.36}$$

$$\rho\left(r\right) = \frac{N}{4\pi\Lambda^{2} r} \exp\left(-\frac{r}{\Lambda}\right) \tag{3.37}$$

$$\alpha = \left(\frac{4}{9\pi}\right)^{1/3} \tag{3.38}$$

The velocity of the ion relative to the electrons, ν_r can be calculated as (Kreussler et al., 1981)

$$\nu_{r} = \begin{cases} \nu\left(1 + \dfrac{\nu_{F}^{2}}{5\nu^{2}}\right); \nu \geq \nu \\ \dfrac{3\nu}{4}\left(1 + \dfrac{2\nu^{2}}{3\nu_{F}^{2}} - \dfrac{\nu^{4}}{15\nu_{F}^{4}}\right); \nu \leq \nu_{F} \end{cases} \tag{3.39}$$

The BK theory assumes that electrons with orbital velocities less than v_r are stripped (Mann et al., 1981) (Ziegler et al., 1985). The reduced relative velocity is defined as

$$y_{r} = \frac{\nu_{r}}{Z_{1}^{2/3}} \tag{3.40}$$

The screening length, Λ can be expressed in terms of the charge fraction q, by solving for the internal energy of the ion and is shown in Eq. (3.41).

$$\Lambda = \frac{2b\left(1-q\right)^{2/3}}{Z_{1}^{2/3}\left[1 - \left(1-q\right)/7\right]} \tag{3.41}$$

The value of constant b is 0.24005 and the charge fraction, q is defined by Eq. (3.42).

$$q = \frac{Z_1 - N}{Z_1} \tag{3.42}$$

Based on fits to experimental data, Ziegler et al. (1985) obtained an expression for q as a function of the reduced relative velocity y_r.

$$q = 1 - \exp[-0.95(y_r - 0.07)] \tag{3.43}$$

However, use of Eq. (3.43) is restricted to $y_r > 0.1$ as there is very little experimental data below this velocity. When $y_r < 0.07$, negative q values will result, which infers that ion will gain electrons rather than lose them. This is clearly nonphysical. An expression for low velocities is desirable but still lacking.

Since the effective charge Z_{eff} can be expressed by the multiplication of the ion charge Z_1 by a correction factor, γ and q is given by Eq. (3.43), Z_{eff} is defined as

$$Z_{eff} = gZ_1 \tag{3.44}$$

where $$g = q + C(1-q)\ln\left[1 + \left(\frac{4L}{r_s}\right)^2\right] \tag{3.45}$$

The first term in Eq. (3.45) describes distant collisions, where electrons see only the charge q. The second term describes close collisions where the electrons have penetrated the electron cloud of the ion. The constant C takes a value of ~0.5 and is weakly dependent on r_s. C has a larger value when r_s is large (small electron density). With the effective charge defined, all that is needed is the stopping of proton, $S_p(\rho, \nu)$ to fully evaluate the electronic stopping. In the ZBL model, the stopping of protons is obtained from a fit of eight parameters that have different values in each elemental target material. The ZBL model is reasonably accurate because of the number of free parameters; hence it is easy to calculate for any material. However, it cannot be used in cases where channeling is predominant since it is a non-local parameterization. In addition, the value of the Fermi velocity in the ZBL model is a constant depending on the target material and can have an empirical correction factor. This implies that the electron density is not spatially varying but treated as constant (thus non-local model). The ion screening lengths can also have an empirical correction factors.

If implantation into single-crystalline targets is considered the local approach has to be used. In a local model, the electronic energy loss in a collision of the projectile with a target atom depends on the impact parameter, P (as shown in Fig. 3.1) i.e. it is determined by the density of the electrons on the path of the projectile. On the other hand, a non-local model is independent of the impact parameter. Hence, local models are able to describe more realistically the physics involved in the motion of a projectile in a crystalline target than non-local models and are prerequisites for the correct description of the channeling effect occurring in implantations into single crystals. Non-local models are mainly employed in the case of amorphous targets. However, it was found that for medium and high energy implantation of P, B and N, known local models did not give satisfactory results for all directions of ion incidence considered (Posselt, 1994). Hence, the modified semi-empirical Oen-Robinson formula is employed in Crystal-TRIM (Oen et al., 1976) and is given by the expression shown in Eq. (3.46).

$$D\mathrm{E}_{\mathrm{el}} = \mathrm{S}_{\mathrm{el}}^{\mathrm{ZBL}} \frac{\exp\left\{-0.3\mathrm{C}_{\mathrm{el}}\left[\mathrm{R}_0\left(\mathrm{E}_0,\mathrm{P}\right)\big/\mathrm{a}\right]\right\}}{\int_0^{\mathrm{P}_{\mathrm{Max}}} 2p\mathrm{PdP}\exp\left\{-0.3\mathrm{C}_{\mathrm{el}}\left[\mathrm{R}_0\left(\mathrm{E}_0,\mathrm{P}\right)\big/\mathrm{a}\right]\right\}} \tag{3.46}$$

Where $\mathrm{R}_0(\mathrm{E}_0,\mathrm{P})$ is the distance of closest approach in a binary collision and the function $\mathrm{S}_{\mathrm{el}}^{\mathrm{ZBL}}$ is the ZBL electronic stopping cross-section which was obtained from a comprehensive database. $D\mathrm{E}_{\mathrm{el}}\left(\mathrm{E}_0,\mathrm{P}\right)$ is normalized to the ZBL stopping cross section where P_{Max} is the maximum impact parameter in the binary collision code which implies that in amorphous simulations, the use of $D\mathrm{E}_{\mathrm{el}}\left(\mathrm{E}_0,\mathrm{P}\right)$ would be nearly equivalent to the use of the ZBL electronic cross section if in both cases the same P_{Max} is employed. This normalization is a reasonable but restrictive condition for the values of $D\mathrm{E}_{\mathrm{el}}\left(\mathrm{E}_0,\mathrm{P}\right)$. To enhance computational speed, the values of $D\mathrm{E}_{\mathrm{el}}\left(\mathrm{E}_0,\mathrm{P}\right)$ are calculated for given values of E_0 and P before the simulation of motion of projectile starts. The empirical parameter C_{el} describes the variation of the electron density as the projectile moves in the <110> direction of the single-crystalline silicon and in any other direction. It is adjusted to the values of the maximum penetration depth obtained from experimental range profiles of channeling implants at low doses where damage accumulation is negligible. The actual values depend on the atomic number and energy of the projectile. For a given implantation energy, nearly the same C_{el} value is found for all directions of ion incidence with the exception of the open <110> channel where channeling is most predominant (Murthy et al., 1996).

The mechanisms of the electronic energy loss are still not fully understood, partly because electrons, unlike nuclei cannot be treated as point masses and an accurate description of electronic stopping is much harder to attain. Unlike the "universal" model for nuclear stopping, there exist many models attempting to describe electronic stopping at low and high velocities. Fig. 3.6 shows the non-local ZBL electronic energy loss in eV/atom/cm^2 calculated for nine ions. Based on the stopping calculated, the elements can generally be classified into two groups. Lighter elements like B, C, N, F and P experience a maximum in the stopping, which is located at $\approx 10^3$keV. Beyond this maximum, stopping decreases as velocity increases. Heavier elements like Ge, As, Sb and In experience a minimum instead at approximately the same energy beyond which stopping increases slowly with incoming velocity. The velocity dependence is a result of two competing phenomena; on one hand, the charge state of an ion increases as its velocity increases, on the other hand, the larger the velocity, the shorter the interaction time. At velocities beyond the maximum, the electronic stopping can be predicted relatively accurately within the framework of the Bethe-Bloch model (Bethe, 1928) (Bloch, 1928, 1933). Prediction is, however more challenging particularly near the maximum.

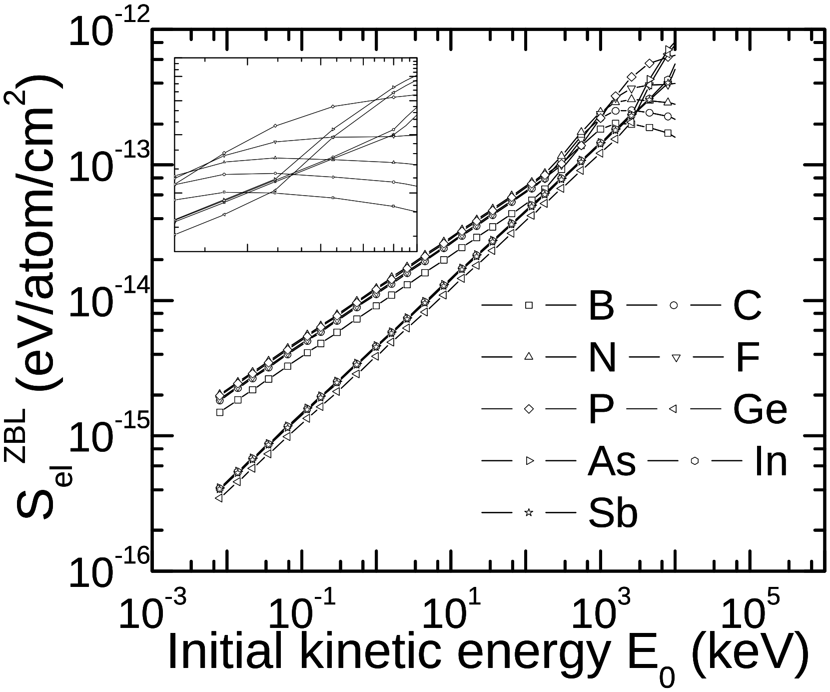

Fig. 3.6 ZBL electronic stopping in eV/atom/cm^2 for nine dopants (B, C, N, F, P, Ge, As, In and Sb). Inset shows electronic stopping between 10^3<E0<10^4 eV.

Fig. 3.7 shows the relative importance of nuclear and electronic stopping in different energy regimes for B and Sb only. Both stopping are described by the ZBL models. In the low energy regime, it is clear that nuclear effects dominate, which increases the importance of the interatomic potential used. This is intuitive when one considers the effect of neighboring atoms on the charged projectile as the ion slows down. At such low energies, the ion has ample time to interact with the target atoms, and hence the importance of nuclei-nuclei interactions is enhanced. On the other hand, at high energies, the fast-moving ion can only experience the polarization effect of the target electron clouds as a whole, similar to a frictional drag force. As the charge state of the ion increases with increasing velocity, the energy loss due to electronic effects increases further, while nuclear stopping diminishes before it becomes negligible in the MeV regime. The threshold energy beyond which electronic stopping dominates increases with atomic mass, as shown in Fig. 3.7, implying that nuclear effects remain important up till higher energies for heavier ions. Based on the reasoning of their electronic configurations explained earlier, heavy ions like Sb provide greater shell screening against the target nuclei and hence a larger repulsive force. The larger screening envelope means that an atom like Sb can move through the crystal lattice at higher velocities before it is significantly affected by the electronic stopping effects of the target electron clouds.

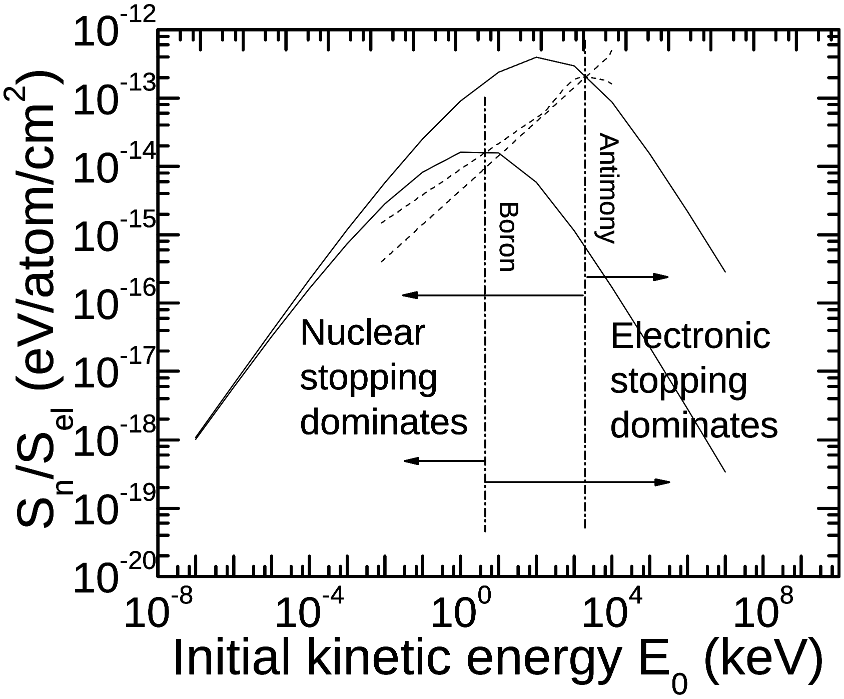

Fig. 3.7 Relative importance of nuclear (ZBL) and electronic (ZBL) stopping for B and Sb in different energy regimes

Fig. 3.8 shows the comparison between the electronic stopping model used in Crystal-TRIM against other known models for B only. This includes the classical non-local Lindhard-Scharff (LS) formula (Lindhard et al., 1961) shown in Eq. (3.47). It assumes that energy loss is proportional to ion velocity and is useful for incident ions that are heavier than the target atoms.

$$S_{el}^{LS} = k_{LS}\sqrt{E_0} = \frac{1.212 Z_1^{7/6} Z_2}{\left(Z_1^{2/3} + Z_2^{2/3}\right)^{3/2} m_1^{1/2}} \sqrt{E_0} \qquad (3.47)$$

This model is highly successful when it is applied to implants in amorphous materials or random equivalent orientation (REO) implants into crystals, especially when a correction factor is used. The correction factor arises due to shell correction to the Thomas-Fermi atoms (Thomas, 1927) (Fermi, 1927) upon which the LS model is based. Due to its average nature, the LS model significantly overestimates the stopping power in the channeling directions where the electron density is lower. Based on the pioneering work of Lindhard, Ma et al. (1992) also calculated the energy loss for a charged particle traveling in a degenerate electron gas within the framework of linear-response theory. All of the calculations were based on the random-phase approximation (RPA) dielectric function. The model of Ma et al. (1992) is also shown in Fig. 3.8 for B. It is known that the modified Oen-Robinson model in Crystal-TRIM alone cannot predict the <100> and <110> channels with the same set of C_{el} parameters (Posselt, 1994). Tian (2003) presented an improved semi-empirical model which has been shown to be able to predict the stopping in different channels without adjusting the parameters. It is a combination of the local part of the Oen-Robinson model and the non-local part of the Lindhard-Scharff model. Tian's model, which is used in codes like IMSIL (Hobler et al., 1987) and UT-Marlowe (Tian, 2003) is also shown in Fig. 3.8.

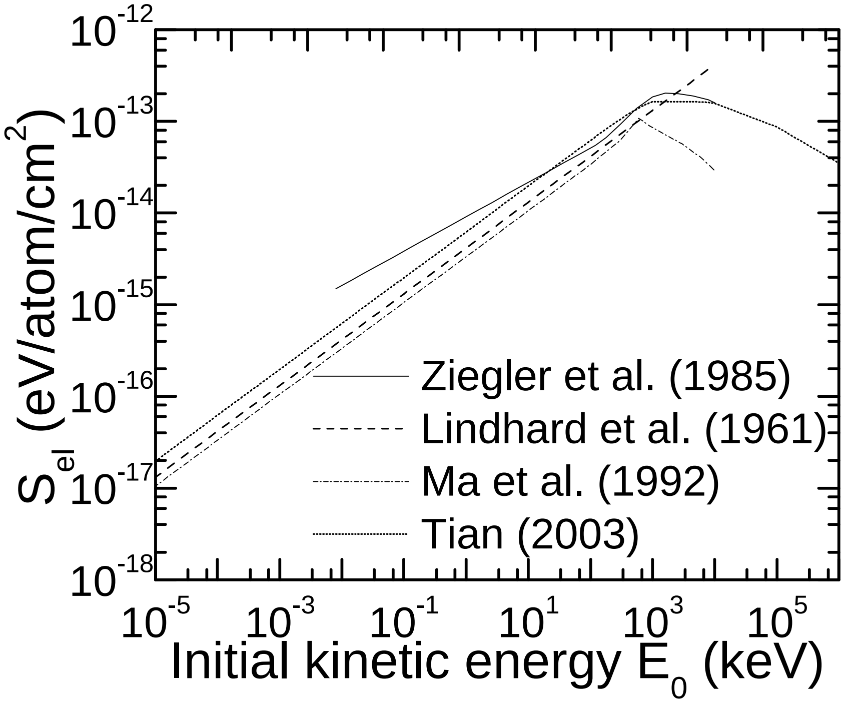

Fig. 3.8 Different electronic stopping models compared against the non-local ZBL model for B only

All the models except the LS model show proportionality with energy up till the maximum beyond which stopping decreases with energy. As mentioned earlier, the ZBL model is reasonably accurate because of the number of free parameters but inaccurate when channeling becomes predominant since it is a non-local parameterization. Similarly, the LS model, and the inspired model of Ma et al. (which was based much on the LS model) predict a proportional relationship between the ion's velocity and the resulting electronic stopping. These models are well-known but the transition between the linear and non-linear regions have yet to achieve universal recognition. Tian's model, on the other hand attempts to account for local parameterization; his work showed excellent agreement with experimentally measured profiles. Though it involves semi-empirical parameters, his work suggests that accounting for localized stopping is necessary to achieve accurate range profiles especially in channeling conditions. The mathematical formulation of Ma and Tian's models are given in Appendix A.

3.2.3 Damage accumulation model

During ion implantation, ballistic atomic displacements initiate the production of radiation defects. Increase in implantation dose results in an accumulation of such defects, which include not only point defects (vacancies and self-interstitials) but also a considerable amount of more complex defects and amorphous pockets. At sufficiently high ion doses, parts of the target crystalline silicon become amorphized. The damage buildup leads to enhanced dechanneling of the implanted ions which in turn, leads to an alteration of the shape of the dopant profiles with growing dose. In order to simulate defect accumulation, the treatment of ion impact into a dynamically changing target structure is required. Due to the lack of detailed microscopic information about the type and the amount of defects created, the damage buildup in Crystal-TRIM is described by a phenomenological model (Posselt et al., 1997). A statistical approach is employed where only the trajectory of the incident ions is followed, hence computational time is saved. The nuclear and electronic energy depositions by recoils in the collision cascade are calculated from the elastic energy transfers of the ion to the primary-knock-on atoms using an analytical formula of Robinson (1970). The energy deposition of the subcascades is assumed to take place where the collision between the ion and the primary-knock-on-atom (PKA) occurs. This approximation is justified provided the range covered by the subcascade initiated by the PKA is small compared to the ion range. This assumption has been proven to be valid even in the case of heavy ion implants (Simionescu et al., 1995).

In the statistical model the ion dose D, is simulated by N pseudo-projectiles. The probability, P_d, that in a certain depth interval of the target a pseudo-projectile is moving in a damaged region is given by Eq. (3.48) where f_d is a damage accumulation function depending on the nuclear energy deposition E_n^A per target atom in the given depth interval deposited by all previous pseudo-projectiles, and on certain empirical parameters C_1 to C_m. The term f_d allows the consideration of various defect types; hence the exact expression for f_d depends on the defect type relevant in the respective damage accumulation model.

$$P_d = f_d\left(E_n^A, C_1 ... C_m\right) \tag{3.48}$$

In Crystal-TRIM, different damage accumulation functions may be employed. Super-linear and sub-linear growth of the defects are modeled by

$$f_d = \begin{Bmatrix} C_a N_d^A \\ P_s \quad \text{or} \quad 1 \end{Bmatrix} \text{if } C_a N_d^A \begin{Bmatrix} \le P_s \\ > P_s \end{Bmatrix} \tag{3.49}$$

or

$$f_d = \begin{Bmatrix} C_a\left[1-\exp\left(-N_d^A\right)\right] \\ P_s \quad \text{or} \quad 1 \end{Bmatrix} \text{if } C_a\left[1-\exp\left(-N_d^A\right)\right] \begin{Bmatrix} \le P_s \\ > P_s \end{Bmatrix} \tag{3.50}$$

where the number of displacements per target atom N_d^A is related to E_n^A via the modified Kinchin-Pease formula (Kinchin et al., 1955) shown in Eq. (3.51) where E_d is the displacement energy of silicon (15eV) and $P_s \le 1$ is the saturation level of the sub-linear growth or the critical value for the onset of the super-linear increase of the damage.

$$N_d^A = \frac{0.4 E_n^A}{E_d} \tag{3.51}$$

During the simulation of the motion of an incident ion after each binary collision the value of P_d is compared with a random number. If P_d is greater than the random number, the next collision is treated in amorphous silicon. If the value of P_d is sufficiently high, amorphous collisions also occur one after another. In this manner the motion of the ion in an amorphous pocket is modeled. The probability P_d is a linear function as shown in Eq. (3.49), in the case of small values of the nuclear energy deposition per target atom but becomes a non-linear function in Eq. (3.50) at higher values of E_n^A. The parameter C_a is a measure for the type and amount of relevant defects remaining after a single ion impact and is determined by the ion species, the target temperature, and the dose rate. It is nearly independent of implantation energy, dose, and direction of incidence. Low values of C_a for light ions indicate that the size and the amount of relevant defects are relatively small. On the other hand, heavy ion bombardment produces more of such defects which are generally larger than those produced by light ion implantation. Therefore, the value of C_a is higher for heavy ions. The parameter P_s is the threshold probability for the onset of total amorphization in the volume element considered and depends only on the ion type. P_s is lower for heavy ions than for light ions, which is intuitive based on the fact that heavy ions induce larger radiation defects which overlap easily to form amorphous pockets, while the extent of damage created by light ions is smaller and sparser. Fig. 3.9 shows the capability of the damage model in taking account the effect of increasing dose on the shape of the impurity profiles for a light ion like B and a heavy ion like Sb.

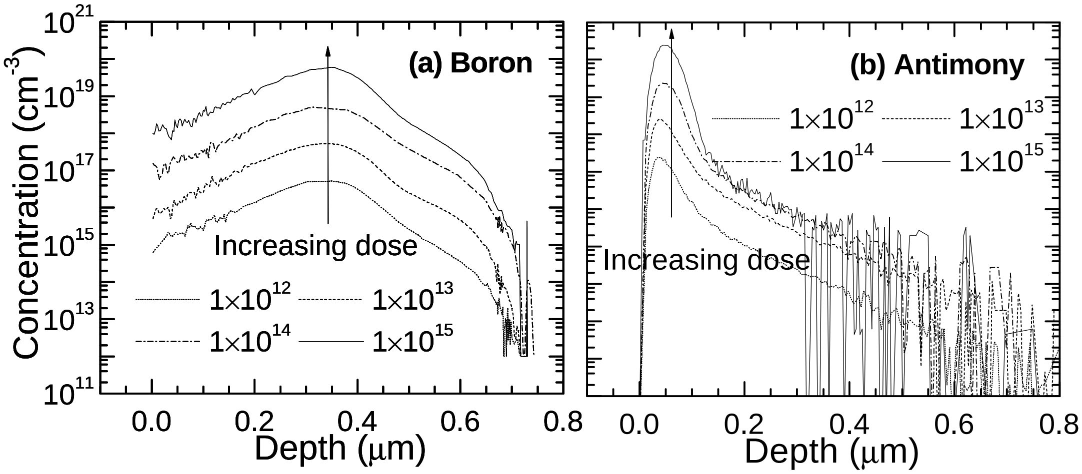

Fig. 3.9 Effect of enhanced dechanneling and damage accumulation on profile shape for (a) B 100keV 7° tilt 22° rotation and (b) Sb 100keV 7° tilt 22° rotation for doses 1×10^{12}-1×10^{15} atoms/cm^2. All simulated profiles are obtained from Crystal-TRIM.

In general, the profiles can be linearly scaled with dose before the amorphization threshold is exceeded. In the case of B, the change in profile shape is observed only for doses above 1×10^{14} atoms/cm^2 while dechanneling is already seen for doses above 1×10^{13} atoms/cm^2 in the case of Sb. As mentioned earlier, this can be attributed to the larger extent of damage and more complex extended defects created by the heavier ions. Enhanced dechanneling of implanted ions also occurs if the originally pristine single-crystalline target has been damaged in a previous implantation step. In this case the simulation of ion implantation taking into account the existing damage is performed in the following manner. In each volume element of the target, the damage probability P_{d0} resulting from the previous implant is summed with the corresponding probability calculated according to Eq. (3.48) for the present implantation. This inherently assumes that P_d has the same effect on the subsequently implanted ions that the pre-implants had on the present implant.

3.2.4 Statistical Enhancement Techniques

3.2.4.1 Trajectory splitting

In order to produce physically realistic profiles, the dopant concentration should be predicted precisely for several decades of magnitude. Regions of low concentration result from deep channeling tails and lateral channeling branches which are caused by a small group of projectiles with long trajectories. This result in large numbers of pseudo-particles to be simulated which in turn prolong the computational time in order to achieve statistically smooth profiles in the low concentration region. A splitting algorithm is necessary to increase the computational efficiency and solve the statistical problem of bad depth resolution without introducing physical errors.

The essence of a splitting algorithm lies in increasing the number of *rare-event* trajectories calculated in regions with low trajectory density, especially in the low concentration region. When one mother projectile reaches the edge of the simulation cell where the trajectory density is low, a splitting point is defined and the mother projectile is automatically replaced by two daughter projectiles, each having half the statistical weight of the mother projectile. The existing status of the mother projectile, e.g. position, energy, direction of motion as well as the positions of neighboring target atoms, as well as those of the last collision partners, is stored. The trajectory of the first daughter particle is followed further. All physical quantities regarding the new statistical weight of the daughter projectile are now stored. Further splitting can occur, leading to a splitting tree related to the mother projectile. As soon as the simulation of one branch of the tree is finished, the next one, starting in the most recent splitting point is considered until the entire tree has been simulated where no splitting points remain and a new projectile enters the target. At a splitting point, both daughter particles start under identical conditions. The difference of their trajectories in a single-crystalline target is solely caused by the thermal vibrations of the collision partners found beyond the splitting point. The splitting criterion is shown in Eq. (3.52). For each volume element *J* considered the weighted sum over the particle trajectory density is determined and stored, where w_i is the weight of a particle i depending on its splitting level L_i $\left(w_i = 1/2^{L_i}\right)$ and l_i is the trajectory segment lying within the volume element J.

$$s_J = \frac{1}{V_J} \sum_i w_i l_i \tag{3.52}$$

The summation is taken over all particles previously registered in the volume element. If a particle enters a new volume element K, the ratio of the values of s_K and of s_S for the first volume element at the target surface entered by the original ion is compared with the instantaneous weight w_m of the particle considered. A splitting point is set if

$$\frac{s_K}{s_S} < 2w_m \tag{3.53}$$

Only a certain fraction of the pseudo-particles are split many times; most of them are split only a few times since splitting points are set only in regions where the trajectory density is low. The splitting algorithm requires a certain "learning" period: In the initial phase of the simulation, the statistical weight of the implanted particles is chosen to be very small and set to the weight at the deepest anticipated split level. The weight is then increased step by step until the full weight is reached.

3.2.4.2 Lateral replication

In the calculation of 2D and 3D implantation profiles, the target structures under consideration are usually very large compared to the length of the trajectory of an implanted ion. This leads to a large number of pseudo-particles required and hence an enormous increase of CPU time. However, in most applications, the lateral regions can have similar properties, like the same depth structure and lateral environment, showing nearly 1D symmetry. Hence, the trajectories of the pseudo-particles started at a given x-coordinate can be replicated to other starting points within these regions. This is termed lateral replication and it increases the number of ion trajectories in these regions without additional computational time. At the beginning of the simulation, all intervals at the boundary line parallel to the x-axis are labeled with the same index assigning them to the same equivalent class. When an ion trajectory encounters a simulation cell, information on the material composition as well as the increment of dopant and damage concentration is stored. The material arrangement and the damage state in the interval are compared to the other intervals. In cases where there are no differences, the 2D distributions are copied to the intervals belonging to the same equivalent class. Else the corresponding starting interval on the boundary line is assigned to a new equivalent class. The replication procedure is complicated; hence it is difficult to estimate the actual number of trajectories simulated, that is, the difference between the total number of incident pseudo-particles and the number of replicated trajectories. No lateral replication is performed when a 1D structure with a 1D grid is considered.

3.2.4.3 Statistical reliability checking

The statistical reliability of the simulated results should be checked, especially after performing trajectory splitting. The contributions to the dopant and damage concentration are classified in each simulation cell with respect to the original pseudo-particles and the replicated particles. For each cell, the number of contributing original particles is counted. As mentioned earlier, the smoothness of the profile in the low concentration regime is increased artificially by trajectory splitting. However, if only a small number of original particles contributed to the low-concentration part of the 2D distribution, the simulation results are not statistically reliable. In general, the data in the simulation cell resulting from less than 10-15 original particles may not be regarded as statistically reliable. Alternatively, the statistical reliability can be checked by counting the number of binary collisions for every original particle. After the simulation, the particle with the maximum number of collisions is stored in a data set. The ratio of the number of collisions of this particle and the total number of collisions in the cell is also stored. If one particle contributes more than 10-20% of the binary collisions in a cell, the simulation cannot be considered as statistically reliable.

3.3 Input parameters to the Crystal-TRIM code

Two versions of the Crystal-TRIM code are used in this work. The older version, Version 98F/1D,3D works under the UNIX operating system and is able to simulate ion implantation of atomic ions into single-crystalline silicon, including recoil cascades and time ordering of ion and recoil motion. It is also able to give the 3D coordinates of the primary ions and the recoils, as well as the 1D interstitial and vacancy profiles. This 3D information sheds light on the morphology of the cascade and the damage. However, due to the lack of a damage model, it is unable to model the dose effect on the profile shape. Since implant dose is not an input parameter in this version, profiles generated, whether impurity, vacancy or interstitial have to be linearly scaled with dose subsequently. This version is primarily used to generate the 3D coordinates of the implanted species.

Basic parameters required in Crystal TRIM Version 98F/1D, 3D:

1. Implant energy (in keV)

2. Tilt (incident beam direction)

3. Rotation (azimuthal orientation of wafer)

4. Beam divergence (usually small, taken to be 0.5)

5. Atomic number of implanted species

6. C_{el} parameters for the local electronic energy loss in the modified Oen-Robinson model (Eq. (3.46)). This is an empirical parameter and assumed to be 1 in the [110] direction and varies with energy for [100] direction. The parameters used for the simulations in this work for different dopants are shown in Eqs. (3.54) to (3.56).

Boron, Carbon, Nitrogen and Fluorine:

$$C_{el[110]} = 1 + \frac{3}{4.5E_0 + 1} + \frac{30}{(4.5E_0 + 1)^4};$$

$$C_{el[100]} = \begin{cases} 1.6E_0^{-0.06} & \text{for } E_0 < 4.5\text{keV} \\ 1.8234E_0^{-0.14221} & \text{for } 4.5 \le E_0 \le 70\text{keV} \\ 1 & \text{for } E_0 > 70\text{keV} \end{cases} \qquad (3.54)$$

Phosphorous:

$$C_{el[110]} = 1;\ C_{el[100]} = 1.7511 - 0.0791 \ln E_0 \qquad (3.55)$$

Arsenic, Germanium, Indium and Antimony:

$$C_{el[110]} = 1;\ C_{el[100]} = 3.0354E_0^{-0.16757} \qquad (3.56)$$

7. Number of statistical particles to be simulated (usually taken to be 20,000 for accuracy)

8. Width of interval in the histograms, *w* shown in Fig. 3.10. The maximum number of depth intervals in version 98F/1D, 3D is 100. The entire profile is split into 100 intervals and calculations are performed sequentially after each interval. Overestimation of this parameter results in broad histograms which reduces the statistical reliability and accuracy of the profile generated (Fig. 3.10a). Underestimation of this parameter results in narrow dense histograms, which could describe the initial portion of the profile accurately but would result in abrupt

termination of the tailing portion of the profile (Fig. 3.10b). The sudden increase in concentration seen in Fig. 3.10b results from statistical errors; the implanted pseudo-particles when reaching the estimated final depth have not yet reached the threshold energy (below which the atoms stop moving) but are forced to stop according to the user-input junction depth (automatically determined when *w* is specified). Hence, there is a build-up of particles with high energy resulting in an accurate concentration peak. Estimation of *w* is very much a trial and error process. A good guess of *w* would result in evenly spaced histograms which can fully describe the entire profile (Fig. 3.10c). Alternatively, the profile could first be simulated in another code like UT-Marlowe so that the entire range of the profile will be known a priori. The new version of Crystal-TRIM is incorporated into the multi-dimensional process simulator DIOS (Integrated Systems Engineering, ISE AG) and is an improvement of the older version, although many of the older features remain. The primary difference is its ability to take the accumulation of damage into account; hence profiles are increasingly dechanneled as the implant dose increases. C_{el} parameters are also automatically calculated given the implant energy rather than user-defined. Unlike the old version, the new version calculates the entire range of the profile without the trial-and-error process of finding the optimum interval width. The profiles are also smoothened by a smoothing algorithm, thus the box-like structure of the profiles is replaced by a continuous function. A check on the two versions concludes that the profiles are nearly identical, with the newer version yielding better statistics near the profile tails because of the presence of statistical enhancement techniques.

In this chapter, the theory of BCA is derived. The main code used in this work, Crystal-TRIM is next elucidated in terms of its universal nuclear and semi-empirical electronic stopping models. A brief description of the damage accumulation model and the statistical enhancement techniques used in Crystal-TRIM is given, followed by the inputs necessary for the proper simulation of 1D and 2D implantation profiles. Unless mentioned otherwise, the new version of Crystal-TRIM is used in all BCA simulations shown in this work.

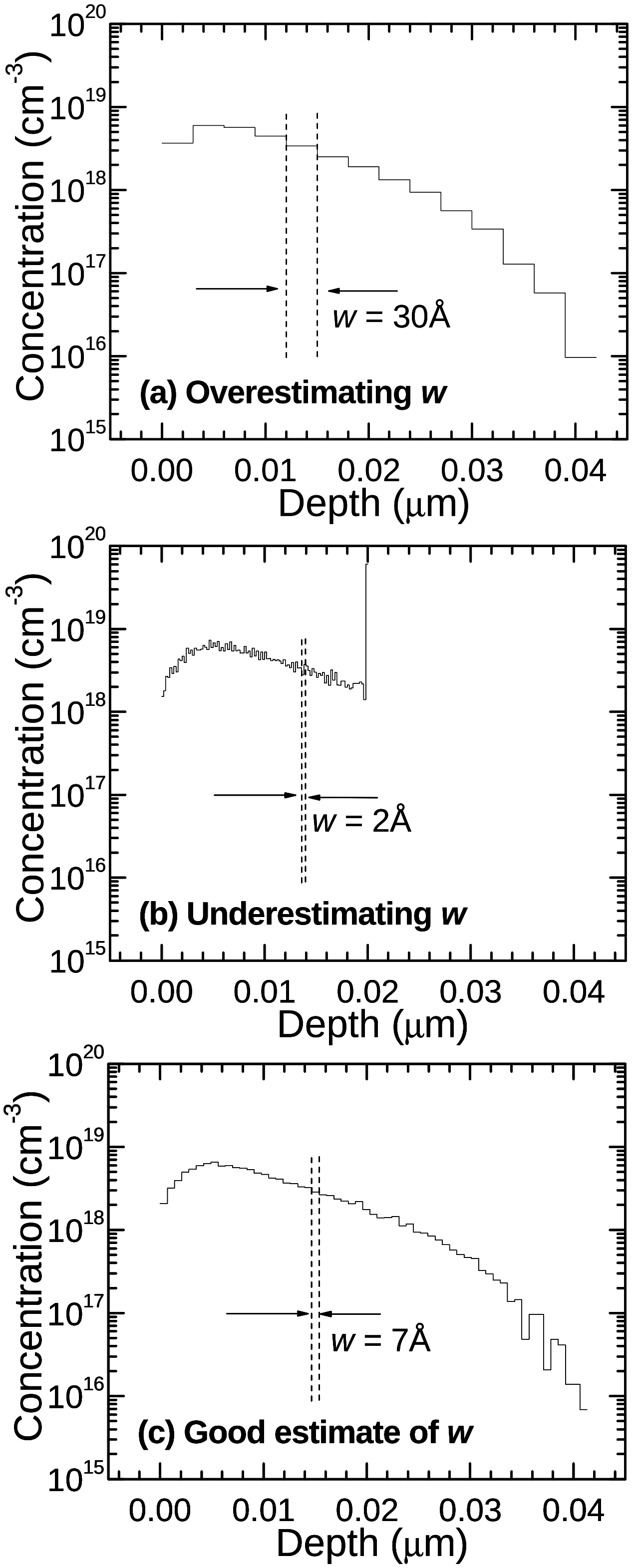

Fig. 3.10 Choice of interval width, *w* on final simulated impurity profile. All simulated results are obtained from Crystal-TRIM Version 98F/1D,3D for B 1keV 1×10^{13} atoms/cm^2 0° tilt 0° rotation using (a) *w* = 30Å (b) *w*=2Å and (c) *w*=7Å

CHAPTER 4 NEW ION IMPLANTATION MODEL

4.1 Limitation of current analytical methods

Before the advent of supercomputers with the speed necessary for the realistic use of molecular dynamics in describing a dynamic process like ion implantation, modeling of the implantation of dopants into the simulation structure are mainly approached in two distinct ways. The first approach using the Monte Carlo or particle methods, as described in the previous chapter, calculates the trajectories of implanted ions through the silicon structures, based on physical models, which assumes that the ion loses its energy through two processes, nuclear scattering and electronic scattering. The crux of the second method is to use parameterized analytical functions to model the as-implanted profiles and to estimate the parameters of the function either from experimental or theoretical data, replacing the calculation of every collision with pre-calculated distribution moments. For a very long time, ion implantation profiles as well as ion implantation induced point defect profiles have been described with the following analytical methods based on statistical distribution functions simply for because it is the simplest method to use and the fastest to execute.

4.1.1 Gaussian (Normal) distribution

The Gaussian function is possibly the simplest distribution to describe the concentration of implanted impurities as a function of depth. Given by Eq. (2.1) previously, the function is specified by only two moments, the mean projected range, R_p and the projected range straggling σ_z (the vertical standard deviation).

$$C(z) = \frac{D_T}{\sqrt{2\pi}\,\sigma_z} \exp\left[\frac{-(z - R_p)^2}{2\sigma_z^2}\right] \tag{2.1}$$

C is the number of ions per unit volume (concentration) and D_T is the number of ions per unit area impacting on the wafer surface (dose). Tables of the Gaussian distribution function parameters for common ion-target combinations were first calculated based upon the Lindhard stopping theory (Lindhard et al., 1963). Fig. 4.1 shows the Gaussian distribution plotted in logarithmic scale for different R_p (a) and σ_z (b). It is well-known for its deficiency in realistically describing one-dimensional (1D) profiles since factors like backscattering of ions and channeling causes the impurity profile to be highly asymmetrical with large channeling tails. Fig. 4.2 shows the impurity profiles measured experimentally with Secondary Ion Mass Spectrometry (SIMS) fitted with the Gaussian function for (a) As and (b) Sb profiles at different energies. In all cases, the normal distribution shows a sudden drop in concentration and fails to describe the channeling portion of the profiles. Apart from the mean projected range and vertical straggling, it has been shown that additional parameters are necessary to account for the deviations from the perfectly symmetrical normal distribution.

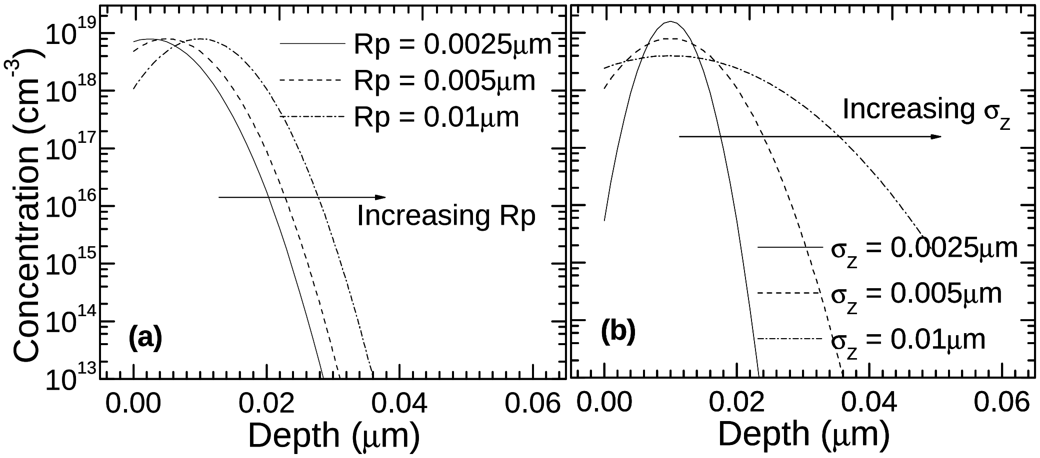

Fig. 4.1 Logarithmic Gaussian function with $D_T = 1\times10^{13}$ atoms/cm^2 (a) different Rp, constant σ_z (0.005μm) and (b) different σ_z, constant Rp (0.01μm)

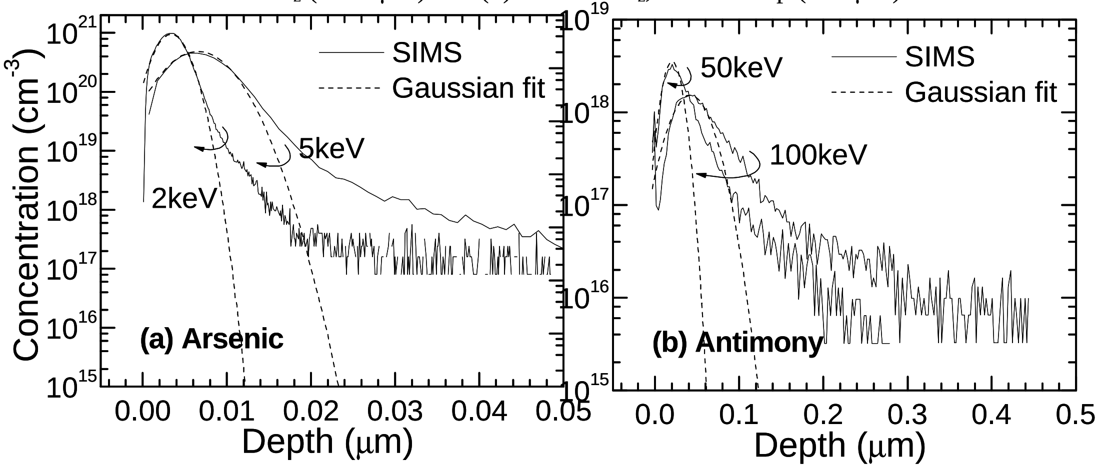

Fig. 4.2 Gaussian fits to SIMS profiles (a) As 2keV and 5keV 5×10^{14} atoms/cm^2 tilt 0° rotation 0° and (b) Sb 50keV and 100keV 1×10^{13} atoms/cm^2 tilt 0° rotation 0°

4.1.2 Pearson IV and dual-Pearson IV distribution

The Pearson IV distribution (Hofker et al., 1975), which takes into account an additional two moments, the skewness and kurtosis, has been commonly used to account for moderate profile asymmetry and channelling, especially occurring in crystalline targets where channelling is significant. The *coefficient of skewness* γ or third moment of the distribution accounts for the asymmetry, usually caused by backscattering of light ions. The fourth moment β is the degree of flattening near the mean, called the *coefficient of excess or kurtosis*. The function is thus defined by four parameters and given by the equations previously shown in Chapter 2.

$$C(x) = D_T f(x) \tag{2.3}$$

where f(x) is given by

$$f(x) = K\left|b_2 z'^2 + b_2 z' + b_0\right|^{\frac{1}{2b_2}} \exp\left\{-\frac{b_1/b_2 + 2b_1}{\sqrt{4b_2 b_0 - b_1^2}} \arctan\left[\frac{2b_2 z' + b_1}{\sqrt{4b_2 b_0 - b_1^2}}\right]\right\} \tag{2.4}$$

z’ is given by (z-R_p) and K is a normalization factor, chosen such that

$$\int_{-\infty}^{+\infty} f(x)\,dx = 1 \tag{2.5}$$

and the constants b_0, b_1 and b_2 are given by

$$b_0 = -\frac{\sigma_z^2\left(4\beta - 3\gamma^2\right)}{10\beta - 12\gamma^2 - 18} \tag{2.6}$$

$$b_1 = -\frac{\sigma_z \gamma (\beta + 3)}{10\beta - 12\gamma^2 - 18} \tag{2.7}$$

$$b_2 = -\frac{2\beta - 3\gamma^2 - 6}{10\beta - 12\gamma^2 - 18} \tag{2.8}$$

Amongst the many workers who used a Pearson distribution to model implant profiles, Hobler et al. (1987) presented a two-dimensional (2D) model whereby the vertical moments of the Pearson IV distribution as a function of energy have been fitted with simple analytical formulae. The spatial moments in Hobler’s work have been derived by fitting the function to profiles obtained from a MC code which was based on the physical fundamentals of TRIM

(Biersack et al., 1980), a code which describes the transport of energetic ions in *amorphous* targets. However, real implantations are almost always performed in crystalline targets where channeling is inevitable; ion implant models should hence account for the tilt and twist dependencies of the profiles, a feature which is clearly absent in Hobler's model based on amorphous targets. Fig. 4.3 show the predictive capability of the simulated profiles for different impurities in both amorphous and crystalline substrates compared with experimental SIMS data. All simulated results shown are obtained from Crystal-TRIM. The comparisons show the lack of a channeling tail in the amorphous profiles, very much like the normal distribution. Because of the propulsion of ions in open channels, deep junction depths are obtained in crystalline substrates even for heavy elements like As and Sb.

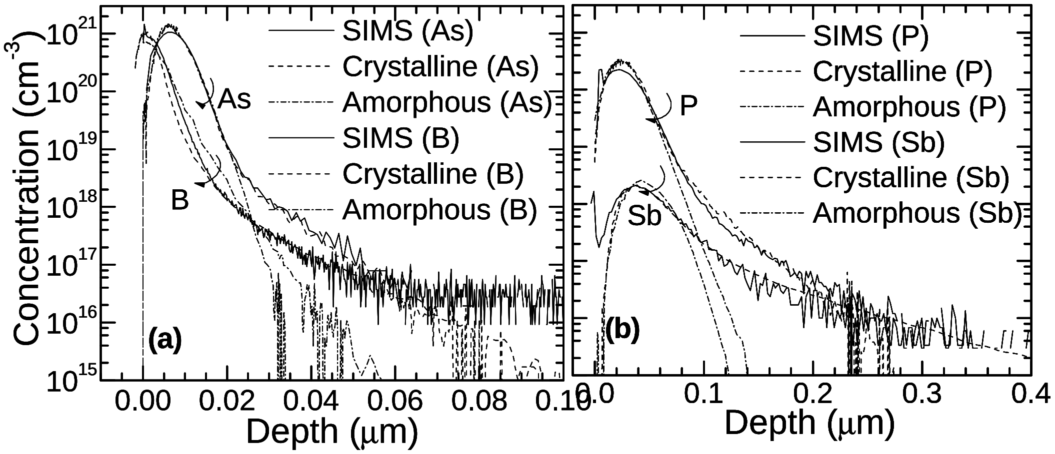

Fig. 4.3 Experimental SIMS and simulated profiles in crystalline and amorphous Si (a) B 500eV 5×10^{14} atoms/cm^2 and As 5keV 1×10^{15} atoms/cm^2 at 0° tilt and 0° rotation (b) P 20keV 1×10^{15} atoms/cm^2 and Sb 100keV 1×10^{13} atoms/cm^2 at 7° tilt and 22° rotation.

The fitting formulae for the vertical moments presented in the work of Hobler et al. (1987) for B, P, As and Sb are shown in Eqs. (4.1) to (4.4). The formulae are functions of implant energy, E only, and are valid only in the range of 10-300keV as extrapolation of the formulae beyond this range would result in considerable fitting errors.

$$R_p(E) = a_1 E^{a_2} + a_3 \qquad (4.1) \qquad\qquad s_Z(E) = a_1 E^{a_2} + a_3 \qquad (4.2)$$

$$g_Z(E) = \frac{a_1}{a_2 + E} + a_3 \qquad (4.3) \qquad\qquad b_Z(E) = \frac{a_1}{a_2 + E} + a_3 + a_4 E \qquad (4.4)$$

Figs. 4.4(a) to (d) show graphical representations of the moments expressed in Eqs. (4.1) to (4.4) for B, as well as the Pearson IV moments extracted from the simulated profiles in Crystal-TRIM from 100eV to 300keV for dose 1×10^{13} atoms/cm^2 at three industrially common tilts/twist angles of 7°/22°, 0°/0° and 45°/45° in single crystalline silicon.

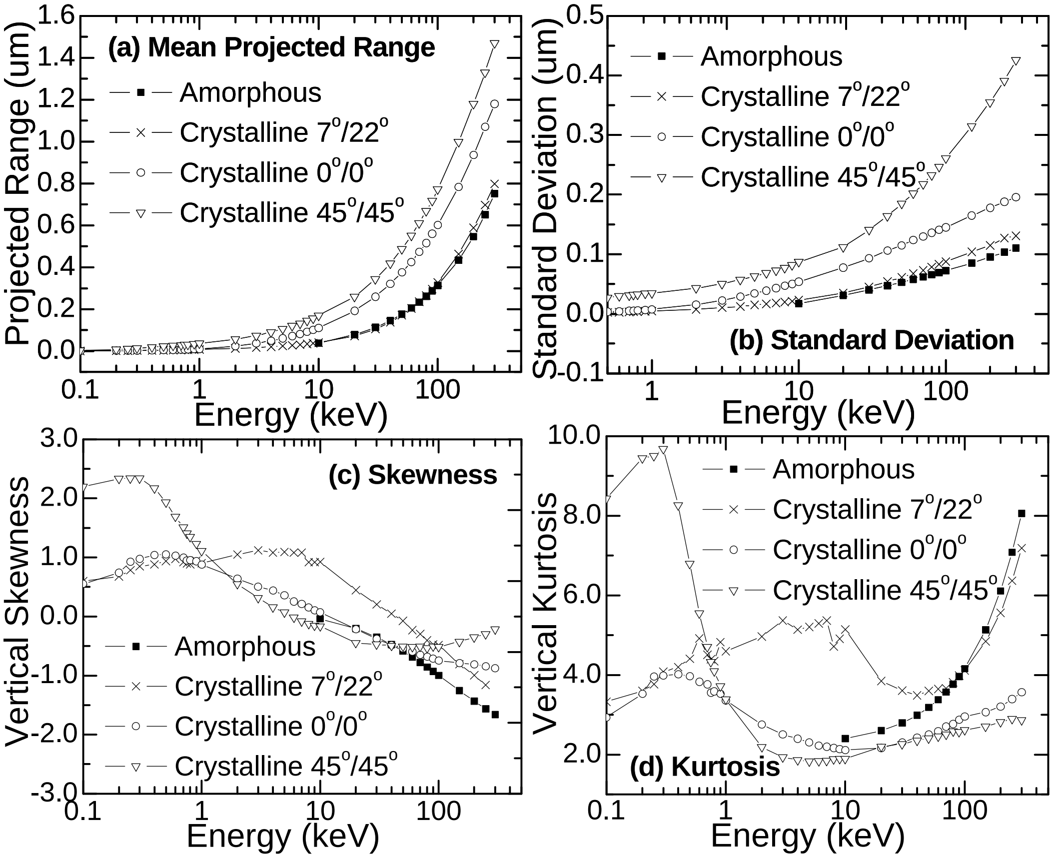

Fig. 4.4 Comparisons between Hobler's fitting formulae (10-300keV) and extracted Pearson IV moments from Crystal TRIM simulated profiles (100eV-300keV) for 3 different tilts/rotations, 7°/22°, 0°/0° and 45°/45° in single-crystalline silicon (a) mean projected range (b) standard deviation (c) skewness (d) kurtosis with implant energy, E

The fact that Hobler's model experienced fitting errors for energies below 10keV hints that the Pearson function faces limitations as implant energy lowers. The following observations can be made from Fig. 4.4. The Pearson moments of 7°/22° most closely resemble Hobler's model; this is intuitive since the beam direction of 7°/22° represents a case of least channeling and is a common protocol used in industries to create ultra-shallow source-drain junctions. Similarly, Hobler's model was derived in amorphous silicon where channeling is absent. In general, profiles of 0°/0° and 45°/45° show larger mean projected ranges and vertical straggling, and are flatter near the peak (smaller kurtosis) and more asymmetrical (larger skewness) compared to their amorphous counterparts. The critical angle of approach and the orientation of the target are two crucial parameters in implantation and it is known that tilt angles 0° and 45° give rise to substantial amounts of channeling (Ziegler, 1992), while tilting the ion beam by 7° can effectively reduce the junction depth by steering the ion out of any open channels. This is clearly reflected in Fig. 4.5(a) where the 3D coordinates of the implanted ions and silicon recoils for 7°/22°, 0°/0° and 45°/45° implants are shown.

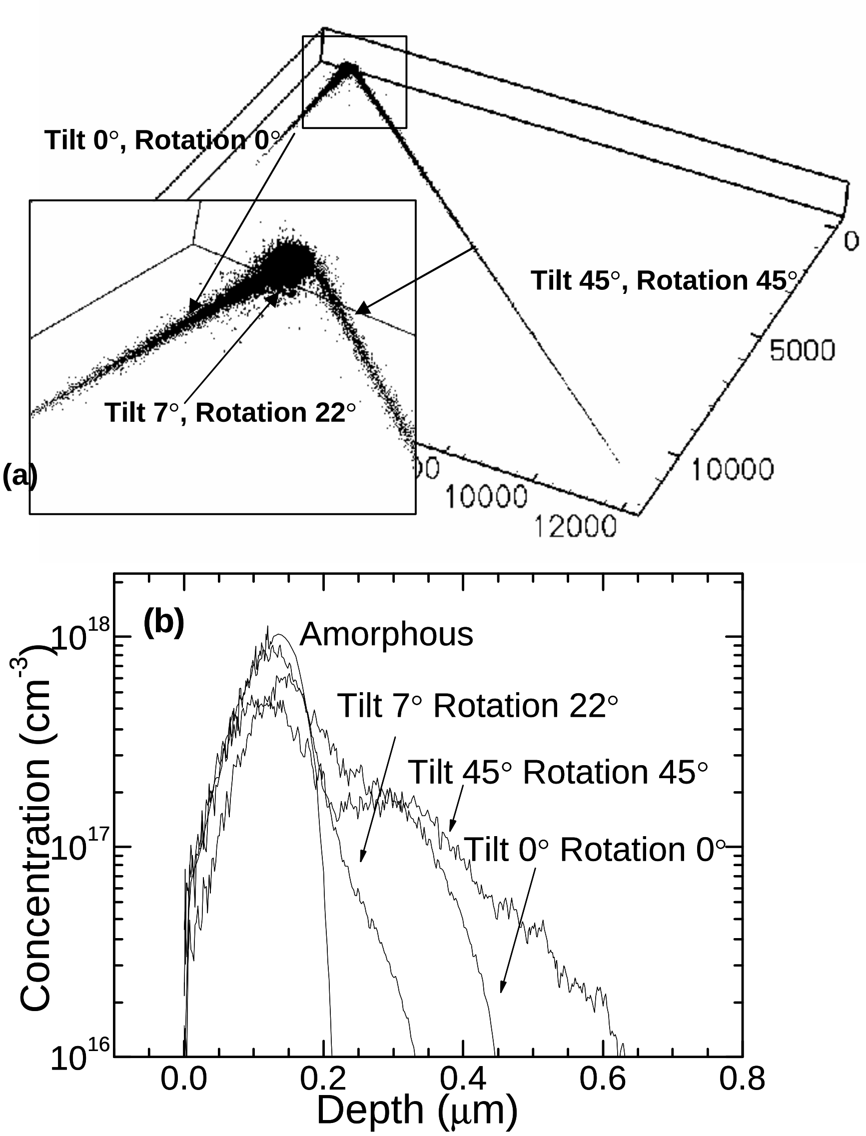

Fig. 4.5 (a) 3D trajectories of each implanted ion and their recoils. The inset in (a) shows the low channeling 7°/22° implant. (b) Extracted 1D impurity profiles in vertical direction.

Results are obtained from Crystal-TRIM using 10,000 pseudo-particles with B implanted in crystalline silicon at 1keV, 1×10^{13} atoms/cm^2 at tilts/rotations of 7°/22°, 0°/0° and 45°/45°. While the ions of 7°/22° are confined within a small cascade, the trajectories caused by the 0°/0° and 45°/45° implants can be propelled as far as 5,000 Å and 12,000Å respectively. Fig. 4.5(b) shows the 1D impurity profiles extracted in the vertical direction with deep junction depths obtained for 0°/0° and 45°/45°, while the non-channeling 7°/22° implant is much shallower and closer to the amorphous profile. Based on Hobler's fitting formulae, least squares regression was performed on the Pearson moments obtained from Crystal-TRIM. Tables 4.1 to 4.4 show Hobler's parameters which are based on amorphous silicon and the new calculated parameters a_i (1= i = 5) for crystalline silicon. The fitting formula for the kurtosis of 45°/45° had to be replaced by a 4th order polynomial ($a_1 + a_2x + a_3x^2 + a_4x^3 + a_5x^4$) to minimize fitting errors. While the MC simulations were conducted over the energy range 100eV-300keV, the regression analysis was performed from 1keV onwards. Figs. 4.4(c) and (d) showed that the third and fourth moments start to show erratic trends with energy in the sub-keV regime; this is especially true for kurtosis, hinting that the Pearson IV distribution may be inadequate to completely describe the profile as energy lowers.

Table 4.1 Parameters for mean projected range

	Literature	**7°/22°**	**0°/0°**	**45°/45°**
a_1	0.00969	0.00928	0.04942	0.06571
a_2	0.76700	0.78860	0.56922	0.55612
a_3	-0.01815	-0.02683	-0.07984	-0.08418

Table 4.2 Parameters for vertical standard deviation

	Literature	**7°/22°**	**0°/0°**	**45°/45°**
a_1	0.05210	0.04427	0.31738	0.03962
a_2	0.21600	0.25887	0.09214	0.42673
a_3	-0.06840	-0.05971	-0.33972	-0.02484

Table 4.3 Parameters for vertical skewness

	Literature	**7°/22°**	**0°/0°**	**45°/45°**
a_1	312.70000	194.88340	25.99118	-0.12471
a_2	122.20000	65.63017	15.47229	-0.01455
a_3	-2.40400	-1.75526	-0.94958	1.64622×10^{-4}
a_4	-	-	-	-6.78104×10^{-7}
a_5	-	-	-	9.59663×10^{-10}

Table 4.4 Parameters for vertical kurtosis

	Literature	**7°/22°**	**0°/0°**	**45°/45°**
a_1	0.00000	25.07488	119.19773	20.30106
a_2	1.00000	-0.89253	78.90659	15.88823
a_3	2.21200	2.23306	3.38755	2.69257
a_4	0.01950	0.01618	0.00155	0.00096

While the single Pearson IV function was able to account for the deviations from the normal distribution, it was still unsatisfactory for profiles with long channeling tails and profiles which are highly skewed with large kurtosis. Moreover, while simple analytical formulae can be applied to all four moments for amorphous targets within the intermediate energy range, the third and fourth moments of the distribution did not show predictable trends with energy for crystalline substrates. To accurately depict a wide range of as-implanted profiles, a combination of two Pearson IV functions had been commonly used to separately model the random scattering and channeling components (Park et al., 1990). In the dual-Pearson approach, it is assumed that the distribution of the implanted ions inside silicon is dependent on two distinct mechanisms: random scattering and channeling. The random scattering component accounts for the peak of the distribution, since this is due to the stopping of ions that have suffered several small impact parameter collisions with the target atoms on account of their random direction. The broad tail of the distribution is attributed to ions that have entered channels in the silicon crystal and hence are not significantly scattered over long distances. Each of the above mechanisms is modeled by a single Pearson IV function. The dual-Pearson is characterized by nine model parameters, each Pearson having four parameters plus an additional parameter that accounts for the fraction of dose allocated to the random component. The model parameter extraction procedure consists of two steps (Furukawa et al., 1972). In the first step, an initial guess for the model parameters is made. This is used as the input for the second step, which is a non-linear least squares fitting algorithm used for extraction of the model parameters from experimental or simulation data. This dual-Pearson model had been quite successful and very widely used. However, the main drawback of the dual-Pearson modeling approach is the need for a reasonably good initial guess for the model parameters in order to ensure convergence of the algorithm. Obtaining a good initial guess is non-trivial, given the complex functional form of the Pearson functions. It is also seen from Eqs. (2.3)-(2.8) that the Pearson functions can have singularities depending on the choice of parameters. This is significant since the non-linear least squares fitting algorithm works by exploring the parameter space near the initial guess, and a singularity might cause it to fail. Although parameter extraction can be achieved automatically by codes written specifically to generate a reasonable initial guess, the parameter set may not be a unique one that provides the best fit for a particular impurity profile.

4.1.3 Legendre polynomials

The UT-MARLOWE group (Li et al., 2002) first proposed the use of Legendre polynomials to model as-implanted impurity and damage profiles. They are a set of polynomials with simple functional forms that satisfy the orthogonality property shown in Eq. (4.5) with a unity weight function in the interval [-1,1].

$$\int_{-1}^{1} L_i(x) L_j(x) dx \neq 0 \text{ if and only if } i=j \tag{4.5}$$

The impurity and damage profiles are modeled as linear combinations of the first 14 Legendre polynomials (L_1-L_{14}) which are given by simple polynomial forms, shown in Table 4.5. Hence, the impurity concentration at a depth z, C(z) is simply the summation of the Legendre polynomials of degree i, $L_i(z')$ where b_1 and b_2 are constants that map z from the interval [z_{min}, z_{max}] to [-1,1]. z_{min} and z_{max} are the depths between which the impurity and damage concentration falls within the range of interest.

$$C(z) = \sum_{i=0}^{13} a_i L_i(z')\,; \; z' = b_1 z + b_2 \tag{4.6}$$

The constants a_i, are determined using the orthogonality property of Legendre polynomials.

$$a_i = \frac{\int_{-1}^{1} C(z').L_i(z').dz'}{\int_{-1}^{1} L_i^2(z')dz'} \tag{4.7}$$

$$b_1 = \frac{2}{z_{\min} + z_{\max}} \; ; \; b_2 = \frac{z_{\min} - z_{\max}}{z_{\min} + z_{\max}} \tag{4.8}$$

Table 4.5 Functional forms of the first 14 Legendre polynomials

i	**Functional Forms ($L_i(x)$)**
0	1.0
1	x
2	$-0.5 + 1.5x^2$
3	$-1.5x + 2.5x^3$
4	$0.375 - 3.75x^2 + 4.375x^4$
5	$1.875x - 8.75x^3 + 7.875x^5$
6	$-0.313 + 6.563x^2 - 19.687x^4 + 14.437x^6$
7	$-2.187x + 19.687x^3 - 43.312x^5 + 26.812x^7$
8	$0.273 - 9.843x^2 + 54.140x^4 - 93.847x^6 + 50.273x^8$
9	$2.460x - 36.093x^3 + 140.765x^5 - 201.093x^7 + 94.960x^9$
10	$-0.246 + 13.535x^2 - 117.304x^4 + 351.914x^6 - 427.324x^8 + 180.425x^{10}$
11	$-2.707x + 58.652x^3 - 351.914x^5 + 854.648x^7 - 902.128x^9 + 344.449x^{11}$
12	$0.225 - 17.595x^2 + 219.946x^4 - 997.089x^6 + 2029.790x^8 - 1894.470x^{10} + 660.194x^{12}$
13	$2.932x - 87.978x^3 + 747.817x^5 - 2706.386x^7 + 4736.176x^9 - 3961.166x^{11} + 1269.604x^{13}$

To check the predictability of the Legendre coefficients, MC simulations were conducted using Crystal-TRIM for B in silicon at dose 1×10^{13} atoms/cm^2, 1-100keV and the a_i coefficients of the polynomials are obtained by fitting as-implanted impurity and interstitial profiles with varying orders of the Legendre function. Fig. 4.6 shows the poor predictability of the coefficients (a_5, a_{10} and a_{15}) over the entire energy range.

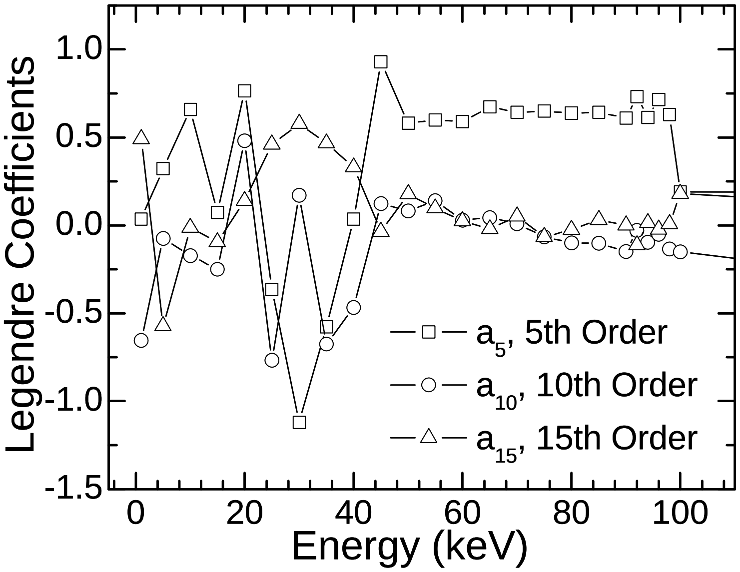

Fig. 4.6 Random trends of the Legendre coefficients (a_5, a_{10} and a_{15}) with implant energies. Implant conditions: B in Si 1-100keV 1×10^{13} atoms/cm^2 7° tilt and 22° rotation.

Although they have simple analytical forms, Legendre polynomials face the problem of predictability like the Pearson method. While it is possible to obtain excellent fits of either experimental or simulated profiles with an analytical function, without good parameter predictability, each profile will possess its own set of parameters which have to be stored individually. This is not only a cumbersome procedure but the storage of the individual parameters will require large computational memory. Besides the unpredictability of the fourteen coefficients of the Legendre polynomials, this method is also found to approach instability with higher orders of polynomial, contrary to the belief that higher orders bring the model closer to the true solution. Fig. 4.7 shows the Legendre fit to a simulated vacancy profile (B in Si 80keV 1e13atoms/cm^2 7^0 tilt 22^0 rotation) from Crystal-TRIM. The same vacancy profile, shown in units of logarithmic concentration (atoms/cm^3) is scaled linearly merely for clearer illustration. The histograms are the simulated profiles from Crystal-TRIM and the solid and dashed lines are analytical fits of the Legendre polynomials of orders 3, 5, 10 and 15. With increasing order of polynomial used, greater oscillations are observed as more coefficients are added, indicating instability of the solution. All of these limitations render Legendre polynomials an inadequate method for profile modeling. In the next section, a robust method is proposed to overcome the common shortcomings of these analytical methods.

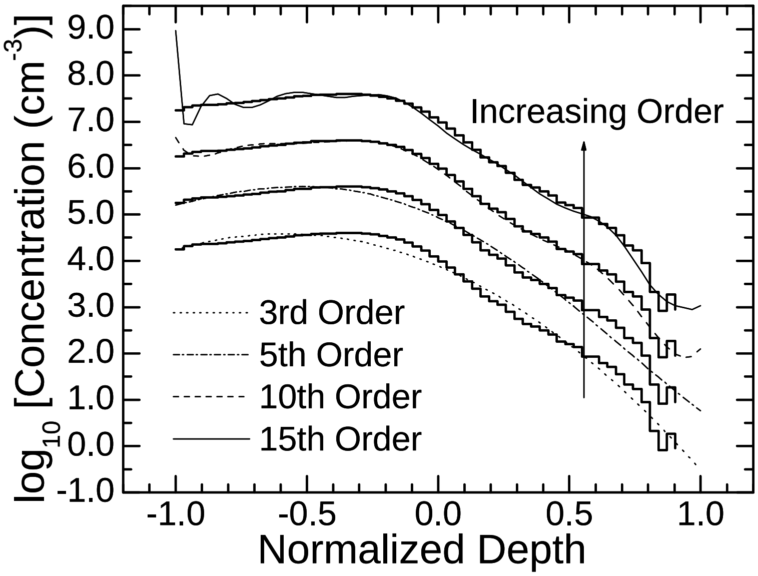

Fig. 4.7 Instability of the fitted profiles with increasing order of Legendre polynomials. Implant conditions: B in Si 1-100keV 1×10^{13} atoms/cm^2 7^0 tilt 22^0 rotation

4.2 Sampling CALibration of Profiles (SCALP)

The advantages and disadvantages of the analytical approach over the Monte Carlo method are apparent. While the computing time is improved by orders of magnitude with use of analytical functions, it has been recognized that with the presence of channeling effects, which are especially predominant in $0^0/0^0$ and $45^0/45^0$ implants, use of common analytical fitting functions like the Gaussian and Pearson IV distributions becomes questionable. With the ultra deep submicron technologies (in the isolation step, for example), many implantation steps are done at zero tilt and twist, resulting in highly skewed profiles with large kurtosis. This renders the analytical distribution functions inapt for good description of both the impurity and damage profiles. Replacement of the dual Pearson function by Legendre polynomials proposed to model both impurity and damage profiles over a wide range of parameters provides little improvement since it faces interpolative difficulties and instability. In summary, a good analytical model should be able to efficiently and accurately describe the impurity and damage profiles, possess simple parameter extraction procedures as well as good interpolation properties. Most importantly, it should not be confined to a particular set of conditions but should be readily transferable to other practical implant conditions. In this section, a new model is proposed which can effectively model crystalline impurity profiles at any energy, taking into account channeling effects with tilt and twist as the varying parameters.

The technique of using sampling calibration of profiles (SCALP) was first proposed by Scheiblin et al. (2001). The original workers used a standard 3^2 Design of Experiments (DoE) in order to obtain the quadratic modeling of the responses depth and concentration as a function of dose and energy. This requires a large number of experiments. In this work, the profiles calibrated are obtained from simulation rather than experiments. The simulated profiles would first have to be verified against experimental data to ascertain the accuracy of the simulation and vice versa. Figs. 4.8-4.16 show some comparisons of the simulated impurity profiles obtained from Crystal-TRIM against experimental SIMS profiles for nine different impurities (B, C, N, F, P, Ge, As, In and Sb) at low and intermediate energies.

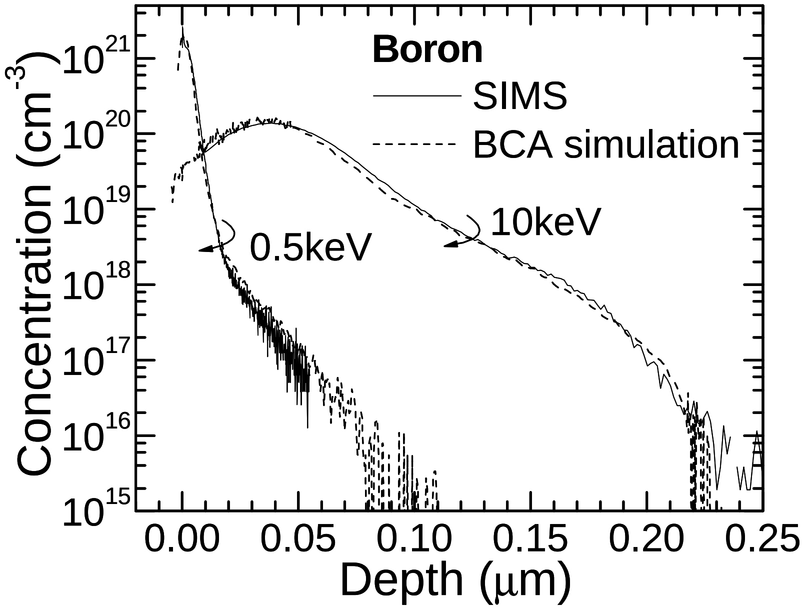

Fig. 4.8 Comparison of experimental SIMS data and simulation for B 0.5keV 1×10^{15} atoms/cm^2 0° tilt and 0° rotation and 10keV 1×10^{15} atoms/cm^2 0° tilt and 0° rotation

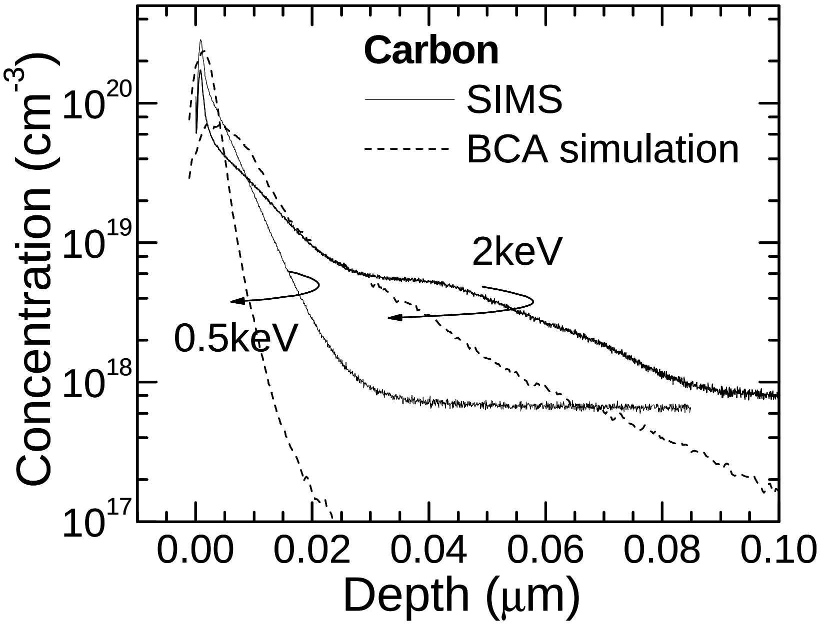

Fig. 4.9 Comparison of experimental SIMS data and simulation for C 0.5keV 1×10^{14} atoms/cm^2 0° tilt and 0° rotation and 2keV 1×10^{14} atoms/cm^2 45° tilt and 45° rotation

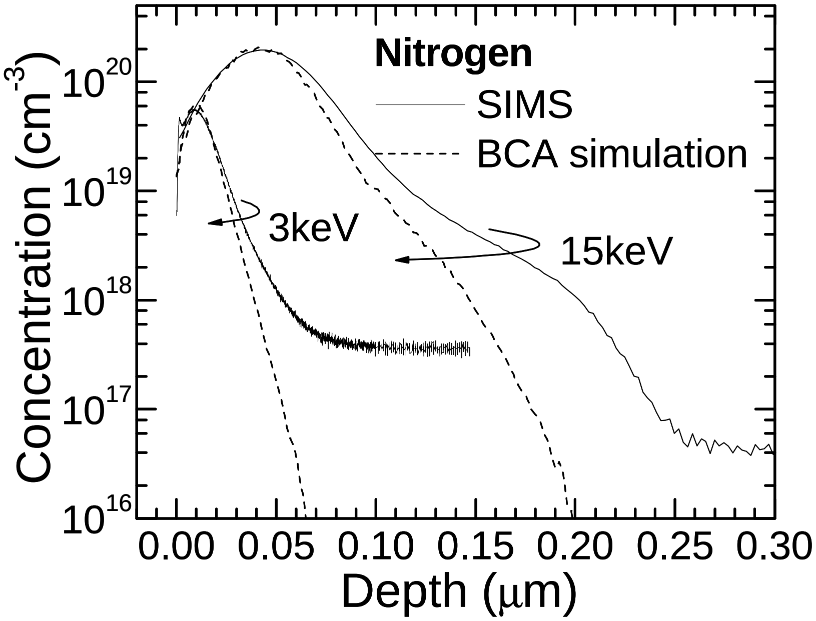

Fig. 4.10 Comparison of experimental SIMS data and simulation for N 3keV 1×10^{14} atoms/cm^2 7° tilt and 22° rotation and 15keV 1×10^{15} atoms/cm^2 5.2° tilt and 17° rotation

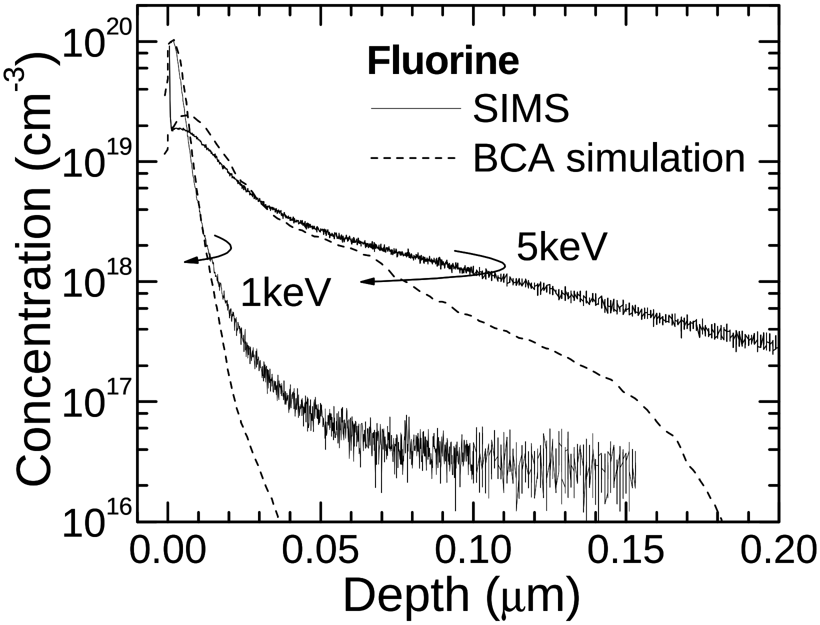

Fig. 4.11 Comparison of experimental SIMS data and simulation for F 1keV 6×10^{13} atoms/cm^2 0° tilt and 0° rotation and 5keV 6×10^{13} atoms/cm^2 45° tilt and 45° rotation

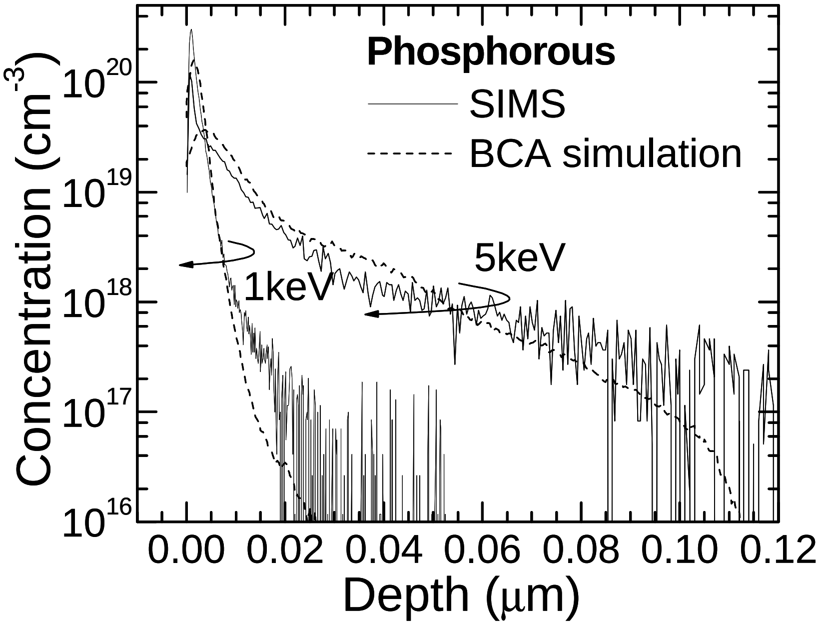

Fig. 4.12 Comparison of experimental SIMS data and simulation for P 1keV 5×10^{13} atoms/cm^2 0° tilt and 0° rotation and 5keV 5×10^{13} atoms/cm^2 45° tilt and 45° rotation

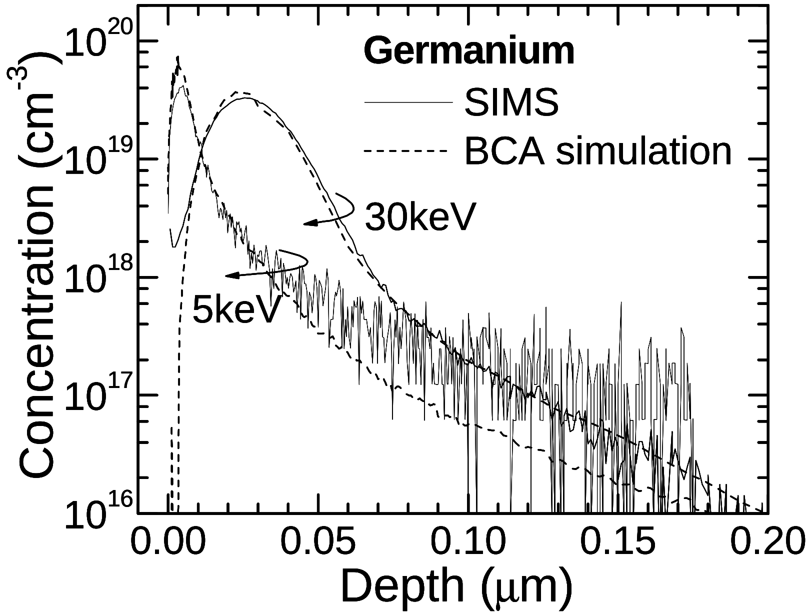

Fig. 4.13 Comparison of experimental SIMS data and simulation for Ge 5keV 5×10^{13} atoms/cm^2 45° tilt and 45° rotation and 30keV 5×10^{13} atoms/cm^2 5.2° tilt and 17° rotation

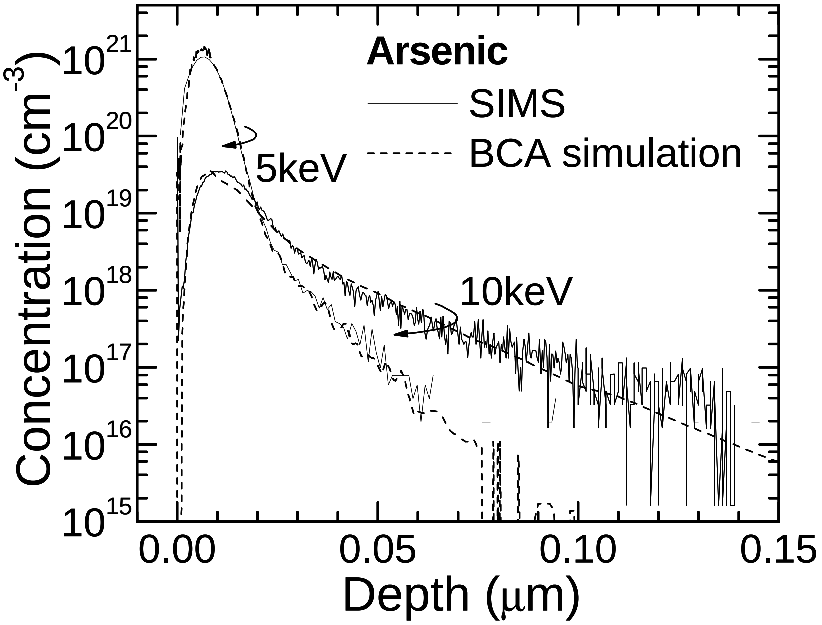

Fig. 4.14 Comparison of experimental SIMS data and simulation for As 5keV 1×10^{15} atoms/cm^2 0° tilt and 0° rotation and 10keV 5×10^{13} atoms/cm^2 0° tilt and 0° rotation

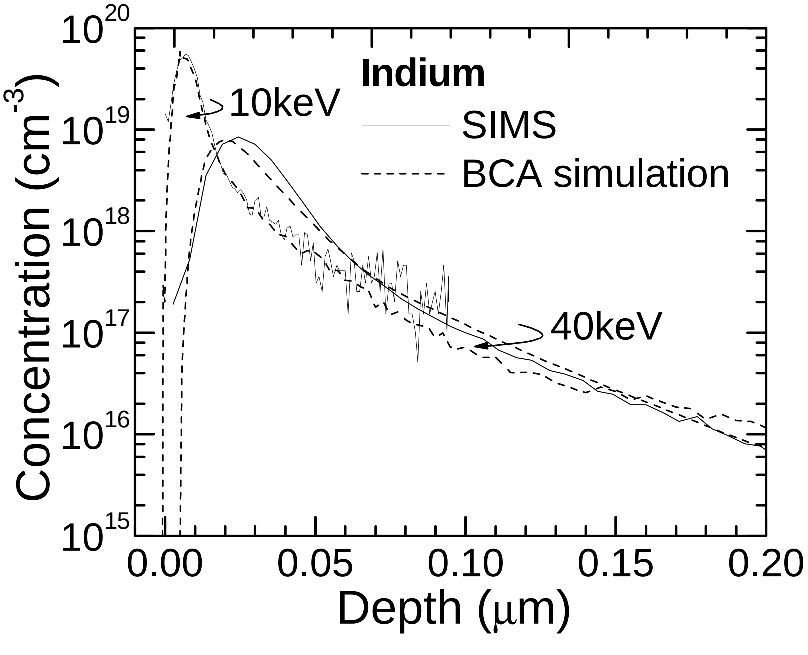

Fig. 4.15 Comparison of experimental SIMS data and simulation for In 10keV 5×10^{13} atoms/cm^2 45° tilt and 45° rotation and 40keV 2×10^{13} atoms/cm^2 7° tilt and 27° rotation

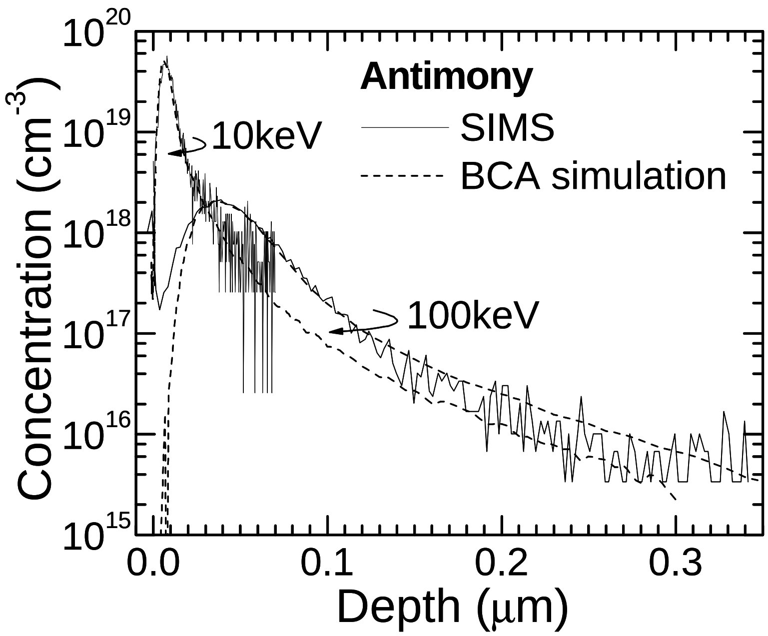

Fig. 4.16 Comparison of experimental SIMS data and simulation for Sb 10keV 5×10^{13} atoms/cm^2 45° tilt and 45° rotation and 100keV 1×10^{13} atoms/cm^2 7° tilt and 27° rotation

The following observations can be made from the comparisons shown in Figs. 4.8-4.15:

1. Excellent agreement between measured data and simulated profiles are seen for dopants like B, As, In and Sb. This is also true for the high energy Ge implant.
2. Simulated profiles of 5keV P and 5keV Ge showed reasonably good agreement with SIMS, with slight underestimation of the channeling tail. Both implants are conducted in the 45° tilt 45° rotation direction where channeling is particularly predominant.
3. Simulated profiles of species like C, N and F, however show poor agreement with SIMS. The degree of channeling is significantly underestimated, and the profiles showed much shallower junction depths than that measured by SIMS.

Discrepancies between experiments and simulation in the cases of C, N, F and low-energy-high channeling P and Ge can be attributed to two main reasons. Firstly, Crystal-TRIM uses the universal ZBL potential in its treatment of nuclear effects. Being a solely repulsive potential, the ZBL potential is able to account for repulsive forces dominant at high implant energies accurately. At lower initial kinetic energies, the use of this potential may introduce inaccuracies since attractive forces that come into play at low energies are not accounted for. Secondly, the electronic stopping is calculated by the semi-empirical Oen-Robinson formula which accounts for local variations of the electron density simply by the empirical parameters C_{el}. While extensive SIMS databases are available for B and other dopants like Ge, As, In and Sb such that the C_{el} parameters are well-known and precisely calibrated with experiments, species like C, N and F are less common (but nevertheless important) industrial dopants where SIMS data are lacking. C_{el} parameters for C, N and F are assumed to be the same as those of B, and this assumption could have led to the poor agreement of simulation with SIMS data. Thus, better electronic stopping parameters are needed for such species. It is also because of the lack of accurate parameters that results in the underestimation of channeling in the case of 45° tilt 45° rotation implants which represents a case of maximum channeling. The study is non-exhaustive; for the scope of this work, we conclude that BCA simulations are accurate for B, P, Ge, As, In and Sb at least up till 5keV, and the SCALP method has been applied to these six species using simulation data obtained from Crystal-TRIM.

The methodology used in this work is modified based on Scheiblin's model and the procedure is summarized in the following points below.

1. The simulated profiles are normalized in depth with respect to the total profile by specifying a cut-off concentration. A cutoff concentration of 1×10^{15} atoms/cm^3 is used. This truncation is necessary to reduce the randomness and noise, which occurs at the tail region of the profiles. The depth where the concentration is 1×10^{15} atoms/cm^3 is defined as *Tdepth*.
2. At different percentages (x%) of *Tdepth*, the concentrations are recorded and the data tabulated. The concentrations at varying percentages of *Tdepth* (Cx%) can be expressed as functions of energy or other parameters by analytical fitting formulae.
3. With the analytical formulae for Cx% determined, any profile can be reconstructed by the reverse procedure with specification of implant parameters like energy, tilt etc.

Fig. 4.8 below shows the graphical interpretation of the SCALP method. *Tdepth* is the depth in μm where concentration is 1×10^{15} atoms/cm^3. Cx% is the concentration at x% of *Tdepth*.

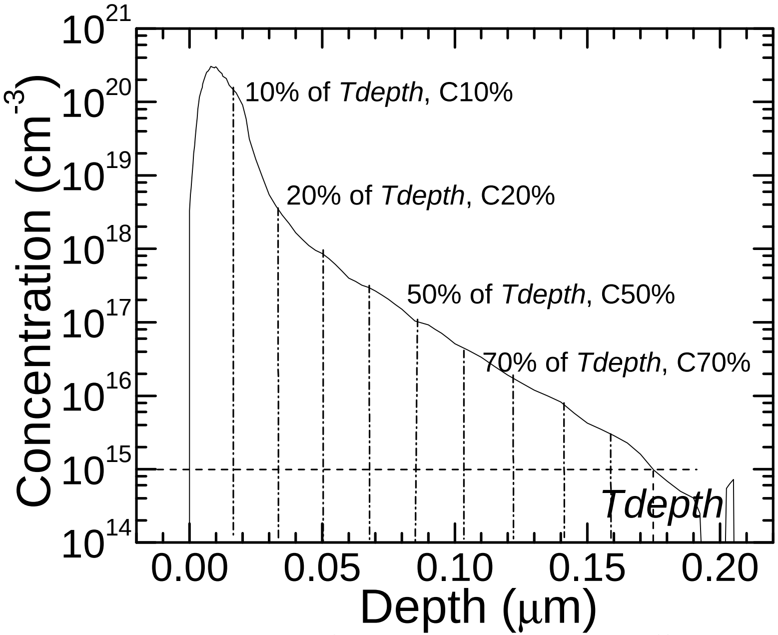

Fig. 4.17 Graphical representation of the SCALP technique. Cutoff concentration of 1×10^{15} atoms/cm^3 is used. Cx% refers to the concentration at x% of *Tdepth*

In this work, Cx% have been extracted from the impurity and damage profiles (interstitial and vacancy) profiles for six species (B, P, Ge, As, In and Sb) over the energy range 1-100keV at 1×10^{13} atoms/cm^2 and typical tilt/rotation angles of 7°/22°, 0°/0° and 45°/45°. For the six species in concern, all implants are non-amorphizing at the dose of 1×10^{13} atoms/cm^2. Hence, the profiles can be linearly scaled for lower doses until the amorphization threshold (10% of silicon density i.e. 10% of 5×10^{22} atoms/cm^3 = 5×10^{21} atoms/cm^3) for that species is reached. Beyond the threshold, the profile shape changes and the SCALP coefficients would have to be recalculated. Concentrations are extracted every 10% of *Tdepth*, with denser extractions at 5% near the surface and end of the profile. Twelve points are deemed sufficient to fully define a profile. An interval of 10% was chosen as the optimum as it was sufficient to give a good fit with any smaller interval offering negligible improvement. Table 4.6 shows the coefficients extracted from the simulated impurity, interstitial and vacancy profiles for a B 7°/22° implant in crystalline silicon at a dose of 1×10^{13} atoms/cm^2 over the energy range 1-100keV. Tabulated data for other tilt/rotation angles and the remaining elements are shown in Appendix B.

Table 4.6 Tabulated SCALP coefficients for (a) impurity (b) interstitial (c) vacancy profiles. B 1-100keV, 1×10^{13} atoms/cm^2, 7° tilt and 22° rotation

(a) Impurity

Energy	Tdepth	C0%	C5%	C10%	C20%	C30%	C40%	C50%	C60%	C70%	C80%	C90%	C95%
1	0.03518	3.072E+18	6.591E+18	8.439E+18	8.319E+18	5.123E+18	1.612E+18	7.759E+17	2.270E+17	8.367E+16	5.571E+16	1.435E+16	7.741E+15
5	0.09957	6.904E+17	1.524E+18	2.168E+18	3.015E+18	2.139E+18	9.416E+17	4.191E+17	1.935E+17	7.585E+16	3.817E+16	8.357E+15	1.132E+16
10	0.16456	3.242E+17	7.931E+17	1.213E+18	1.912E+18	1.376E+18	6.824E+17	2.340E+17	1.010E+17	3.023E+16	1.806E+16	5.543E+15	1.848E+15
20	0.22759	1.416E+17	2.838E+17	4.308E+17	8.674E+17	1.150E+18	9.405E+17	4.006E+17	1.648E+17	5.861E+16	1.248E+16	1.354E+16	7.068E+15
40	0.35659	4.945E+16	8.763E+16	1.543E+17	3.167E+17	6.073E+17	7.972E+17	5.668E+17	1.998E+17	6.073E+16	2.473E+16	7.821E+15	2.829E+15
60	0.46191	1.808E+16	3.566E+16	5.235E+16	1.530E+17	3.109E+17	5.682E+17	6.503E+17	2.593E+17	6.407E+16	2.166E+16	8.583E+15	2.155E+15
80	0.55566	7.638E+15	1.892E+16	3.187E+16	8.663E+16	2.191E+17	3.694E+17	5.676E+17	3.336E+17	7.981E+16	1.892E+16	6.971E+15	2.320E+15
100	0.64120	6.231E+15	1.077E+16	2.044E+16	5.034E+16	1.186E+17	2.682E+17	4.914E+17	4.018E+17	9.800E+16	2.243E+16	7.975E+15	1.745E+15

(b) Interstitial

Energy	Tdepth	C0%	C5%	C10%	C20%	C30%	C40%	C50%	C60%	C70%	C80%	C90%	C95%
1	0.03874	9.235E+19	1.444E+20	1.317E+20	6.494E+19	2.233E+19	5.916E+18	1.862E+18	6.582E+17	1.523E+17	8.555E+16	1.340E+16	1.331E+16
5	0.11383	9.617E+19	1.809E+20	1.896E+20	1.066E+20	3.228E+19	1.147E+19	4.238E+18	1.390E+18	4.756E+17	8.705E+16	3.115E+16	4.222E+16
10	0.18582	1.213E+20	1.903E+20	1.878E+20	1.213E+20	4.330E+19	1.010E+19	3.184E+18	1.175E+18	2.330E+17	3.194E+16	5.543E+15	1.252E+16
20	0.26187	1.299E+20	1.602E+20	1.631E+20	1.514E+20	8.869E+19	2.647E+19	6.965E+18	1.992E+18	5.357E+17	1.416E+17	3.302E+16	1.888E+16
40	0.38581	9.317E+19	1.098E+20	1.187E+20	1.341E+20	1.266E+20	8.022E+19	2.206E+19	4.133E+18	1.137E+18	3.571E+17	6.716E+16	1.197E+16
60	0.50489	6.477E+19	7.888E+19	8.772E+19	1.053E+20	1.242E+20	9.715E+19	3.991E+19	6.735E+18	9.755E+17	3.527E+17	5.106E+16	1.540E+16
80	0.59950	5.148E+19	6.167E+19	6.841E+19	8.474E+19	1.066E+20	1.032E+20	5.210E+19	9.043E+18	1.244E+18	2.172E+17	4.659E+16	1.247E+16
100	0.68000	4.177E+19	5.034E+19	5.613E+19	6.819E+19	9.092E+19	1.077E+20	6.720E+19	1.774E+19	2.672E+18	5.304E+17	4.765E+16	9.969E+15

(c) Vacancy

Energy	Tdepth	C0%	C5%	C10%	C20%	C30%	C40%	C50%	C60%	C70%	C80%	C90%	C95%
1	0.03874	1.072E+20	1.491E+20	1.267E+20	6.288E+19	2.129E+19	5.643E+18	1.779E+18	5.969E+17	1.660E+17	7.958E+16	1.437E+16	1.227E+16
5	0.11378	9.918E+19	1.848E+20	1.877E+20	1.063E+20	3.189E+19	1.147E+19	4.213E+18	1.374E+18	4.743E+17	8.371E+16	3.203E+16	4.062E+16
10	0.18579	1.252E+20	1.903E+20	1.877E+20	1.213E+20	4.291E+19	1.010E+19	3.136E+18	1.136E+18	2.417E+17	2.912E+16	5.543E+15	1.252E+16
20	0.26188	1.338E+20	1.602E+20	1.641E+20	1.514E+20	8.840E+19	2.618E+19	6.847E+18	2.000E+18	5.407E+17	1.328E+17	3.175E+16	1.921E+16
40	0.38581	9.396E+19	1.088E+20	1.197E+20	1.341E+20	1.266E+20	8.025E+19	2.196E+19	4.104E+18	1.118E+18	3.610E+17	6.568E+16	1.197E+16
60	0.50489	6.517E+19	7.898E+19	8.782E+19	1.053E+20	1.242E+20	9.706E+19	3.971E+19	6.725E+18	9.686E+17	3.546E+17	5.195E+16	1.540E+16
80	0.59940	5.178E+19	6.170E+19	6.841E+19	8.474E+19	1.066E+20	1.033E+20	5.242E+19	9.195E+18	1.266E+18	2.221E+17	4.805E+16	1.295E+16
100	0.68000	4.197E+19	5.034E+19	5.613E+19	6.819E+19	9.092E+19	1.077E+20	6.710E+19	1.774E+19	2.672E+18	5.284E+17	4.815E+16	9.471E+15

The relationship between the SCALP coefficients (extracted concentrations at different percentages of *Tdepth*) and implant energy can be largely described by low order polynomials or power law functions. Fig. 4.18 shows the power law ($y=ax^b$) relationship of C0%, C5%, C90% and C95% with energy based on the SCALP coefficients shown in Table 4.6.

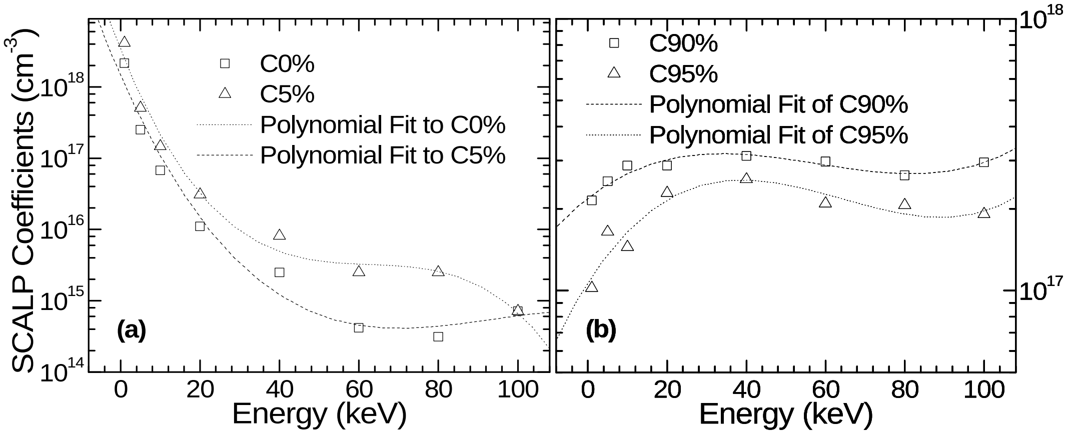

Fig. 4.18 Correlation of (a) C0%, C5% and (b) C90%, C95% with implant energy. Implant conditions are the same as for Table 4.6. Power law ($y=ax^b$) coefficients for 7°/22° are $a=2.8113\times10^{18}$, $b=-1.05791$

Prediction of the impurity profile can be done by determining each Cx% at the desired energy based on the fitting formulae. Alternatively, linear interpolation between the tabulated values can also give the SCALP coefficients at the desired energy. Similarly, the depth abscissa can be obtained by interpolating for *Tdepth* at the desired energy. For example, Table 4.7(a) shows the *Tdepth* and Cx% for the impurity profile of B 15keV, 1×10^{13} atoms/cm^2, 7° tilt and 22° rotation by direct interpolation between 10 and 20keV. The desired profile can then be obtained by plotting the corresponding x% of *Tdepth* versus the interpolated Cx%, as shown in Table 4.7(b). In this work, it was found that better results could be obtained by using different polynomial sets for different energy ranges ($y_1 = a_1 x^{b_1}$ for E<50keV; $y_2 = a_2 x^{b_2}$ for E>50keV) rather than with a universal polynomial function for the entire energy range. It was also found the best and most accurate fit to the as-implanted impurity and damage profiles was achieved by linearly interpolation of the tabulated data compared to the use of fitting polynomial functions. Fig. 4.19 shows the interstitial profile obtained for B 30keV, 1×10^{13} atoms/cm^2, 7° tilt and 22° rotation by linear interpolation of Cx% between 20 and 40keV.

Table 4.7 Prediction of impurity profile at 15keV by interpolation between 10 and 20keV

(a) Interpolated *Tdepth* and Cx% values for 15keV (shown in bold)

E (keV)	10	**15**	20
***Tdepth* (mm)**	0.16456	**0.19608**	0.22759
C0%	3.242E+17	**2.329E+17**	1.416E+17
C5%	7.931E+17	**5.384E+17**	2.838E+17
C10%	1.213E+18	**8.219E+17**	4.308E+17
C20%	1.912E+18	**1.390E+18**	8.674E+17
C30%	1.376E+18	**1.263E+18**	1.150E+18
C40%	6.824E+17	**8.115E+17**	9.405E+17
C50%	2.340E+17	**3.173E+17**	4.006E+17
C60%	1.010E+17	**1.329E+17**	1.648E+17
C70%	3.023E+16	**4.442E+16**	5.861E+16
C80%	1.806E+16	**1.527E+16**	1.248E+16
C90%	5.543E+15	**9.540E+15**	1.354E+16
C95%	1.848E+15	**4.458E+15**	7.068E+15

(b) Reconstruction of desired profile by reverse SCALP method

% of *Tdepth*	**Depth (mm)**	**Concentration**
0	0.00000	**2.329E+17**
5	0.00980	**5.384E+17**
10	0.01961	**8.219E+17**
20	0.03922	**1.390E+18**
30	0.05882	**1.263E+18**
40	0.07843	**8.115E+17**
50	0.09804	**3.173E+17**
60	0.11765	**1.329E+17**
70	0.13726	**4.442E+16**
80	0.15686	**1.527E+16**
90	0.17647	**9.540E+15**
95	0.18528	**4.458E+15**
100	0.19608	**1.000E+15**

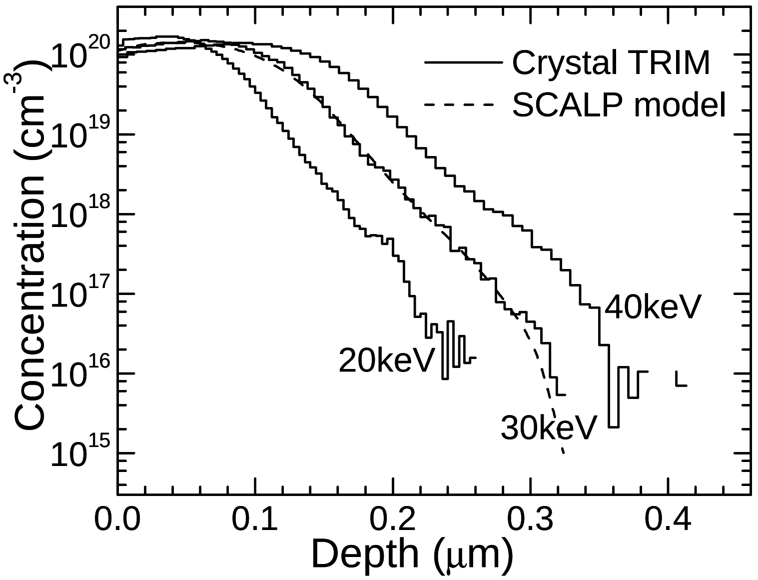

Fig. 4.19 Interpolated 30keV interstitial profile (B 1×10^{13} atoms/cm^2, 7° tilt and 22° rotation)

The SCALP technique is indeed useful as a fitting tool for any kinds of profiles at any implant conditions, since the coefficients can usually be correlated by simple analytical formulae. More importantly, it overcomes many limitations of the Pearson IV model which can have singularities depending on the choice of parameters. Moreover, the 3rd and 4th Pearson moments in the low energy regime show no predictable trend with energy, which makes interpolation impossible. The usefulness of this technique depends on the availability of a large number of simulated profiles, which are more readily available than experimental profiles. The good agreement between the simulated profiles obtained from Crystal-TRIM and SIMS data warrants the use of simulated rather than experimental profiles in the SCALP method for the six elements in concern. Figs. 4.20-4.22 show the excellent agreement between impurity, interstitial and vacancy profiles obtained from the SCALP method and the simulated profiles for different species at different energies between 1 and 100keV.

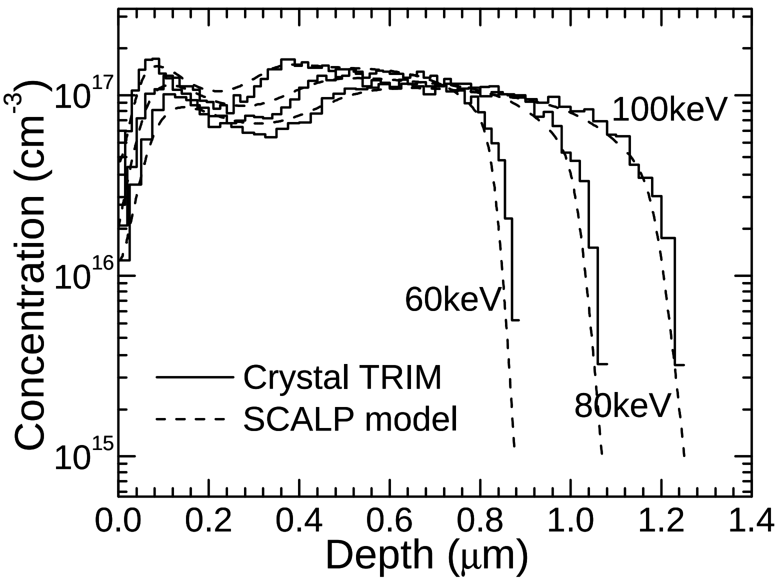

Fig. 4.20 Modeling of impurity profiles with SCALP coefficients (P 60keV, 80keV and 100keV, 1×10^{13} atoms/cm^2 at 45° tilt and 45° rotation)

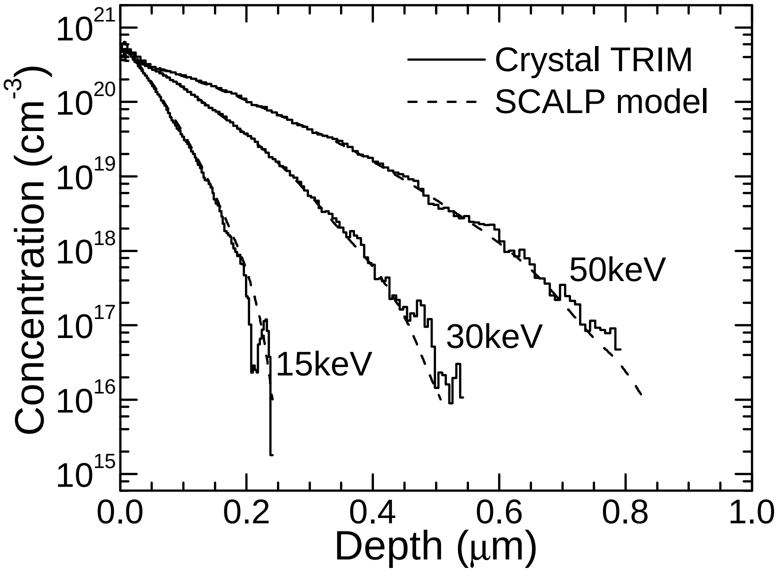

Fig. 4.21 Modeling of interstitial profiles with SCALP coefficients (Sb 15keV, 30keV and 50keV, 1×10^{13} atoms/cm^2 at 0° tilt and 0° rotation)

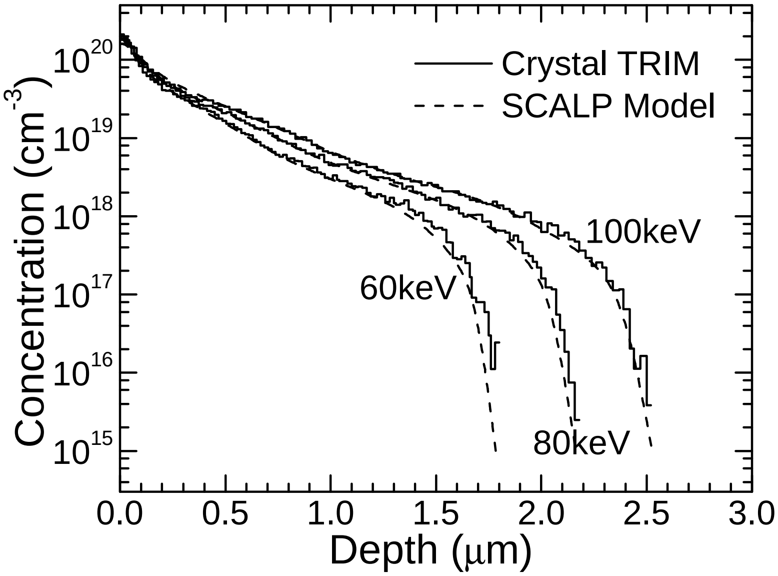

Fig. 4.22 Modeling of vacancy profiles with SCALP coefficients (As 60keV, 80keV and 100keV, 1×10^{13} atoms/cm^2 at 45° tilt and 45° rotation)

4.3 Assimilation of SCALP in process simulators

The large database of SCALP coefficients, shown in Appendix B can be assimilated in a multi-dimensional process simulator like DIOS (Integrated Systems Engineering, ISE AG), producing any 1D vertical impurity or damage profile given the implant conditions. This is aided by a C++ code which has been written to act as an interface between the SCALP tables and the process simulator. It first reads in the user-input implant conditions (species, implant energy, dose, tilt and rotation). It then searches the database based on these inputs. Suppose the input energy corresponds to one of the energies in the tables, the profile is generated based on the coefficients found in the tables. If the input energy is a value between two energy entries, interpolation is automatically performed, and the profile is created based on the reverse procedure shown in Table 4.7. To make the extraction of the SCALP coefficients more effective, a C++ code is also written to automatically generate the coefficients in tabulated form from the read-in simulated profiles. The syntaxes of the codes are shown in Appendix C.

In DIOS, the 1D vertical impurity profile generated from the SCALP methods can be extended in the lateral direction (2D) with the specification of the lateral straggling or standard deviation. In general, the ion beam need not be in the plane containing the 2D simulation domain and only its projection into the simulation domain is handled by the 2D simulator in DIOS. To calculate the concentration C(y,z) of the implanted element at a point (y,z) of the 2D simulation domain from the vertical profile, the 2D distribution functions are always assumed to be given as a product of two 1D distributions orthogonal to each other: a primary function and a lateral function. In this work, the primary function C(z) is taken to be the vertical profile calculated from the SCALP tables, and the lateral function is assumed, by default, to be a Gaussian function. As shown in Fig. 4.23, the eventual 2D profile spreading under the poly gate can be obtained with the specification of the lateral straggling, σ_{LAT}. Both vertical and lateral straggling are computed in Crystal-TRIM automatically by statistical means. σ_{LAT} can be taken directly from the prior Crystal TRIM run or taken to be identical to the vertical straggling, σ_Z as done in most process simulators. Fig. 4.24 shows both vertical and lateral straggling obtained over the energy range 100eV to 100keV for As 5×10^{14} atoms/cm^2 at the three different tilts and rotations.

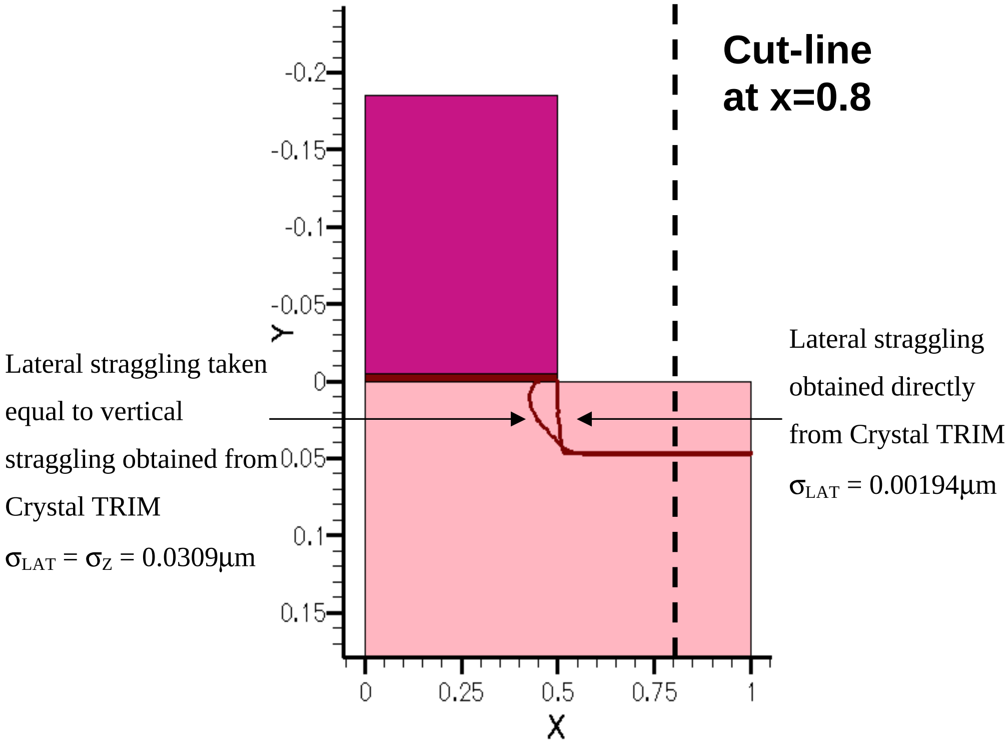

Lateral straggling taken equal to vertical straggling obtained from Crystal TRIM

$\sigma_{LAT} = \sigma_Z = 0.0309\mu m$

Lateral straggling obtained directly from Crystal TRIM

$\sigma_{LAT} = 0.00194\mu m$

Fig. 4.23 Lateral spreading accounted for by specification of σ_{LAT} in DIOS

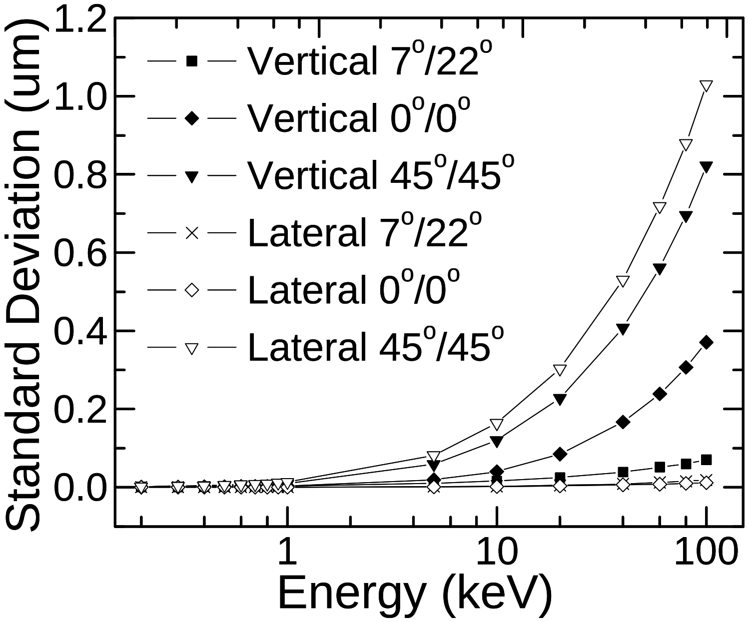

Fig. 4.24 Vertical and lateral standard deviation for As 0.1-100keV, 5×10^{14} atoms/cm^2 at 7°/22, 0°/0° and 45°/45°.

Assumption of $\sigma_{LAT} = \sigma_Z$ as done in most process simulators may result in excessive or insufficient lateral spreading depending on the implant tilt and wafer orientation. This assumption is reasonable for 7°/22° as can be seen in Fig. 4.24 where σ_{LAT} and σ_Z taken from simulated As profiles over the energy range 0.1-100keV are shown. While the difference between the vertical and lateral straggling is small for 7°/22°, taking $\sigma_{LAT} = \sigma_Z$ results in an overestimation of lateral spreading for 0°/0°. On the other hand, assuming the same for 45°/45° would have led to an underestimation of lateral spreading. Fig. 4.25 shows the excellent agreement between the vertical profile extracted from this 2D plot at x=0.8μm and SIMS data for As 10keV, 5×10^{14} atoms/cm^2, 0° tilt 0° rotation.

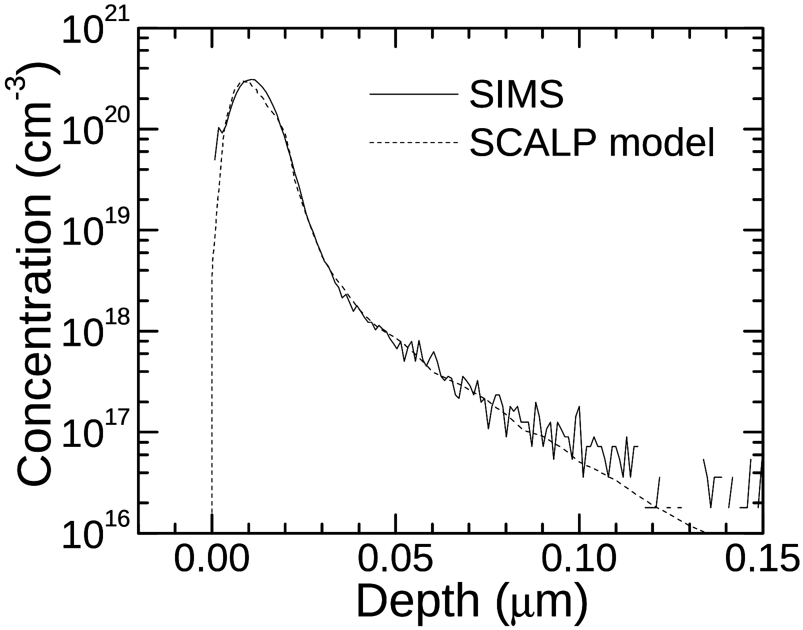

Fig. 4.25 Vertical impurity profile obtained by one-dimensional cut (Fig. 4.23) at x=0.8μm. SIMS data is shown for comparison (As in Si 10keV, 5×10^{14} atoms/cm^2 0° tilt 0° rotation)

To summarize this chapter, the usefulness of the Gaussian and Pearson IV models in modeling ion implantation profiles in crystalline silicon was investigated. Previously published models, like the model of Hobler et al. (1987) which had been derived in amorphous silicon are deemed inadequate to account for profile asymmetry and channeling phenomena commonly occurring in crystalline targets. New parameters for the Pearson IV model based on Hobler's analytical formulae are extracted for the crystalline impurity profiles obtained from MC simulations conducted with the BCA code Crystal-TRIM. They are apt for use at different implant tilts and wafer orientations over a wide energy range. However, there is a limit to the justifiable range of use for the Pearson model, especially as implant energy lowers. This is reflected by the increasingly random and unpredictable trends shown by the Pearson moments as energy lowers.

A new model, based on sampling calibration of profiles (SCALP) was presented. Coefficients presented in these tables are extracted by the SCALP technique, a method overcoming many of the limitations plaguing existing implant models. Because a large database of profiles is required for this technique, simulation rather than experimental profiles are used. Comparisons of experimentally measured profiles with simulated profiles show that excellent agreement can be obtained for many dopant species, including B, P, Ge, As, In and Sb over a wide energy range of 1keV to 100keV, justifying the use of simulation. Implant tables for impurity and damage (interstitial and vacancy) profiles created in single crystal silicon, which take into account the tilt and twist dependencies are presented for these six species. The use of the SCALP tables requires simply energy, dose, tilt/rotation as inputs and is a simple method over the complicated parameter extraction procedure of the Pearson IV technique. The technique can also be easily automated by the use of a C++ code which can perform the extraction of the coefficients automatically. In addition, lateral spreading can be studied by the generation of the lateral profiles via another C++ interface once the 1D implant profiles are loaded into the process simulators. The use is not yet straightforward but the accuracy and reliability of the SCALP tables warrants its implementation in process simulators in time to come.

CHAPTER 5 METHODOLOGY II: MOLECULAR DYNAMICS METHODS

5.1 Theory of Molecular Dynamics (MD)

The ingredients to molecular dynamics (MD) are not exactly new; the theoretical underpinnings amount to little more than Newton's laws of motion. For systems in thermal equilibrium, theory in the form of statistical mechanics had met with success in describing a system in equilibrium. Once out of equilibrium, simulations of various kinds, including MD help fill the gaps on the equilibrium side, but in the more general case, it is only by simulation, principally MD, that progress is possible. The equations of motion can only be solved numerically, and the phenomena that can be investigated must occur on length and time scale that are encompassed by the computation due to hardware limitations on the amount of computation that can be performed over a period of time, thus restricting the number of atoms that can be handled, as well as storage limitations.

The basic idea of MD is to calculate how a system of particles evolves in time. The two-body motion problem was solved by Newton, but the N-body problem cannot be solved analytically. Hence, MD provides a numerical way of solving the N-body problem. Consider a set of atoms at positions r_i and an interaction model which gives the potential energy of the system $V(r_i)$. In Newtonian mechanics, the following equations are valid.

$$\frac{dr_i}{dt} = \nu_i \tag{5.1}$$

$$\frac{d}{dt}(M_i \nu_i) = F_i = -\nabla_{x,y,z} V = -\nabla_{x,y,z}\left[\sum_i V_1(r_i) + \sum_{i,j} V_2(r_i, r_j) + \sum_{j,k} V_3(r_i, r_j, r_k) + \ldots\right] \tag{5.2}$$

Numerical solution to the above sets of equations gives us *dr* over a short time interval *dt*. Fig. 5.1 shows the flowchart of a simplified MD algorithm while Fig. 5.2 shows a schematic of a MD simulation of thermal motion over 100 time steps. The displacement over a time step Δt is denoted by Δr which has to be much smaller than the distance between nearby atoms.

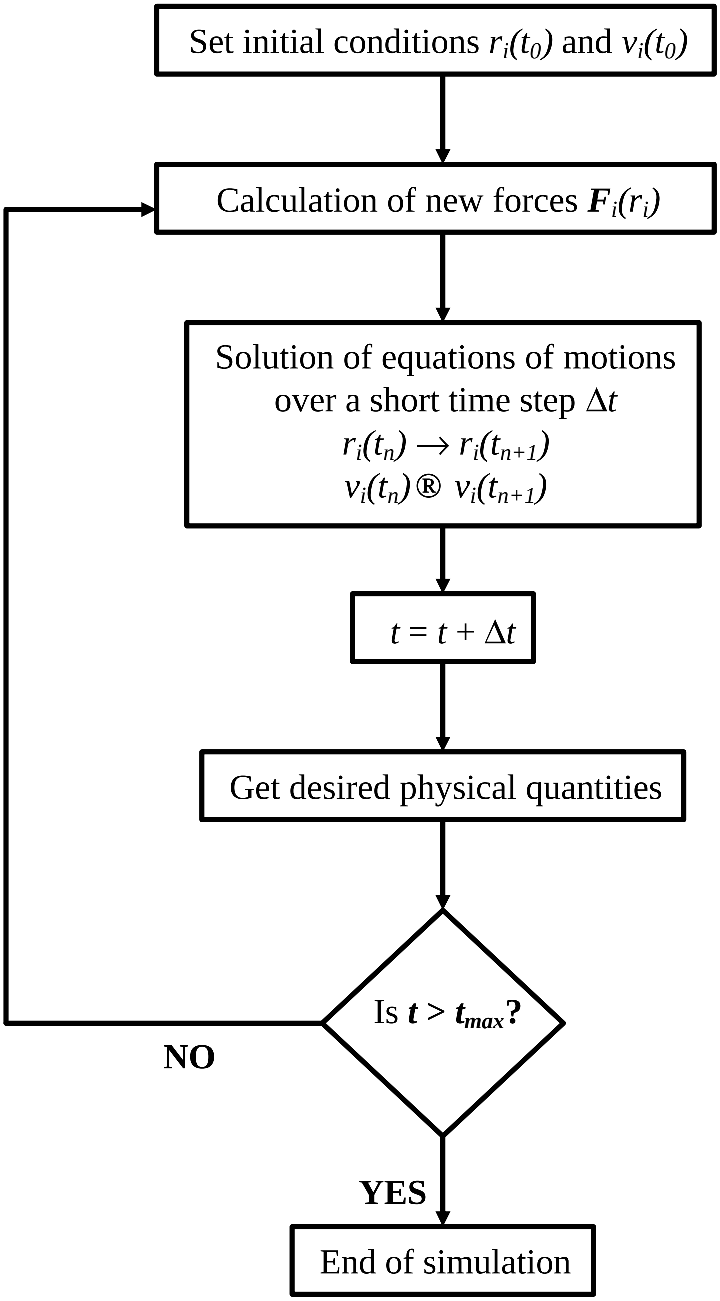

Fig. 5.1 Simplified flowchart depicting MD algorithm

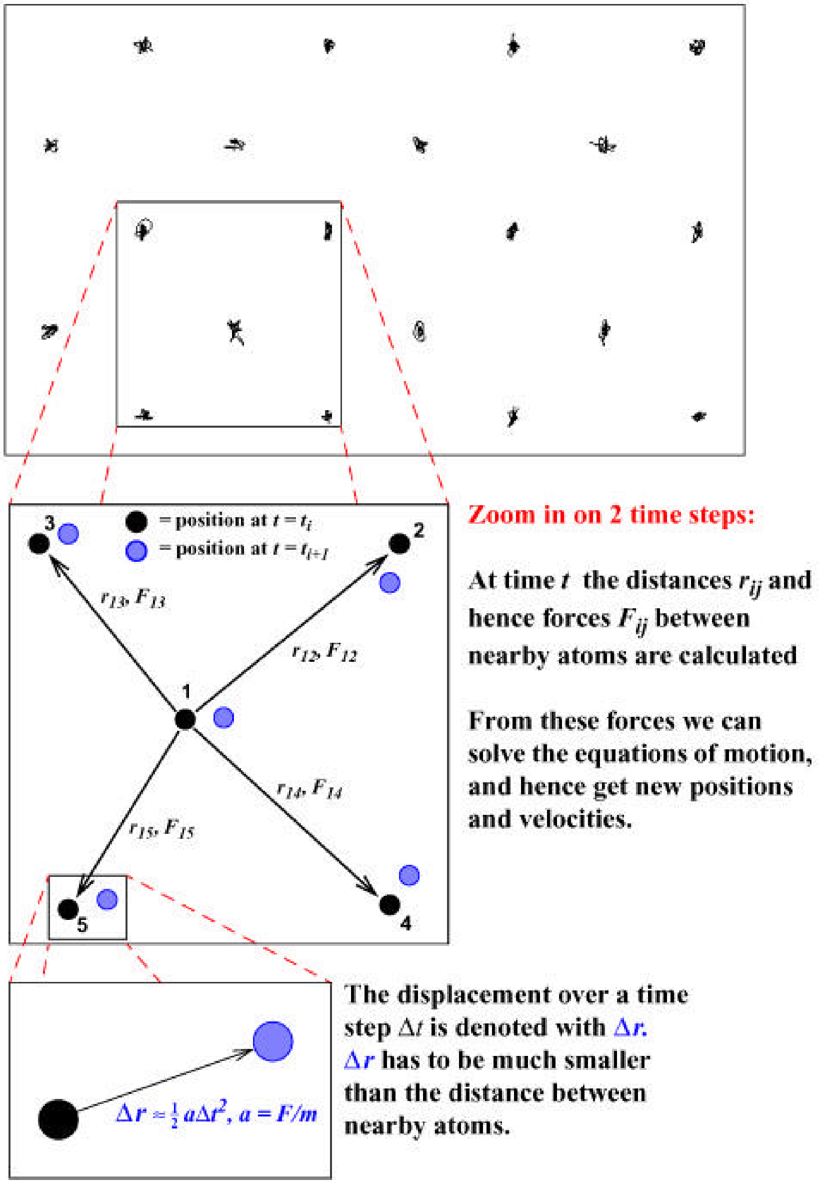

Zoom in on 2 time steps:

At time t the distances r_{ij} and hence forces F_{ij} between nearby atoms are calculated

From these forces we can solve the equations of motion, and hence get new positions and velocities.

The displacement over a time step Δt is denoted with Δr. Δr has to be much smaller than the distance between nearby atoms.

Fig. 5.2 Schematic diagram of MD simulation of thermal motion for 100 time steps (Courtesy of lecture notes from K. Nordlund)

5.1.1 Integration algorithm

The classical Newton's equations of motion for an object of mass *m*, moving at velocity *v* and coordinate *r* at time *t* in a system is given by Eq. (5.3) where F is the force acting on the object.

$$\frac{\mathrm{dv(t)}}{\mathrm{dt}} = \frac{\mathrm{d^2 r(t)}}{\mathrm{dt^2}} = \frac{\mathrm{F(t)}}{\mathrm{M}} \qquad (5.3)$$

Using Taylor's expansion theory, at an increased or reduced time step of Δ*t*, the coordinate *r*(*t*±Δ*t*) at time *t*±Δ*t* can be approximated as shown in Eq. (5.4).

$$r(t \pm \Delta t) \approx r(t) \pm \frac{dr(t)}{dt}\Delta t + \frac{1}{2}\frac{d^2r(t)}{dt^2}\Delta t^2 = r(t) \pm v(t)\Delta t + \frac{1}{2}\frac{F(t)}{M}\Delta t^2 \qquad (5.4)$$

The summation of *r*(*t*+Δ*t*) and *r*(*t*-Δ*t*) in Eq. (5.4) leads to a formula known as Verlet's algorithm (Verlet, 1967) to calculate the coordinate *r*, at time *t*+Δ*t* from *r* at *t*-Δ*t* and *t*.

$$r(t + \Delta t) \approx r(t) + \frac{dr(t)}{dt}\Delta t + \frac{1}{2}\frac{d^2r(t)}{dt^2}\Delta t^2 \qquad (5.4a)$$

$$r(t - \Delta t) \approx r(t) - \frac{dr(t)}{dt}\Delta t + \frac{1}{2}\frac{d^2r(t)}{dt^2}\Delta t^2 \qquad (5.4b)$$

$$r(t + \Delta t) + r(t - \Delta t) = 2r(t) + \frac{d^2r(t)}{dt^2}\Delta t^2$$

$$\therefore r(t + \Delta t) = -r(t - \Delta t) + 2r(t) + \frac{d^2r(t)}{dt^2}\Delta t^2 = -r(t - \Delta t) + 2r(t) + \frac{F(t)}{M}\Delta t^2 \qquad (5.5)$$

The velocity of the object, *v*(*t*) can be derived from the difference of *r*(*t*+Δ*t*) and *r*(*t*-Δ*t*).

$$r(t + \Delta t) - r(t - \Delta t) = 2\frac{dr(t)}{dt}\Delta t$$

$$\therefore v(t) = \frac{dr(t)}{dt} = \frac{r(t + \Delta t) - r(t - \Delta t)}{2\Delta t} \qquad (5.6)$$

The leapfrog method (Potter, 1972) is another representation of the Verlet algorithm, with which *r*(*t*) and *v*(*t*+Δ*t*/2) leads to of *r*(*t*+Δ*t*).

$$v\left(t + \frac{\Delta t}{2}\right) = v(t) + \frac{dv(t)}{dt}\frac{\Delta t}{2} = v(t) + \frac{1}{2}\frac{F(t)}{M}\Delta t$$

$$= \left[v(t) - \frac{1}{2}\frac{F(t)}{M}\Delta t\right] + \frac{F(t)}{M}\Delta t = v\left(t - \frac{\Delta t}{2}\right) + \frac{F(t)}{M}\Delta t \qquad (5.7)$$

$$r(t + \Delta t) = r(t) + v(t)\Delta t + \frac{1}{2}\frac{F(t)}{M}\Delta t^2 = r(t) + v(t)\Delta t - \frac{1}{2}\frac{F(t)}{M}\Delta t^2 + \frac{F(t)}{M}\Delta t^2$$

$$= r(t) + v(t)\Delta t - \frac{1}{2}\frac{dv(t)}{dt}\Delta t^2 + \frac{F(t)}{M}\Delta t^2 = r(t) + \Delta t\left[v(t) - \frac{dv(t)}{dt}\frac{\Delta t}{2} + \frac{F(t)}{M}\Delta t\right]$$

$$\therefore r(t + \Delta t) = r(t) + \Delta t\left[v\left(t - \frac{\Delta t}{2}\right) + \frac{F(t)}{M}\Delta t\right] = r(t) + v\left(t + \frac{\Delta t}{2}\right)\Delta t \qquad (5.8)$$

In the leapfrog method, both the coordinates and the velocity can be stored and their time evolution can be calculated. It is useful when the velocity is required at the same instant for kinetic energy calculations. For each time step, the velocities for the current time *t* can be calculated by the following equation.

Since $v\left(t+\frac{\Delta t}{2}\right)=v(t)+\frac{dv(t)}{dt}\frac{\Delta t}{2}$ and $v\left(t-\frac{\Delta t}{2}\right)=v(t)-\frac{dv(t)}{dt}\frac{\Delta t}{2}$

$$\therefore v(t)=\frac{v\left(t+\frac{\Delta t}{2}\right)+v\left(t-\frac{\Delta t}{2}\right)}{2}=\frac{\left[v\left(t-\frac{\Delta t}{2}\right)+\frac{F(t)}{M}\Delta t\right]+v\left(t-\frac{\Delta t}{2}\right)}{2}$$

$$=\frac{2v\left(t-\frac{\Delta t}{2}\right)+\frac{F(t)}{M}\Delta t}{2}=v\left(t-\frac{\Delta t}{2}\right)+\frac{1}{2}\frac{F(t)}{M}\Delta t \tag{5.9}$$

The total energy can be calculated at the same time *t* by summation of the kinetic energy and potential energy. This is necessary because for an isolated system, the total energy should be conserved; hence this is a good indication of whether the MD program has proceeded correctly.

5.1.2 Interatomic potentials and force calculations

The interactions between atoms are described in the form of potential energy as a function of interatomic distance. At the simplest level, the interactions occur between pairs of atoms and are responsible for providing the two principal features of an interatomic force. The first is a resistance to compression, hence the interaction repels at close range. The second is to bind the atoms together in solid and liquid states, and for this reason, the atoms must attract each other over a range of separations. Classical potential functions exhibiting these characteristics can adopt a variety of forms, and can be written in the form

$$V=\sum_{i}V_1(r_i)+\sum_{i,j}V_2(r_i,r_j)+\sum_{j,k}V_3(r_i,r_j,r_k)+\ldots \tag{5.10}$$

V is the total potential energy of an N-body system. In principle, the summation involves atoms 1 to N. However, in practice, the calculations have to be reduced for feasibility. V_1 is the single particle potential, which experiences external forces like an electric or magnetic field. In systems with no external forces V_1 = 0. V_2 is a pair potential which only depends on the distance between atoms, r_{ij}. V_3 is a three-body potential which may have an angular dependence, hence the potential depends only on three variables, i.e. $V_3 = V_3\ (r_{ij}\ ,\ r_{ik}\ ,\theta_{ijk})$. In general, V_2 and V_3 are enough to describe the basic mechanical and structural properties of most elements and simple compounds. The force on particle i can be given by the derivative of the potential function, as given in Eq. (5.2)

$$F_i = -\nabla_{x,y,z} V = -\nabla_{x,y,z}\left[\sum_i V_1(r_i) + \sum_{i,j} V_2(r_i, r_j) + \sum_{j,k} V_3(r_i, r_j, r_k) + \ldots\right] \tag{5.2}$$

As the number of atoms in the system increases, potential calculations get larger and longer simulation time is required. For the calculation of m-body potential in a system with N atoms, the number of pairs considered amounts to the order of N^m. In order to reduce computational time, in most simulations, the potential function is designed to have a cut-off radius r_C, the maximum distance in which a surrounding atom affects the central atom. Atom pairs with $r_{ij} < r_C$ do not interact. The cut-off radius is usually a few angstroms. By introducing the cut-off radius, the computational time can be reduced from the order of N^m to N. In cases where the potential extends to infinity, an analytical correction can be made in the form of energy E_C, the energy calculated assuming the material is continuous.

$$V_{Total} = V_2 + V_{correction} = E_C + 2\pi N\rho\int r^2 V(r) dr \tag{5.11}$$

This automatically assumes that when $r > r_C$, the atom density ρ is constant everywhere, and thus does not work when for example a surface is present.

5.1.3 Boundary and initial state conditions

The difference between finite and infinite systems lies in the problem of surface effects. A system that is bounded but free of physical walls can be constructed by the use of periodic boundary conditions (PBC). A schematic of 2D-PBC is shown in Fig. 5.3. The central box is replicated throughout the space to form an infinite lattice, If an atom moves in the original box (in bold) its periodic image in each of the neighboring boxes moves in exactly the same way. Thus, if an atom leaves the central box, like atom ‘a’ in Fig. 5.3, one of its images will enter through the opposite face, which is shown as ‘a′’. The introduction of periodic boundaries is equivalent to considering an infinite space-filling array of identical copies of the simulation region. Atoms lying within a distance, r_C of a boundary interact with atoms in an adjacent copy of the system, or, equivalently with atoms near the opposite boundary. This is similar to mapping the region onto the equivalent of a torus in four dimensions (a 2D system mapped onto a torus); then there would be no physical boundaries. In this way, it is possible to model systems that are effectively bounded but are nevertheless spatially homogeneous.

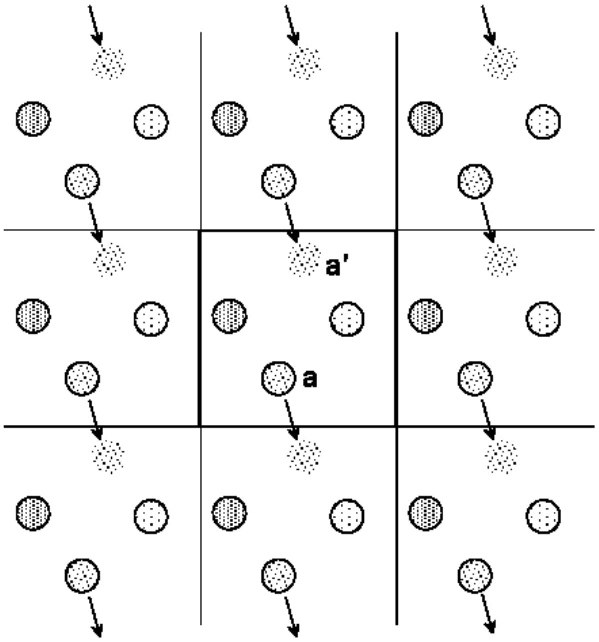

Fig. 5.3 Schematic of two-dimensional periodic boundary condition (Aoki, 2000)

In order to simplify the implementation of PBC, the periodic length should be larger than double the cut-off radius, otherwise the force calculation will take into consideration both the contributions of original and duplicated atoms. For this reason, the PBC cannot be applied if the interatomic force governing the system is a long-ranged potential. Periodic boundaries are most easily handled if the region is rectangular in two dimensions or a rectangular prism in three dimensions. In reality, any space-filling convex region can be used. This is to enlarge the volume to surface ratio, and thus increase the maximum distance between atoms before periodic ambiguity arises. Even with PBC, finite-size effects may occur. The size of the system required depends both on the type of system and properties of interest. The periodicity of the simulation cell brings an artificial interaction over the simulation cell borders which can distort some simulation cell results. For instance, a strain field arising from a point source or a vacancy in a silicon lattice will be distorted at the periodic borders. To overcome this problem, different cell sizes should be tested until results remain constant with increasing size. In a simulation where a lot of energy is brought into the simulation cell in a local region, like ion implantation, the energy has to be scaled out from the system to model a much cooler 'heat bath' in a realistic system. The energetic processes may also introduce a lot of momentum into the cell, which could cause the entire cell to move. The solution is to fix all boundary atoms except at the surface, and do temperature scaling in a few atom layers.

In order for MD to be useful, it must be capable of sampling a representative region of the total phase space of the system. This implies that the results of the simulation of adequate duration should be insensitive to the initial state such that any convenient initial state is allowed. An obvious choice would be to start with the atoms at the sites of a regular lattice, such as a square or simple cubic lattice, spaced to give the right density. The initial velocities can be assigned random directions and a fixed magnitude based on temperature such as the Maxwell-Boltzmann distribution $f(v_{i\alpha})$, which works well even in crystals. T is the temperature, M_i is the mass of the particle moving at velocities $v_{i\alpha}$ where α can be directional and k_B is the Boltzmann constant 1.38066×10^{-23} J/K.

$$f(\nu_{i\alpha}) = \left(\frac{M_i}{2\pi k_B T}\right)^{1/2} \exp\left(-\frac{M_i \nu_{i\alpha}^2}{2k_B T}\right); \alpha = x, y, z. \tag{5.12}$$

The initial velocities should also be adjusted so that the total momentum of the cell is zero and the centre of mass of the system is at rest. Random number generation is needed at least for initial velocity calculations. The equilibration to a state where there is no memory of the arbitrary selected initial configuration is usually quite rapid.

5.1.4 Acceleration methods

5.1.4.1 Neighbor list method

In MD, the force calculations require knowledge of the distances between atoms. This calculation is very time consuming if we consider each atom pair separately, and especially so when N approaches infinity. However, a large fraction of the neighbors remain the same during each time step, and computational time is wasted in recalculations at every time step. In the Verlet neighbor list method (Verlet, 1967), each atom has a list of neighboring atoms which reside within the cut-off sphere. This list can be updated after a certain number of time steps. The cut-off radius for the neighbor list should be long enough for another atom not to come into the r_m sphere until the next update. Thus, the minimum r_m is given by

$$r_m \geq r_C + u.\nu_{max} Dt \tag{5.13}$$

where u and v_{max} are frequency of list-update and maximum velocity in the system respectively. Fig. 5.4 shows that neighbor list method reduces the number of atoms considered significantly.

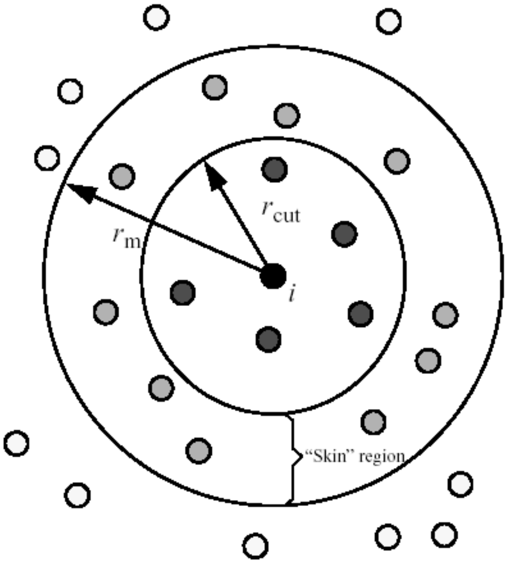

Fig. 5.4 Schematic of the neighbor-list or book-keeping method. Time for usual potential calculations reduced from $\Theta(N^2)$ to $\Theta(N)$

This method has two major advantages. Firstly, the simulation will not diverge when an atom suddenly starts to move much faster than the average, and secondly, when the system cools down (lower velocities), the neighbor list update interval will increase.

5.1.4.2 Linked cell or cellular method

In this method, the simulation space is divided into smaller sub-cells, as shown in Fig. 5.5. The length of the cell is set larger than r_m and every atom in the system is distributed in one of these cells at similar frequency with the neighbor list method. When the neighbors of atom *i* are needed, the program need only search through the sub-cell where *i* is, and its neighboring sub-cells, but not the entire simulation cell. In the linked cell method, the number of atoms considered is much larger than that in the neighbor list method. However, every procedure such as distributing the atoms and searching neighboring atoms are within the order of Θ(N) and less memory resources are required are compared to the neighbor list method where updating the list takes a time of $\Theta(N^2)$. Ideally, atoms can first be distributed in sub-cells, followed by the use of neighbor lists made in the manner of the linked cell method. Hence, both methods are complementary and should be used simultaneously if sufficient memory resources are available.

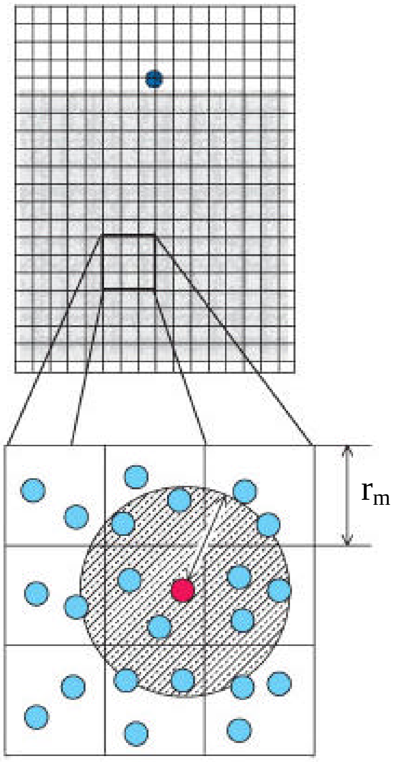

Fig. 5.5 Schematic of linked cell method

5.1.4.3 Variable time step method

The variable time step method is a way to use different time steps for each atom according to its velocity. In this way, the calculation speed of high-energy atomic collision processes can be accelerated. Suppose the maximum displacement per time step, Δr is given, the minimum time step can be given by $\Delta t_{\text{short}} = \Delta r / v_i$ where v_i is the maximum velocity in the system, which usually corresponds to the velocity of the incident atom. Similarly, the maximum time step $\Delta t_{\text{long}} = \Delta r / v_s$ can be used where v_s is considered the slowest velocity in the system, usually that of the substrate atoms. In pure MD, there is no way to increase the time step above ~10fs in atom systems of almost any real material at ordinary temperatures. This is the main limitation of MD, when all the atom movements in the system are tracked.

5.2 Molecular Dynamics code MDRANGE

The MD code used in this dissertation is a simulation program MDRANGE, tailored for effective calculation of ion ranges, mainly for energies practical in use. The simulation algorithms are based on the conventional Newton formalism and utilize the Verlet neighbor list method to enhance computational efficiency. Besides the neighbor list method, a variable time step method is also used to speed up the simulations, where the time step is made inversely proportional to the recoil velocity. For strong collisions, the time step is made inversely proportional to the product of the total force F on the recoil atom and its velocity. Unlike conventional full MD codes where the movements of all energetic atoms are calculated, only the interactions that are involved in the slowing down process, range and deposited energy distributions at higher energies are simulated in MDRANGE. Thus in calculations of ion ranges and deposited energies, the interactions between the recoil ion and its nearest neighbors are assumed to be much stronger than the interactions between lattice atoms. This approximation is termed Recoil Ion Approximation (RIA). By neglecting the weaker interactions, the code is capable of simulating high energy impact processes within a reasonable time frame without loss of accuracy. A brief summary of the physical principles and models used in the code will be given in this section (Nordlund, 1995).

5.2.1 Initial and Boundary Conditions

Initial displacement calculations are first performed to obtain realistic thermal displacements of the atoms from their initial sites. The atom positions are initialized to a crystalline or amorphous structure and given initial velocities in random directions according to the Maxwell-Boltzmann distribution for a particular temperature T. A Morse-type potential, of the form given in Eq. (5.14), where D and α are constants, is used for metals, while a modified Morse potential with a harmonic well (Mazzone, 1991) is used for tetrahedral semiconductors like silicon in the initial state calculations.

$$V_{Morse} = D\left(1 - e^{-\alpha x}\right)^2 \tag{5.14}$$

This simulation of thermal movement utilizes a constant time step and periodic boundary conditions and is continued until the average temperature taken over the last 100 time steps approaches the desired temperature T. The stability of the solution of the equations of motion can be tested by checking the total energy of the system which should be conserved. Since the RIA is employed, the lattice-lattice interactions are neglected; lattice atoms which do not interact with the recoil ion are held fixed at the positions determined in the initial state calculations. The velocity vector calculated in the initial state calculations will be used on the lattice atoms when they start interacting with the recoil ion.

A few factors should be considered when selecting the size of the simulation cell. Since the interaction between two atoms is included in the calculation only if their interatomic distance is less than the cut-off radius r_C, all atoms within a sphere of r_C should be present at all times during the simulation. With r_C values typically around 3Å, this necessitates a simulation cell length of at least 10-15Å to contain all relevant atoms. However, for computational efficiency, the simulation cell should be kept as small as possible. Another important consideration is the continuous movement of the ion which should always be surrounded by lattice atoms. Since it is computationally impossible to track the entire ion path in one simulation cell, and the use of PBC is unrealistic since the recoil ion cannot move in a simulation cell damaged by its own previous motion, a cell translation method is employed to ensure that the ion does not encounter its mirror cell. Fig. 5.6 shows the schematic of the cell translation technique. A critical approach distance R_{Si} is first defined for the three space coordinates (i = x, y and z). Intuitively, R_{Si} should be larger than the cut-off radius but less than half the size of the simulation cell. Hence, a good choice would be to select R_{Si} as the size of the unit cell or some integer fraction of it. When the ion approaches the boundary of R_{Si}, the ion and all atoms surrounding it are translated a distance of R_{Si} away from the simulation border. The shifted atoms retain their previous velocities and accelerations while the new strata layer contains atoms whose positions and velocities are taken from the initial state calculations. This method ensures that the ion movement can be simulated in a sufficiently large cell without actually increasing the number of atoms in the system.

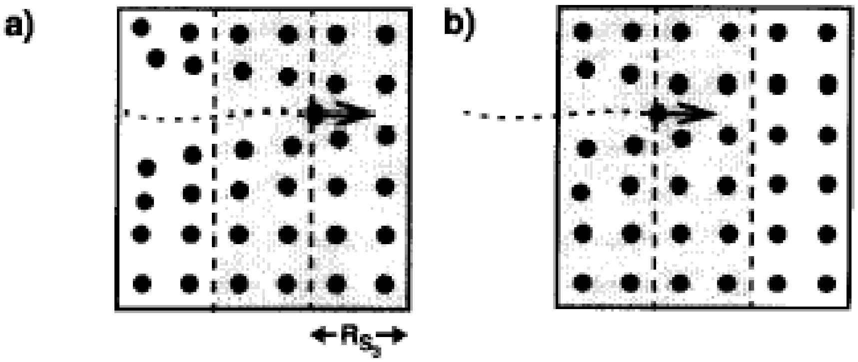

Fig. 5.6 Schematic two-dimensional view of cell translation technique (a) before and (b) after ion movement (Nordlund, 1995)

5.2.2 Nuclear energy loss: Density functional theory potential

By default, the treatment of nuclear effects in MDRANGE entails the use of the ZBL potential described in detail previously (see Section 3.2.1). The code allows modification of the parameters of the ZBL potential to yield a more realistic description of atomic interactions. However, despite the flexibility of parameters, the functional form of the ZBL potential is a positive one, implying that attractive forces are unable to be accounted for. Nordlund et al. (1997) has found that density functional theory (DFT) calculations utilizing numerical basis sets and Hartree-Fock (HF) calculations using decontracted standard basis sets provide potentials which are significantly improved compared to the standard universal ZBL potential. The four diatomics C-C, H-Si, N-Si and Si-Si were studied in their work. In this work, a similar approach using DFT is employed to calculate the interatomic potentials for nine dopant-silicon systems, namely B-Si, C-Si, N-Si, F-Si, P-Si, Ge-Si, As-Si, In-Si and Sb-Si. The DFT package, DMOL (DMOL is a trademark of Accelrys Inc., California, USA) will be used for all the potential calculations mentioned in this work. A brief description of the chemical and mathematical theory upon which DMOL is based will be given.

5.2.2.1 Density Functional Theory (DFT)

In classical mechanics, energy is conserved through Newton's laws. In quantum mechanics (QM), energy conservation takes the form of the Schrodinger equation. The laws of QM states that the energy and other related properties of a system can be obtained by solving the Schrodinger equation, a wave equation in terms of the wavefunction ψ which predicts analytically and precisely the probability of events or outcome. The Schrodinger equation gives the quantized energies of the system and gives the form of the wavefunction so that other properties may be calculated.

Schrodinger equation: $H\psi = E\psi$ (5.15)

E is the energy eigenvalue of the system while the Hamiltonian operator H is the QM counterpart of the classical kinetic and potential energies which acts upon ψ to generate the evolution of the wavefunction in time and space. Exact solutions to this equation cannot be obtained in practice; hence QM methods are characterized by their various mathematical approximations to its solution. Semi-empirical methods use parameters derived from experimental data to simplify the computation, and solve the approximate form of the Schrodinger equation. *Ab-initio* methods, on the other hand, use no experimental parameters in their computations, but are based solely on the laws of quantum mechanics, and on fundamental quantities like the speed of light, the masses and charges of electrons and nuclei, and Plank's constant. Density functional theory (DFT) methods, like the first two methods, aim at predicting molecular or solid geometrical structures and electronic properties. However, unlike the other methods, DFT assumes that the electron density, and not the wavefunction, is the fundamental quantity that determines the properties of the molecular or solid systems. In the DFT approach, the Kohn-Sham (KS) equations (Kohn et al., 1965), based on the theorem of Hohenberg et al. (1964), are self-consistently solved.

$$\left[-\frac{\hbar^2}{2m}\nabla^2 + V_S(r) + V_{XC}(r)\right] f_i(r) = e_i f_i(r) \qquad (5.16)$$

The first term is the kinetic energy of the system, V_S is the electrostatic potential due to nuclei and the electron charge distribution and e_i are Lagrangian multipliers. The key quantity, the electron charge density ρ(r) is summed over all molecular orbitals f_i(r) and given by the simple sum shown in Eq. (5.17).

$$r(r) = \sum_i |f_i(r)|^2 \qquad (5.17)$$

The molecular orbitals f_i(r) are expanded as a linear combination of atomic orbitals c_j.

$$f_i(r) = \sum_j C_{i,j} c_j(r) \qquad (5.18)$$

V_{XC} is the exchange and correlation potential obtained by differentiating e_{XC}, the exchange and correlation energy which includes all many-body contributions and requires some approximation for computational tractability.

$$V_{XC} = \frac{d[r(r) e_{XC}]}{d[r(r)]} \qquad (5.19)$$

The local density approximation (LDA) (Kohn et al. 1965) is a simple and good approximation which is based on the known e_{XC} of a uniform electron gas. It assumes that the charge density varies slowly on an atomic scale, i.e. each region of a molecule resembles a uniform electron gas. The total exchange-correlation energy can be obtained by integrating the uniform electron gas result, where e_{XC}(ρ) is the exchange-correlation energy per particle in a uniform electron gas and ρ is the number of particles.

$$e_{XC}(r) \cong \int r(r) e_{XC}[r(r)] dr \qquad (5.18)$$

5.2.2.2 Atomic basis sets

In DMOL, the atomic basis sets are generated numerically. The use of exact DFT spherical atomic orbitals has several advantages. Firstly, the molecule can be dissociated exactly to its constituent atoms, and secondly, because of the quality of these orbitals, basis set superposition effects (Delley, 1990) are minimized, and an excellent description of even weak bonds is possible. The atomic basis functionsc_j used in DMOL consist of two numerically tabulated atomic basis functions for each occupied atomic orbital. The basis set size is doubled by solution of the atomic DFT equations once for the neutral atom and once for the doubly charged cation; this is referred to as a double-numerical (DN) set. The ionic wavefunctions are then orthogonalized to those of the neutral atom. This method provides a way of generating basis sets that increase the electron density in the region close to the atom where bonding effects are important. The orthogonalization result in the removal of functions that may form linearly dependent sets. Hence, these DN basis sets are not always exactly twice the size of minimal bases. However, because these functions are essentially exact for the atom, they are significantly more accurate than other atomic bases.

The DMOL method is not fully numerical since the atomic orbitals are kept fixed during the calculations while all the integrals are computed numerically. In this work, the Vosko-Wilk-Nusair (VWN) Hamiltonian with no gradient corrections is used. Polarization functions can be accounted for by the use of hydrogenic orbitals which can be generated for different nuclear charges. They can be optimized by varying the nuclear charge used to generate the orbitals. Additional hydrogenic orbitals were added to all the systems investigated to account for polarization. For $Z_1<11$ (B, C, N and F), the standard basis sets are automatically augmented with hydrogenic orbitals. For $Z_1>11$ (P, Ge, As, In and Sb), hydrogenic orbitals have been added to two nuclear charges, Z_1 as well as Z_1-1. For the special case of Si, hydrogenic orbitals are added for four different nuclear charges Z_1=14, 13, 11 and 15. The orbitals added are 1s, 2p, 3d and 4f orbitals. It was found that these additional basis sets had a significant effect on the energies obtained, especially at close separations. The actual implementation of the hydrogenic orbitals to the basis set is achieved by construction of a new basis set using the *DATOM* utility supplied with the DMOL package; details are given in Appendix D.

5.2.2.3 Single-point energy calculations

The potential energy V(r) between two atoms can be evaluated by the difference between the total energy at an interatomic separation r and the total energy of the isolated atoms.

$$V(r) = E(r) - E(\propto) \qquad (5.19)$$

The interactions, at the simplest level, occur between pairs of atoms and are responsible for providing firstly, a resistance to compression. The second is the binding of the atoms in the solid state, hence attraction of the atoms over a range of separations. A pair potential, which is repulsive at short range and attractive at long range is commonly used. The interatomic potential V(r) is hence obtained by calculating the total energy of the diatomic system at different interatomic separations r. It has been suggested that the diatomic potential does not differ much from a bulk potential at energies ≥ 10eV (Nordlund et al., 1997). This can be explained when one considers the bulk potential energy of a system of atoms, which is at most 5eV. When the atoms move away from each other, each pair contribution decreases. When the atoms approach each other, the bond energy of the other atoms further away will at most contribute some 5eV to the energy, which becomes negligible when the close-range repulsive forces become greater than 10eV. While the pair potential is a simple approximation to the true interacting forces in the attractive and repulsive-attractive transition regions, the negligible contribution of the neighboring atoms at close separations warrants its use in this work.

The input files used in DMOL are described in detail for the different diatomic systems in Appendix D. Given the basis sets, coordinate system and calculation parameters, the total energy of the system can be evaluated and the potential energy curve can be found. In summary, the following conditions are used when simulating the total energy of the system:

1. Single point energy calculation (at different inter-atomic separations)
2. Functional: Vosko-Wilk-Nusair (VWN) Hamiltonian with no gradient corrections
3. Spin restricted and fine integration grid

4. Basis set: Double Numerical (DN) with added hydrogenic orbitals (For all systems involving Si, the DN basis set was extended with the hydrogenic orbitals for Z=14,13,11 and 15, each containing the 1s, 2p, 3d and 4f hydrogenic orbitals)

Fig. 5.7 shows the pair potentials obtained from the DFT calculations utilizing the above mentioned conditions for nine common dopant-silicon systems.

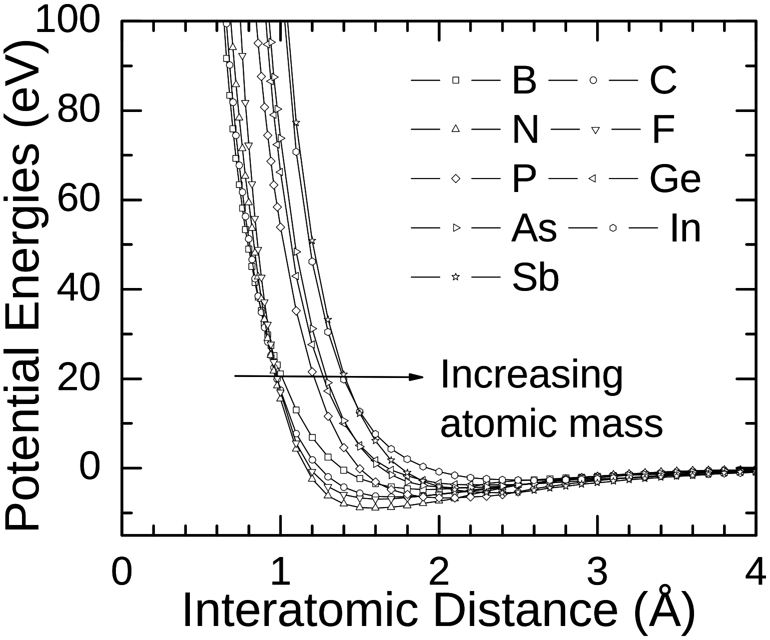

Fig. 5.7 Energies (in eV) obtained from DFT calculations utilizing the DMOL package for nine dopants (B, C, N, F, P, Ge, As, In and Sb)

The pair potentials calculated from this first-principles study will be referred to extensively in subsequent chapters and will be denoted as DMOL potentials henceforth. The potential calculations have been made from r=0Å to r=10Å at regular intervals of 0.1Å. However, only values up to r=4Å are displayed since the potential approaches zero as r approaches infinity. This is similar to the ZBL potential where the field effect of one atom on the other diminishes until the total energy of the two atoms approaches that of two isolated atoms, i.e. zero when the two atoms move away from each other. The energy increase to infinity as the electron clouds of the two atoms overlap is also depicted in the DMOL potentials. Like the ZBL potential, the DMOL potential energy curves consist of large positive values representing strong repulsive forces between the two atoms at close separations, which govern the trajectories of ions at high velocities. The main difference between the two potentials lies in the presence of an attractive region absent in the positive ZBL potential. The potentials calculated from DFT show a negative energy regime, describing the attractive forces between the two atoms at certain interatomic separations, before strong repulsion occurs at even closer separations. It is this attractive force that holds all the atoms together in the solid phase and it is especially important when an ion approaches the target at low energies since the ion now has more time to interact with the target atoms. The equilibrium distance r_0, i.e. the interatomic separation where the energy is lowest and the system is most stable, increases with increasing atomic mass. This is intuitive when one considers the increasing size and sheltering effect of electron shells as atomic mass increases. From the electronic configurations, B [$1s^2$ $2s^2$ $2p^1$] is much less shielded from the silicon atom compared to a heavier atom like Sb [$1s^2$ $2s^2$ $2p^6$ $3s^2$ $3p^6$ $3d^{10}$ $4s^2$ $4p^6$ $4d^{10}$ $5s^2$ $5p^3$] whose d electrons provide stronger screening. The DMOL potentials will be used in the MD simulations and compared with results obtained with the ZBL potentials.

5.2.3 Electronic energy loss

MDRANGE offers the flexibility of calculating the stopping due to electrons either by the non-local ZBL model or the local model by Brandt-Kitagawa (BK), both described clearly in Chapter 3. The newest version supports the use of a local model which uses the local electronic density in the target material and phaseshifts for the calculations. Unlike models based on the BK theory, this local model takes the structure of the electron cloud of the ion into account and does not employ any scaling laws. This electronic stopping will be denoted as PENR model henceforth, after the co-authors Puska et al. (1983) and Echenique et al. (1981). In this section, only the PENR model will be described. This method is based on DFT calculations of the electronic structure of atoms embedded in a homogeneous electron gas. The scattering cross sections which the embedded atoms induce for Fermi-surface electrons can be expressed in phaseshifts which are basically quantities produced by the interaction of the atoms in the electron gas and therefore characterize the scattering process in a potential V(r). The mathematical formulation of the scattering phase shifts is beyond the scope of this work, but is given in Appendix E for completion.

A common approach for obtaining stopping powers is first to derive a stopping power for a proton, and the stopping power of heavier ions can then be calculated by scaling the proton stopping. Models based on the scattering phaseshifts for Fermi-surface electrons were first proposed by Ferrell et al. (1977) and are very popular for calculating the proton stopping power since it has been proven successful for some technologically important ion-target combinations such as B-Si, P-Si, and As-Si (Cai et al., 1996) (Beardmore et al., 1998). The original model by Ferrell and Ritchie offers another frequently overlooked approach to obtain stopping powers for heavy ions. Instead of using scaling laws, it is possible to explicitly calculate phaseshift factors for any given ion-target atom combinations. The phaseshift factors can be calculated directly within the DFT formalism for a proton embedded in a homogeneous electron gas, so this approach does not use any empirical or fitted input factors. For an ion traveling at a velocity below the Fermi velocity of the electrons i.e. $v < v_F$, the non-linear density-functional calculations of Puska et al. (1983) gives the stopping of a proton as

$$S_{el}^{PENR} = \frac{3v}{k_F r_s^3} \sum_{l=0}^{\infty} (l+1) sin^2 \left[d_l (E_F) - d_{l+1} (E_F) \right] \tag{5.20}$$

k_F is the Fermi momentum of electrons of the target given by Eq. (5.21) which relates the electron density ρ to the Fermi momentum.

$$k_F = \left(3p^2 r \right)^{1/3} \tag{5.21}$$

$$r = \left(\frac{3}{4pr_s} \right)^{1/3} \tag{5.22}$$

The electron density ρ given by Eq. (5.22) is in turn obtained from a spherically symmetric distribution where r_S is the one-electron radius, a density parameter in atomic Bohr units. $d_l(E_F)$ is the phaseshift for the scattering of an electron at the Fermi energy E_F. The phaseshifts are obtained from the self-consistent solution of the Kohn-Sham DFT equations, Eq. (5.16). A nucleus of charge Z_1 is embedded in a homogeneous electron gas of density ρ and the LDA is invoked for exchange and correlation. The phaseshifts are calculated from the DFT code ***jellium*** (courtesy of Prof. M.J. Puska) for the nine dopant systems (B, C, N, F, P, Ge, As, In and Sb). Original calculations of Puska et al. (1983) include $d_l(E_F)$ values only for $Z_1=1$ up to $Z_1=15$ and r_S from 1.5 through 5.0. In this work, calculations are made for $Z_1=5$ (B) to $Z_1=51$ (Sb) and $d_l(E_F)$ are calculated for a dense grid of one-electron radius at an interval of 0.1 for $0.1<r_S<6.0$. In cases where convergence is impossible, the r_S values are calculated with a sparser grid and the tabulated values are then used to interpolate for phaseshifts at a desired electron density, as was done in the work of Sillanpaa et al. (2001). Calculations for partial waves up to $l=10$ were made, although phaseshifts for $l>5$ were very small. For the self-consistent calculations, the phaseshifts should obey the Freidel sum rule due to the complete screening of the nuclear charge Z_1.

$$\frac{2}{p}\sum_{l}(2l+1)d_l(E_F)=Z_1 \tag{5.23}$$

The schematic in Fig. 5.8 shows the algorithm for the phaseshift calculations. For every charge Z_1 at a particular quantum number l and position in the charge distribution (r_S), the phaseshifts are first determined by solving the Kohn-Sham electron wave functions. The calculations are repeated until $l=10$. From the stopping power given in Eq. (5.20), a useful expression Q can be derived from the phaseshifts, which is simply S_{el}^{PENR} without the velocity component.

$$Q=\frac{3}{k_F r_s^3}\sum_{l=0}^{\infty}(l+1)\sin^2\left[d_l(E_F)-d_{l+1}(E_F)\right] \tag{5.24}$$

When Q is multiplied by the velocity of the slow ion, the electronic contribution to the stopping power will be known. The Friedel sum is also checked by Eq. (5.23). If unsatisfied, the calculation should exit immediately. Upon satisfaction of the Friedel sum, the aggregated phaseshift for a particular r_S is calculated and the algorithm is repeated for another r_S value. In cases where convergence is not possible (small r_S and large Z_1), interpolation is performed to obtained the phaseshift at a particular r_S. This is done only for Z_1=49 (In) and Z_1=51 (Sb) since convergence is possible for all cases. The stopping power in atomic units is finally converted to S.I. units by a constant factor before the values are loaded into MDRANGE where Q is multiplied by the instantaneous velocity to give the electronic stopping power.

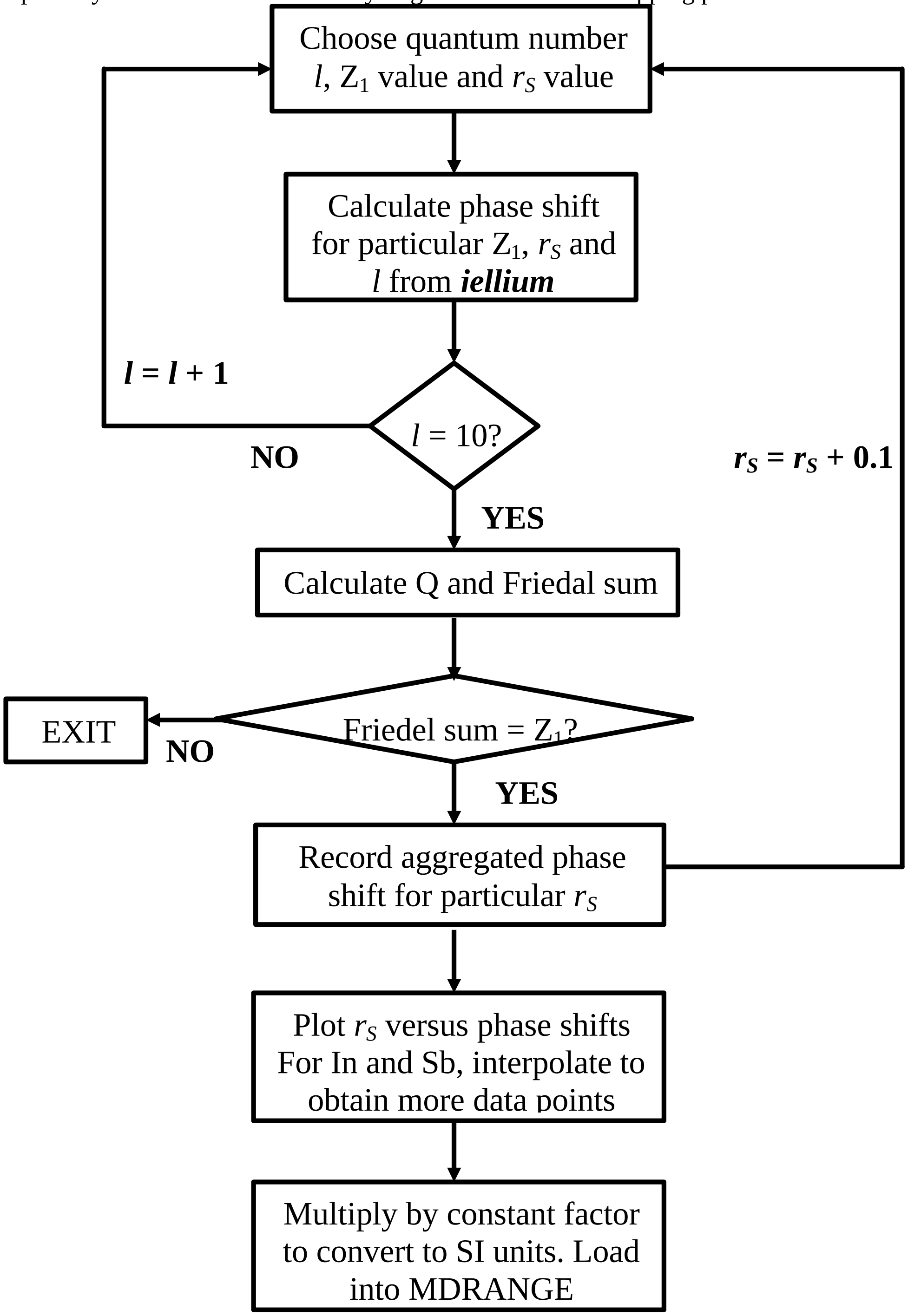

Fig. 5.8 Algorithm for calculation of Q and scattering phaseshifts

An example of the phaseshifts calculations made for Z_1=5 (Boron) will be shown here. The phase shifts are calculated using the DFT code ***jellium*** for different quantum numbers from *l*=0 to *l*=10 for different one-electron radius r_S. Table 5.1(a) and (b) shows the phaseshifts values obtained for B from the DFT calculations for *l*=0 to *l*=10. Column 6 in Table 5.1(b) corresponds to the electron density ρ calculated from Eq. (5.22) while column 7 is the Fermi momentum calculated from Eq. (5.21). Q is the summation value given by Eq. (5.24), simply S_{el}^{PENR} without the velocity component and the last column is the electronic stopping values in S.I. units that will be imported into MDRANGE as a r_S versus Q file. The last column gives the Q values divided by a factor of 4.25e+4. This conversion factor can be obtained by:

1 Hartree = $4.3597438134 \times 10^{-18}$ Joules = 27.21136875 eV

1 eV = $1.60217733 \times 10^{-19}$ Joules and a_0 = 0.52917724924A

Therefore, (Hartree/a_0) = 21.21136875eV/0.52917724924 = 51.42203071 (eV/A)

Similarly, the velocity component in atomic units can be converted to S.I. units by the Fermi velocity expression $\mathrm{v} = \alpha \mathrm{c} = 2.187691396 \times 10^6$ m/s where c is the speed of light given by 2.99792458×10^8 m/s and α is the fine structure constant given by

$$\alpha = \frac{\mu_0 \mathrm{ce}^2}{2\mathrm{h}} = \frac{\left(1.256637061\times10^{-6}\right)\left(299792458\right)\left(1.60217733\times10^{-19}\right)^2}{2\left(6.6260755\times10^{-34}\right)} = 7.297353011\times10^{-3}$$

Hence, to convert the atomic form Q to stopping power in S.I units, one has to divide the Q values by 2.187691396×10^6/51.42203071 = **4.254385457´10^4**.

Table 5.1 Phase shifts obtained from DFT calculation for B using the code ***jellium*** from (a) *l*=0 to *l*=7 for r_S up to 1.0 only. Actual calculations are done up till r_S=6.0.

r_S	***l* = 0**	***l* = 1**	***l* = 2**	***l* = 3**	***l* = 4**	***L* = 5**	***l* = 6**	***l* = 7**
0.1	0.545684	0.29305	0.178935	0.118947	0.077718	0.05285	0.038019	0.023335
0.2	0.96467	0.460767	0.250642	0.148101	0.088201	0.054501	0.035433	0.020297
0.3	1.318507	0.575523	0.280529	0.14904	0.081294	0.046007	0.027262	0.014617
0.4	1.625025	0.664516	0.292325	0.141392	0.071315	0.03734	0.020365	0.010256
0.5	1.890004	0.737064	0.293616	0.130342	0.061204	0.029828	0.015028	0.007089
0.6	2.119564	0.798408	0.288357	0.118191	0.051926	0.023644	0.010998	0.004813
0.7	2.319908	0.851683	0.278798	0.106026	0.043749	0.018653	0.007977	0.003177
0.8	2.496592	0.898803	0.266318	0.094367	0.036675	0.014658	0.005716	0.001997
0.9	2.65421	0.940952	0.251828	0.083455	0.030615	0.011471	0.004025	0.001145
1.0	2.796407	0.978882	0.235978	0.073387	0.025451	0.008932	0.002759	0.000527

(b) *l*=8 to *l*=10, including calculations for electron density ρ, Fermi momentum k_F and the final electronic stopping (Q*conversion factor)

***l* = 8**	***l* = 9**	***l* = 10**	d**(E_F)*(2*l*+1)**	**Sum**	r	**k_F**	**Q**	**Stopping**
0.010805	0.003756	0.00101	2.91003933	0.113698	238.7324	19.19158	17.77303	4.18E-04
0.009042	0.003076	0.000816	3.84128288	0.376776	29.84155	9.595791	14.72426	3.46E-04
0.006271	0.002089	0.000547	4.1237672	0.706781	8.841941	6.397194	12.27589	2.89E-04
0.004238	0.001381	0.000357	4.22851416	1.03207	3.730194	4.797896	10.08323	2.37E-04
0.002805	0.000889	0.000225	4.25937944	1.308721	1.909859	3.838317	8.183095	1.92E-04
0.001798	0.000547	0.000134	4.26152323	1.524571	1.105243	3.198597	6.619965	1.56E-04
0.001087	0.000306	7.04E-05	4.25618281	1.685363	0.696013	2.741655	5.376601	1.26E-04
0.000581	0.000135	0.000025	4.25336345	1.802337	0.466274	2.398948	4.402167	1.03E-04
0.000218	1.28E-05	-7.8E-06	4.25748001	1.886116	0.327479	2.132398	3.639938	8.56E-05
-4.3E-05	-7.6E-05	-3.2E-05	4.27007275	1.944889	0.238732	1.919158	3.040222	7.15E-05

Fig. 5.8(a) to (c) shows Q (in S.I units) for all species. The open symbol points are literature values taken from Puska et al. (1983) and shown here for comparison. Note that only a few r_S values are shown since only data for r_S=1.5, 2, 3, 4, 5 from Z_1=1 to Z_1=15 are published. Fig. 5.9 shows that the current calculations coincide with the literature values from Puska et al. (1983). It was imperative for stopping powers to be calculated explicitly over a larger r_S range in order to accurately determine the range profiles at high implant energies (where electronic stopping dominates) and in channeling directions where the electronic density is significantly lower than in other directions and the choice of the local electronic model used is non-trivial. This is particularly useful for the present work where low implant energies in channeling directions are investigated. The subsequent chapters will illustrate the advantage of this local model over other electronic stopping models. At small r_S values, the electron density ρ, given by Eq. (5.22) is high and we can expect the stopping due to electrons to be infinitely high due to the proximity to the core nucleus. This is true for all species shown. The electronic stopping power decreases with increasing r_S since the electron cloud density decreases with increasing distance from the nucleus. In order to describe phenomenon like channeling accurately, a realistic charge distribution which accounts for the anisotropy of the material is used for all MD simulations. The 3D charge distribution of silicon is calculated using the Dawson-Stewart-Coppens (Dawson, 1967) (Stewart, 1973) (Hansen et al., 1978) formalism and the HF wave functions calculated by Clementi and Roetti (Clementi et al., 1974). Sillanpaa et al. (2001) has

found this to be an efficient scheme to produce the values of electron density in a huge number of grid points. The authors have also compared the values at representative points with those obtained from first-principles DFT methods, and found only small differences. Using the 3D charge distribution, the electronic stopping power is then obtained by employing the local response theory where the stopping power at a given point depends only on the electron density at that point. The range profiles obtained by employing the PENR local model will be compared to those obtained from a non-local model like ZBL in the next chapter.

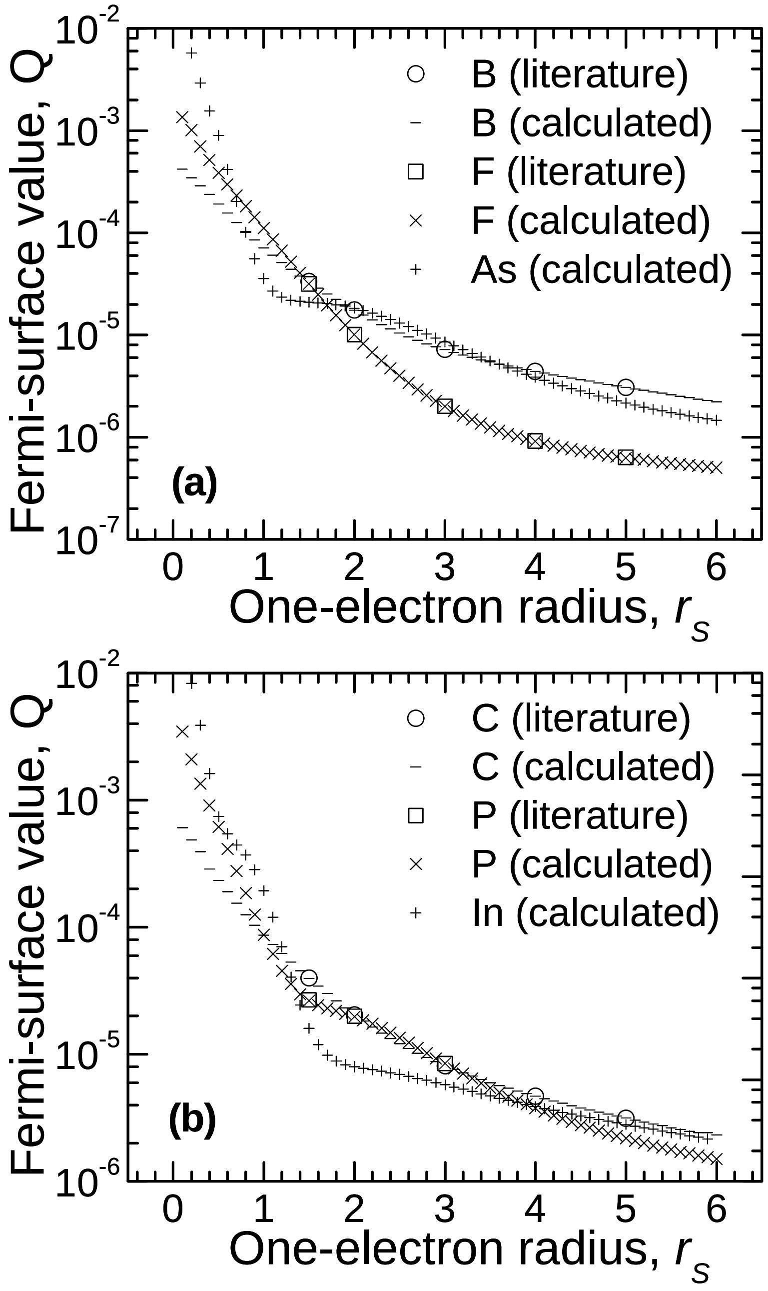

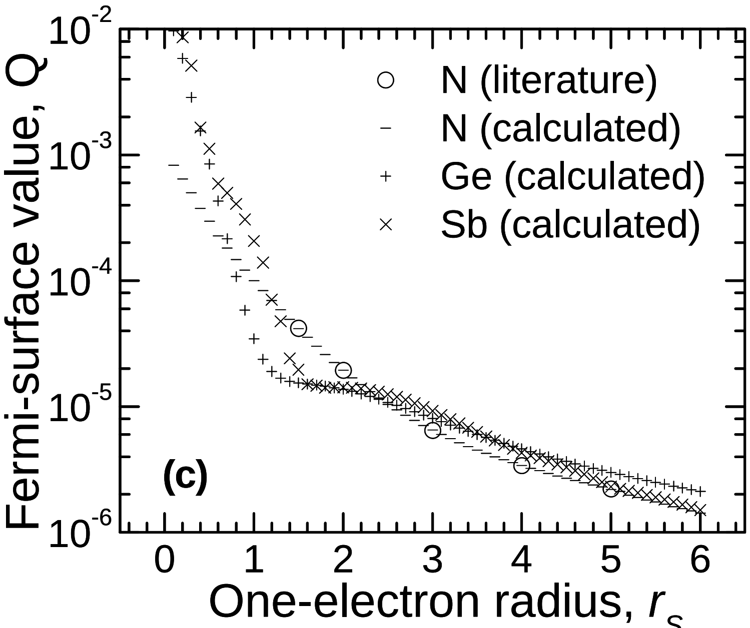

Fig. 5.9 Fermi surface value Q versus one-electron radius, r_S for nine dopant systems (a) B, F and As (b) C, P and In (c) N, Ge and Sb. Multiplication of Q by the ion velocity gives the electronic stopping power

5.2.4 Damage accumulation model

Unlike the phenomenological model used in Crystal-TRIM, MDRANGE accounts for the damage buildup in the substrate by making use of its cell translation technique, which allows the combination of the slowing down calculations with changes in the amorphization state of the target. Details of this technique can be found in the work of Peltola et al. (2002, 2003). The incoming ion loses its energy in two primary modes, nuclear and electronic scattering. Damage induced in the originally pristine target material can be largely attributed to the energy deposited in the elastic collisions with the target atoms. The nuclear energy deposited to the primary knock-on atoms by the incident ion F_D, can be calculated as a function of the number of implanted ions, *n* and the depth *z* in the material, which can be defined in steps of unit calls. F_D is dependent on the implanted dose since the higher the dose, the greater the amount of energy deposited in the region, and the higher the probability of amorphization and dechanneling. The deposited dose, D(*z*,*n*) in units of eV/atom for each layer at depth *z*, can be expressed as shown in Eq. (5.25), where ρ is the atom density (atom/ $Å^3$) and S is a factor given by S = D_{exp} (ions/cm^2)/n_{max} (ions), relating the number of experimental ions corresponding to one simulated ion in some region. Hence the larger the number of simulated ions, the smaller S is and more accurate statistics can be obtained.

$$D(z,n) = F_D(z,n) S \frac{1}{\rho} \tag{5.25}$$

Depending on the energy deposited by the previous ions, the current initial coordinate box to be used can be chosen from 20 pre-damaged coordinate boxes of various damage levels. Nord et al. (2002) used full MD to study the amorphization mechanisms and the effect of different many-body potentials on the amorphization process in silicon. Based on a simulation cell of 17 ×17×17 unit cells and PBC, the cell was then bombarded with low energy silicon (3 eV to 2 keV) at random locations according to a precalculated primary recoil spectrum until the cell is totally amorphous. The cell was relaxed to zero temperature and pressure in between successive bombardments, and the atom coordinates were stored. Hence, the 20 predamaged boxes represent different amorphization doses (eV/atom) with a constant dose increment in the region from 0 to 14.3 eV/atom, with the final value corresponding to complete amorphization.

When an ion comes close to the simulation cell border at a certain depth, the damage accumulated to the unit cell layer in front of the ion is taken as the dose deposited, D(*z*,*n*) in that layer, and the initial box with the right amount of damage is selected out of the 20 for the simulation. Fig. 5.10 shows a schematic of the damage accumulation model.

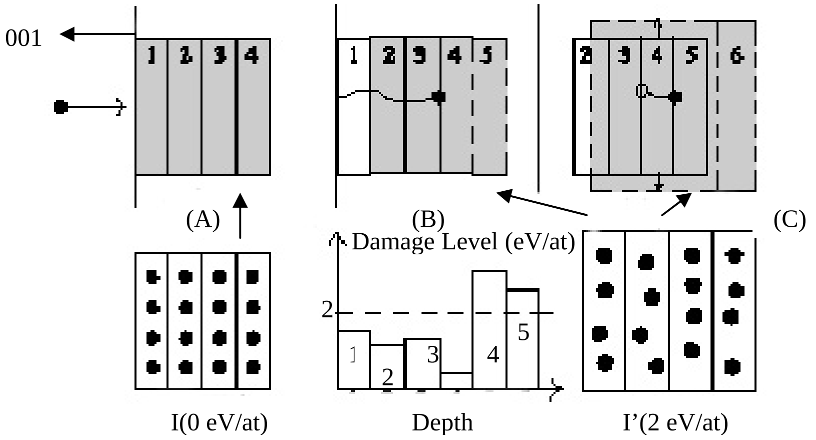

Fig. 5.10 Schematic of the damage accumulation model (Peltola et al., 2003)

The dotted line in the figure of the damage level (2 eV/atom) is an example of the possible separation of two levels of damage in the two initial boxes I and I’. In the first box, the damage level of layers 1 to 4 is checked. The dose is less than 2 eV/atom in these layers, hence the first initial box of atom coordinates (I) without damage is copied in front of the moving ion (shaded region). When the ion approaches the end of layer 4, layer 1 is deleted and the dose is checked for layer 5. Suppose the damage level is greater than 2eV/atom, the atom coordinates for that layer are copied from the initial box I’ with D=2 eV/atom to the simulation box and scaled to match the volume of layer 4. When the ion has moved to the next boundary, the ion is entering a layer whose volume is larger than the previous layer. The volume of the whole simulation cell is scaled to match the actual volume of layer 5. Layer 2 is then deleted. The scaling is necessary not only to ensure that the layer where the ion is moving always has the correct volume but also ensures that the channels were continuous for the ions. This was done by scaling the ion coordinates in the simulation box so that the ion was in the same place in every box respective to the centre. When the coordinate box with the right amount of damage is selected for the simulation at a particular point, it actually takes into account the cumulative damage build-up process without free parameters and probabilities as was used in the phenomenological model in Crystal-TRIM.

Fig. 5.11 shows the capability of the damage model in taking account the effect of increasing dose on the shape of the impurity profiles for a light ion like B and a heavy ion like Sb. The implant conditions are identical to those shown in Fig. 3.9 previously. Similarly to Fig. 3.9, the profiles show enhanced dechanneling at high doses. However, unlike the linearity of the BCA-simulated profiles with dose before the amorphization threshold, the tails of the profiles obtained with MD at different doses are somewhat independent and do not show linear scaling with dose. Fig. 5.12 shows only the dechanneled profiles at dose 1×10^{15} atoms/cm^2 for B and Sb, comparing the effect of both damage models (Crystal-TRIM and MDRANGE) on the range profiles. In order to achieve a fair comparison, all simulation parameters are kept identical for both types of simulation. The nuclear stopping is treated by the use of ZBL universal potential in both cases while the electronic stopping is calculated by the ZBL model. Hence, any discrepancies can be attributed to the damage accumulation model.

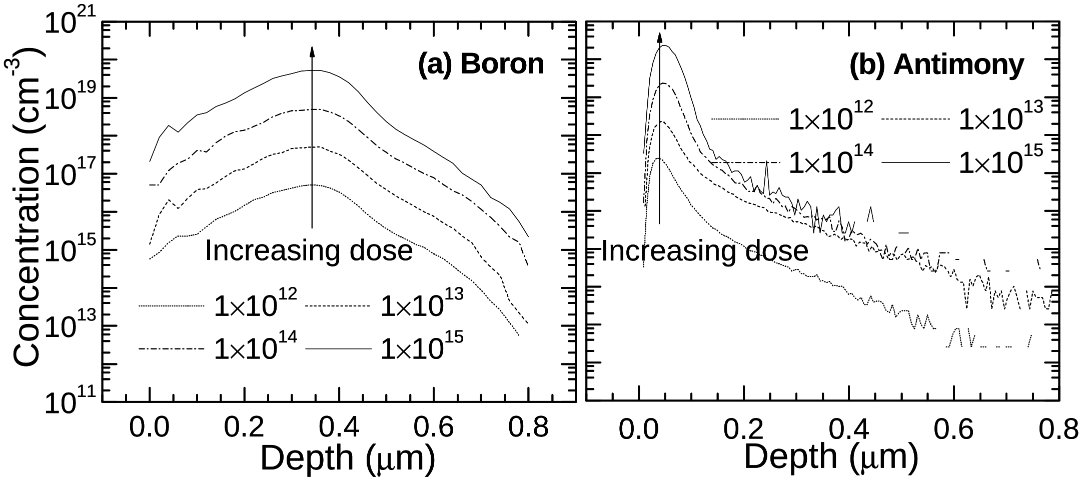

Fig. 5.11 Effect of enhanced dechanneling and damage accumulation on profile shape for (a) B 100keV 7° tilt 22° rotation and (b) Sb 100keV 7° tilt 22° rotation for doses 1×10^{12}-1×10^{15} atoms/cm^2. All simulated profiles are obtained from MDRANGE.

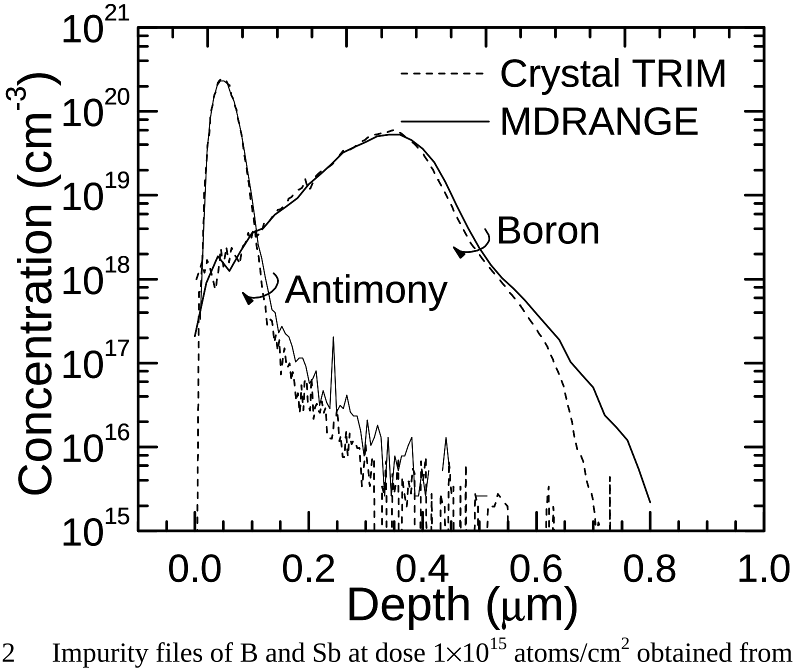

Fig. 5.12 Impurity files of B and Sb at dose 1×10^{15} atoms/cm^2 obtained from Crystal-TRIM and MDRANGE

It can be seen that the phenomenological model in Crystal-TRIM tends to overestimate the degree of dechanneling compared to the damage model used in MDRANGE. This can be attributed to the use of constant parameters in the phenomenological model in Crystal-TRIM.

While the damage model in MDRANGE is a dynamic one where the damage state is changing with time, the model in Crystal-TRIM utilizes a parameter which measures the ratio of the amount of defects relevant for dechanneling to the total amount of ballistic atomic displacements. Although both the amount of relevant defects and ballistic atomic displacements vary from one location in the target to another, the ratio is assumed constant. Hence, the profiles simulated in Crystal-TRIM, keeping all other simulation conditions constant, generally show more dechanneling and damage buildup than the model in MDRANGE.

5.2.5 Statistical enhancement techniques

MDRANGE utilizes a modified rare-event algorithm based on the work of Beardmore et al. (1998) not only to obtain statistically reliable results over the range of several orders of magnitude in the dopant concentration, but also to minimize simulation time. A brief description of the Rare Event Enhanced Domain following method termed REED will be given here, which aims to calculate a statistically significant concentration profile at all depths into the material. Sillanpaa et al. (1999) later implemented a version of REED into MDRANGE.

This method was motivated by the redundancy in simulating multiple pseudo-particles near the peak for every one ion that stops in the tail, although such computations do little in enhancing the accuracy. An “atom splitting” scheme was employed to increase the sampling probability in the tailing portion of the profile. Like the trajectory splitting method used in Crystal-TRIM, each actual ion is replaced by several virtual ions, each with an associated weighting. At certain splitting depths, each ion is split into two ions, each with a weighting half that prior to splitting. Each daughter ion is then tracked separately, with the weighting recorded along with its final depth. This scheme allows the same number of virtual ions to be used at any depths, but their weightings decrease with depth. The splitting depths are continuously updated such that a correct distribution of splitting depths is obtained from an approximate concentration profile. The initial profile loaded can either experimentally measured profiles or a crudely calculated simulated profile based on the known ion mass, energy, incident direction etc. Fig. 5.13 shows the algorithm for determining the splitting depths from a given profile. The ions are split at depths where the total number of ions becomes half of the actual implanted ions. In the REED algorithm used in MDRANGE, ten such splitting depths, d*ᵢ* are chosen such that

$$\int_0^{d_i} C(x)dx = \left[1-\left(\frac{1}{2}\right)^i\right]\int_0^{\infty} C(x)dx \tag{5.26}$$

C(x) is the dopant concentration profile as a function of depth x that is loaded in. In the original algorithm of Beardmore et al. (1998), the statistical weights were ignored when determining the splitting depths. The splitting depths are given large initial values which will be updated during the simulation. Storage requirements are minimized by simulating each ion until it comes to rest. The state of the domain is recorded at each splitting depths passed.

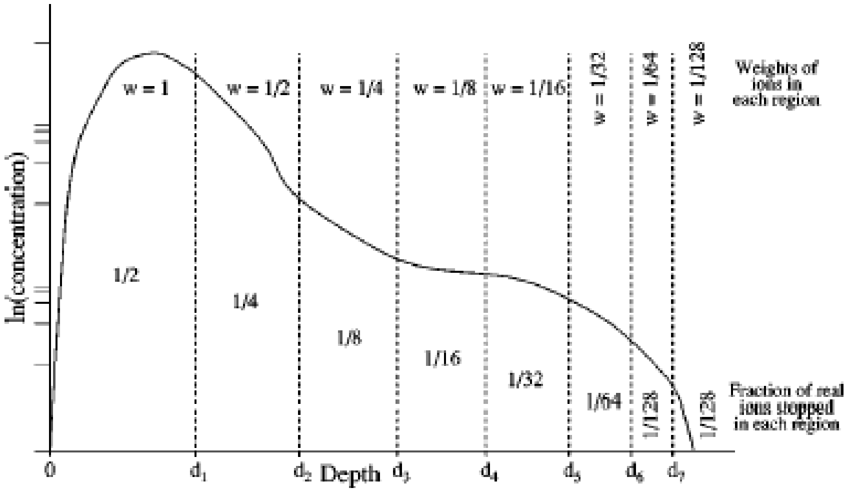

Fig. 5.13 REED algorithm (Beardmore et. al., 1998) for generating splitting depths from the integrals of initial profile, with weights associated with split ions at each depth

Use of the REED algorithm allows statistical reliable results to be obtained over many decades of concentration. Fig. 5.14 shows the enhancement of the accuracy of the tailing portion of the impurity profile obtained from the MD simulation of Indium into silicon at 40keV, 2×10^{13} atoms/cm^2. The REED algorithm can be implemented with no significant increase in computational time and is used for all the simulations done in this work unless otherwise stated.

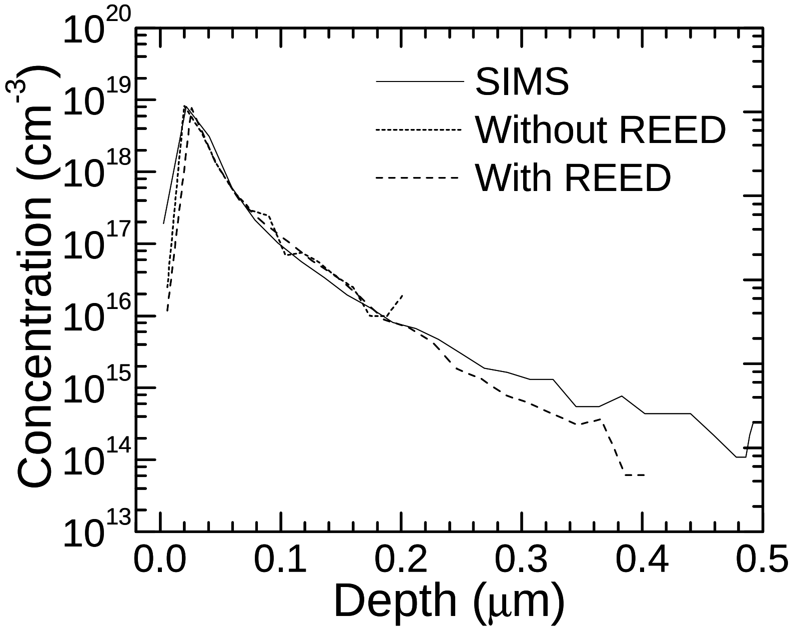

Fig. 5.14 Comparison of experimental SIMS data and simulation for In 40keV, 2×10^{13} atoms/cm^2 7° tilt and 27° rotation with and without REED algorithm

In summary, this chapter first explained the theory of molecular dynamics: simply the numerical evaluation of Newton's laws of motion, with elucidation of the integration algorithm, the initial and boundary conditions used typically in MD methods as well as the calculation of forces from the interatomic potentials and commonly used acceleration methods. The physics underlying the models of the MD code used in this work, MDRANGE is then described. Not only does this code offer the flexibility of using nuclear stopping potentials derived from first-principles DFT calculations, the use of local electronic stopping parameters derived from DFT calculations of a proton stopping in a homogeneous electron gas further enhances the accuracy of the final range profiles, as will be shown in the subsequent chapter. Details of the calculations can be found in appendices D and E. In the next chapter, the usefulness of these models will be examined and compared against conventional nuclear and electronic stopping models typically used in BCA codes.

CHAPTER 6 APPLICATION OF MOLECULAR DYNAMICS IN ION IMPLANTATION

The two commonly used methodologies in simulating ion implantation had been covered in previous chapters. In the binary collision approximation (BCA) method, the impact process of ions in solids is often treated by binary sequences of the projectile atom and one target atom in a solid. The approximation is supported by the fact that the range of significant interatomic force for the collision is shorter than distances of target atoms in the bulk because of the screening effect and that the collision process lasts for time periods in the order of 10^{-15} seconds, which is significantly shorter than the lattice vibration period of atoms. Because this method invokes the use of random numbers, it is also a Monte Carlo method where the implant range and distribution of implanted atoms in a solid can be determined by analytical solution of the stochastic process. However, as the demand continues for improving key technological parameters in silicon-based ion implantation technology, smaller device feature sizes are required down to the nanometer regime, which equates to ultra-shallow highly doped junctions in devices structures. Lower implantation energies are necessary for device scaling and the dopant profiles should be controlled to tolerances of a few tenths of nm.

The basic assumption of BCA stating the potential energy of the ion at the start of the collision to be negligible compared to its kinetic energy should be questioned and its use re-examined at very low implantation energies when the kinetic energy of the ion approaches the interatomic potential energy of the ion and target atom. Another deficiency of BCA is that it neglects multi-body interactions, which become important when the interatomic potentials of not only the nearest target, but of more distant ones, become non-negligible. This can happen at low ion energies, as well as in crystal channels at higher energies. At low energies however, the effects of multi-body interactions are especially pronounced. In order to accurately analyze the collision process between ion and target at low energies, it is desirable to describe the motion of all the atoms involved in the process, and this can be done by numerically solving Newton's equations of motion for all atoms in the system. While molecular dynamics (MD) simulations are limited in time and space as compared to BCA, the advent of supercomputers and the fact that the collision cascades formed at low energies are small makes MD a feasible and popular solution these days. Moreover, the number of free parameters is limited and its accuracy in many-body collisions in the low energy regime warrants its use. In this chapter, the energy at which BCA reaches the brink of its applicability is first calculated from the potential energy curves, calculated using density functional theory (DFT) methods for each specific ion-target pair, for a wide range of industrially important dopants. Then the effect of using such calculated potentials against the universal ZBL potential in MD simulations is investigated, as well as the effect of using a local electronic stopping model against a non-local one.

6.1 First-Principles study of BCA breakdown

The validity of BCA and the useful range of application of MD simulations with the Recoil Ion Approximation (RIA) have been addressed by many workers. Hobler et al (2001) found that the validity of MD-RIA extends down to energies well below 100eV. BCA, however, has a more restricted range of applicability. The upper limit, $E_{\min}^{BCA}$ at which BCA breaks down had been estimated by Hobler et al. (2001) as a function of the projectile's mass, M_X, in amu.

$$E_{\min}^{BCA} = 30 M_X^{0.55} \mathrm{eV} \tag{6.1}$$

The actual breakdown limit has never been clearly defined because BCA fails gradually as the energy lowers. Moreover, the limits also depend on the accuracy level used. $E_{\min}^{BCA}$ has been calculated for the nine industrially common dopants B, C, N, F, P, Ge, As, In and Sb based on Eq. (6.1) and the values are given in the second column of Table 6.1. Column 3 shows the lower energy limit for some elements taken from the University of Texas Range Parameter tables, also known as Al Tasch tables (Balamurugan et al., 1998). The 4th column reflects this limit for another Monte Carlo BCA code UT-MARLOWE (Obradovic et al., 1999). The limit is not shown for Crystal-TRIM as it is not explicitly given. Clearly, the low values calculated from Eq. (6.1) seem to suggest that BCA is valid down to the sub-keV range, even for heavy species like In and Sb, while the justifiable range of use for common BCA codes is restricted to much higher energies for heavier elements.

Table 6.1 Estimated energy limits (keV) below which BCA breaks down

Element (X)	**(Hobler et al., 2001)**	**Tasch tables**	**UTMarlowe**	**DFT(NN_{SI})**
B	0.111	0.5	0.5	0.429
C	0.118	-	-	0.515
N	0.128	-	-	0.601
F	0.152	0.5	2	0.772
P	0.198	15	5	1.287
Ge	0.317	-	10	2.746
As	0.322	0.5	1	2.832
In	0.407	-	5	4.205
Sb	0.421	-	-	4.377

The last column reflects estimations of the breakdown limit based on DFT calculations for each projectile-target pair. The interatomic potential energies for each projectile-target pair have been calculated with the DMOL package, details of the DFT calculations can be found in the previous chapter. Based on the single-point energy calculations at different interatomic separations, the values are obtained based on the assumption that BCA fails when the kinetic energy of the ion becomes comparable to the unscreened nucleus-nucleus Coulombic repulsion of the ion and target atom, at a distance corresponding to the nearest neighbor separation. For silicon, this distance corresponds to 2.351Å, which is given by Eq. (6.2) where a is the lattice cell parameter, 5.431Å.

$$R_{NNSI} = \frac{\sqrt{3}a}{4} = \frac{\sqrt{3}\times 5.431}{4} = 2.351\,\text{Å} \tag{6.2}$$

Although the breakdown limits for the different species have been calculated with diatoms, which are simple approximations to the true multi-body interacting forces in the repulsive, repulsive-attractive transition and attractive regions, it has been suggested that the diatomic potential does not differ much from a bulk potential at energies ≥ 10eV (Nordlund et al., 1997). The limiting kinetic energies shown in the last column are taken to be the *absolute* coulomb nuclear repulsion energies at interatomic distances corresponding to R_{NNSI}. The calculated limits are significantly higher compared to the limits given by Eq. (6.1) while they show more coherence with the limits given by UT-MARLOWE for B and In. Fig. 6.1 shows the trend of the breakdown limits calculated in the last column of Table 6.1 against the atomic number Z_X and mass of the element, M_X. Similar to the analytical form suggested by Hobler et al (2001), the breakdown limit estimated from the DFT-calculated pair potentials in this work suggests a power-law relationship with the atomic mass, and a linear relationship with atomic number.

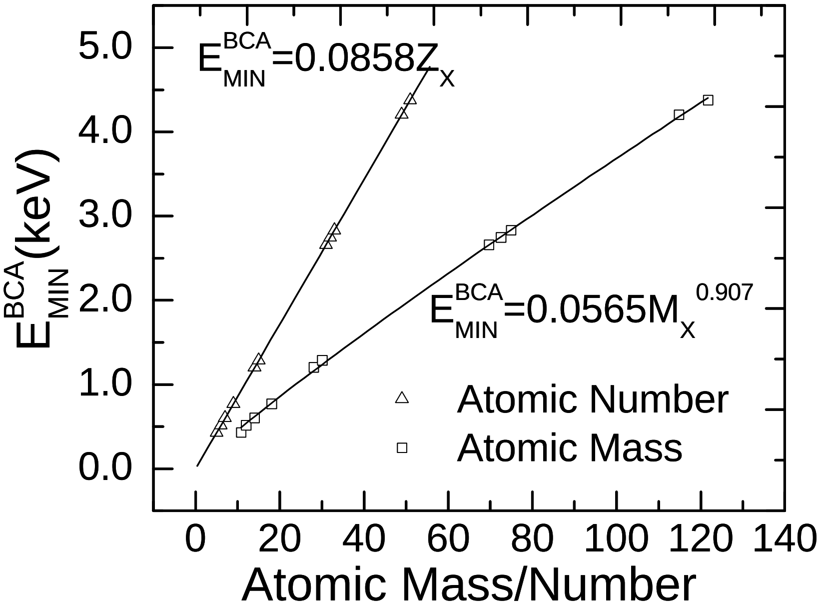

Fig. 6.1 Correlation of BCA breakdown limits calculated by DFT with atomic mass (power law) and atomic number (linear)

The dependence of the breakdown limit on the mass of the projectile can be explained from the DMOL potential energy curves shown in Fig. 5.7. For a quantitative analysis, we focus on two elements, the lightest and heaviest elements studied: B and Sb. Fig. 6.2(a) shows the DMOL potentials for these two elements. The increase in the breakdown energy with atomic mass can be largely attributed to the interaction distance between the ion and target atom. Suppose the projectile approaches with an initial kinetic energy of 200eV, the incoming ion can achieve an interaction potential of at most 100eV in a head-on collision based on energy conservation in a center-of-mass coordinate system. For a small atom like B, the distance of closest approach with the target atom Si is circa 0.6Å. On the other hand, for a large atom like Sb, this screening envelope extends to approximately 1.1Å. From Fig. 6.2(b), it is apparent that the interaction distance increases with atomic mass. This larger screening effect of heavy ions negates the importance of many-body nuclear effects as compared to the smaller ions, which experiences a higher probability of simultaneous collisions with the neighboring target atoms as energy lowers. The light ions' susceptibility to the multi-body interactions defeats the binary collision approximation and explains their lower breakdown limit compared to the heavy ions, which are more effectively shielded against the surrounding atoms.

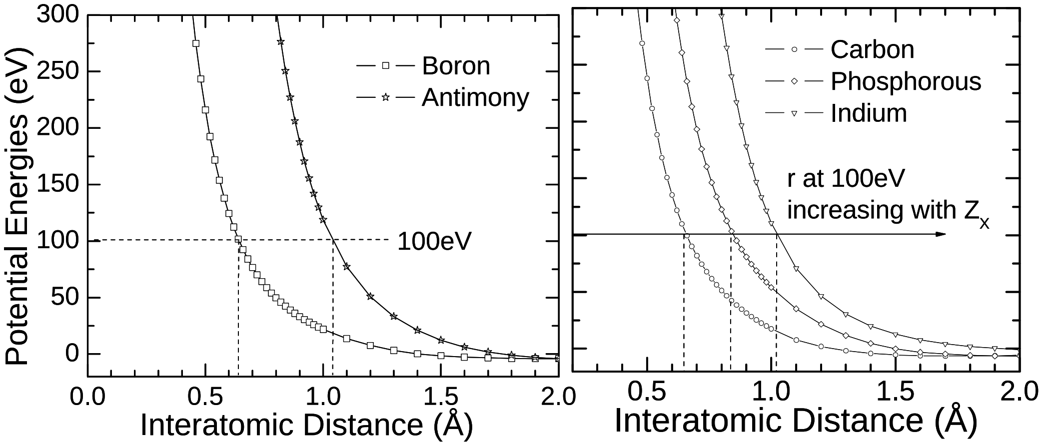

Fig. 6.2 Energies (in eV) obtained from DFT calculations utilizing the DMOL package for (a) B and Sb (b) C, P and In

6.2 SIMS database (Intermediate to High energy)

The experimentally measured profiles shown in this chapter are obtained from Secondary Ion Mass Spectrometry (SIMS). Most of the SIMS data shown are obtained from ***TCAD Fab Package***, a measurement database and process simulation package by Integrated Systems Engineering (ISE AG), set up in cooperation with Applied Materials, Inc. (AMAT). The experimental database contains experimental data for deep submicron technology and a wide range of process recipes for advanced technology with the main focus being ultra-shallow junction, halo, and well formations in deep submicron CMOS fabrication. The recipes are designed for a physically-based calibration of implantation and diffusion models. The species and conditions covered in the database consisted mainly of B, BF_2, As, In and Sb at energies 1keV (B, BF_2 and As) and 50keV onwards (In and Sb). Table 6.2 summarizes the parameter range and as-implanted conditions covered by the database.

Table 6.2 SIMS database (intermediate to high energy): range of implant conditions

Element	Energy range (keV)	Dose range (atoms/cm^2)	Deep submicron CMOS application
Boron	0.2 - 150	5×10^{12} - 5×10^{15}	drain extension; source/drain; channel; well
BF_2	1 – 10	3×10^{13} - 1×10^{15}	drain extension
Arsenic	0.5 – 10	3×10^{13} - 1×10^{15}	drain extension; source/drain
Indium	50 – 150	3×10^{13} - 1×10^{14}	halo; channel
Antimony	50 - 150	1×10^{13} - 1×10^{14}	halo; channel

From Table 6.2, the widest range of conditions is covered by the most common industrial dopant boron, while those of heavy elements like In and Sb cover energies mainly in the high keV regime. Only experimental data for five elements are available. Inasmuch as dopants like B and As are extensively used in semiconductor applications (eg. source-drain extensions, CMOS retrograde wells, latch-up/electrostatic discharge protection), other dopants like In and Sb also play a crucial role in minimizing punch-through, channel engineering and threshold voltage adjustment. Although energies in the 50-150 keV range are applicable for In and Sb in present manufacturing processes, the energy requirement is lowering down to intermediate keV regime (1-10 keV) with device scaling, especially for threshold voltage adjustments. Not only is it imperative to accurately predict dopant profiles for these heavy elements at low energies, it is also necessary to investigate other elements like C, N, F and Ge which has important applications as well. Due to the lack of low energy profiles in the sub-keV range for these atypical dopants and also heavy elements, an experimental database based on low energy implants will be set up for comparison and calibration of the MD code. This part of the work will be elaborated upon in the following chapter. For this chapter, all low/intermediate energy SIMS data shown for elements like N and Sb are courtesy of Axcelis Technologies.

6.3 Simulation of range profiles using MD

In this section, the ion range distributions will be calculated by MD using the code MDRANGE, where the treatment of nuclear and electronic stopping effects is approached with different models. Firstly, the effect of using a solely repulsive potential like the universal ZBL on the range profiles versus a potential calculated from first-principles is investigated. Electronic losses are treated with both the non-local semi-empirical ZBL electronic stopping model and the local PENR model based on Fermi level phase shifts. Comparisons against experimentally measured SIMS profiles will be shown to ascertain the predictive capability of different interatomic potentials and electronic stopping models for any elemental profile in crystalline silicon obtained at different energy ranges in various implant direction, especially in channelling directions where the atom and electron densities are significantly lower than average. All simulations shown in this work have been obtained with the MDRANGE code. The Recoil Ion Approximation (RIA) is invoked in all cases, where only the ion-recoil interactions are considered. This is based on the assumption that the interactions between the ion and its nearest neighbors are much stronger than the lattice-lattice interactions. In all simulations, initially crystalline silicon is used as a target material. The ambient temperature, 300K was used and realistic atomic thermal displacements were obtained by setting the Debye temperature of silicon to 519K. The number of simulated pseudo-particles used was 20,000, and deemed sufficient for good statistics. In order to determine the profiles over more than four decades of concentration, the modified version of a rare-event algorithm REED was implemented. An atom splitting scheme is employed so that at certain splitting depths the ion is split into two virtual ions with a statistical weight of half that of the unsplit ion. This ensured accurate dopant profiles with good statistics and feasible computational overhead. The effect of damage build-up on range profiles at high implant doses and low energies is especially pronounced and is taken into account by the dynamic damage accumulation model explained in the previous chapter. Basically, the material structure in front of the path of the incoming ion is changed, depending on the nuclear energy deposition.

6.3.1 Effect of interatomic potential: ZBL versus DMOL

The universal ZBL potential, constructed by fitting a universal screening function to theoretically obtained potentials calculated for 261 atom pairs has been most commonly used in BCA as well as MD codes. While the pair potential has been known to well describe the projectile-nucleus interaction at high velocities, the validity of the solely-repulsive ZBL potential becomes questionable at low velocities, since it cannot account for attractive forces that start to dominate as the incoming ion slows down in the host material. Unlike the ZBL potential which is repulsive over the entire interatomic range, the DMOL potentials calculated from DFT utilizing numerical basis sets consist of a steep repulsive region and an attractive well. They are found to be significantly improved potentials compared to the ZBL potential for four diatomic systems C-C, H-Si, N-Si and Si-Si (Nordlund et al., 1997). Using these two potentials, two systems differing in their masses, B-Si (Z_1=5, Z_2 =14) and As-Si, (Z_1=33, Z_2=14) were studied at low implant energies. Fig. 6.3(a) shows both ZBL and the DMOL pair potentials for B and As systems only. For r ≤ 0.529Å, which is the Bohr radius, the difference between the two potentials is not more than 12% but the disparity increases with interatomic separation and proves to affect the heavy elemental profile more significantly.

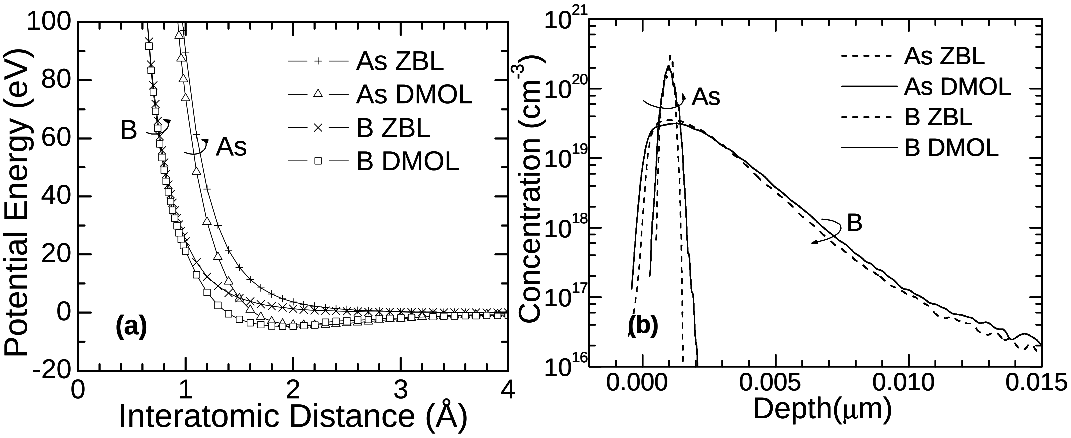

Fig. 6.3 (a) ZBL and DMOL potentials for B-Si and As-Si (b) MD simulated profiles of B and As in Si (200eV 1×10^{13} atoms/cm^2 7° tilt and 22° rotation) using potentials in (a)

Fig. 6.3(b) shows the simulated MD profiles of B and As in crystalline silicon at 200eV, 1×10^{13} atoms/cm^2, tilt 7° and rotation 22° using both potentials. These two potentials (i) solely-repulsive ZBL (no attractive well) (ii) DMOL (with attractive well) provide a comparative study of the impact of the presence of the attractive well on the range profiles. At such low energies, nuclear scattering is the dominant stopping mechanism and inclusion of electronic losses is trivial. The electronic energy loss has been neglected in these simulations so as to isolate the effect of the interatomic potential on the range profiles. Even in this low energy regime where attractive forces are predominant, the B profiles show little dependence on the potentials used. The absence of a potential well in the ZBL affected the junction depths negligibly. Range profiles obtained for As, however, depend strongly on the potential employed. Absence of an attractive well in the ZBL resulted in an unusual profile significantly different from that obtained with the DMOL potential and an anomalous congregation of impurities occurs within a narrow region. Profiles obtained with the ZBL potential also tend to underestimate the degree of channeling, showing shallower junction depths than those obtained with the DMOL potential.

Similar to the argument provided in the previous section for the increase in BCA breakdown energy with increasing atomic mass, the weak dependence of the B profiles on the potential can be attributed to the significantly smaller interaction distance of the B-Si system. Having an initial kinetic energy of 200eV, both B and As can achieve an interaction potential of at most 100eV. Based on Fig. 6.3(a), the distance of closest approach between B and Si at 100eV is at most 0.7Å, while that for As and Si is $\approx$1Å. As the B atoms spend relatively more time at close interatomic separations, the differences between the two potentials are insignificant and affect the eventual profiles weakly. As atoms, on the other hand, is repelled further from the Si lattice atoms, and are likely to be found at larger interaction distances where the two potentials differ significantly. Hence, the final As profile is more strongly affected by the form of the potential, especially at low implant energies. With increasing incoming kinetic energy, this dependence on the potential for heavy elements will diminish, not only because the difference between the potentials is trivial at high energies but also because the stopping mechanism is no longer dominated by nuclear but electronic losses.

Figs. 6.4 and 6.5 show the effect of the interatomic potential on light (B) and heavy (As) range profiles compared against SIMS data at two implant energy ranges without electronic stopping effects. In the low-energy regime (0.5keV for B, 1keV for As), the absence of electronic stopping effects is inconsequential, as shown in Figs. 6.4(a) and 6.5(a) since the stopping mechanism is dominated much by nuclear effects. With an increase in the initial kinetic energy of the incoming ion (Figs. 6.4(b) and 6.5(b)), exclusion of electronic stopping resulted in profiles with deep tails, showing poor agreement with the SIMS data. At higher energies, the ion interacts mainly with the electrons in the target material; the energy transferred in the collision process is no longer negligible and the change in direction is significant. Because the stopping mechanism at high energies is dominated by electronic effects, the choice of the interatomic potential used is trivial, as shown by the indistinguishable profiles obtained with both ZBL and DMOL potentials. Conversely speaking, nuclear stopping is the dominant mode of energy transfer at low velocities where the ion can lose most of its energy in a single collision, changing its direction considerably. This is especially true for a heavy element like As (Fig. 6.5(a)) where the profiles obtained with different potentials differed significantly. While the disparity is less significant in the case of B (Fig. 6.4(a)), the use of the DMOL potentials yielded profiles which showed better agreement with experimental results in both cases. This can be largely attributed to the presence of an attractive well absent in the ZBL potential. Attractive forces while negligible at high ion velocities become non-trivial as the ion slows down and the ZBL potential fails to depict the right attractive nuclear forces at low energies. In the next section, we investigate the influence of non-local and local electronic stopping models, keeping nuclear stopping effects constant by using only the DMOL potentials. The accuracy of the DMOL potentials warrants the assumption that any discrepancies between simulated and experimental results to be caused solely by discrepancies in the electronic stopping models. Both the non-local ZBL stopping and the local PENR models will be studied.

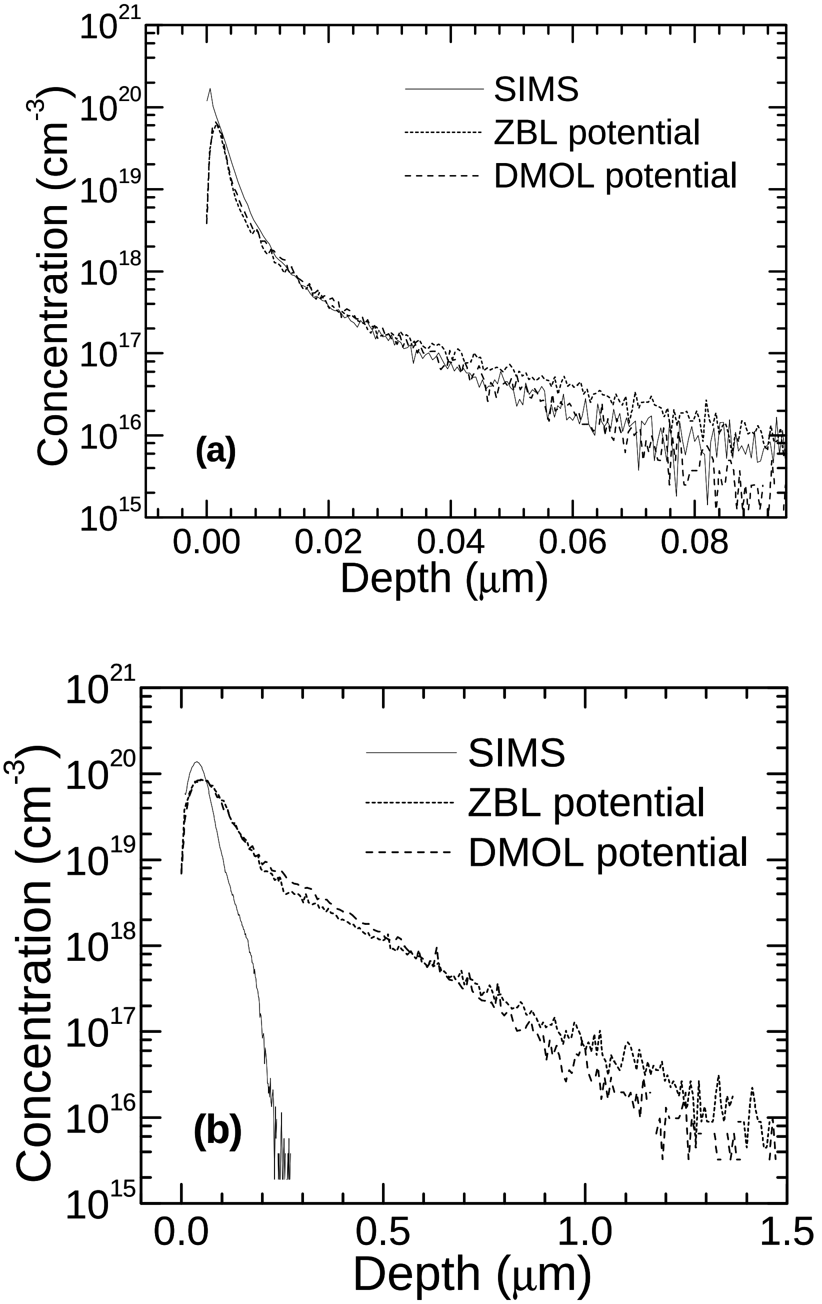

Fig. 6.4 Comparison of experimental SIMS and MD simulation (ZBL versus DMOL potential) for B (a) 0.5keV 5×10^{13} atoms/cm^2 45° tilt and 0° rotation (b) 10keV 1×10^{15} atoms/cm^2 0° tilt and 0° rotation

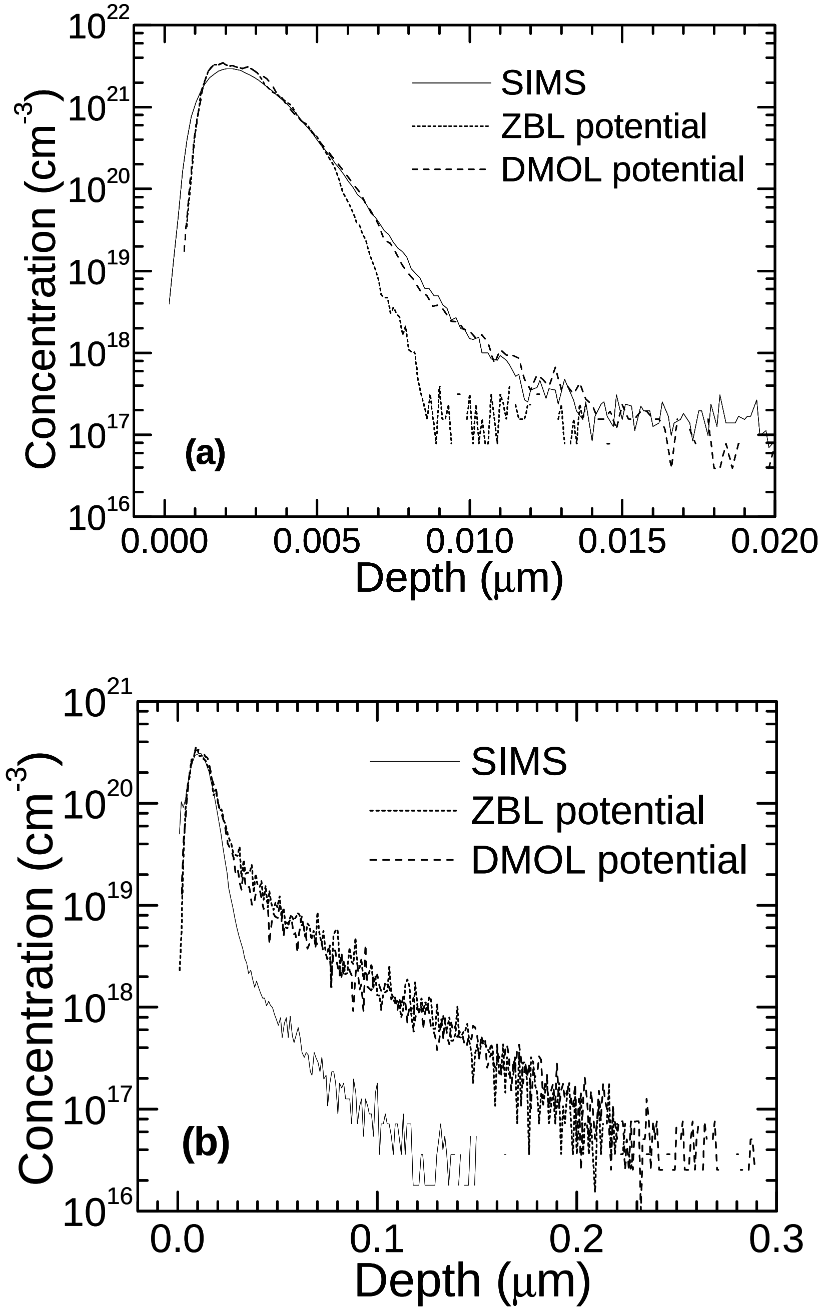

Fig. 6.5 Comparison of experimental SIMS and MD simulation (ZBL versus DMOL potential) for As (a) 1keV 1×10^{15} atoms/cm^2 5.2° tilt and 17° rotation (b) 10keV 5×10^{14} atoms/cm^2 0° tilt and 0° rotation

6.3.2 Effect of electronic stopping model: ZBL versus PENR

Separation of the energy loss of the ion into two separate components, nuclear and electronic scattering, inherently assumes all possible correlations between the elastic nuclear collisions and inelastic losses due to electronic excitation to be negligible. This assumption is valid considering the correlation is insignificant when many collisions are averaged over, as when an ion penetrates a solid. Unlike atoms, quantum mechanics stipulates that electrons have strong wave characteristics and cannot be localised. Therefore electrons cannot be treated as point masses and an accurate description of electronic stopping is a much more complicated issue. As mentioned, electronic stopping parameterizations are either local or non-local. In local models like the PENR model, the scattering of the ion is dependent on the position in the crystal and largely on the electron charge density. In non-local models like the ZBL model, the stopping is uniform throughout the crystal and independent of the density of the electrons. The charged ion is hindered by an induced drag force among the electron sea. Like many non-local electronic stopping models, the ZBL model is based on the Brandt-Kitagawa (BK) theory (Brandt et al., 1982), which factorizes the electronic stopping of a heavy ion into an effective charge and the electronic stopping of a proton. It does not take the shell structure of the ions' electron cloud into account, utilizing instead a centrosymmetric charge density which does not directly account for the quantum mechanical stopping cross section between the ion and the target atom electrons. In the ZBL model, the Fermi velocity is constant depending on the target material and can have an empirical correlation factor. The stopping of protons is obtained from a fit of eight parameters that have different values in each elemental target material. In this section, the non-local ZBL model will be compared against the local PENR model.

The PENR model is based on the density-functional formalism. Unlike models based on the BK theory, the PENR model takes the structure of the ion's electron cloud into account and does not require any scaling factors. The local electronic stopping power S_{el}^{PENR}, of an ion traveling at velocity v ($v \leq$ Fermi velocity v_F) in a homogeneous electron gas can be expressed as shown previously in Eq. (5.20), where k_F is the Fermi momentum of electrons of the target, r_S is the one-electron radius (function of the electron density) and $d_l(\mathrm{E_F})$ is the phase shift at quantum number l for the scattering of an electron at the Fermi energy $\mathrm{E_F}$.

$$S_{el}^{PENR} = \frac{3v}{k_F r_s^3} \sum_{l=0}^{\infty} (l+1) \sin^2 \left[d_l(E_F) - d_{l+1}(E_F) \right] \tag{5.20}$$

This model is based on scattering phase shifts for Fermi-surface electrons which has been determined within the density functional theory for atoms embedded in a homogeneous electron gas for $Z_1=5$ through $Z_1=51$ for a wide range of industrially important dopants. A dense grid of one-electron radius r_S values $0.1\text{Å} \leq r_S \leq 6\text{Å}$ is employed and components up to $l=10$ were used. Details of the calculations have been shown in the previous chapter. The anisotropy of the electron distribution is taken into account by using a three-dimensional charge distribution of silicon calculated using the Dawson-Stewart-Coppens formalism and the Hartree-Fock wave functions.

The range profiles of a light (N) and a heavy (Sb) element were simulated with both ZBL and PENR stopping models and compared against experimental SIMS data. Figs. 6.6 and 6.7 show the effect of both electronic stopping models on the range profiles of N and Sb respectively. For both elements, two energy ranges were studied (N: 0.5 and 15 keV; Sb: 10 and 50keV). The poor agreement in the tail region of the sub-keV N profile in Fig. 6.6(a) can be attributed to experimental artifacts resulting in high detection limit of N. Measurement of low level N concentrations requires good precision of SIMS instruments with improved vacuum and better primary beam intensity, as well as improved analysis protocol. Results shown represent the best detection limits under experimental constraints. The DMOL potentials have been employed for all simulations shown in this section; with all other simulation parameters kept constant, any discrepancies between the simulations can be solely attributed to the electronic stopping model. In all the cases shown, the local electronic stopping model produced profiles which show significantly better agreement with SIMS compared to the non-local ZBL model.

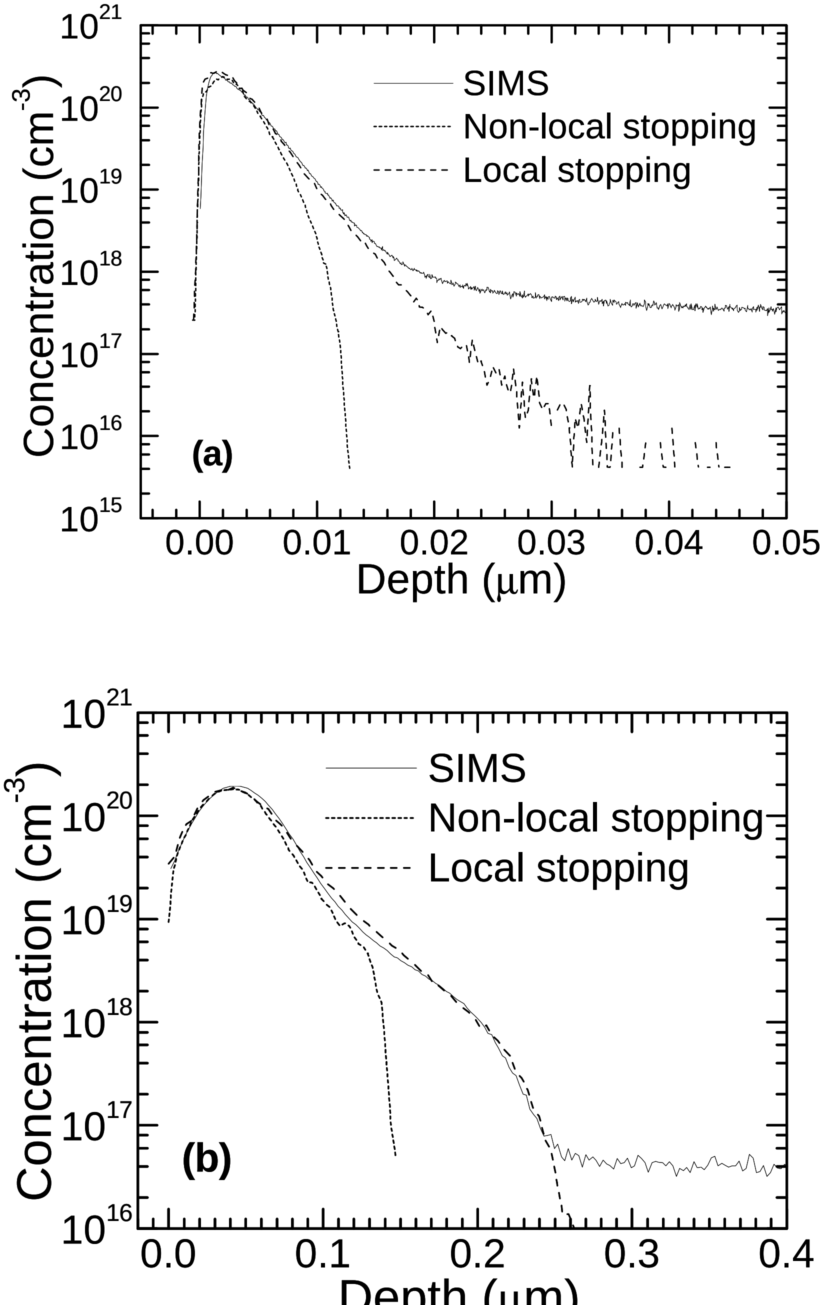

Fig. 6.6 Comparison of experimental SIMS and MD simulation (ZBL versus PENR electronic stopping) for N (a) 0.5keV 1×10^{14} atoms/cm^2 0° tilt and 0° rotation (b) 15keV 1×10^{15} atoms/cm^2 5.2° tilt and 17° rotation

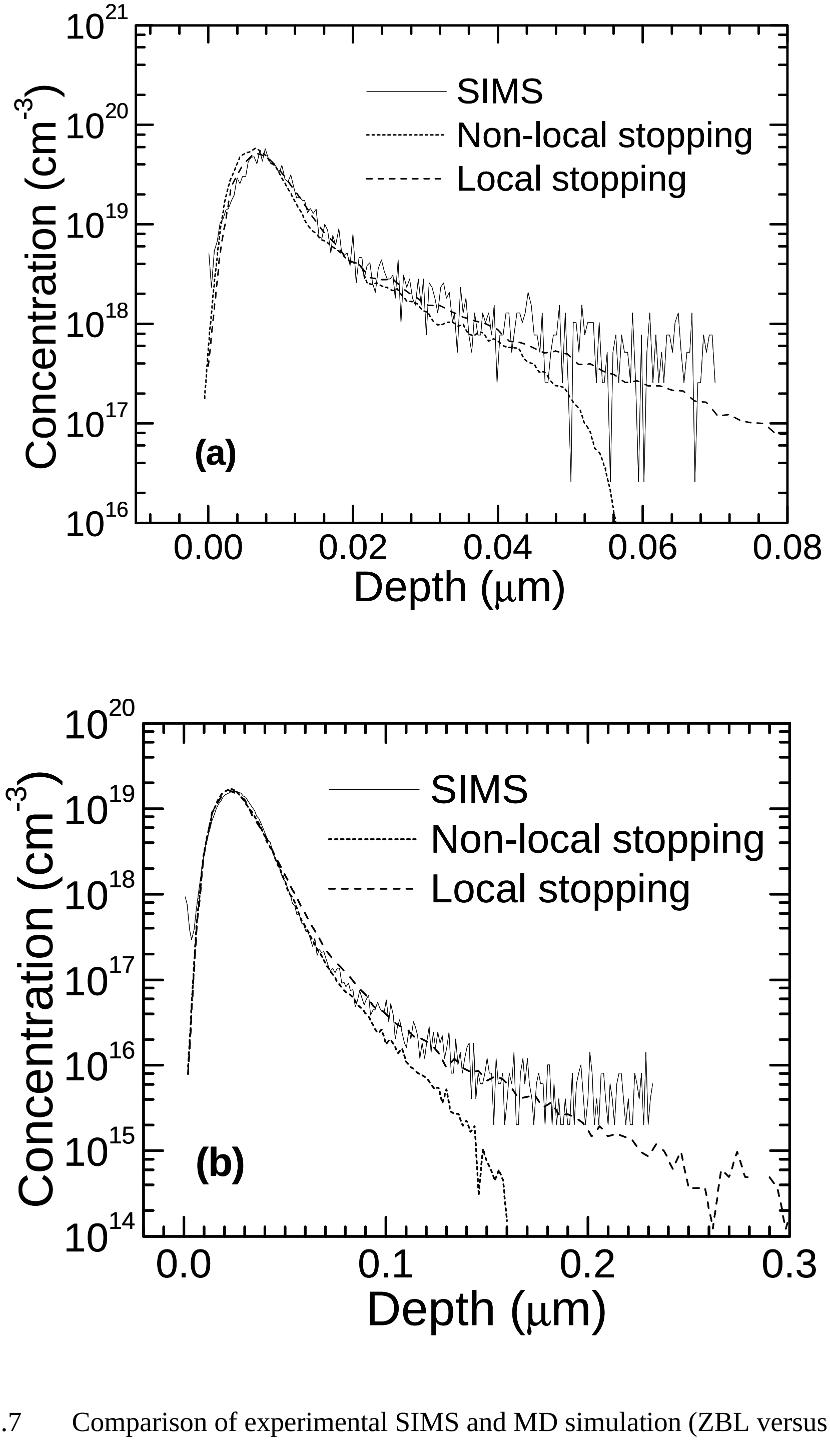

Fig. 6.7 Comparison of experimental SIMS and MD simulation (ZBL versus PENR electronic stopping) for Sb (a) 10keV 5×10^{13} atoms/cm^2 45° tilt and 45° rotation (b) 50keV 3.85×10^{13} atoms/cm^2 30° tilt and 0° rotation

The non-local ZBL model which assumes the stopping to be uniform throughout the crystal tends to underestimate the degree of channeling even in cases where channeling is not predominant, as in Figs. 6.6(b) and 6.7(b) where the implants are tilted 5.2° and 30° respectively from the surface normal to reduce channeling effects. In cases where channeling is prevalent, especially in normal (Fig. 6.6(a)) and 45° tilted implants (Fig. 6.7(a)), the ZBL model severely overestimates the drag force due to the electrons, and produced profiles with much shallower junction depths than predicted by the local model and experiments. The channeling of ions during the slowing down process has an important impact on the concentration profiles both in the vertical and lateral directions. In crystal channels, where the atomic and electronic densities are significantly lower than average, the importance of nuclear stopping is reduced relative to the electronic stopping and it is imperative that the electronic stopping model predict the ranges of the channeled ions accurately. From the results shown, it is obvious that the local model is capable of predicting the range profiles more accurately, especially where the electron density in a channel is significantly lower than in other directions. Contrary to the results of Sillanpaa et. al (2000) which showed deficiencies of the PENR model in channeling directions, results in this work suggest that the PENR model remains accurate with 45° tilt angle. A wafer orientation of 45° in the azimuthal direction, in addition to the 45° tilt angle, represents one of the worst scenarios in axial and planar channeling (Ziegler, 1992) and Fig. 6.7(a) shows that the PENR model is still sufficiently accurate under such conditions for a slow heavy ion, without the need of a charge averaging scheme for improvement in the channels (Sillanpaa et al., 2000). The model contains no free parameters and useful for any ion-target system where the electron distribution is known.

6.4 Comparisons of experiments with simulation (high energy)

In the previous section, the effect of treating nuclear stopping with both the ZBL universal potential as well as potentials calculated from DFT was investigated. The influence of electronic effects on the range profiles for various elements at different energies were also accounted for by both the local PENR electron stopping model based on Fermi phase shifts and the non-local ZBL model. From this study, it was found that profiles obtained with the commonly used repulsive universal ZBL potential, while adequate at high implant energies due to the dominance of electronic stopping over nuclear stopping, failed to describe the attractive forces that come into play at low ion velocities. Conversely, the DMOL potentials were able to depict the right force mechanisms at low energies. At higher energies, where electronic stopping starts to dominate over nuclear stopping, the choice of potentials used is inconsequential. Electronic stopping, on the other hand, proves to be crucial at both low and high ion velocities, especially when channelling effects are non-negligible. Non-local models like the ZBL model overestimate the stopping force due to electrons and give rise to shallow profiles that underestimate the degree of channelling. This is detrimental to transistor modelling which requires accurate ion implantation profiles for predicting device characteristics. Local models like the PENR model on the other hand, are able to predict accurately the final dopant positions and can be applied to any ion in any target whose electron distribution can be calculated without a parameter fitting process. The use of the universal potential and non-local electronic models should hence be exercised with caution since they provide inaccurate descriptions of the range profiles for certain non-calibrated species and underestimates the degree of channeling in the low and intermediate energy regime. On the contrary, local electronic models like the PENR model are capable of describing not only typical non-channeling implants, but its accuracy extends to describing long-ranged profiles propagated in crystal channels.

In this section, range profiles will be simulated by MD where only the pair-specific DMOL potentials and the phase-shift based PENR electronic stopping model will be used for various species implanted at different conditions, and compared against SIMS data. All other simulation parameters are kept identical to those described in the previous section. Implant energies covered here belong to the intermediate to high keV regime, which are still applicable for present semiconductor manufacturing applications. However, with device scaling, the need for ultra-shallow source drain junctions is pushing implant energies to lower limits. The capability of MD in predicting the profiles at low energies will be addressed in the next chapter. Figs. 6.8 to 6.12 show the excellent agreement of MD simulation against SIMS data for species B, Ge, As, In and Sb at different implant conditions. Besides the agreement with experimental data in the peak and tail regions, it can be seen that most of the simulated profiles can extend up to five orders of magnitude while a technique like SIMS, despite being one of the most sensitive analytical methods available, is capable of at most four orders of magnitude (except for As where high data resolution can be obtained) with high noise levels and inaccuracies setting in at low concentrations. Hence, simulation is a useful tool in predicting concentrations beyond the measurement capabilities of SIMS. For now, it is suffice to conclude that MD coupled with accurate pair-specific DFT potentials and a phase-shift based electronic stopping model makes it a robust technique to predict dopant profiles in the intermediate to high energy range at any implant direction for any species in question.

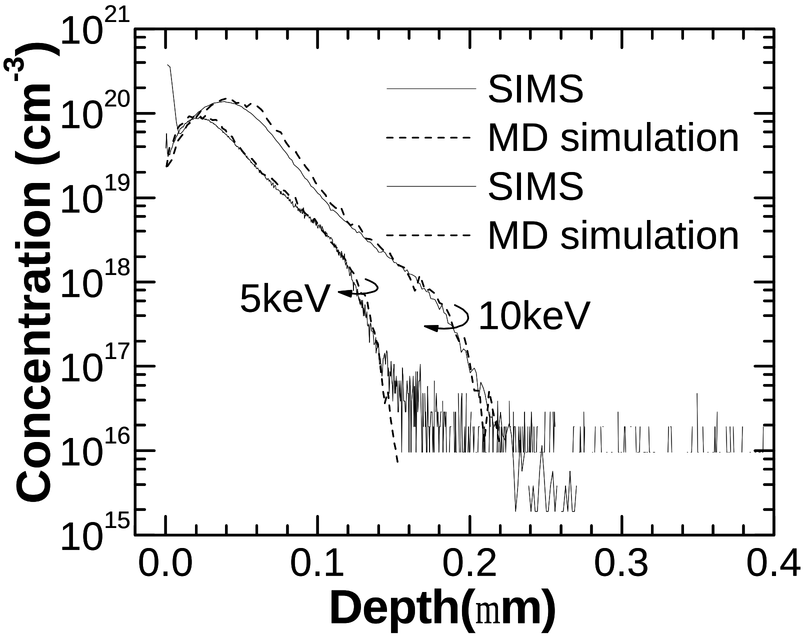

Fig. 6.8 Comparison of experimental SIMS data and MD simulation for B 5keV 5×10^{14} atoms/cm^2 0° tilt and 0° rotation and 10keV 1×10^{15} atoms/cm^2 0° tilt and 0° rotation

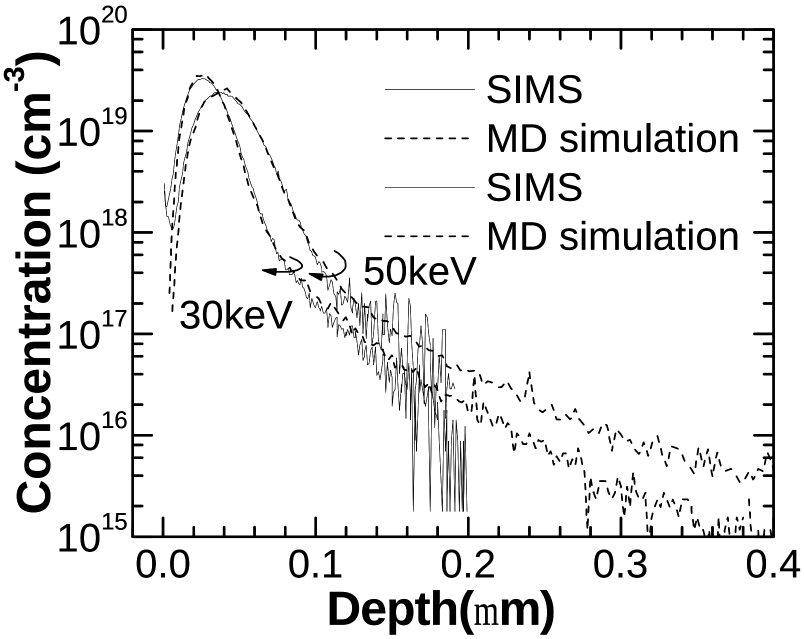

Fig. 6.9 Comparison of experimental SIMS data and MD simulation for Ge 30keV 1×10^{14} atoms/cm^2 5.2° tilt and 17° rotation and 50keV 1×10^{14} atoms/cm^2 5.2° tilt and 17° rotation

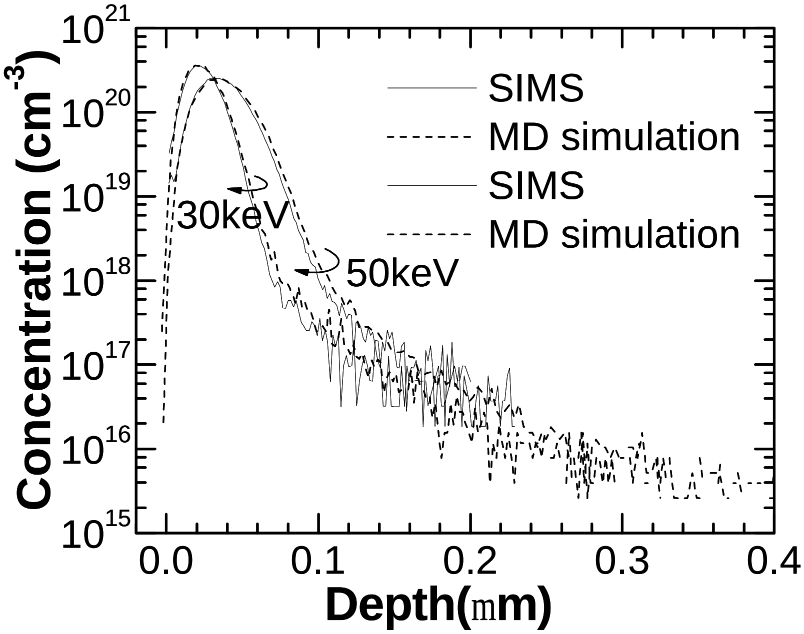

Fig. 6.10 Comparison of experimental SIMS data and MD simulation for As 30keV 1×10^{15} atoms/cm^2 7° tilt and 23° rotation and 50keV 1×10^{15} atoms/cm^2 7° tilt and 23° rotation

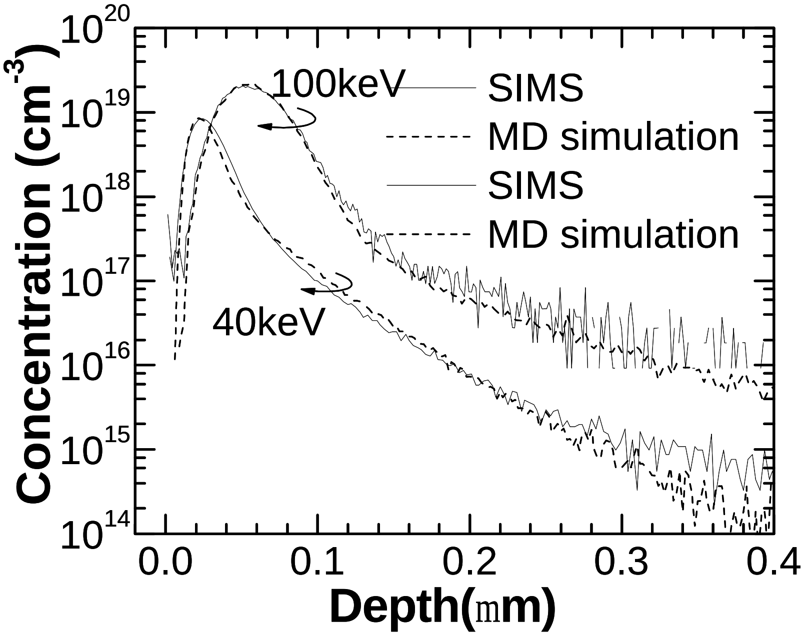

Fig. 6.11 Comparison of experimental SIMS data and MD simulation for In 40keV 2×10^{13} atoms/cm^2 7° tilt and 27° rotation and 100keV 1×10^{14} atoms/cm^2 0° tilt and 0° rotation

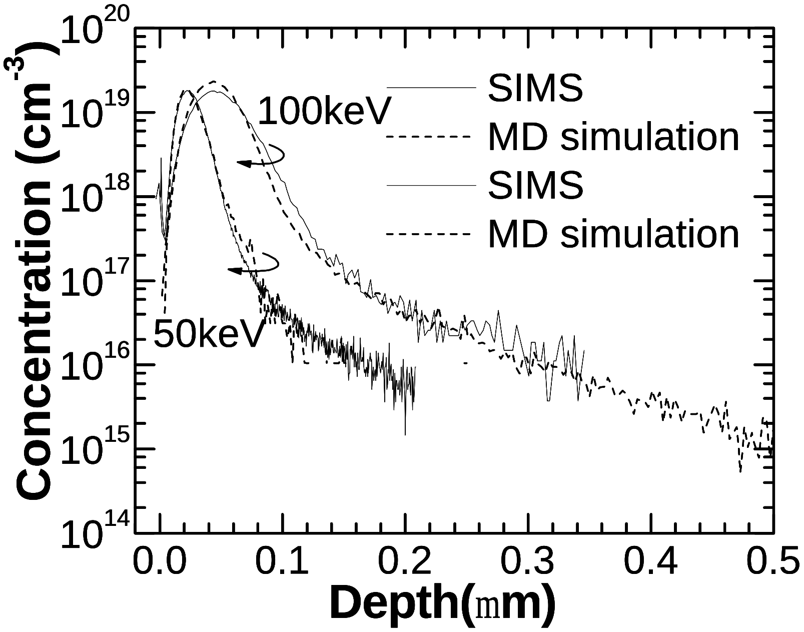

Fig. 6.12 Comparison of experimental SIMS data and MD simulation for Sb 50keV 4.14×10^{13} atoms/cm^2 30° tilt and 18° rotation and 100keV 1×10^{14} atoms/cm^2 0° tilt and 0° rotation

CHAPTER 7 EXPERIMENTAL VERIFICATION AND CALIBRATION

The various methods available for measuring the range distributions have been mentioned in Chapter 2. One of the most popular analytical techniques, SIMS (Secondary Ion Mass Spectrometry) has also been highlighted; including a brief description of the three main instruments used namely time-of-flight (ToF), quadrupole (Q) and magnetic-sector (MS), as well as the basic principle behind this technique. SIMS is popular not only because it is an extremely sensitive method with detection limits of less than a ppm, the measurements can be interpreted easily with knowledge of any stopping mechanisms. For this dissertation, all experimental profiles shown are measured by this technique. In this chapter, the quantitative analysis of SIMS will first be briefly explained, as well as a comparison of the mass resolution capabilities, sensitivities, detection limits etc of the different instruments, followed by the setting up of a low energy SIMS database for calibration of ultra-shallow profiles, and finally the discrepancies between simulation and experiments will be addressed in view of the limitations plaguing the different analyzing equipments and experimental artifacts.

7.1 Quantitative analysis of SIMS

Secondary Ion Mass Spectrometry (SIMS) is merely the bombardment of a sample surface with a primary ion beam followed by mass spectrometry of the emitted secondary ions constituents. During SIMS analysis, the sample surface is slowly sputtered away. Continuous analysis while sputtering produces information as a function of depth, called a depth profile. The bombarding primary ion beam produces monatomic and polyatomic particles of the sample as well as resputtered primary ions, along with electrons and photons. The secondary particles may be negatively, positively, and neutrally charged and they have kinetic energies ranging from zero to several hundred eV. Typical primary beam species useful in SIMS include Cs^+, O_2^+, O, Ar^+, and Ga^+ with incoming energies between 0.5 to 30 keV. Sputter rates depend on primary beam intensity, the sample material, crystal orientation etc and vary between 0.5 and 5 nm/s. The sputter yield is the ratio of the number of atoms sputtered to the number of impinging primary ions. Typical SIMS sputter yields fall in a range from 5 and 15. After the sputtering process and the collection of secondary ions, it is necessary to convert the raw output (ion counts versus time) to useful data (concentration versus depth of sample) by the use of a conversion factor, known as the relative sensitivity factor (RSF) which is dependent on the primary beam species and energy, as well as the impurity and target species.

The RSF is defined according to Eq. (7.1). RSF_E is the relative sensitivity factor for element E, I_E is the secondary ion intensity/ion counts for element E, I_R is secondary ion intensity/ion counts for reference element R, while C_E and C_R are the atomic concentrations of elements E and R respectively.

$$\frac{I_R}{C_R} = RSF_E \times \frac{I_E}{C_E} \tag{7.1}$$

The matrix element (target material) is usually chosen as the reference. Substituting M (matrix) for R (reference) gives Eq. (7.2).

$$C_E = RSF_E \times \frac{I_E C_M}{I_M} \tag{7.2}$$

In trace element analysis, the matrix elemental concentration can be assumed constant. C_M can then be combined with RSF_E to give a more convenient constant, RSF, given in Eq. (7.3).

$$RSF = C_M \times RSF_E \tag{7.3}$$

This RSF is a function of the element of interest and the sample matrix. The elemental concentration can then be expressed as the multiplication of the RSF constant with the ratio of intensities of both element and matrix. RSF and C_E have the same concentration units. This is the most common form of the RSF equation.

$$C_E = RSF \times \frac{I_E}{I_M} \tag{7.4}$$

The intensities can be obtained directly from the SIMS measurements while the RSF is obtained by analyzing a sample from a calibration standard with an accurately known dose. RSF tables have been constructed for many elements. Since the work by Wilson et al. (1989), work has continued to expand and refine previously published RSF values and to obtain results for elements for which data were not given in that publication. Implanted standards of all of the stable elements in the periodic table have since been prepared and studied in silicon, GaAs and diamond (Wilson, 1995). Fig. 7.1(a) shows the RSF values published by Wilson (1995) which have been measured for oxygen primary ion bombardment and positive secondary ions while Fig. 7.1(b) shows the values measured for cesium primary ion bombardment and negative secondary ions. Both sets of measurements were conducted on a silicon matrix and give an indication on how sensitivity depends on the element of interest. Low RSFs reflect high sensitivity. While the relative sensitivity factors convert the vertical axis from ion counts into atomic concentration (atoms/cm^3), the conversion of time into depth is achieved by using a profilometer to measure the sputter crater depth. A profilometer is a separate instrument that determines depth by dragging a stylus across the crater and noting vertical deflections. The average sputter rate can then be obtained by dividing the total crater depth by the total sputter time. The conversion of the raw output to concentration units based on an average sputter rate inevitably introduced inaccuracies in the measured profile since the sputter rate varies with several parameters, and especially with time. The time variation can be accounted for by employing a function of sputtering yield versus time rather than a constant sputter rate. Depth resolution depends on flat bottom craters. Modern instruments provide uniform sputter currents by sweeping a finely focused primary beam in a raster pattern over a square area. In some instruments, apertures select secondary ions from the crater bottoms, but not the edges. Alternatively, the data processing system ignores all secondary ions produced when the primary sputter beam is at the ends of its raster pattern.

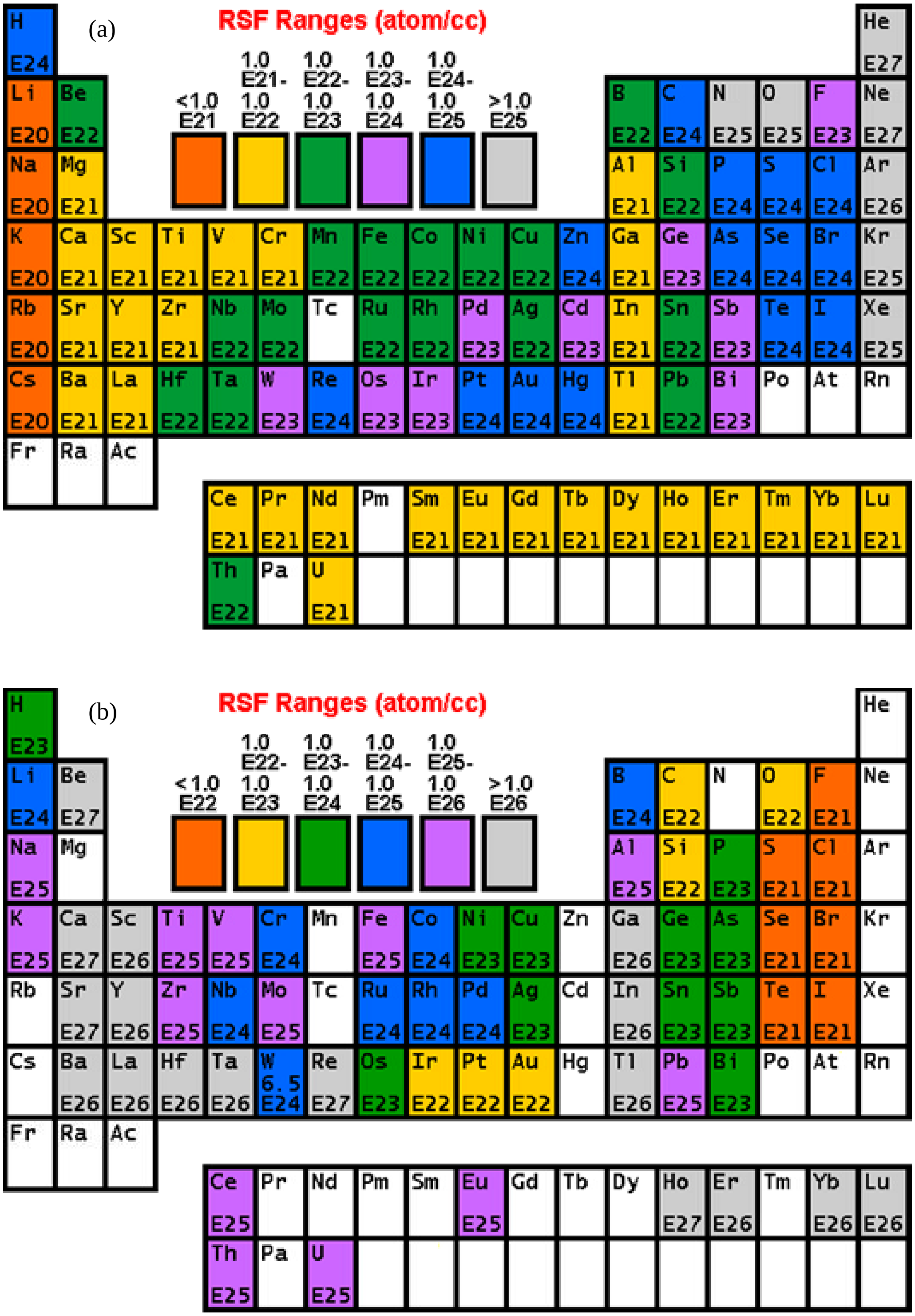

(a)

RSF Ranges (atom/cc)

<1.0 E21	1.0 E21- 1.0 E22	1.0 E22- 1.0 E23	1.0 E23- 1.0 E24	1.0 E24- 1.0 E25	>1.0 E25
🟧	🟨	🟩	🟪	🟦	⬜

H E24																	He E27
Li E20	Be E22											B E22	C E24	N E25	O E25	F E23	Ne E27
Na E20	Mg E21											Al E21	Si E22	P E24	S E24	Cl E24	Ar E26
K E20	Ca E21	Sc E21	Ti E21	V E21	Cr E21	Mn E22	Fe E22	Co E22	Ni E22	Cu E22	Zn E24	Ga E21	Ge E23	As E24	Se E24	Br E24	Kr E25
Rb E20	Sr E21	Y E21	Zr E21	Nb E22	Mo E22	Tc	Ru E22	Rh E22	Pd E23	Ag E22	Cd E23	In E21	Sn E22	Sb E23	Te E24	I E24	Xe E25
Cs E20	Ba E21	La E21	Hf E22	Ta E22	W E23	Re E24	Os E23	Ir E23	Pt E24	Au E24	Hg E24	Tl E21	Pb E22	Bi E23	Po	At	Rn
Fr	Ra	Ac															

Ce E21	Pr E21	Nd E21	Pm	Sm E21	Eu E21	Gd E21	Tb E21	Dy E21	Ho E21	Er E21	Tm E21	Yb E21	Lu E21
Th E22	Pa	U E21											

(b)

RSF Ranges (atom/cc)

<1.0 E22	1.0 E22- 1.0 E23	1.0 E23- 1.0 E24	1.0 E24- 1.0 E25	1.0 E25- 1.0 E26	>1.0 E26
🟧	🟨	🟩	🟦	🟪	⬜

H E23																	He
Li E24	Be E27											B E24	C E22	N	O E22	F E21	Ne
Na E25	Mg											Al E25	Si E22	P E23	S E21	Cl E21	Ar
K E25	Ca E27	Sc E26	Ti E25	V E25	Cr E24	Mn	Fe E25	Co E24	Ni E23	Cu E23	Zn	Ga E26	Ge E23	As E23	Se E21	Br E21	Kr
Rb	Sr E27	Y E26	Zr E25	Nb E24	Mo E25	Tc	Ru E24	Rh E24	Pd E24	Ag E23	Cd	In E26	Sn E23	Sb E23	Te E21	I E21	Xe
Cs	Ba E26	La E26	Hf E26	Ta E26	W 6.5 E24	Re E27	Os E23	Ir E22	Pt E22	Au E22	Hg	Tl E26	Pb E25	Bi E23	Po	At	Rn
Fr	Ra	Ac															

Ce E25	Pr	Nd	Pm	Sm	Eu E25	Gd	Tb	Dy	Ho E27	Er E26	Tm	Yb E26	Lu E26
Th E25	Pa	U E25											

Fig. 7.1 RSF values for all stable elements measuring (a) positive secondary ions with O^+ primary beam and (b) negative secondary ions with Cs^+ primary beam

The SIMS detection limits for most trace elements fall between 10^{12} and 10^{16} atoms/cm^3. In addition to ionization efficiencies (RSF's), two other factors can limit sensitivity. The output of an electron multiplier, known as *dark counts* or *dark current* if no secondary ions are striking it, arises from stray ions and electrons in instrument vacuum systems, and from cosmic rays. Count rate-limited sensitivity occurs when sputtering produces less secondary ion signal than the detector dark current. If the SIMS instrument introduces the analyte element, then the introduced level constitutes background limited sensitivity. Oxygen, present as residual gas in vacuum systems, is an example of an element with background limited sensitivity. Analyte atoms sputtered from mass spectrometer parts back onto the sample by secondary ions constitute another source of background. Mass interferences also cause background limited sensitivity. Quantitative SIMS analysis requires standard materials from which to measure RSF values. Because ion yields depend on the analyte element, the sputtering species, and the sample matrix, separate RSF's must be measured for each. Ion implants are good standards. It is possible to implant virtually any element into any matrix. Ions can be passed through a mass analyzer before implantation to insure implant purity. Typical implant ion energies range from 50 to 300 keV. Higher energies are usually used for heavier ions, producing typical implant depths centered about 0.2 µm. Most importantly, the implant ion current can be integrated to determine total ion dose. However, care must be taken to exclude secondary electron and ion currents from the total measurement.

Besides sensitivity, the SIMS ionization efficiency also called ion yield (fraction of sputtered atoms that become ionized) is also an important factor which affects the measured profiles. Ion yields can vary over many orders of magnitude for the various elements. The most obvious influences on ion yield are ionization potential for positive ions and electron affinity for negative ions. Variations depend both on the sample matrix and on the element itself, and known to be strong functions of the surface content. For example, the presence of oxygen in the sample enhances positive ion yields for most elements, but fluorine exhibits anomalously high positive ion yields in nearly all samples. Other factors also affect the secondary ionization efficiencies in SIMS measurements. Oxygen bombardment increases the yield of positive ions and cesium bombardment increases the yield of negative ions. The increases can range up to four orders of magnitude.

Oxygen enhancement occurs as a result of metal-oxygen bonds in an oxygen rich zone. When these bonds break in the ion emission process, the oxygen becomes negatively charged because its high electron affinity favors electron capture and its high ionization potential inhibits positive charging. The metal is left with the positive charge. Oxygen beam sputtering increases the concentration of oxygen in the surface layer. The enhanced negative ion yields produced with cesium bombardment can be explained by work functions that are reduced by implantation of cesium into the sample surface. More secondary electrons are excited over the surface potential barrier. Increased availability of electrons leads to increased negative ion formation. The variability in ionization efficiencies leads to different analysis conditions for different elements.

All SIMS profiles shown in the work utilizes a Cs+ primary ion beam, except for the measurement of B which uses a primary O+ beam. All analysis conditions investigated have been optimized to obtain the best sensitivities and ionization efficiencies. The bombarding energy is deemed low enough to minimize any fallse enhancement in ion yields.

7.2 SIMS database (Low to Intermediate energy)

In the previous chapter, the MD code had been validated with experimental profiles obtained from SIMS for intermediate to high energies. Excellent agreement of the MD simulated profiles with SIMS data had been obtained for various species, ascertaining the capability and validity of molecular dynamics in the high energy range. However, the high-energy MD simulations are much more time-consuming than BCA simulations; this limitation offsets the advantage of using MD in simulating high energy profiles especially since BCA had been proven capable of simulating accurate range profiles for intermediate to high energies, down to energies of 5 keV for common species like P and As (see Sec. 4.2). MD is touted to replace BCA in the low energy regime; hence it is necessary to calibrate and validate the MD code not only for intermediate to high energies, but especially for low energies where BCA breaks down. Moreover, it is imperative to qualify range profiles in the low energy regime as integrated-circuit device size shrinks, not only for common calibrated source-drain dopants like B and As, but also for heavy elements like In and Sb which play increasingly challenging roles in minimizing punch-through, channel engineering and threshold voltage adjustment. With the exception of the two most commonly used dopants, B and As, SIMS data in the low energy (< 10 keV) regime are relatively scarce, especially so for heavy dopants. This can be attributed to the fact that current industrial applications of dopants like In and Sb utilize implant energies greater than 50keV. However, as device dimensions traverse the nanometer regime, accurate modeling of ultra-shallow profiles within the first few atomic layers becomes more crucial. Moreover, it is no trivial task implanting heavy dopants into the silicon substrate at low energies since the ions lack sufficient momentum to penetrate the substrate fully and may only adhere on the surface.

The ideal mode of operating any ion implanter is the "drift mode," in which all the ions are extracted at the final implant energy. As implant energies lower below 2 keV, the drift mode starts to face a significant loss in beam current at the wafer because of space charge limitation of these low-energy beams leading to low extraction and poor transportation efficiency. The low beam currents lead to a sharp drop in productivity levels, which are not suitable for high-volume manufacturing. To address the issue of decreasing productivity at low energies, “decel mode” is becoming the preferred approach for low-energy ion implantation. In this mode, ions are extracted at much higher potentials than the desired energies to draw higher beam currents from the ion source, and are decelerated electrostatically to the desired low energy just before they reach the wafer. A consequence of decel-mode operation is the introduction of energy contamination caused by dopant ions that are neutralized by charge exchange with the background gas and collisions prior to deceleration (Lenoble et al., 2002). These neutralized dopant atoms cannot be decelerated and hence arrive at the wafer with higher energies. The contamination resulting from these higher-energy atoms manifests itself in the source/drain extension doping profiles as deeper tails, thereby affecting the junction depth and transistor characteristics. Hence, with such problems, precise energy control is imperative yet challenging for low energy ion implantation.

In this section, the set up of a low energy SIMS database to calibrate the ultra-shallow profiles obtained from low energy implants is described. Apart from the dopants covered by external databases shown in Table 6.2 (B, As, In and Sb), five other dopants are investigated, including C, F, N, P and Ge. Although C, F and N are not yet extensively used in transistor manufacturing, they have important applications relevant for semiconductor processes as well. Recent work (Ngau et al., 2001) has indicated that silicon when richly doped with carbon shows a suppression of boron transient enhanced diffusion (TED). It is believed to be caused by non-equilibrium point defect concentrations, specifically the under-saturation of silicon self-interstitials that result from the coupled out-diffusion of carbon interstitials via the kick-out and Frank--Turnbull reactions. Fluorine when doped into silicon oxide reduces the dielectric constant (k-value) of silicon oxide, depending on the F concentration (Cote et al., 1999). Use of low-k materials leads to lower total capacitance, decreasing the interconnection delay and power dissipation, and thus enhancing performance. Nitrogen is a well-known barrier of boron penetration into the gate oxide. Phosphorous is an essential element for channel engineering, CMOS retrograde and noise isolation wells while germanium is the primary dopant used for preamorphization implants to reduce channeling effects. The energy range for each dopant was chosen such that the energies span across the BCA breakdown limits calculated from DFT in the last column of Table 6.1 (0.2 – 10 keV). The purpose is to investigate the predictive capabilities of both BCA and MD codes in the low energy regime.

Table 6.1 BCA breakdown energy limits (keV). Only DFT calculations are shown.

Element (X)	DFT(NN_{SI})
B	0.429
C	0.515
N	0.601
F	0.772
P	1.287
Ge	2.746
As	2.832
In	4.205
Sb	4.377

Table 7.1 summarizes the implant conditions used in setting up the database. 200 mm (8") and 300 mm (12") wafers were used in this experimental study; 72 different implant conditions were studied. The dose ranges from 5×10^{13} to 1×10^{15} atoms/cm^2 and the implant tilt/twist angles investigated are 7°/22°, 0°/0° and 45°/45°, which corresponds to increasing levels of channeling respectively. The tilt angle is the angle between the incident ion beam and the normal of the wafer plane, while the azimuthal angle is measured with respect to the (100) plane in which the dopants are implanted. While tilting the wafer surface relative to the incident ion beam direction by 7° is a widely adopted procedure to minimize channeling, the use of self-aligned (0° tilt) source-drain extension doping is inevitable. Although tilt angles of 45° are not yet common in wafer fabrication process, a wafer orientation of 45° in the azimuthal direction, in addition to the 45° tilt angle, represents one of the worst scenarios in axial and planar channeling. Such profiles should be well calibrated for profiles implanted in any direction to be modeled accurately.

Table 7.1 Implant conditions for 72-wafer split involving nine species

	Element (X)	Energy (keV)	Dose (atoms/cm^2)	Tilt angle (°)	Twist angle (°)
1.	B	0.2	8×10^{14}	45°	0°
2.	B	0.5	5×10^{13}	45°	0°
3.	B	0.5	5×10^{13}	45°	9°
4.	B	0.5	5×10^{13}	45°	18°
5.	B	0.5	5×10^{13}	45°	27°
6.	B	0.5	5×10^{13}	45°	36°
7.	B	0.5	5×10^{13}	45°	45°
8.	B	0.5	5×10^{13}	45°	54°
9.	B	0.5	5×10^{13}	0°	0°

10.	B	0.5	5×10^{14}	0°	0°
11.	B	0.6	1×10^{15}	7°	22°
12.	C	0.5	1×10^{14}	0°	0°
13.	C	0.5	1×10^{14}	45°	45°
14.	C	1.0	1×10^{14}	0°	0°
15.	C	1.0	1×10^{14}	45°	45°
16.	C	2.0	1×10^{14}	0°	0°
17.	C	2.0	1×10^{14}	45°	45°
18.	N	0.5	1×10^{14}	0°	0°
19.	N	0.5	1×10^{14}	45°	45°
20.	N	1.0	1×10^{14}	0°	0°
21.	N	1.0	1×10^{14}	45°	45°
22.	N	2.0	1×10^{14}	0°	0°
23.	N	2.0	1×10^{14}	45°	45°
24.	N	3.0	1×10^{14}	7°	22°
25.	N	3.0	1×10^{15}	7°	22°
26.	N	5.0	1×10^{14}	7°	22°
27.	N	8.0	5×10^{14}	7°	22°
28.	N	10.0	5×10^{14}	7°	22°
29.	F	1.0	6×10^{13}	0°	0°
30.	F	1.0	6×10^{13}	45°	45°
31.	F	2.0	6×10^{13}	0°	0°
32.	F	2.0	6×10^{13}	45°	45°
33.	F	5.0	6×10^{13}	0°	0°
34.	F	5.0	6×10^{13}	45°	45°
35.	P	1.0	5×10^{13}	0°	0°
36.	P	1.0	5×10^{13}	45°	45°
37.	P	2.0	5×10^{13}	0°	0°
38.	P	2.0	5×10^{13}	45°	45°
39.	P	3.0	1×10^{14}	7°	22°
40.	P	3.0	1×10^{15}	7°	22°
41.	P	5.0	5×10^{13}	0°	0°
42.	P	5.0	5×10^{13}	45°	45°
43.	P	5.0	1×10^{14}	7°	22°
44.	Ge	2.0	5×10^{13}	0°	0°
45.	Ge	2.0	5×10^{13}	45°	45°
46.	Ge	3.0	5×10^{13}	0°	0°
47.	Ge	3.0	5×10^{13}	45°	45°
48.	Ge	5.0	5×10^{13}	0°	0°
49.	Ge	5.0	5×10^{13}	45°	45°
50.	As	1.0	1×10^{14}	7°	22°
51.	As	1.0	1×10^{15}	7°	22°
52.	As	2.0	5×10^{13}	0°	0°
53.	As	2.0	5×10^{13}	45°	45°
54.	As	2.0	1×10^{15}	7°	22°
55.	As	5.0	5×10^{13}	0°	0°
56.	As	5.0	5×10^{13}	45°	45°
57.	As	5.0	1×10^{14}	7°	22°
58.	As	10.0	5×10^{13}	0°	0°

59.	As	10.0	5×10^{13}	45°	45°
60.	In	2.0	5×10^{13}	0°	0°
61.	In	2.0	5×10^{13}	45°	45°
62.	In	5.0	5×10^{13}	0°	0°
63.	In	5.0	5×10^{13}	45°	45°
64.	In	10.0	5×10^{13}	0°	0°
65.	In	10.0	5×10^{13}	45°	45°
66.	Sb	2.0	5×10^{13}	0°	0°
67.	Sb	2.0	5×10^{13}	45°	45°
68.	Sb	5.0	5×10^{13}	0°	0°
69.	Sb	5.0	5×10^{13}	45°	45°
70.	Sb	5.0	1×10^{14}	7°	22°
71.	Sb	10.0	5×10^{13}	0°	0°
72.	Sb	10.0	5×10^{13}	45°	45°

The implants for tilt/twist 0°/0° and 45°/45° were performed on Axcelis Technologies' next generation beamline test stand at the Advanced Technology Center (ATC). The test consisted of implants to evaluate low energy, channeled SIMS profiles for $^{11}B^+$, $^{12}C^+$, $^{14}N^+$, $^{19}F^+$, $^{31}P^+$, $^{72}Ge^+$, $^{75}As^+$, $^{115}In^+$ and $^{121}Sb^+$. For these axial channeling implants, 300mm n-type and p-type wafers were used. An alignment verification test was performed to verify the proper angles were selected to get the channeled implants desired. The data showed that no adjustment was needed for tilt angle while a -1° adjustment should be made to the twist angle. Therefore the 0°/0° implants were run at recipe settings of 0°/359° and 45°/45° implants were run at 45°/44°. The non-channeling 7°/22° implants were conducted in Chartered Semiconductor Manufacturing's inhouse implant equipment using 200mm p-type wafers. Oxide thickness was measured prior to implantation using a Phillips SD3400 Ellipsometer. No post implant oxide measurement was made prior to shipping the wafers. The implanted wafers were then shipped to Cascade Scientific (U.K.) for quadrupole SIMS analysis. A Phi Adept 1010 quadrupole SIMS instrument has been used; a 750eV, 100nA Cs+ beam looking at negative secondary ions at 60° incidence angle with the sample potential held at zero voltage. All SIMS profiles shown in the following section were measured with a Cs+ primary beam, except for B which was measured on quadrupole equipment with a primary O+ beam looking at positive secondary ions. There was no voltage offset on the samples.

7.3 Comparisons of experiments with simulation (low energy)

Fig. 7.2 to 7.10 shows the comparison of some of the representative SIMS profiles against simulated profiles at energies about the calculated BCA breakdown limits for the nine dopants studied (B, C, N, F, P, Ge, As, In and Sb). The BCA simulations have been performed using Crystal-TRIM where the nuclear effects are treated with the universal ZBL potential and electronic stopping treated by both the non-local ZBL model and the semi-empirical Oen-Robinson model. The CEX parameters (Oen-Robinson model) were optimized in all cases so that channelling effects could be modelled accurately. The oxide model was also included in the simulations since a native oxide layer of about 11Å exists for all samples studied. For the low energies studied, local amorphization is easily reached near the surface where damage concentrations are high. Thus the damage model plays an important role in this study. The MD simulations are performed using the code MDRANGE. Previously calculated DMOL potentials are used to depict the force mechanisms at low energies. The phase-shift based PENR model is able to predict accurately the final dopant positions and can be applied to any ion in any target whose electron distribution can be calculated without a parameter fitting process; hence this local model is used for all simulation in this section. All other simulation parameters are kept identical to those described in the previous chapter. The recoil ion approximation is invoked in all cases, where only the ion-recoil interactions are considered. Initially crystalline silicon is used as a target material. The ambient temperature, 300K was used and realistic atomic thermal displacements were obtained by setting the Debye temperature of silicon to 519K. For both BCA and MD simulations, the number of simulated pseudo-particles used was 20,000, and deemed sufficient for good statistics. Statistical enhancement techniques like MDRANGE's modified version of REED and Crystal-TRIM's atom splitting scheme were employed so that dopant profiles over more than four decades of concentration with good statistics and feasible computational overhead can be obtained. The differences in the physics and models used in the codes do not warrant a quantitative one-to-one comparison of the eventual range profiles. However, this section aims to give a qualitative description of the capabilities and limitations of both techniques in the low energy regime based on the individual models.

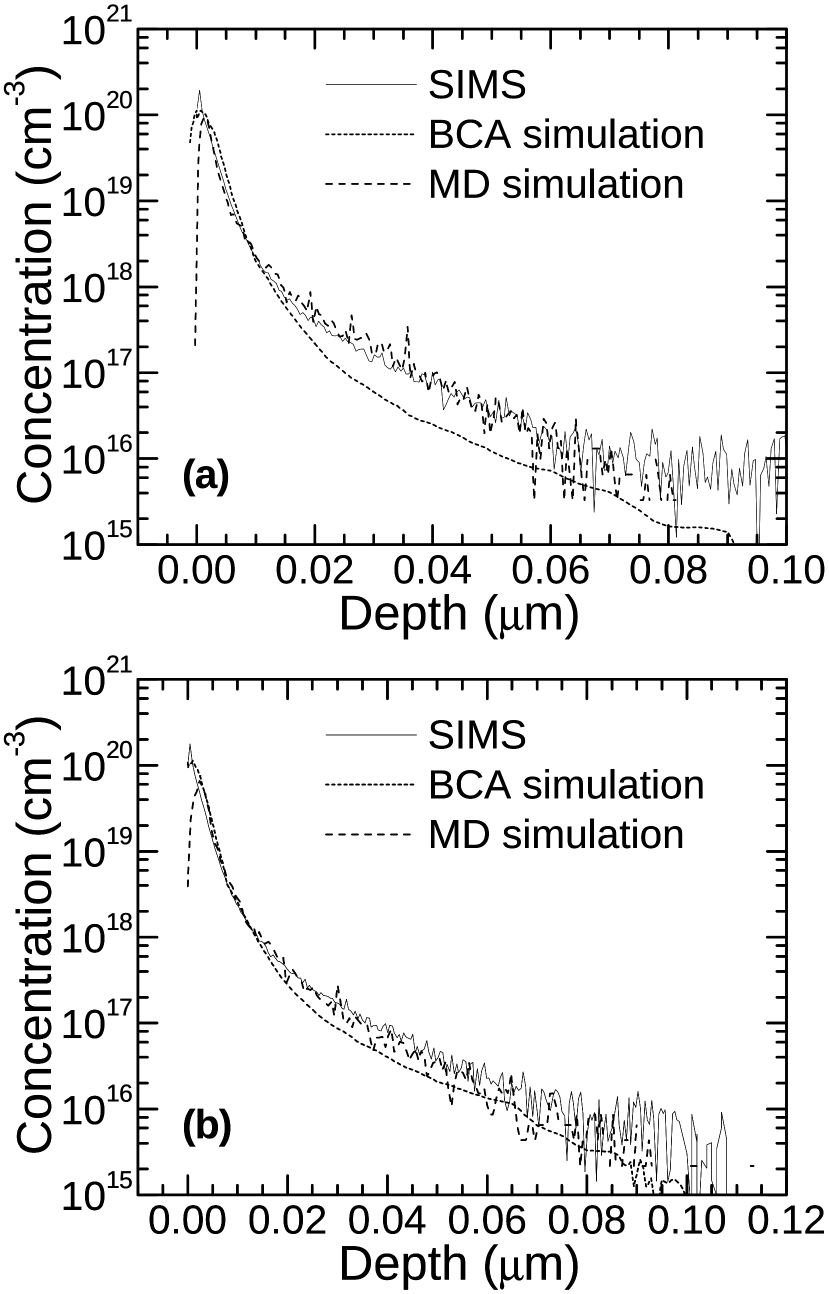

Fig. 7.2 Comparison of experimental SIMS and simulation (BCA versus MD) for B (a) 0.5keV 5×10^{13} atoms/cm^2 45° tilt and 0° rotation (b) 0.5keV 5×10^{13} atoms/cm^2 45° tilt and 18° rotation

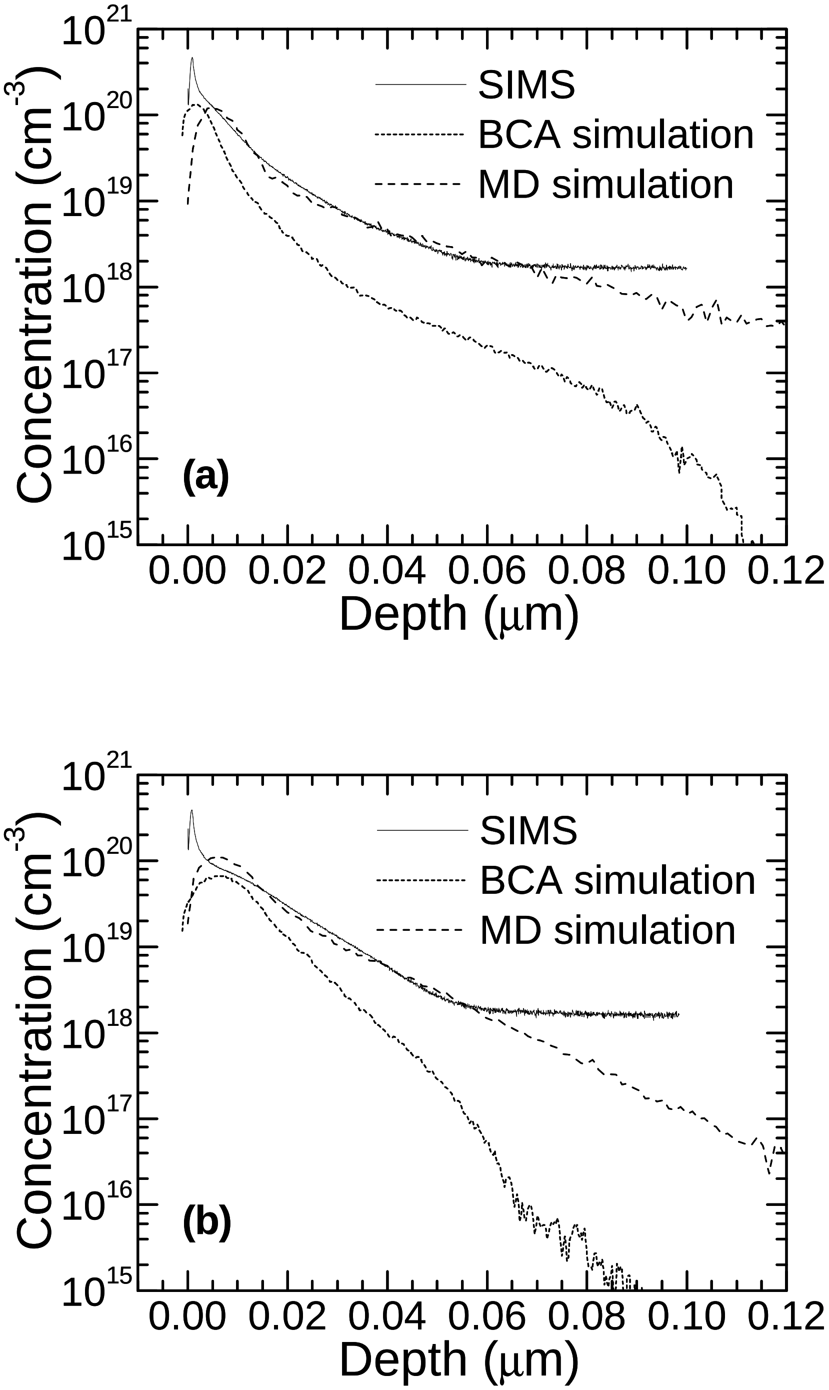

Fig. 7.3 Comparison of experimental SIMS and simulation (BCA versus MD) for C (a) 1keV 1×10^{14} atoms/cm^2 45° tilt and 45° rotation (b) 2keV 1×10^{14} atoms/cm^2 0° tilt and 0° rotation

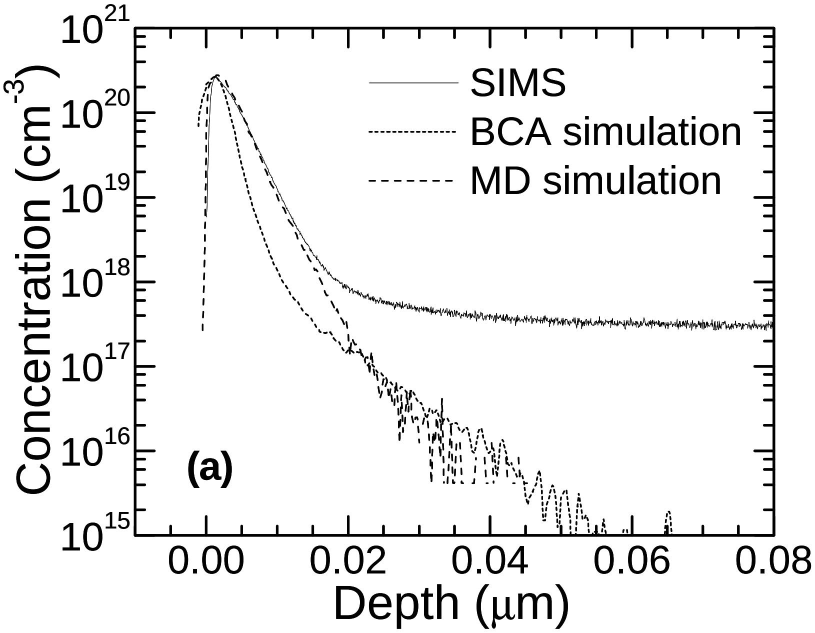

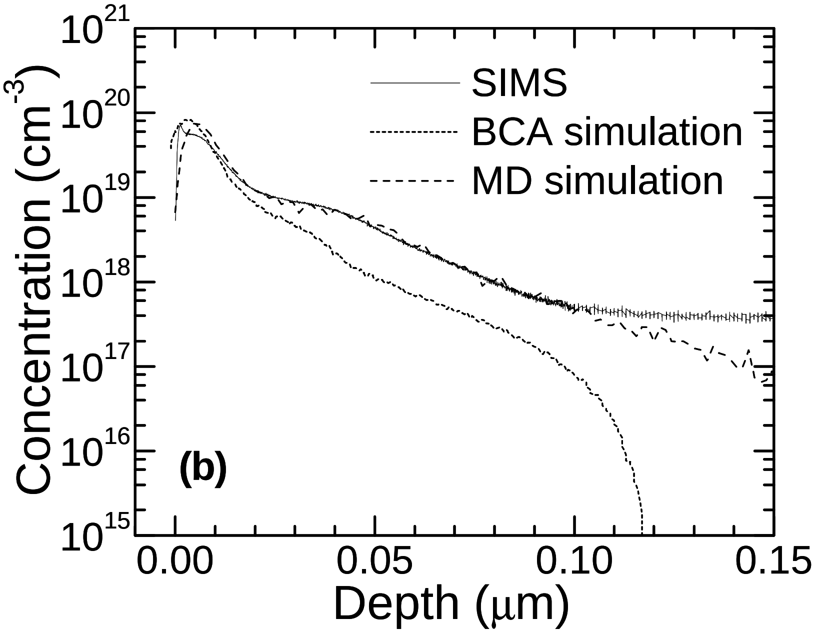

Fig. 7.4 Comparison of experimental SIMS and simulation (BCA versus MD) for N (a) 0.5keV 1×10^{14} atoms/cm^2 0° tilt and 0° rotation (b) 2keV 1×10^{14} atoms/cm^2 45° tilt and 45° rotation

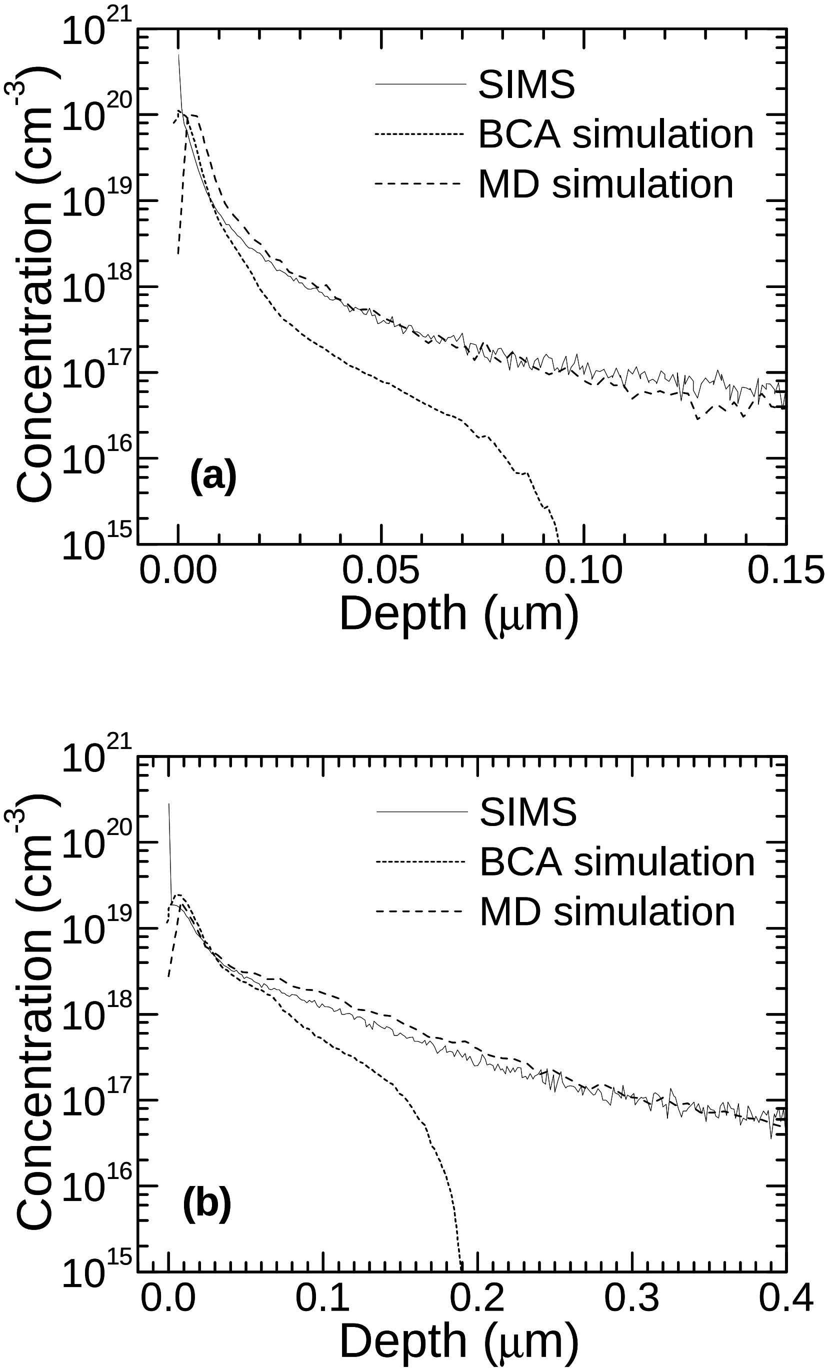

Fig. 7.5 Comparison of experimental SIMS and simulation (BCA versus MD) for F (a) 1keV 6×10^{13} atoms/cm^2 45° tilt and 45° rotation (b) 5keV 6×10^{13} atoms/cm^2 45° tilt and 45° rotation

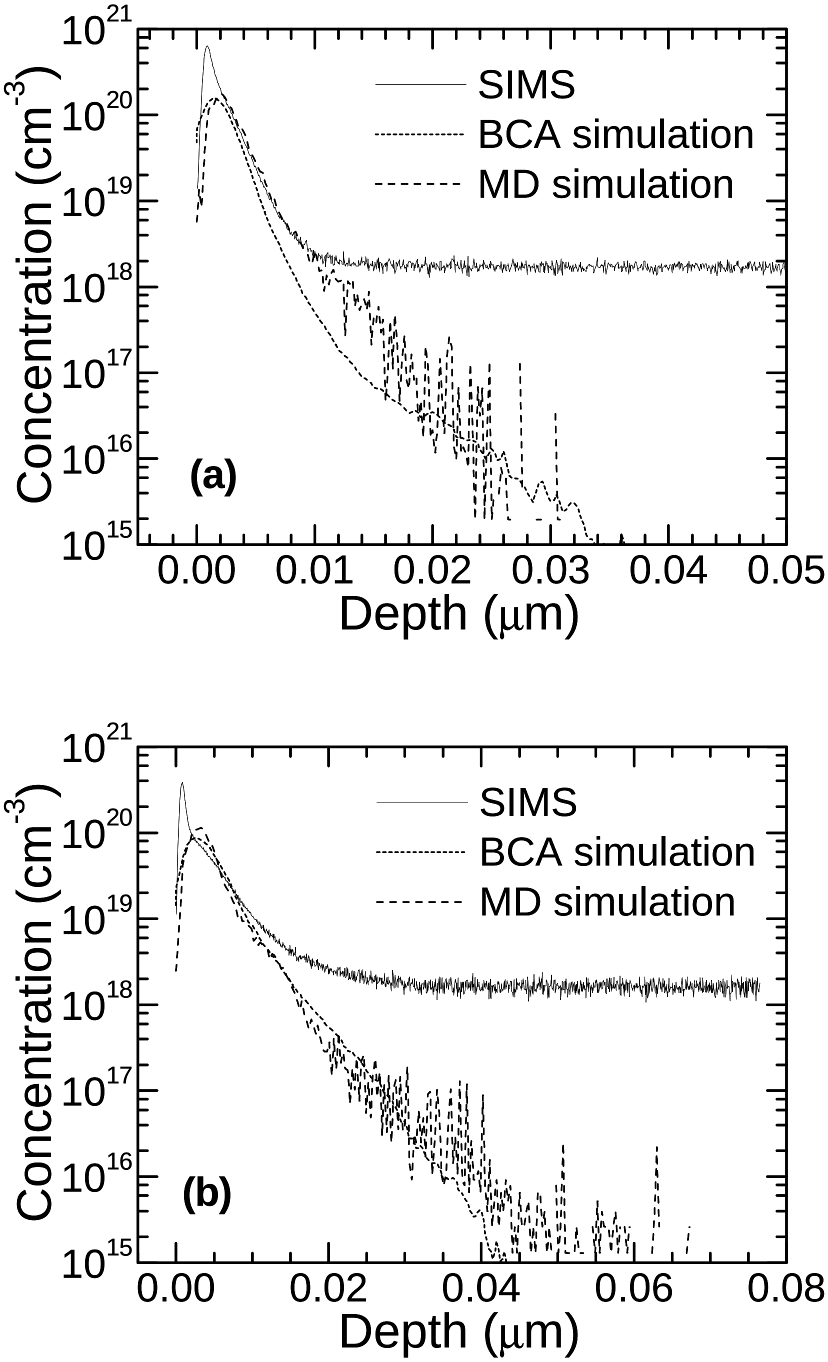

Fig. 7.6 Comparison of experimental SIMS and simulation (BCA versus MD) for P (a) 1keV 5×10^{13} atoms/cm^2 0° tilt and 0° rotation (b) 2keV 5×10^{13} atoms/cm^2 0° tilt and 0° rotation

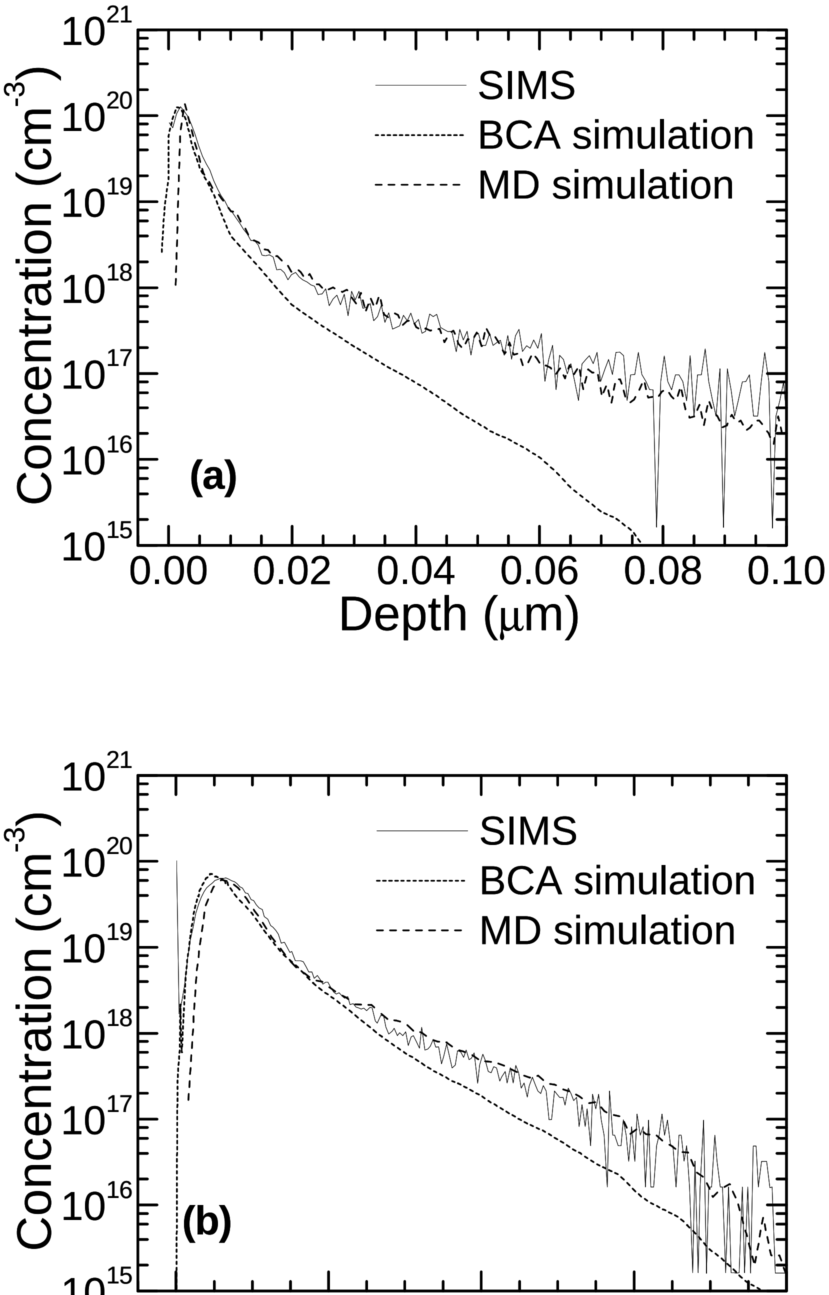

Fig. 7.7 Comparison of experimental SIMS and simulation (BCA versus MD) for As (a) 2keV 5×10^{13} atoms/cm^2 45° tilt and 45° rotation (b) 5keV 5×10^{13} atoms/cm^2 0° tilt and 0° rotation

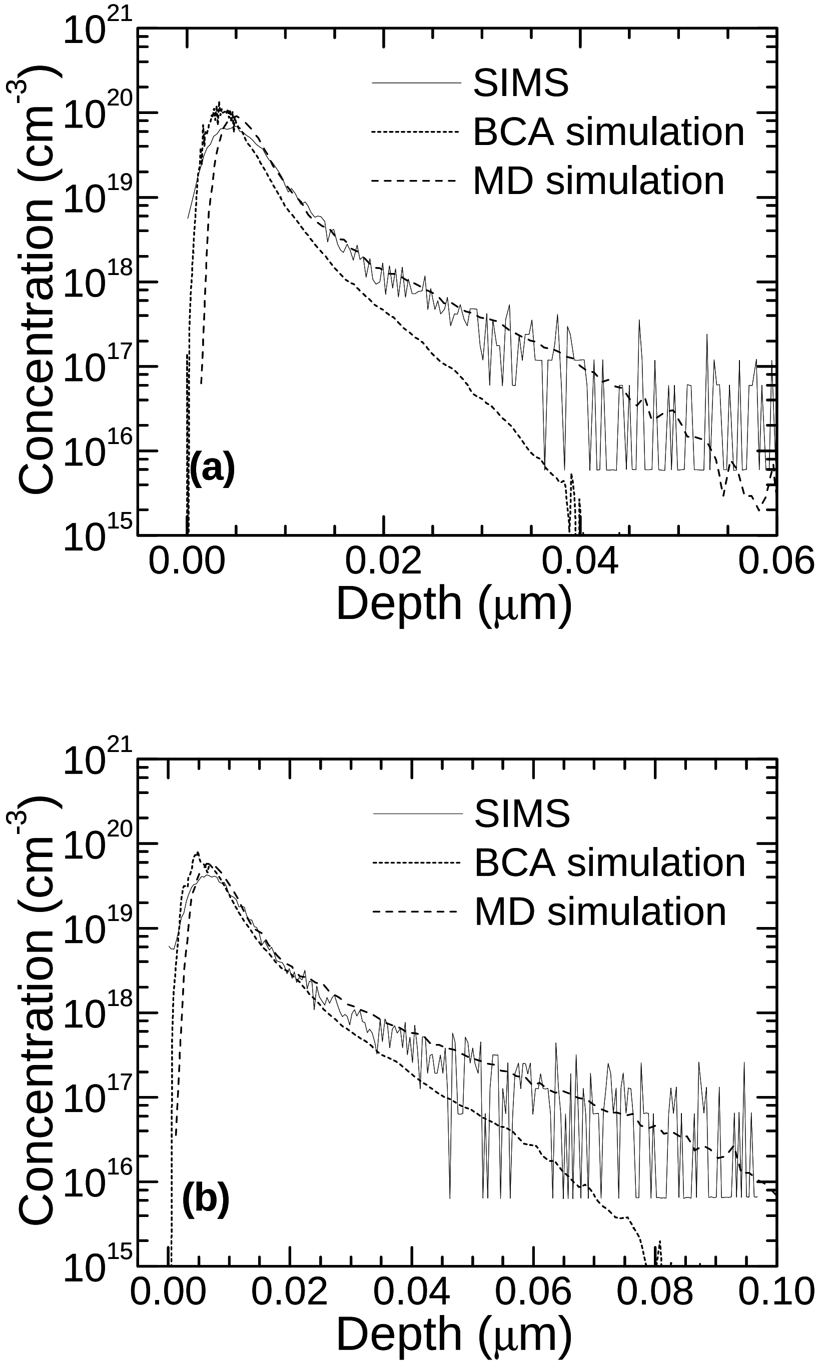

Fig. 7.8 Comparison of experimental SIMS and simulation (BCA versus MD) for Ge (a) 3keV 5×10^{13} atoms/cm^2 0° tilt and 0° rotation (b) 5keV 5×10^{13} atoms/cm^2 0° tilt and 0° rotation

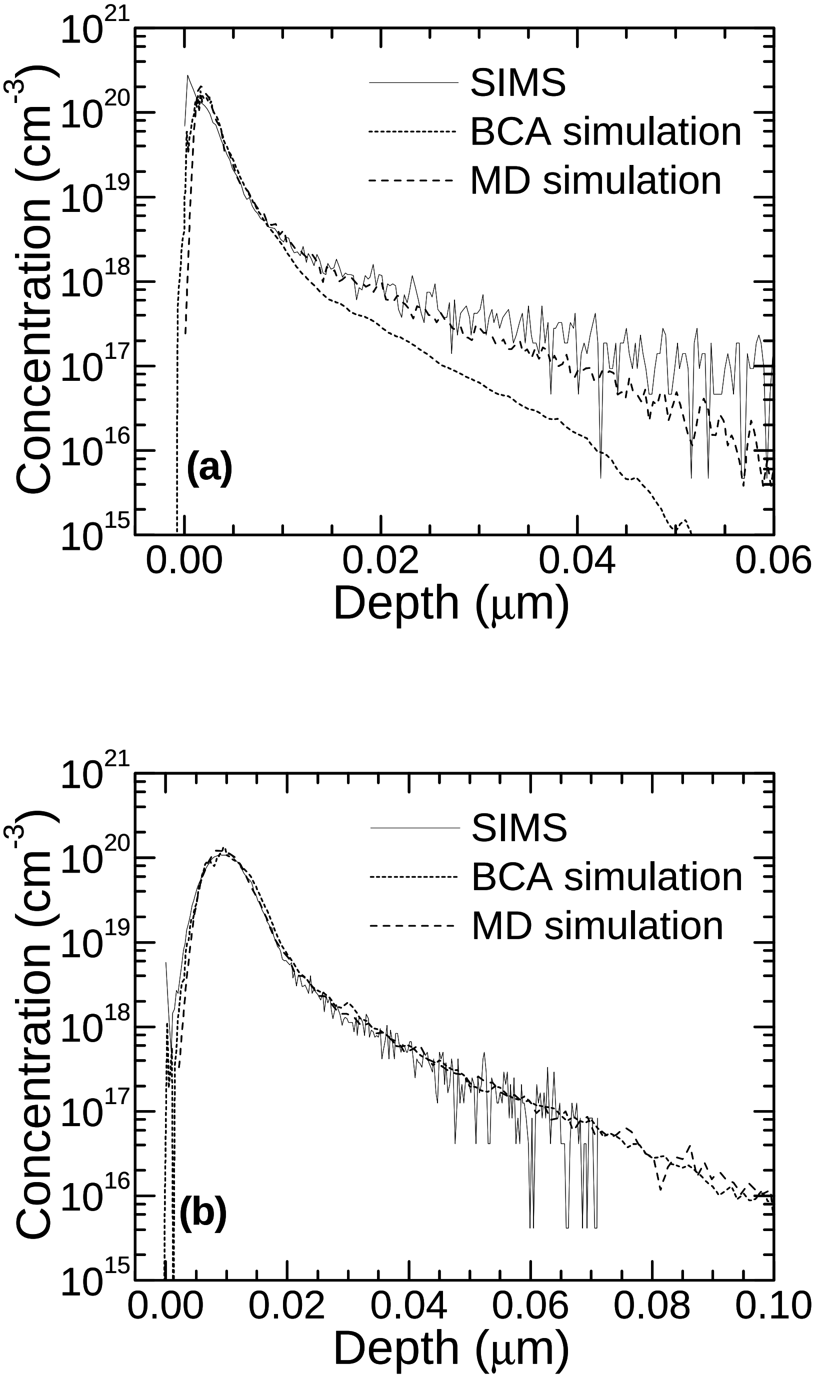

Fig. 7.9 Comparison of experimental SIMS and simulation (BCA versus MD) for In (a) 2keV 5×10^{13} atoms/cm^2 45° tilt and 45° rotation (b) 10keV 5×10^{13} atoms/cm^2 0° tilt and 0° rotation

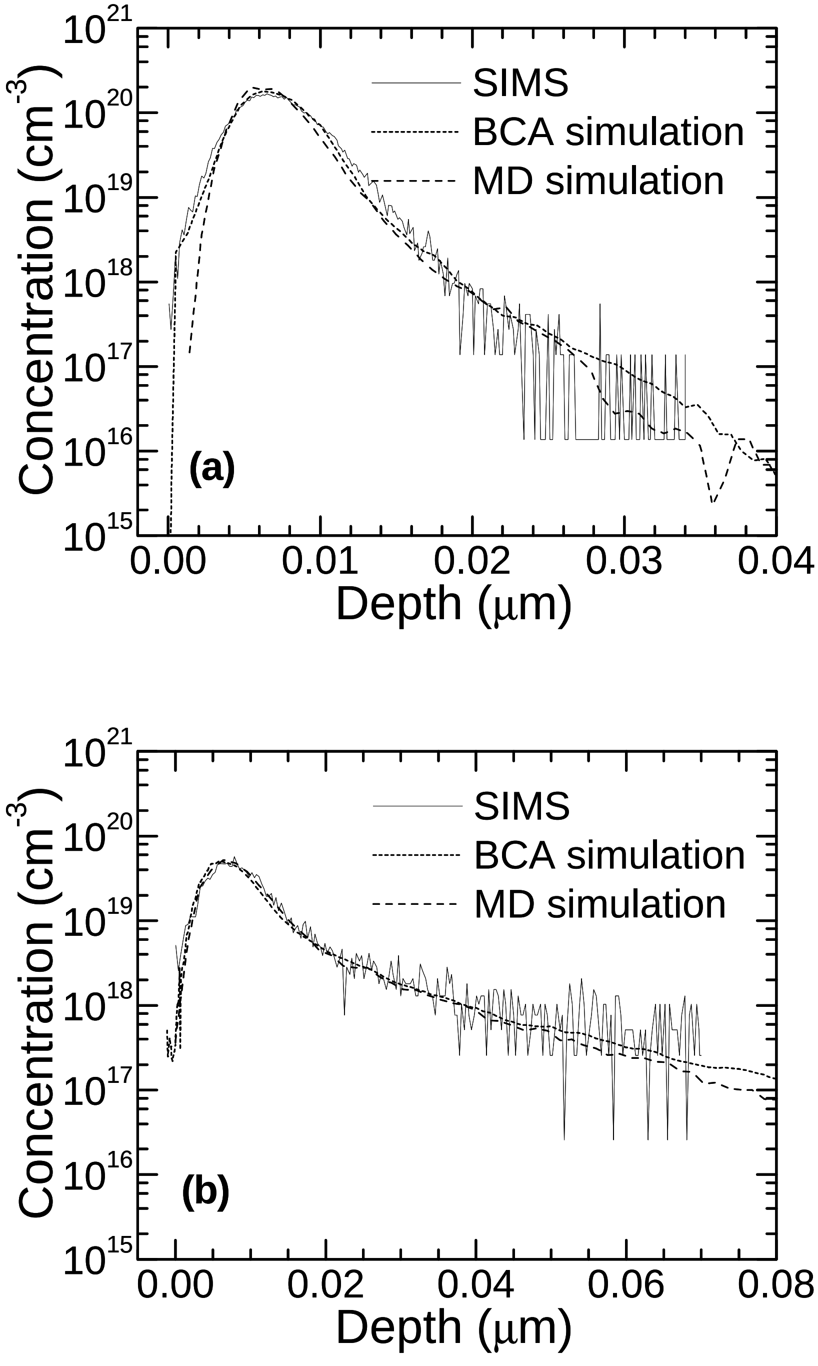

Fig. 7.10 Comparison of experimental SIMS and simulation (BCA versus MD) for Sb (a) 5keV 1×10^{14} atoms/cm^2 7° tilt and 22° rotation (b) 10keV 5×10^{13} atoms/cm^2 45° tilt and 45° rotation

In general, Figs. 7.2 to 7.10 show that the tailing portion of the range profiles obtained from MD simulations agree very well with the experimental data (except for C, N and P where the discrepancies will be further elaborated), while profiles generated from the BCA code Crystal-TRIM tend to underestimate the degree of channeling at low energies, deviating from SIMS by at least half an order of magnitude. Besides the inherent inability of BCA to account for simultaneous multiple collisions significant at low energies, part of the discrepancy can be attributed to the solely repulsive universal ZBL potential which fails to describe attractive forces that come into play as energy lowers. For the cases of high channeling directions (0°/0° and 45°/45°), the underestimation of the channeling tail can be largely attributed to the electronic stopping model instead. The channeling of ions during the slowing down process has an important impact on the concentration profiles both in the vertical and lateral directions. In crystal channels, where the atomic and electronic densities are significantly lower than average, the importance of nuclear stopping is reduced relative to the electronic stopping in crystal channels; hence the choice of the electronic stopping model affects the accuracy of the ranges of the channeled ions. In all of the cases, especially for sub-keV implants, the local PENR model appears to predict better than the ZBL/Oen-Robinson models used in Crystal-TRIM which tend to overestimate the electronic drag force in channeling directions where the electronic density is lower.

However, significant improvement in the BCA simulated profiles against SIMS can be observed as the initial kinetic energy of the incoming ion increases. Beyond the estimated BCA breakdown limits, conditions limiting the use of BCA become insignificant. This is reflected in the good agreement of the simulated profiles with SIMS at higher implant energies (Figs. 7.9(b) and 7.10(b)). It also suggests that the breakdown limits calculated for the various species in Table 6.1 provide reasonable estimates of the breakdown points. Besides the use of inappropriate electronic stopping models, the poor agreement of BCA may also be due to the lack of calibrated parameters (eg. CEX parameters) for certain uncommon species like C, F and N. Conversely speaking, the excellent agreement obtained with MD for all species may be attributed to the local electronic model, where the phase shifts were *specifically* calculated for each target-projectile pair. Finally, the discrepancies between simulation and experiment may be due to the defect accumulation model used, especially since damage concentrations easily exceed the amorphization threshold in the low energy regime. The phenomenological model used in Crystal-TRIM assumes damage parameters that are independent of position, analogous to the non-local electronic stopping model, while the dynamic damage model in MDRANGE monitors the damage level in front of the moving ion with time and chooses the appropriate coordinate boxes. Use of a 'non-local' damage model could possibly have resulted in an overestimation of the cumulative damage, resulting in ultra-shallow profiles seen in the BCA profiles. The enhanced dechanneling effect would be more pronounced in channeling directions since atoms are assumed to be displaced even where the atomic density is much lower than the surrounding environment.

The following observations can be summarized from this study of experimentally measured and simulated low energy range profiles:

1. Agreement of BCA results with SIMS is poor for B and As despite the fact that extensive experimental data and well-calibrated parameters exist for such widely used dopants. This is especially so for 45°-tilted implants which represent severe axial channeling. This could indicate that the electronic stopping models used in Crystal-TRIM are inappropriate for such high tilt implant simulations.
2. The lack of calibrated parameters for uncommon species like C, N and F results in poor prediction of the channeling tails obtained by BCA. CEX values in the Oen-Robinson model are semi-empirical parameters derived from fits with available experimental data. Parameters for B are often used in place for species in the same periodic row like C, N and F, resulting in inaccurate modeling of the profiles.

3. For all cases shown, results from MD are able to produce profiles that agree excellently with SIMS especially in the tail region (except for cases C, N and P where SIMS shows a plateau, resulting from experimental artifacts). This is particularly important when predicting the source-drain junction depths which would eventually affect transistor characteristics. In the case of heavy species (As, Ge, In and Sb) MD shows a shift in the initial portion of the profile towards the bulk. The shift occurs only for the heavy elements in question and is especially pronounced for energies ≤ 5keV. This occurrence can be attributed to the shift of the oxide-silicon interface when a heavy ion bombards the silicon surface. This is not seen for BCA simulated profiles since the profile begins where x=0 is the air-oxide interface. For MD however, x=0 defines the oxide-silicon interface. Light elements do not reflect this shift as the momentum transfer during ion implantation is not large enough to displace the oxide interface. Heavy elements at low energies however push the oxide-silicon interface towards the substrate bulk and result in an anomalous shift of the profiles. The shift disappears as energy increases.
4. It should be noted that at least part of the surface spike in the P profiles is SIMS artifact and merged into the actual peak, resulting in the high surface concentration. The plateaus in the profiles of C, N and P can be attributed to experimental artifacts resulting in high detection limits. Measurement of low level C and N concentrations requires good precision of SIMS instruments with improved vacuum and better primary beam intensity, as well as improved analysis protocol since these species are ubiquitous in the ambient and within the equipments. The poor resolution of P can be attributed to the mass interference of $Si^{30}H^{1}$. Results shown represent the best detection limits of the quadrupole mass analyzer under experimental constraints. In the next section, a round-robin study involving different SIMS instruments are utilized to address and counter these problems. A technique will also be proposed not only to improve the predictive capability of the simulation code but also to detect and prevent experimental artifacts more accurately.

7.4 Further SIMS study: different techniques and instruments

The SIMS profiles shown in the previous section had been obtained with a quadrupole system. Quadrupole mass analyzers have been described briefly in chapter 2. The system consists of four closely spaced circular rods applied with alternating and direct voltages causing the ions traveling between the rods to oscillate after entering the quadrupole. Various factors affect the accuracy of the eventual profile measured, like the species to be detected, the mass resolution, the abundance sensitivity, the detection limits etc. Figs. 7.2 to 7.10 show that SIMS profiles obtained from the quadrupole instrument are limited in certain aspects: C, N and P show high detection limits (~10^{18} atoms/cm^3), offering little information at low atomic concentrations while C, F and P shows high surface peaks which is clearly due to experimental artifacts. The artificial peaks in the C and F profiles can be easily separated from the true profile since the peaks are clearly defined from the actual peak concentration. For P, however, the artificial peaks are merged into the actual profiles and location of the true R_p of a P profile is no trivial task. The occurrences of such surface peaks can be attributed to surface mixing, where atoms from the sample's outer monolayer are driven in by the bombardment of the primary beam, thus producing knock-on effects. High detection limit, on the other hand, is largely caused by mass interference effects where the element to be measured is contaminated with species of similar mass; separation requires instruments with high mass resolution. For instance, the mass interferences, $^{31}P/^{30}Si^{1}H$, $^{56}Fe/^{28}Si_2$, $^{75}As^{28}Si/^{28}Si^{29}Si^{30}Si^{16}O$ are well-known analytical problems when concentration level in the ppm range must be measured. Besides these factors, the mass spectrometer transmission, the acquisition time, the energy of the primary beam all play important roles in the final output, and these factors vary with different instruments.

7.4.1 Use of other mass analyzers

To identify the capabilities and limitations associated with the quadrupole SIMS instrument and to obtain better range profiles, different instruments are utilized to measure the same samples under optimized conditions. Only P and As samples will be discussed in this round-robin study. Henceforth, SIMS profiles measured with a quadrupole mass analyzer will be denoted by Q-SIMS. The other widely used dynamic SIMS mass analyzer is the magnetic sector (MS) instrument which utilizes the relationship between the magnetic field, the ion accelerating voltage, the mass-to-charge ratio and the radius of ion curvature in the magnetic field to filter the desired species. Time-of-flight (ToF) SIMS is also employed to provide a more comprehensive study of the different instruments. Unlike the aforementioned instruments, ToF-SIMS is a static SIMS technique where a pulsed primary ion beam, rather than a continuous, focused beam is used to sputter material from the top monolayer of a sample. Mass separation is performed by measuring the length of time it takes secondary ions to reach the detector. The three instruments, quadrupole (Q), magnetic sector (MS) and time-of-flight (ToF) SIMS will provide a quantitative analysis of the capabilities and limitations of the different instruments. The conditions of analysis for the different instruments are given below. Two different MS equipments were used; Cameca Wf was used only for P analysis.

Q-SIMS (Cascade Scientific): Phi Adept 1010 SIMS instrument, Cs^+ 750 eV ion beam with 100 nA current was used at 60° incidence angle with the sample.

MS(I)-SIMS (National University of Singapore, Physics department): Cameca IMF 6f instrument. A 10 nA Cs^+ beam with net impact energy of 3 keV was used to bombard the sample biased at -1 kV at grazing 24° incidence angle.

MS(II)-SIMS (Chartered Semiconductor, Failure Analysis department): Cameca IMF Wf instrument with a 60° float column. A 10 nA Cs^+ beam with net impact energy of 520 eV was used to bombard the sample biased at -3 kV at grazing 70° incidence angle.

ToF-SIMS (Institute of Materials Research and Engineering): ION-TOF IV instrument. A 10 nA Cs^+ beam with net impact energy of 1 keV for depth profiles of P, and 3 keV for As. The analysis beam was Ga 15 keV going in 1 ns pulses at 10 kHz with average beam current 2 pA. The incident angle of both beams was 45^{o}. There was no voltage offset on the samples for all Q-, MS- and ToF-SIMS measurements. Fig. 7.11 show the SIMS profiles measured for As using the three types of instruments. Simulated profiles are omitted in this section.

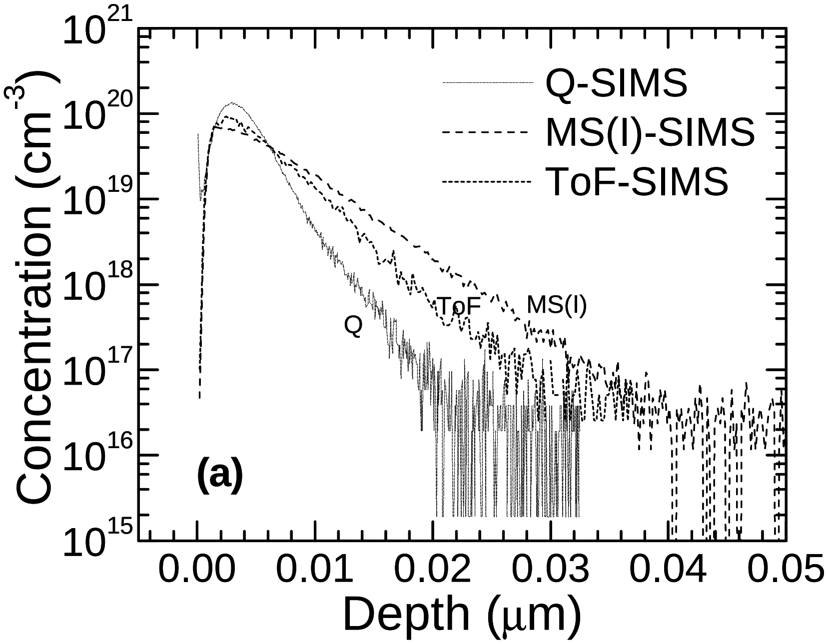

Fig. 7.11 Comparison of SIMS (Q, MS and ToF) for As (a) 2keV 5×10^{13} atoms/cm^2 0° tilt and 0° rotation

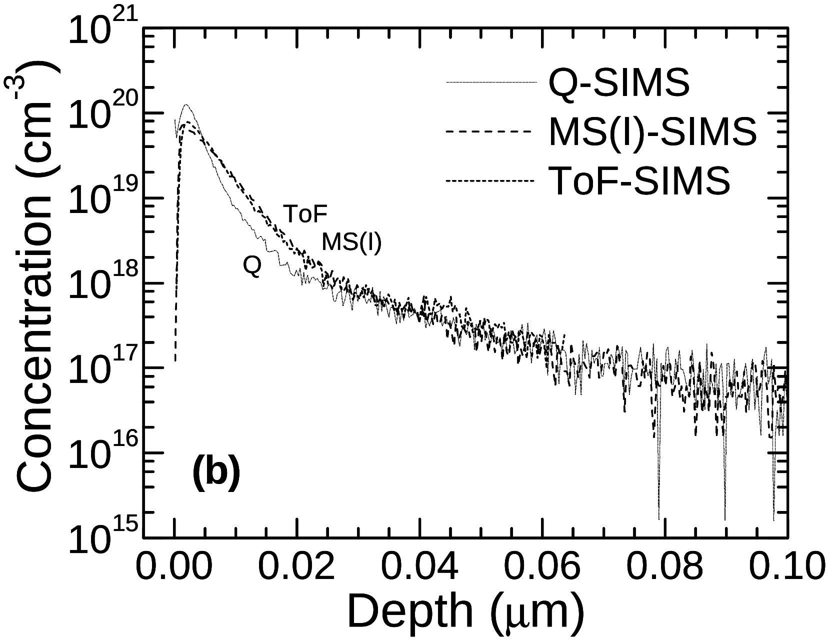

Fig. 7.11 Comparison of SIMS (Q, MS and ToF) for As (b) 2keV 5×10^{13} atoms/cm^2 45° tilt and 45° rotation

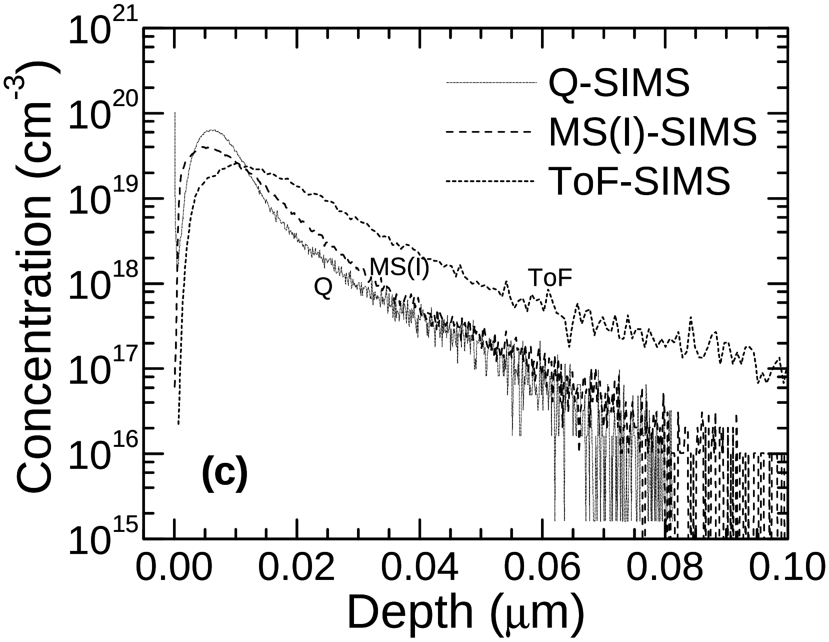

Fig. 7.11 Comparison of SIMS (Q, MS and ToF) for As (c) 5keV 5×10^{13} atoms/cm^2 0° tilt and 0° rotation

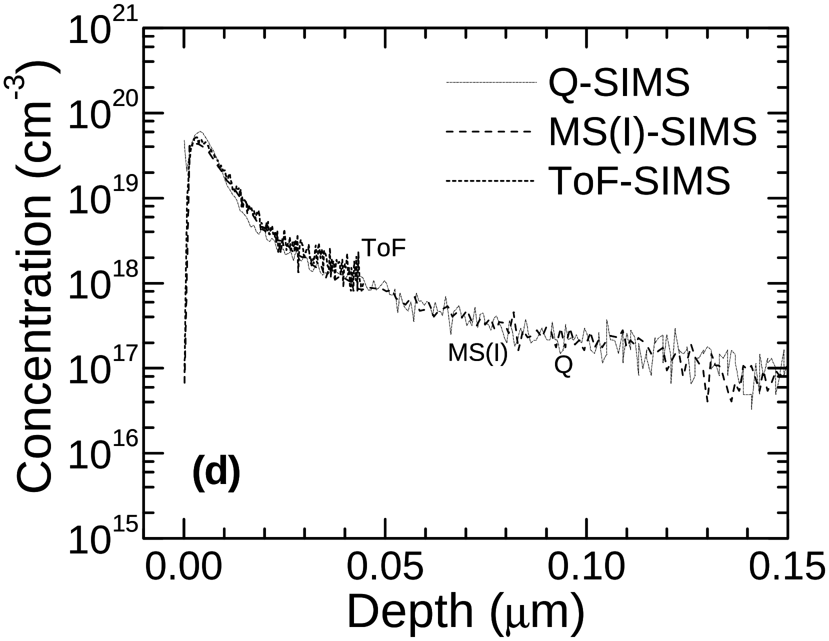

Fig. 7.11 Comparison of SIMS (Q, MS and ToF) for As (d) 5keV 5×10^{13} atoms/cm^2 45° tilt and 45° rotation

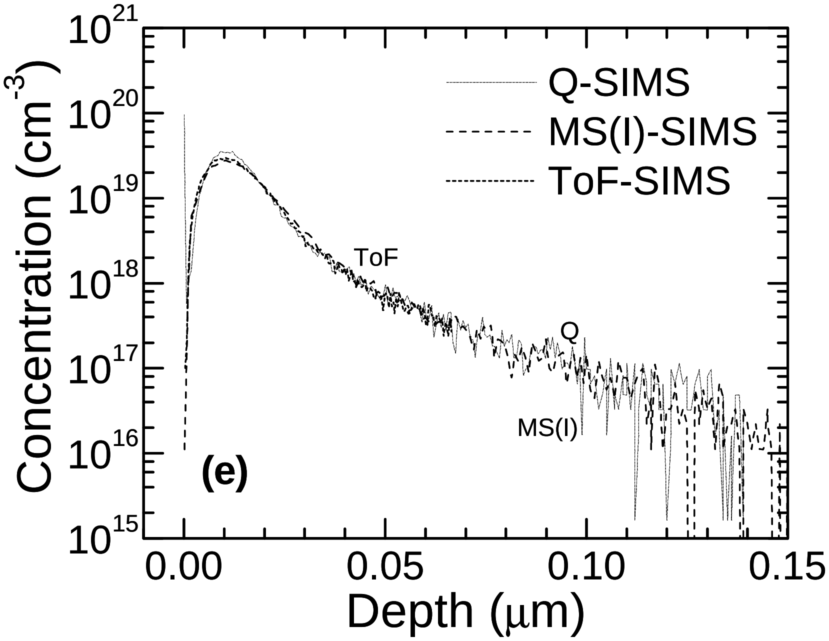

Fig. 7.11 Comparison of SIMS (Q, MS and ToF) for As (e) 10keV 5×10^{13} atoms/cm^2 0° tilt and 0° rotation

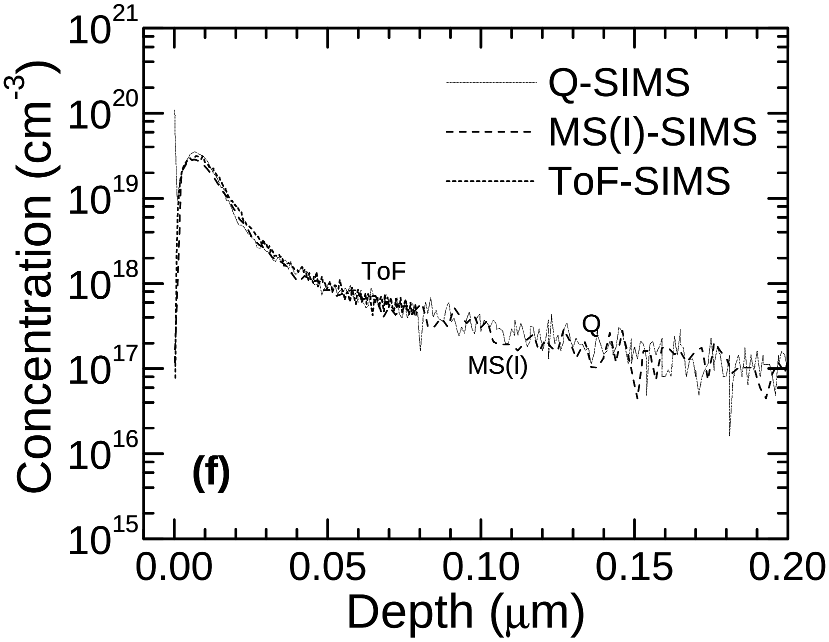

Fig. 7.11 Comparison of SIMS (Q, MS and ToF) for As (f) 10keV 5×10^{13} atoms/cm^2 45° tilt and 45° rotation

Three energies are investigated for As: 2 keV, 5 keV and 10keV at tilt/twist angles of 0°/0° and 45°/45°. The following observations can be made from Fig. 7.11.

1. At low implant energies, the discrepancy among the range profiles obtained by the three mass analyzers is most significant, especially for normal implants. For the 2 keV profiles (a), the difference amounts to almost an order of magnitude.
2. For all cases, Q-SIMS shows the least spreading, while ToF and MS(I)-SIMS shows different degrees of spreading depending on the implant conditions. Broadening of the profile during sputtering is undesirable yet inevitable during SIMS measurement since momentum transfer by the primary ions pushes the dopant and target atoms towards the substrate. While such a phenomenon should be avoided within experimental constraints; it seems to be aggravated with respect to ToF and MS-SIMS for the 2 keV and 5 keV normal implants.
3. Agreement amongst the three techniques can be seen for the 2 keV and 5 keV 45°/45° implants and 10 keV implants, which are all long-ranged profiles (45° tilted profiles produce significant channeling). Like many other analytical techniques, SIMS is extremely surface sensitive. Hence, the capabilities and limitations amongst the different instruments are best elucidated by depth profiling of ultra-shallow profiles. In this case, the 2 keV and 5 keV normal implants challenge the surface sensitivity of the ToF and MS instruments.
4. ToF-SIMS data is often truncated at low concentrations. This is a major disadvantage of using static SIMS for depth profiling. While MS and Q-SIMS analyze only the dopant species, ToF-SIMS track the movements of *all* the species that are sputtered. Hence, it is extremely resource-intensive to record the profile data for all the sputtered elements. In this case, the full length of the profile can be measured but at the expense of considerable memory space.

From these observations, it can be concluded that Q-SIMS provide the most profile information, good mass resolution and least profile broadening amongst the three instruments where As is concerned. Fig. 7.12 show the SIMS profiles measuring P obtained with the same three instruments, with the inclusion of data obtained from a Cameca Wf instrument, which is an upgrade of the 6f system and is optimized for trace element depth profiling of ultra-thin structures with high sensitivity and high depth resolution.

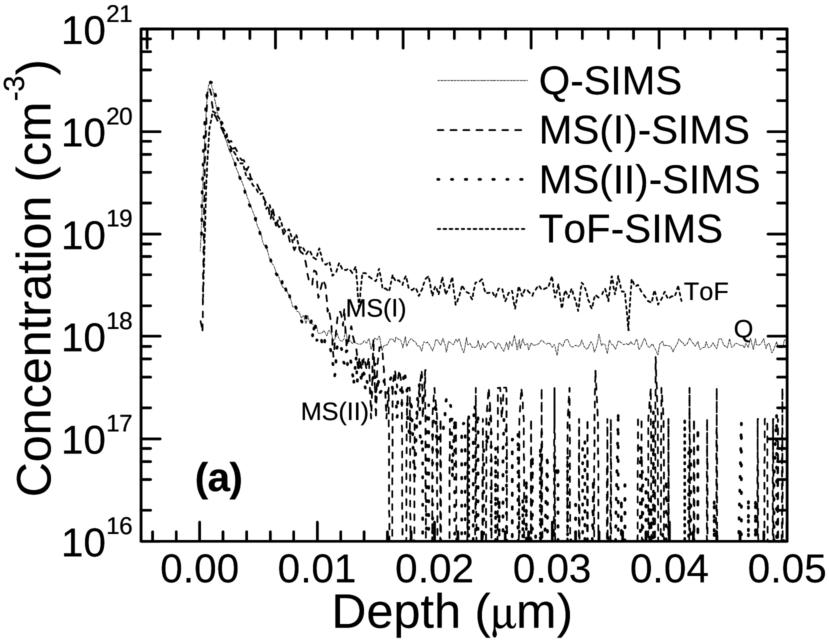

Fig. 7.12 Comparison of SIMS (Q, MS(I), MS(II) and ToF) for P (a) 1keV 5×10^{13} atoms/cm^2 0° tilt and 0° rotation

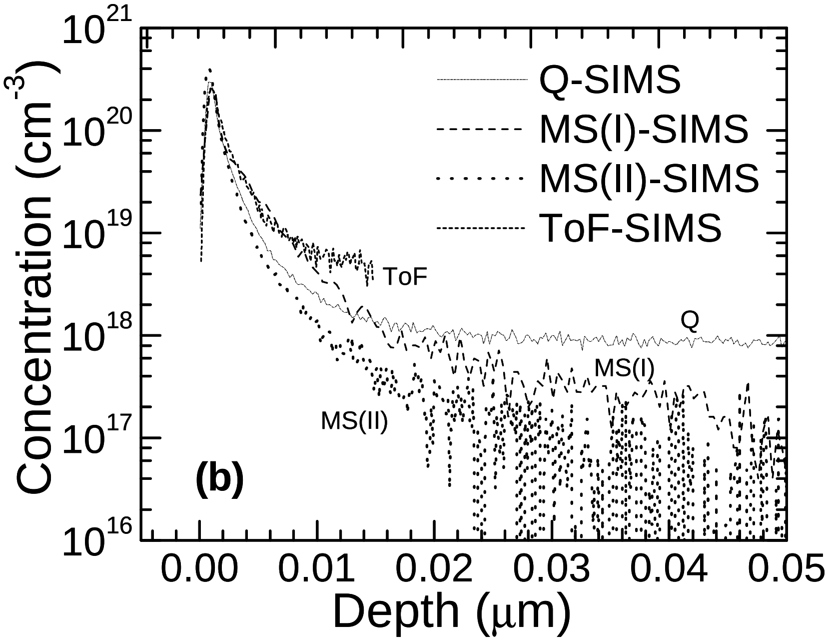

Fig. 7.12 Comparison of SIMS (Q, MS(I), MS(II) and ToF) for P (b) 1keV 5×10^{13} atoms/cm^2 45° tilt and 45° rotation

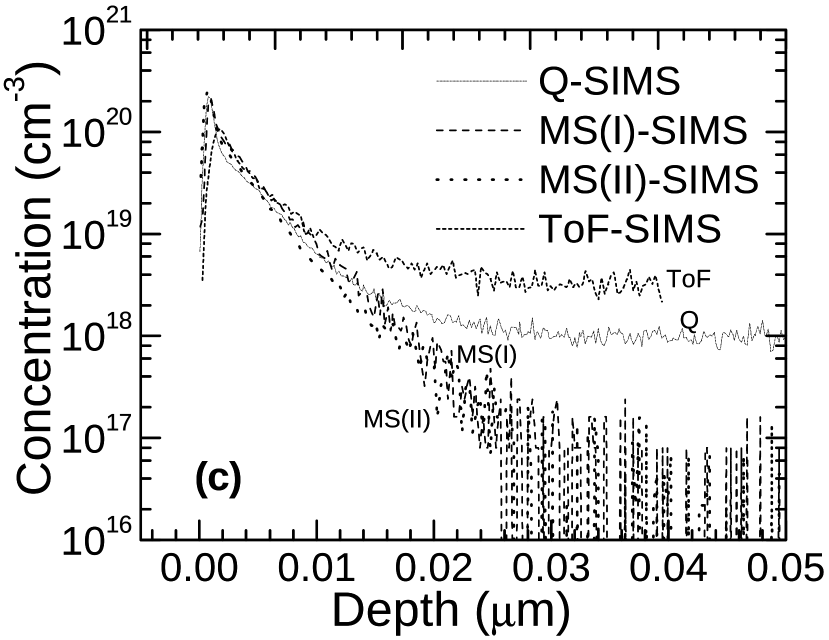

Fig. 7.12 Comparison of SIMS (Q, MS(I), MS(II) and ToF) for P (c) 2keV 5×10^{13} atoms/cm^2 0° tilt and 0° rotation

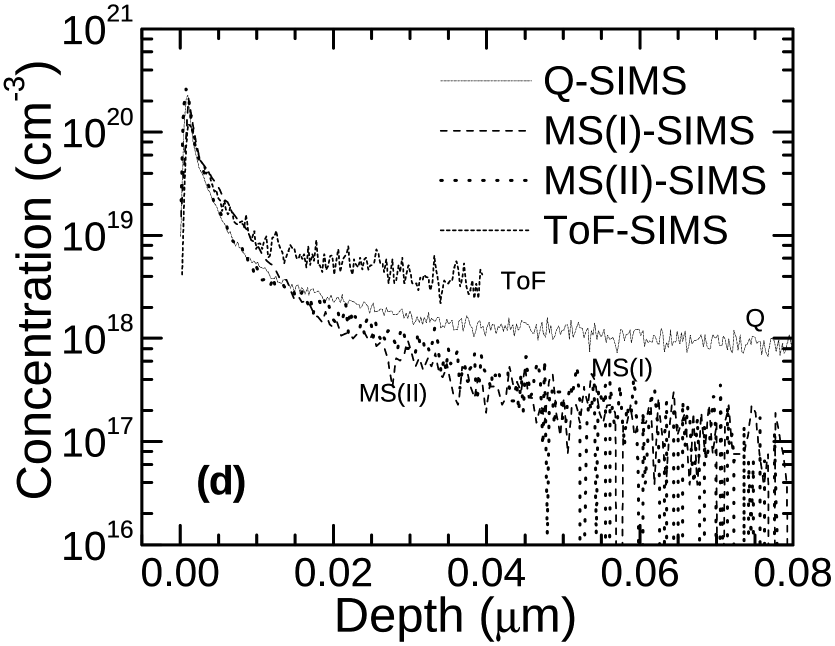

Fig. 7.12 Comparison of SIMS (Q, MS(I), MS(II) and ToF) for P (d) 2keV 5×10^{13} atoms/cm^2 45° tilt and 45° rotation

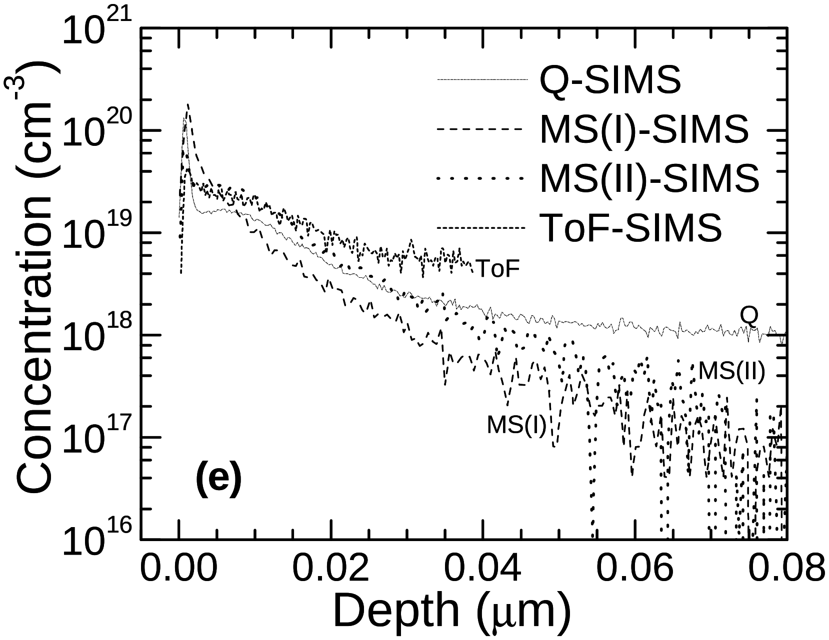

Fig. 7.12 Comparison of SIMS (Q, MS(I), MS(II) and ToF) for P (e) 5keV 5×10^{13} atoms/cm^2 0° tilt and 0° rotation

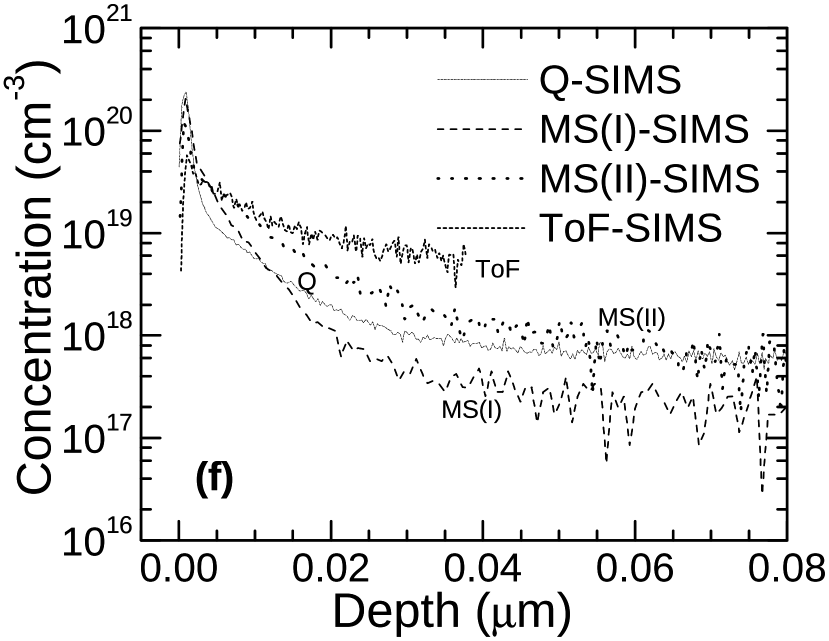

Fig. 7.12 Comparison of SIMS (Q, MS(I), MS(II) and ToF) for P (f) 5keV 5×10^{13} atoms/cm^2 45° tilt and 45° rotation

Fig. 7.11 shows that the capabilities of ToF and MS-SIMS are stretched when profiling ultra-shallow profiles. Not only is broadening significant for the 2 keV and 5 keV normal implants, ToF-SIMS becomes memory-intensive when profiling long-range profiles. Despite the spreading, MS(I)-SIMS shows slightly better depth resolution than Q-SIMS. These findings for a well-calibrated element like As, hint that ToF-SIMS may be inadequate for a problematic species like P while MS-SIMS may be able to counter the detection limit barrier faced by Q-SIMS. Based on the profiles shown in Fig. 7.12, this is indeed the case.

1. For all cases shown, ToF-SIMS was unable to fully resolve the profiles at low atomic concentrations; not only are the profiles broader than those measured from Q or MS-SIMS, ToF-SIMS could only cover two decades of concentration with a detection limit at least half an order of magnitude higher than Q-SIMS.
2. However, ToF-SIMS has an important merit. From Fig. 7.12, it is capable of accurately measuring the profile within the first few atomic layers. The use of a pulsed beam in static SIMS decreases the effect of surface mixing significantly and the surface peaks can be resolved excellently. For both Q and MS-SIMS, the surface spikes are still very pronounced and merged into the actual peak, resulting in exceedingly high surface concentrations.
3. Only MS-SIMS proved capable to resolve P at low atomic concentrations. Despite the surface peak, MS-SIMS can span four decades of concentrations, a remarkable feat considering the interference of $^{30}Si^{1}H$ present in the form of silane, a common gas unavoidably used in semiconductor processing. This was not possible with either Q or ToF-SIMS which showed much higher detection limits.
4. For most of the implants (especially the 1 keV implants), the MS(II)-SIMS coincided with the Q-SIMS within the first tens of nanometer, extending beyond the detection limit of Q-SIMS at lower concentrations. Not only is profile broadening restrained, low detection limits can be obtained with the new Cameca system. However, as energy increases, use of the Wf does not offer much improvement to the existing 6f system. In

fact for the 5 keV profiles, the 6f system produced profiles (MS(I)-SIMS) with less spreading compared to the MS(II)-SIMS.

From these observations, MS-SIMS seems to be the ideal choice for measuring P. At low energies, the Cameca Wf system is able to achieve detection limits down to 10^{17} atoms/cm^3, while the Cameca 6f seems to offer better profiles at higher energies. For As, Q-SIMS was deemed the appropriate instrument due to minimized profile broadening at low energies and low detection limits. Hence, the choice of mass analyzers depends not only on the element in concern but also analyzing conditions like primary beam energy and bombarding species. It is suffice to say that dynamic SIMS is a more appropriate technique for depth profiling compared to static SIMS which is not only a cumbersome technique in this aspect but provides poor detection limits. However, its excellent surface sensitivity is a major advantage especially for ultra-shallow profiles; ToF-SIMS may be used in combination with either MS or Q-SIMS when measuring species with significant surface artifacts like C, N and P.

7.4.2 Equipment capabilities and limitations

Based on the data shown in the previous section and the physical aspects of the technique itself, the performance of the ToF, MS and Q-SIMS instruments can be evaluated and summarized in terms of a few key analytical features:

(a) *Mass spectrometer transmission:* Since secondary ions emitted from the sample surface are collected by means of an electrical field, better collection efficiency can be obtained with a stronger electrical field. A MS mass spectrometer requires a strong extraction field for mass analysis, while Q-type mass spectrometer can achieve mass filtering of secondary ions of low kinetic energy only (i.e., collected within a weak electrical field). Hence, MS instruments are more sensitive than Q instruments. The ToF analyzer also possesses high transmission, collecting and analyzing between 20% and 60% of all secondary ions generated.

(b) *Mass resolution:* Figs. 7.11 and 7.12 have shown that the MS instrument is capable of high mass resolution, R, which is defined by M/ΔM where ΔM is the differential mass between isotopes, elements or compounds having similar masses. In applications of silicon-based semiconductor technology, SIMS instruments must be able to provide at least R=4500 in order to provide good data. It can be achieved by magnetic sector SIMS instruments but is beyond the capabilities of Q-SIMS. In the case of P using Q-SIMS, a sample introduction into the analysis chamber long before running analyses helps because the better the vacuum in the analysis chamber the lower the $^{30}Si^{1}H$ contribution onto the ^{31}P peak; but this results in a reduced analysis throughput and does not work when SiH ions are formed from H contained in the analyzed matrix, for instance, in the case of amorphous silicon analysis. For ToF-SIMS, high mass resolution can only be achieved by using short primary ion pulses: the shorter the pulse, the more precise the determination of the time it takes ions to reach the detector. For the cases investigated, ToF SIMS has the best mass resolution.

(c) *Detection limits:* Figs. 7.11 and 7.12 show that depending on the species measured, both MS-SIMS and Q-SIMS offer good performance in terms of detection limits compared to a ToF system. ToF-SIMS offers poor performance in this aspect, allowing profiles to be resolved only over two decades of concentration. The detection limit can be affected by mass spectrometer transmission, mass resolution capability or sputter rate capability.

(d) *Profile broadening:* Spreading of the profile is inevitable especially when the dopants to be measured are clustered near the surface (low energy implants). In practice, this can be minimized by using low primary beam energies, but at the expense of low sputtering yield. In the case of As, Q-SIMS offered the least spreading at low energies compared to MS or ToF-SIMS. Even for P, minimum profile broadening is observed for Q-SIMS within the first tens of nanometer despite the high detection limits. At low energies, ToF and MS(I)-SIMS show significant profile broadening which could be due to the high primary beam energy. When the primary beam energy is small (in the case of MS(II)-SIMS), less spreading is observed but at the expense of low throughput.

(e) *Acquisition time:* The acquisition time for a SIMS analysis depends on the volume of matter to be sputtered and the primary beam density. Assuming a constant primary beam density capability for both instruments, MS-SIMS is about 50 times faster than Q-SIMS to measure a concentration level with the same precision. This is because MS systems have high sputter rates while keeping a lateral resolution of just a few microns when they work in the microscope mode. In this mode, the analyzed area is defined with a lateral resolution fixed by the primary beam size. The main advantage of the microscope mode is to make independent the lateral resolution and the primary beam size. Thus, analyses can be run at high sputter rates, which require the use of a primary beam of a few tens of microns in diameter. Therefore the ratio of sputtered area to analyzed area can be adjusted to minimize analysis acquisition time. Needless to say, ToF-SIMS is the most time-consuming technique since all species are measured.

(f) *Transient surface effects:* This is the only aspect where ToF-SIMS is superior compared to MS and Q-SIMS. Strong surface sensitivity and low doses of primary ions ensure that every secondary ion comes from an undisturbed region of the surface, hence allowing true surface analysis. Thus, even for low energy P profiles, ToF-SIMS is able to resolve surface artifact spikes from the true profile peak.

In view of the capabilities and limitations of the different instruments, it seems reasonable to use simulation as a benchmark for calibrating such ultra-shallow profiles. MD has shown good accuracy in dynamically modeling the trajectories of the implanted ions, just like dynamic SIMS but without experimental artifacts. The ranges of coincidences between simulation and measurement can be combined to ascertain the true dopant profile. Based on the results shown in Fig. 7.11 and 7.12, we can conclude that ToF-SIMS is good for the first few nm, followed by Q-SIMS for the next 10-20nm, and MS-SIMS for the trailing portion. Fig. 7.13 shows an example of how simulation can be a useful tool in calibrating a SIMS profile and vice versa.

MS(II)-SIMS is used in place of MS(I)-SIMS since the profile obtained from the Cameca Wf system shows better agreement with the rest of the SIMS profiles as well as simulation.

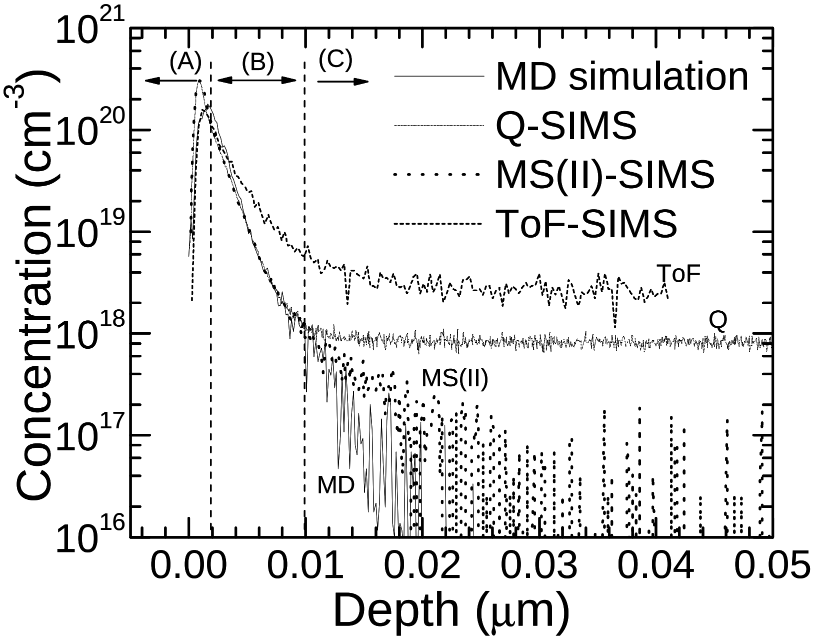

Fig. 7.13 Comparison of experimental SIMS and simulation (Q, MS(II), ToF versus MD) for P 1keV 5×10^{13} atoms/cm^2 0° tilt and 0° rotation

The solid line in Fig. 7.13 shows the simulated profile obtained from MD. From Fig. 7.13, it is clear that the simulated profile coincides with the different SIMS profiles at various depths. In region (A), both Q and MS-SIMS show large surface spikes absent in the simulated profile. ToF-SIMS, however show excellent agreement with the MD profile. In region (B), coincidence occurs between the simulated profile and both MS and Q-SIMS. Towards the trailing portion of the simulated profile in region (C), MS-SIMS is the only instrument able to detect intensity signals at low concentration levels. Although agreement between simulation and SIMS in region (C) is not perfect, MS-SIMS seems to be the only instrument amongst the three techniques capable of such detection limits, considering the aforementioned problems involved in measuring P. MD is used here since BCA is shown to be inefficient in predicting range profiles at low energies and for certain species. Use of this technique requires not only different SIMS optimized at the analyzing conditions, good simulation data is also imperative. While this is a labor-intensive method, this is the only way low-energy range profiles can be well-calibrated considering the uncertainties involved in SIMS measurement and simulation. For this work, four species have been calibrated in this manner: F, P, Ge and As. The remaining species have only been calibrated with Q-SIMS, and it is necessary to continue the work utilizing different SIMS, especially for problematic elements like C and N with high detection limits and low mass resolution.

In this section, depth profiles of implanted dopants P and As were measured with both static (ToF) and dynamic (MS and Q) SIMS. On the rising slope of the dopant concentration, ToF-SIMS was able to resolve the profile with little, if any, surface mixing effects. Dynamic SIMS, on the other hand, produced profiles with significant surface spikes, but generally showed better mass resolution and lower detection limits in the descending slope. Direct comparison of experimental SIMS profiles and profiles simulated using MD allows the refinement of SIMS data by identifying the ranges of coincidence between the measured and calculated profiles. In this way, the contribution of experimental artefacts can be reduced, and the capabilities and limitations of different instruments at various implant conditions can be ascertained. This method also permits calibration and validation of the models in the MD code; hence it is a beneficial two-way technique for both experimentalists and theorists.

CHAPTER 8 SUMMARY OF WORK

8.1 Major contributions of present work

Analytical models for ion implantation have been reviewed and their limitations in modeling range profiles for crystalline silicon substrates have been addressed (Chapters 2 and 4). Atomistic models must replace analytical models not only because the latter are inadequate to meet current predictive standards, but also because the advent of supercomputers gradually permits the use of time-consuming atomistic methods in simulating individual trajectories of the implanted ions and their recoils. Two main atomistic methods are used in this work: Monte Carlo (MC) and Molecular Dynamics (MD) methods. The physics underlying these methods and the approximations that must be made to ensure a reasonable compromise between computational time and accuracy of the eventual range profiles have been outlined in detail (Chapters 3 and 5). Amongst the various assumptions, the Binary Collision Approximation (BCA) and Recoil Ion Approximation (RIA) are two important ones that are made in MC and MD methods, respectively. The two approximations are analogous; BCA assumes that the incoming ion will interact with only one target atom at a time while RIA negates the importance of target-target interactions and calculations are based only on ion-target interactions. The primary difference lies in this: while the equations governing BCA are based on only two atoms, MD-RIA simulations are based on a system of atoms and force calculations are made between the ion and its nearest neighbors. In other words, MD is able to account for multiple interactions, unaccounted for in MC-BCA simulations. This limitation is inconsequential in the past since typical processing energies fall in the intermediate to high keV regime; ion-target interactions can be safely derived from two-body classical mechanics with little or no effect on the eventual range profiles. However, as processing energies traverse the sub-keV regime, approximating the behavior of a system of atoms with two-body equations becomes unacceptable for two reasons:

1. At low energies, the slow ion has sufficient time to interact with more than one neighbor. The multiple collisions involved cannot be trivially accounted for by equations governing binary systems.
2. The basic assumption of BCA stating that the kinetic energy of the ion is much greater than the potential energy of the atoms no longer holds at low energies.

The usefulness of MC-BCA simulations in predicting range profiles implanted in the intermediate to high energy regime have also been demonstrated (Chapter 4). Crystal-TRIM is the main BCA code used in this work and its validity is ascertained by comparisons with a large set of experimental data available from external software databases. A new ion implantation model based on the sampling calibration of profiles (SCALP) has been proposed to model profiles of any kind by a simple extractive procedure. Not only does the SCALP technique overcome many of the limitations plaguing other modeling methods, it combines the accuracy of atomistic methods and the simplicity of analytical methods. Based on extensive implant simulations from Crystal-TRIM for many species at various conditions, comprehensive implant tables have been set up with the SCALP parameters tabulated in a convenient form that can be easily assimilated and called upon in typical process simulators. Nine industrially important dopants (B, C, N, F, P, Ge, As, In and Sb) have been investigated at a non-amorphizing dose of 1×10^{13} atoms/cm^2 over the energy range 1-100 keV for tilt/twist angles of 7°/22, 0°/0°, and 45°/45°. While the SCALP method is a simple analytical technique to obtain range profiles, the effectiveness of this method is dependent on the accuracy of the simulated profiles, which have been validated with existing experimental Secondary Ion Mass Spectrometry (SIMS) data over the energy range 5-100 keV. SIMS data for implants performed in the sub-keV regime are relatively scarce, especially for certain species like C and N. Hence, the SCALP coefficients are validated only in the intermediate to high energy range. The accuracy of the coefficients in the low energy regime needs to be validated for the following reasons:

1. BCA will reach the brink of its applicability at low energies but the exact breakdown energy for different elements is not known.
2. The accuracy of the profiles is highly dependent on the nuclear and electronic stopping models used but parameters for these models, while well-calibrated for common dopants like B and As, are lacking for other species, especially in high channeling directions (eg. for tilts/twists 0°/0°, and 45°/45).
3. BCA may not be the ideal method for simulation at low energies since it can neither take multiple collisions into consideration nor can it account for attractive forces with a solely repulsive potential like the ZBL potential.
4. Lastly, experimental data for low energy range profiles are limited but necessary not only for the calibration of simulated profiles but also experimental profiles since SIMS artifacts are unavoidable when profiling ultra-shallow profiles.

The aforementioned reasons warranted an alternative method for simulating range profiles in the low energy regime. MD is the best choice; not only is this proven with a large source of experimental data, the above problems plaguing current modeling methods have been successfully countered in this work.

The theory of MD has been described; the models used in the MD code, MDRANGE and the physics underlying these models have also been elucidated in extent (Chapter 5). Three features of this code are particularly attractive, and fully counter the limitations posed by BCA. Firstly, the code allows the flexibility of using both the ZBL potential as well as an externally calculated potential, which is loaded in as a V (potential) versus r (interatomic distance) file. Hence, force calculations are not confined to repulsive potentials but first-principles potentials, like the DMOL potentials calculated in this work, can be used. This is important especially since the DMOL potentials consist of a highly repulsive region and an attractive well that is able to depict attractive forces that come into play as the initial kinetic energy of the ion lowers. Secondly, the code allows the flexibility of using not only non-local electronic stopping models like the ZBL model, but also local stopping models like the PENR model which are based on first-principles study of scattering phase shifts and cross-sections. The PENR stopping is specifically calculated for each ion-target pair in a realistic three-dimensional charge distribution. The consequence of using the PENR model is this: not only is the stopping for any dopant easily calculated, the stopping in channels where the electron density is low, is also well-described. Lastly and most importantly, the inherent ability of MD to account for multiple collisions makes it an ideal choice to describe low energy ion implantation. Comparison studies with different interatomic potentials and electronic stopping models conclude that MD when coupled with first-principles potentials and a pair-specific local electronic stopping model makes it just as robust a technique as BCA when describing impurity profiles for any species in any direction in the intermediate to high energy regime (Chapter 6). The question now lies in its predictive capability in the low energy regime, and verification of this would not have been possible without a large pool of experimental data.

A low energy experimental database is necessary not only to calibrate such low energy profiles but also to verify the BCA breakdown limits for different species which had been estimated from DFT calculations (Chapter 6). SIMS is the key experimental technique used in this work not only because it is one of the most surface sensitive techniques available, it can measure concentrations down to the ppm range, making it the most suitable method for analyzing ultra-shallow range profiles. A comprehensive set of implant conditions had been set up for nine different dopants: B, C, N, F, P, Ge, As, In and Sb with energies about the estimated BCA breakdown limits in both channeling and non-channeling directions (Chapter 7). It was found that BCA is indeed ineffective below 5 keV, not only because it often fails to describe the trailing portion of the profiles adequately in channeling directions, the profiles obtained for non-calibrated species like C, N and F differ significantly from the SIMS profiles. On the other hand, comparisons with the low energy SIMS profiles show that MD seems to offer realistic profiles albeit the longer computational time. Also, the study over the investigated energy range suggests that the BCA breakdown limits calculated in this work, though significantly different from published literature, are close to the true limits. Note that the breakdown limits are not clearly defined values but vary with species, energy and other implant conditions. In this work, the limits have been conservatively calculated from DFT and intentionally underestimated by considering the worst scenarios of channeling.

Like all other experimental techniques, SIMS is plagued by constraints and shortcomings. The accuracy of the measured profiles depend not only on the individual characteristics of the mass analyzers, but also on a large number of parameters like the primary beam energy, sputtering yield, crater depth uniformity etc. Both static (time-of-flight ToF) and dynamics (magnetic sector MS and quadrupole Q) SIMS have been utilized in this work to compare and contrast the individual capabilities and limitations of the instruments (Chapter 7). From an in-depth study of different species in the low energy regime, we can conclude that for depth profiling of ultra-shallow profiles, MS-SIMS provide the best detection limits while Q shows the least profile broadening. ToF-SIMS despite its high detection limits and large profile spreading is able to minimize surface mixing and resolve accurately the profile peaks. Combination of the attributes of the different SIMS instruments and MD simulation allows precise calibration of ultra-shallow profiles. This proposed method is a double-edged sword which serves to identify and eliminate experimental artifacts, and also to validate the models within the simulation code. While it is extremely labor-intensive, this work is significant and imperative especially since device scaling necessitates the accurate modeling of ultra-shallow source-drain junctions. In utilizing and optimizing the various experimental and simulation techniques, the following dissertation objectives have been met:

1. A robust and predictive ion implantation model had been proposed that can be easily assimilated in commercial process simulators. The SCALP model not only counters the limitations of typical ion implantation models, it combines the merits of other techniques, like the accuracy of atomistic models and simplicity of analytical models.

2. The accurate calibration of low and intermediate energy ion implantation profiles for modeling of ultra-shallow junction formation had been achieved. This was possible with the acquisition of the following information:
    a. An accurate nuclear stopping model in the form of interatomic potentials that have been specifically calculated from first-principles calculations for each ion-target pair. Typical potentials used, like the ZBL potential consist of only a highly repulsive region while these potentials consist of both repulsive and attractive regions that can account for the attractive forces that dominate at low ion kinetic energies.
    b. An accurate local electronic stopping model that is specifically calculated for each ion-target pair in a realistic three-dimensional charge distribution. There are no free parameters in this model and provides excellent results for both short- and long-ranged profiles in different crystal orientations.
    c. Reliable experimental ion implantation profile data for a wide variety of industrially important dopants in the low and intermediate energy regime at different crystal orientations. The SIMS database consists of both static and dynamic SIMS data that have been set up for the calibration and optimization for both experimental and simulated profiles.

The work presented in this thesis serves as a good starting ground for subsequent diffusion studies. Ultimately, the accuracy and credibility of the final annealed profiles is dependent on well-calibrated initial ion implantation profiles. The problem of diffusion is not new and encompasses numerous topics beyond the scope of this thesis. The following section shows supplementary work which aims to predict post-implant-pre-anneal damage distributions taking into account microscopic interactions between point defects and dopant atoms. It is by no means complete, but serves as a useful initiator for future simulation work on diffusion.

8.2 Recommendations for future work: Diffusion studies

An accurate implantation model is insufficient; reliable diffusion models are needed for the full modeling and optimization of the shrinking transistor. Ultra-shallow source and drain junctions must be accurately predicted because progress of the semiconductor industry follows Moore's law, which states that the size of a transistor on a silicon chip must be reduced by a factor of two every 18 months. With every generation, the tolerance limits for predictive standards reduce. Modelling can no longer be confined to continuum techniques but must be replaced by atomistic techniques like MC and MD methods. This is not only the case for ion implantation modelling but applies to diffusion studies as well. This thesis has addressed the use of atomistic methods in modelling ion implantation; this section attempts to utilize the profiles that have been generated for modelling of room-temperature diffusive processes.

The diffusion constant, D in Fick's law (Fick, 1855) describes only the macroscopic diffusion in thermal equilibrium while the diffusion that limits scaling of transistors today takes place in a microscopic scale far from equilibrium. As much as diffusion is undesired especially when enhanced, annealing is nevertheless needed to fulfill sheet resistance demands. Transient enhanced diffusion (TED) (Stolk et al., 1997) in silicon remains one of the greatest challenges in device scaling. TED is known to be associated with elevated levels of silicon self-interstitials from implant which agglomerate to form "rod-like defects" known as {311} defects. This anomalous diffusion is further complicated by the presence of small interstitial clusters (SIC) which contribute significantly to the creation of larger clusters by a process called Ostwald ripening (Claverie et al., 1999). A qualitative simulation study of the clustering phenomena of a hypothetically-uniform point defect distribution with and without recombination effects will be conducted. The results are then compared against a theoretical diffusion model and the evolution of the point defect clusters with time is also investigated. Spatially-variant damage distributions obtained from BCA simulations are finally employed for clustering and recombination studies.

8.2.1 Diffusion-limited reaction model and simulation method

The high concentration of point defects generated by the implantation process and their significant diffusivities result in mutual annihilation even at room temperature (RT). Further complicating the process, they form complexes by clustering with similar defect species, eventually morphing into {311} defects and dislocation loops. A simplified reaction model on the mutual annihilation, clustering and cluster recombination of the point defects is presented here. In the equations to follow, I represents mono-interstitials, V represents mono-vacancies, I_N and V_N represent interstitial and vacancy clusters of size N, while D denotes the diffusivities of a certain species indicated by the subscript and asterisks denote equilibrium quantities.

The governing rate equations in this work are given in Table 8.1, with the rate constants (Mathiot et al., 1984) using a constant capture radius (r = 0.235nm) to avoid a large number of unknown parameters. The forward clustering and recombination reactions are based on the assumption of a diffusion-limited process, and hence depend only on the diffusivities, cluster size and capture radii.

Table 8.1 Forward and backward reaction rates in diffusion model. Constants r and a represent the capture radius (r=0.235nm) and average interatomic spacing (a=0.271nm) respectively. Point defect clusters assumed immobile ($D_{IN} = D_{VN} = 0$ except when N=1)

Process	**Reaction**	**Forward Rate**	**Backward Rate**
Bulk Recombination	**I + V Û Æ**	$4\pi r\,(D_I + D_V)$	Equal to forward rate
Point Defect Clustering	**I + I_N Û I_{N+1}** **V + V_N Û V_{N+1}**	$4\pi r\,N^{1/3}(D_I + D_{IN})$ $4\pi r\,N^{1/3}(D_V + D_{VN})$	$D_I \exp(-E_N^{\,1}/kT)/a^2$ $D_V \exp(-E_N^{\,V}/kT)/a^2$
Cluster Recombination	**I_N + V Û I_{N-1}** **V_N + I Û V_{N-1}**	$4\pi r\,N^{1/3}(D_V + D_{IN})$ $4\pi r\,N^{1/3}(D_I + D_{VN})$	See Eq. (8.3) See Eq. (8.6)

Assuming only I and V to be mobile, the diffusivities of I_N and V_N are taken to be zero. The diffusivities of I and V are given by $D_I = 0.01\exp(-0.9/kT)$ and $D_V = 0.001\exp(-0.43/kT)$ respectively (Jaraiz et al., 1996). The backward rates of the clustering reactions depend on the reverse energy barrier and the binding energies of the small clusters (N<5) are taken from MD calculations (Giles, 1991), while the binding energies for the larger clusters (N>5) are taken from the work of Pelaz et al. (1997). The backward reaction rate constants for cluster recombination are derived from detailed equilibrium as shown in Eqs. (8.1) to (8.6).

I-cluster recombination: $I_N + V \Leftrightarrow I_{N-1}$ (Forward rate = k_{FI1}, Backward rate = k_{RI1})

At equilibrium, $$R_{ICR} = k_{FI1}[I_N][V^*] - k_{RI1}[I_{N-1}] \approx 0 \tag{8.1}$$

I-clustering: $I_{N-1} + I \Leftrightarrow I_N$ (Forward rate = k_{FI2}, Backward rate = k_{RI2})

At equilibrium, $$R_{IC} = k_{FI2}[I_{N-1}][I^*] - k_{RI2}[I_N] \approx 0 \tag{8.2}$$

Subst. (2) into (1), $$k_{RI1} = k_{FI1}\left[\frac{k_{FI2}}{k_{RI2}}\right][I^*][V^*] \tag{8.3}$$

V-cluster recombination: $V_N + I \Leftrightarrow V_{N-1}$ (Forward rate = k_{FV1}, Backward rate = k_{RV1})

At equilibrium, $$R_{VCR} = k_{FV1}[V_N][I^*] - k_{RV1}[V_{N-1}] \approx 0 \tag{8.4}$$

V-clustering: $V_{N-1} + V \Leftrightarrow V_N$ (Forward rate = k_{FV2}, Backward rate = k_{RV2})

At equilibrium, $$R_{VC} = k_{FV2}[V_{N-1}][V^*] - k_{RV2}[V_N] \approx 0 \tag{8.5}$$

Subst. (5) into (4), $$k_{RV1} = k_{FV1}\left[\frac{k_{FV2}}{k_{RV2}}\right][I^*][V^*] \tag{8.6}$$

The equilibrium concentrations of interstitials (I*) and vacancies (V*) have been taken from tight-binding calculations of Tang et al. (1997). Using this model, user-defined rate equations are set up in the continuum process simulator DIOS. Results are presented at RT, since complex interactions of the defects are known to occur immediately after implantation and may be dominant even at low temperatures (Privitera et al., 1996).

8.2.2 Theoretical diffusion model

The problem of the kinetics of the diffusion-limited reaction had been addressed and the solution formulated in terms of pair probability densities of the reacting particles by Waite (1957). In his work, the variation of the distribution of reactants in the diffusion-limited reaction A + B → AB with the distance of each A from each B and with time was presented. This in turn determined the rate of the reaction, since the rate depends on the number of pairs having the appropriate AB separation for reaction. For uniform initial distributions of A's with respect to B's, the final concentrations of A and B are given by Eqs. (8.7) and (8.8), where $\kappa = 4\pi r D$ and $D = D_A + D_B$

$$\frac{1}{C_A} = \frac{1}{C_B} = \frac{1}{C_A^0} + \kappa\left[1 + \frac{2r}{\sqrt{\pi D t}}\right]t \qquad C_A^0 = C_B^0 \qquad (8.7)$$

$$C_A = \frac{\left(C_A^0 - C_B^0\right)C_A^0}{C_A^0 - C_B^0 \exp\left\{-\kappa\left(C_A^0 - C_B^0\right)\left[1 + \frac{2r}{\sqrt{\pi D t}}\right]t\right\}} \qquad C_A^0 \neq C_B^0 \qquad (8.8a)$$

$$C_B = \frac{\left(C_B^0 - C_A^0\right)C_B^0}{C_B^0 - C_A^0 \exp\left\{-\kappa\left(C_B^0 - C_A^0\right)\left[1 + \frac{2r}{\sqrt{\pi D t}}\right]t\right\}} \qquad C_A^0 \neq C_B^0 \qquad (8.8b)$$

C_A^0 and C_B^0 denote the concentrations of the reactants A and B at time t = 0. D_A and D_B are the diffusivities of A and B. The capture radius r describes the critical separation between A and B for reaction to occur followed by their subsequent removal from the population of A's and B's. This theoretical diffusion model can be applied to the self-annihilation process of interstitials and vacancies where C_A and C_B now represent the instantaneous concentrations of I and V at time t. The capture radius r is the same quantity that has been defined previously (r = 0.235nm) while D is simply the sum ($D_I + D_V$). The amount of remaining damage obtained from Waite's theoretical diffusion model will be compared with that obtained from the numerical model presented earlier.

8.2.3 Spatially uniform point defect distributions

The clustering kinetics of point defects is first examined by employing hypothetically uniform distributions of I and V at 10^{20} cm^{-3}. This section of work concentrates only on the clustering of point defects without diffusion and recombination (both bulk and cluster) effects, and hence a uniform defect concentration is deemed sufficient for this qualitative study. Following the reaction rates for clustering given in Table 8.1, and assuming a maximum cluster size of N=10, the evolution of the point defect clusters with time is given in Fig. 8.1 (a) and (b) for I and V respectively.

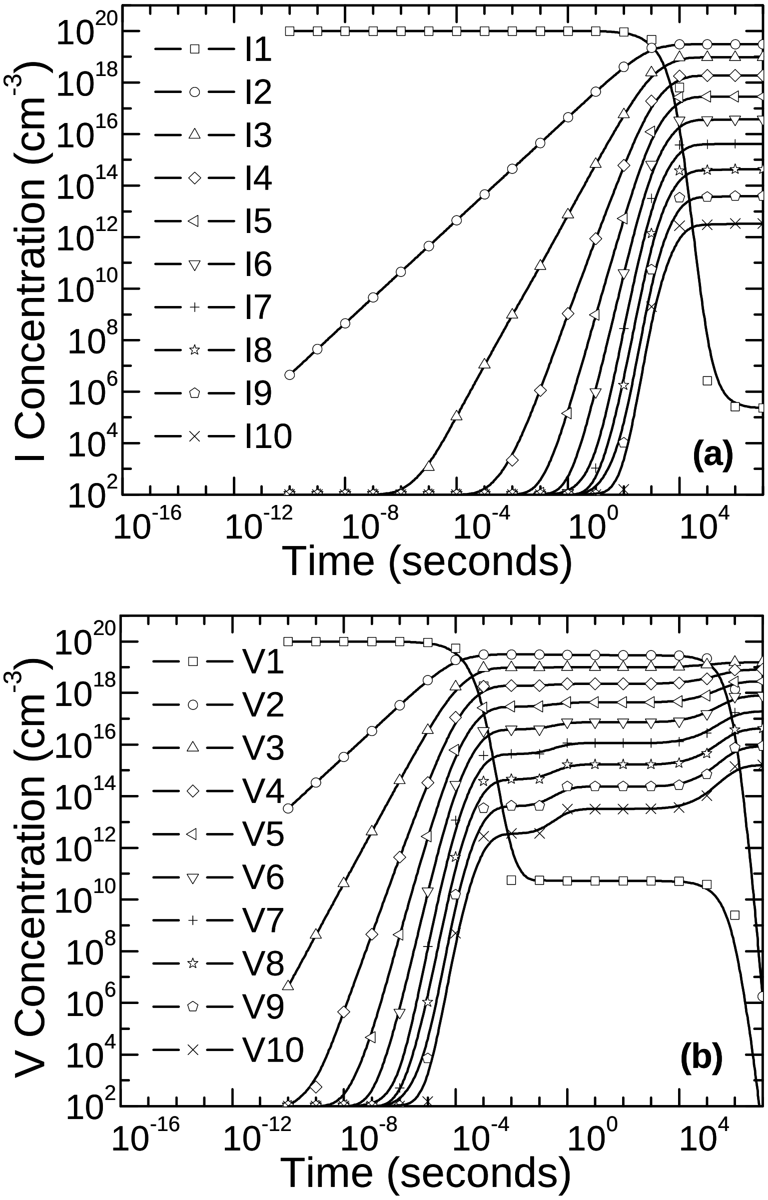

Fig. 8.1 Concentration of (a) I and (b) V in clusters ($N \leq 10$) at RT. Only clustering reactions are included. Time evolution from 10^{-10} - 10^{7}s is shown.

Starting with V at 10^{20} cm^{-3}, V_N start to form quickly. By 10^{-4}s, V_2 start to pre-dominate, followed by smaller clusters. V_2 remain metastable for about 10^{5}s (28hrs) before dissolving, and a slight increase in the concentration of larger clusters is seen. Throughout this period of time, V concentration has dropped several orders of magnitude from the initial 10^{20} cm^{-3}, reaching a meta-stable state at about 6×10^{10} cm^{-3} after 10^{-3}s, and finally reducing to negligible amounts in one day. The remaining species consists of mainly V_3 and larger sized clusters. The formation of I_N, on the other hand, takes place at a much slower rate. I_2 become predominant only after 1000s, and do not dissolve within the time frame simulated, unlike V_2. I concentration remains constant at 10^{20} cm^{-3} for a much longer period before finally depleting. V_N form more quickly and readily than I_N because of the larger diffusivity of V at RT, leading to a higher forward clustering rate. This finding is consistent with Deep Level Transient Spectroscopy (DLTS) measurements which see V_2 as the only stable defect species at RT (Privitera et al., 1996).

Expanding the system size to N=50, the same rate equations are solved for clustering at the typical annealing temperature of 850°C. The results are shown in Figs. 8.2(a) and (b) for I and V respectively after time periods of 1s and 10s. From Fig. 8.1, we know that clustering begins as early as 10^{-4}s for V while significant amounts of I_N are seen only after 1000s at RT. At 850°C, I_N are already seen after 1s, although I still dominate and only small cluster sizes (N = 20) are present. After 10s, the formation of larger I_N is seen. A particularly low concentration of I_2 clusters is observed; interstitials are mainly trapped in I_3 clusters (and as I). This can be attributed to the high binding energy (2.25eV) of the I_3 cluster (Giles, 1991), which impedes the de-clustering process. The dissolution of I_4 also contributes to the unusually high I_3 concentration since the energy barrier for I_4 dissolution (1.29eV) is smaller. V_N, on the other hand, show no such peculiarities since the binding energies increases monotonically with N. They evolve more rapidly than I_N and the behaviour of vacancies follow a Gaussian-like distribution, with mean cluster sizes of N=15 and N=25 after 1s and 10s respectively. Negligible amounts of V and small V_N (N = 10) are present. This phenomenon follows the Ostwald ripening theory where cluster density decreases while mean cluster size increases with time, consistent with the experimental findings of Eaglesham et al. (1994).

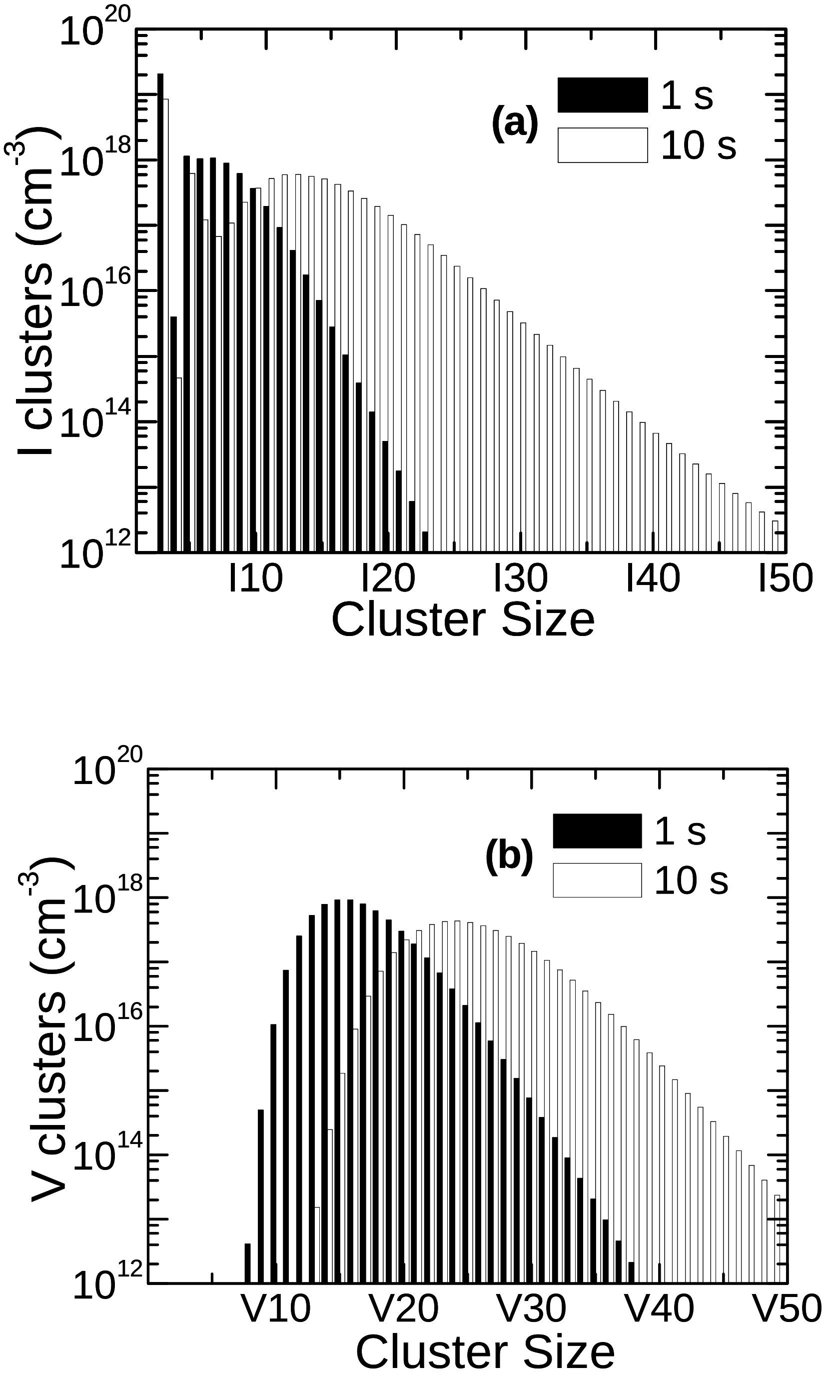

Fig. 8.2 Distribution of (a) I and (b) V in clusters (N ≤ 50) at 850°C after different time periods (1s and 10s). Only clustering reactions are included.

8.2.4 Spatially variant point defect distributions

Up till this point, we have studied only the impurity profiles obtained either from BCA or MD simulations or measured via SIMS. Besides the distribution of the implanted dopants, damage (I and V) profiles can also be obtained with Crystal-TRIM utilizing its full cascade capability. However, unlike impurity profiles, measurement of interstitials and vacancies is not a straightforward task, and simulation remains the only viable way to examine the morphology and interactions of post-implantation damage. Fig. 8.3 shows the simulated as-implanted impurity, interstitial and vacancy profiles obtained from a 10keV As implant at dose 1×10^{13} atoms/cm^2 into crystalline silicon. Also shown in Fig. 8.3 are the net excess point defect concentrations. While both I and V before recombination are nearly indistinguishable, the net I and V profiles indicate that net V's are produced close to the surface and net I is concentrated in the bulk. The widely-used +1 model (Giles, 1991) stipulates one remaining interstitial after IV annihilation leading to identical impurity and damage profiles; the net damage created in this case for As is in fact larger than that predicted by the +1 model.

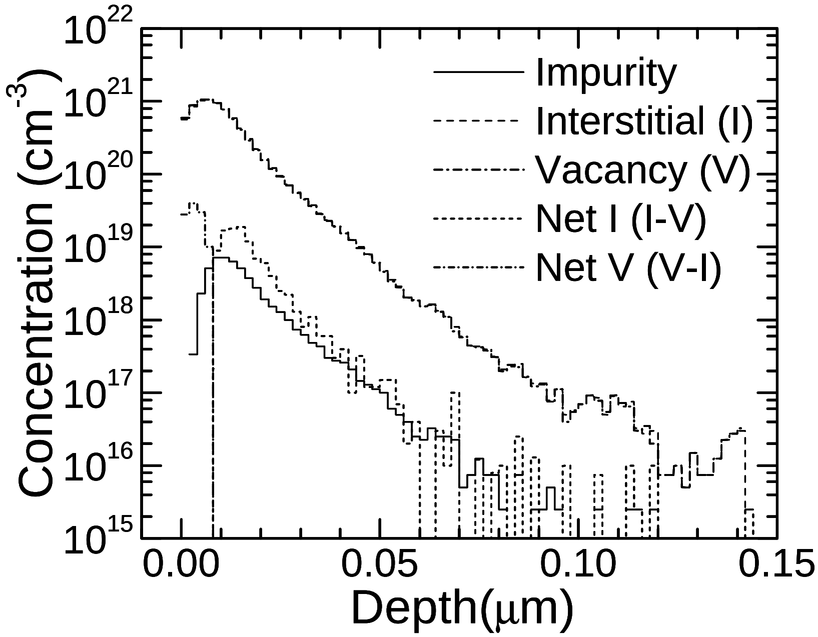

Fig. 8.3 Simulated impurity, damage (I and V) and net excess point defect concentrations for 10keV As implant at dose 1×10^{13} atoms/cm^2 into crystalline silicon

Deviations from the +1 model are often described by the effective plus factor, defined as the ratio of the amount of TED actually observed and the amount of TED according to the +1 model. The effective plus factor in this work is determined by taking the ratio of the integral over the time of the transient to that obtained from using the +1 model (Hobler et al., 2000b). The plus factor is calculated from the resulting concentration profiles obtained from DIOS for different diffusion times and also calculated for the remaining I concentration calculated from the Waite model. C_A^0 and C_B^0 in Eqs. (8.7) and (8.8) are obtained from the starting concentration profiles taken from the BCA simulations (Fig. 8.3). The depletion of the plus factor with time is shown in Fig. 8.4 using both the Waite model and our current numerical model. Both models show the same initial plus factor of ≈150 since the initial I profiles were the same for both. Simulations were conducted at RT.

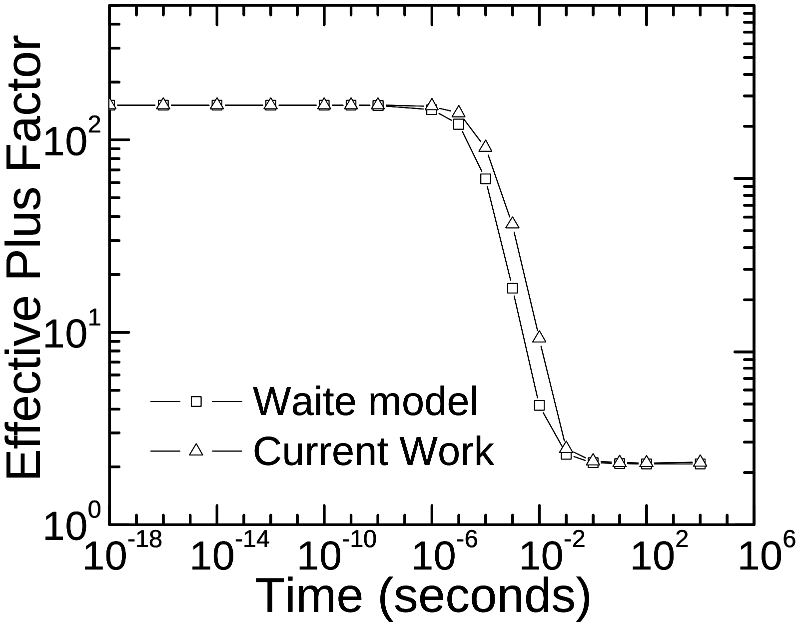

Fig. 8.4 Plus factors calculated from remaining I concentrations (As 10keV, 1×10^{13} atoms/cm^2) after different diffusion periods using the Waite model and current model

Self-annealing of I and V starts to take place after 10^{-6}s as indicated by the steady decrease in plus factor (I dose) before finally levelling at 2 after 10s. Although the two models do not agree during the transition period (10^{-6} to 10s), the eventual plus factors obtained at t=1000s by Waite's theoretical model and our proposed model are nearly identical. Thus, assuming only bulk recombination to take place without clustering effects, the remaining I is almost twice that obtained from the +1 model. This finding is consistent with previous studies (Hobler et al., 2000b) which found a plus factor of approximately 2 for As in the same energy regime. Such deviations from +1 model have been known to exist for heavy ions (Pelaz et al., 1998) and low doses (Packan et al., 1990). The inclusion of diffusion, clustering and cluster recombination effects leads to the results shown in Fig. 8.5.

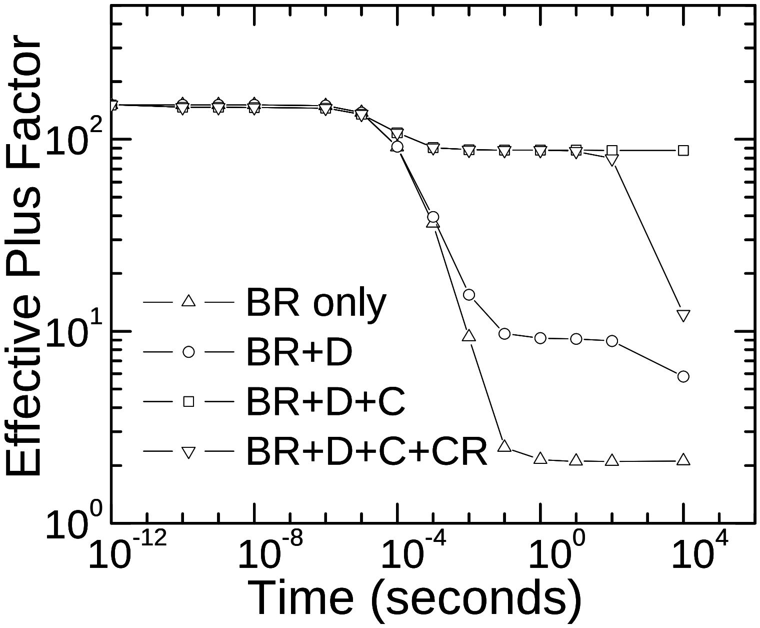

Fig. 8.5 Plus factors calculated from remaining I concentrations (As 10keV, 1×10^{13} atoms/cm^2) after different diffusion periods using current model. BR: Bulk Recombination; D: Diffusion of I and V; C: Clustering; CR: Cluster Recombination

When I is allowed to diffuse, the plus factor initially decreases, reaches a plateau after 0.01s, and finally decreases to a value which is much higher than that obtained without diffusion effects. The initial portion is identical to that without diffusion and represents the bulk recombination of I and V. During this period, out-diffusion of V takes place since it is the faster diffusing species, leaving behind the slower diffusing I. When the V's have diffused away from the region, it is followed by a plateau region where I remains almost constant since they are too slow in diffusing to the surface and are unable to recombine with the depleted V's. The final decrease results from eventual I out-diffusion. Considering bulk recombination together with clustering, about 42% of all point defects are annihilated in 10^{-3}s, and the remaining I stay trapped in clusters, resulting in a large final plus factor. When the clusters are allowed to recombine, further annihilation occurs between I_N and V after 10s. Dissolution of I_N results in a rapid drop in the plus factor and gives an eventual plus factor that is much lower than that obtained neglecting cluster recombination. Within the simulated time frame, the point defect clusters are not completely dissolved. Although the above study is confined only to a particular case for As, similar investigations have been conducted on different species at different conditions. It can be concluded that the effective plus factor is not only a function of time and temperature; it depends significantly on point defect clustering and recombination processes. It should also be noted that the maximum cluster size that can be simulated in this study is 50 due to inherent limitations of the simulator, but while the results vary numerically with different cluster sizes, the variation is not more than 10% and any increase in cluster size beyond 50 would be computationally exhaustive and unproductive.

The simplified diffusion model presented here takes into account the bulk recombination, clustering and cluster recombination of point defects (interstitials and vacancies) formed immediately after implantation and during the initial stages of annealing. When only the clustering model is applied to hypothetically uniform point defect distributions at RT, the point defect clusters evolve in a way that follows the Ostwald ripening theory, which sees larger clusters forming at the expense of smaller ones. The vacancy clusters show an increase in cluster size with time while interstitials are mainly trapped in I_3 clusters. These microscopic point defect clusters are important precursors to {311} defects and dislocation loops which directly influence TED. The model was also applied to spatially variant damage concentrations obtained from atomistic BCA simulations. The fast annihilation of intrinsic point defects as predicted by the current model is in good agreement with Waite's theoretical diffusion-limited model which predicts the same plus factor. Inclusion of clustering and cluster recombination effects leads to much lower effective plus factors and should be considered for accurate modeling of point-defect mediated TED.

CHAPTER 9 CONCLUSIONS

This dissertation has brought a more comprehensive understanding on the characterization methodologies for ultra-shallow geometries, source-drain junctions and low dopant levels. Ion implantation is and will remain the most widely used technique for introducing dopants into silicon substrates in integrated circuit manufacturing; it is no longer sufficient to adhere to current process recipes and continuum simulation techniques with device miniaturization. The major contributions of this work have been reviewed. This dissertation has not only presented a new implantation model which can be easily assimilated into process simulators, it has been shown that this model counters many of the limitation plaguing common analytical techniques. Additionally, it combines the accuracy of atomistic methods with the simplicity of analytical techniques. The capabilities and limitations of the two atomistic methods, BCA and MD under different implant conditions have been discussed and ascertained. It can be concluded that BCA retains well its predictive capabilities in the intermediate to high energy regime. However, as energy traverses the sub-keV regime, it becomes inadequate to describe range profiles, especially in channeling directions and for non-calibrated species. On the other hand, MD offers a time-effective yet accurate solution for the modeling of ultra-shallow profiles. The use of a flexible MD code allows the use of interatomic potentials calculated from DFT and a local electronic stopping model that has proven to be robust even in large channeling orientations. With pair-specific potentials and electronic stopping parameters, MD proves to be a suitable candidate for ultra-shallow profile modeling.

For the first time, a comprehensive low energy SIMS database has been set up which contains experimental profiles for a large number of industrially important dopants at different implant conditions. The species covered include B, C, N, F, P, Ge, As, In and Sb. While a few in this list may not yet possess immediate applications in the semiconductor industry, species like C and N are already intensively researched upon to reduce transient enhanced diffusion and boron penetration in the gate oxide. This work is significant and imperative in the calibration of the models used in the MD code and at the same time, much insight is gained on the merits and limitations of the different SIMS instruments used today by comparisons with simulation. It is beyond the scope of this work to investigate all Group III and V dopants at different implant conditions; work should continue to ensure that the round-robin SIMS study extend to more species at optimized analyzing conditions (eg. by varying the bombarding species, primary beam energy, incidence angle). The experimental and simulation database represents a useful and comprehensive tool both for the Technology Computer Aided Design (TCAD) field and for the SIMS arena. This work also serves as an important initiator to future studies which could extend to amorphizing doses or various temperature annealing conditions necessary for subsequent diffusion studies. Based on the accurate and well-calibrated low energy implant profiles obtained from this work and preliminary diffusion studies based on a simple diffusion model, much remains to be elucidated on the microscopic interactions between dopants and point defects, and the effect of such interactions on TED. Only with the precise calibration of implantation profiles in the manner of which is proposed, will subsequent implantation and diffusion studies be meaningful and productive.

REFERENCES (in alphabetical order)

(Allen et al., 1987) Allen, M.P. and D. J. Tildesley. Computer simulation of liquids, Oxford: Clarendon Press. 1987.

(Aoki, 2000) Aoki, T. Molecular Dynamics Simulation of cluster ion impact on solid surfaces. Ph.D Thesis, Kyoto University. 2000.

(Arias et al., 1995) Arias, J., M. Jaraiz, L. Pelaz, L.A. Bailon and J. Barbolla. Low energy ion implantation simulation using a modified binary collision approximation code. Nucl. Instrum. Meth. B, 102, pp. 228-231. 1995.

(Arista, 2002) Arista, N.R. Energy loss of heavy ions in solids: non-linear calculations for slow and swift ions. Nucl. Instrum. Meth. B, 195, pp. 91–105. 2002.

(Azziz et al., 1985) Azziz, N., K.W. Brannon and G.R. Srinivasan. Electronic stopping power for low energy ions. Mat. Res. Soc. Symp. Proc., 45, pp. 71-79. 1985.

(Azziz et al., 1987) Azziz, N., K.W. Brannon and G.R. Srinivasan. Impact parameter dependent electron energy losses. Phys. Stat. Sol. b, 142, pp. 35-42. 1987.

(Balamurugan et al., 1998)
Balamurugan, G., B.J. Obradovic, G. Wang, Y. Chen and A.F. Tasch. New analytic models and efficient parameter extraction for computationally efficient 1-D and 2-D ion implantation modeling. Technical Digest of IEEE, IEDM 1998, pp. 517-520. 1998.

(Beardmore et al., 1998)Beardmore, K.M. and N. Gronbech-Jensen. Effiicient molecular dynamics scheme for the calculation of dopant profiles due to ion implantation. Phys. Rev. E, 57, pp. 7278-7287. 1998.

(Beeler et al., 1963) Beeler, J.R and D.G. Besco. Range and damage effects of tunnel trajectories in a Wurtzite structure. J. Appl. Phys., 34, pp. 2873-2878. 1963.

(Benninghoven et al., 1987)
Benninghoven, A., F. G. Rudenauer and H.W. Werner. Secondary Ion Mass Spectrometry: Basic Concepts, Instrumental Aspects, Applications, and Trends. New York: Wiley. 1987.

(Bethe, 1928)	Bethe, H. Theorie der Beugung von Elektronen in Kristallen, Ann. Phys., 87, pp. 55-128. 1928.
(Bethe, 1930)	Bethe, H. Zur Theorie des Durchgangs schneller Korpuskularstrahlen durch Materie. Ann. Phys., 5, pp. 324–400. 1930.
(Bichsel, 1972)	Bichsel, H. American Institute of Physics Handbook. pp. 8-142, New York: McGraw-Hill. 1972.
(Biersack et al., 1980)	Biersack, J.P. and L.G. Haggmark. A Monte Carlo computer program for the transport of energetic ions in amorphous targets. Nucl. Instrum. Meth., 174, pp. 257-269. 1980.
(Biersack et al., 1991)	Biersack, J.P., E. Steinbauer and P. Bauer. A particularly fast TRIM version for ion backscattering and high energy ion implantation. Nucl. Instrum. Meth. B, 61, pp. 77-82. 1991.
(Bloch, 1928)	Bloch, F. Über die Quantenmechanik der Elektronen in Kristallgittern, Z. Phys., 52, pp. 555-600. 1928.
(Bloch, 1933a)	Bloch, F. Zur Bremsung rasch bewegter Teilchen beim Durchgang durch Materie. Ann. Phys., 16, pp. 285–320. 1933.
(Bloch, 1933b)	Bloch, F. Bremsvermogen von Atomen mit mehreren Elektronen. Z. Phys., 81, pp. 363–376. 1933.
(Bohr, 1913a)	Bohr, N. On the theory of the decrease of velocity of moving electrified particles on passing through matter. Phil. Mag. 25, pp. 10–31. 1913.
(Bohr, 1913b)	Bohr, N. On the constitution of atoms and molecules. Phil. Mag., 26, pp. 1-25. 1913.
(Bohr, 1940)	Bohr, N. Scattering and stopping of fission fragments. Phys. Rev., 58, pp. 654-655. 1940.
(Bohr, 1941)	Bohr, N. Velocity-Range Relation for Fission Fragments. Phys. Rev., 59, pp. 270-275. 1941.
(Bohr, 1948)	Bohr, N. The penetration of atomic particles through matter. Mat. Fys. Medd. Dan. Vid. Selsk., 18, No. 8. 1948.

(Bonderup, 1967) Bonderup, E. Stopping of swift protons evaluated from statistical atomic model. Mat. Fys. Medd. Dan. Vid. Selsk., 35, pp. 1-20. 1967.

(Brandt, 1975) Brandt, W. Atomic collisions in solids. pp. 261. New York: Plenum Press. 1975.

(Brandt et al., 1982) Brandt, W. and M. Kitagawa. Effective stopping-power charges of swift ions in condensed matter. Phys. Rev. B, 25, pp. 5631–5637. 1982.

(Cai et al., 1996) Cai, D., N. Gronbech-Jensen, C.M. Snell and K.M. Beardmore. Phenomenological electronic stopping-power model for molecular dynamics and Monte Carlo simulation of ion implantation into silicon. Phys. Rev. B, 54, pp. 17147-17157. 1996.

(Cai et al. 1998) Cai, D., C.M. Snell, K.M. Beardmore and N. Gronbech-Jensen. Simulation of phosphorus implantation into silicon with a single parameter electronic stopping power model. Int. J. Mod. Phys. C, 9, pp. 459-470. 1998.

(Claverie et al., 1999) Claverie, A., L.F. Ciles, M. Omri, B. De Mauduit, G. Ben Assayag, D. Mathiot. Nucleation, growth and dissolution of extended defects in implanted Si: impact on dopant diffusion. Nucl. Instrum. Meth. B, 47, pp. 1-12. 1999.

(Clementi et al., 1974) Clementi, E. and C. Roetti. Roothaan-Hartree-Fock atomic wavefunctions: basis functions and their coefficients for ground and certain excited states of neutral and ionized Atoms, Z <= 54, Atomic Data and Nuclear Data Tables, 14, pp. 177-478. 1974.

(Cote et al., 1999) Cote, D.R., S.V. Nguyen, A.K. Stamper, D.S. Armbrust, D. Tobben, R.A. Conti and G.Y. Lee. Plasma-assisted chemical vapor deposition of dielectric thin films for ULSI semiconductor circuits. IBM J. Res. Dev., 43, pp. 5-39. 1999.

(Curie et al., 1898) Curie, P., Mme. P. Curie and G. Bémont. On a new, strongly radioactive substance contained in Pitchblende. Comptes rendus de l'Académie des Sciences, 127, pp. 1215-1217. 1898.

(Dawson, 1967) Dawson, B. The covalent bond in silicon. Proc. R. Soc. London, Ser A 298, pp. 379-444. 1967.

(Delley, 1990)	Delley, B. An all-electron numerical method for solving the local density functional for polyatomic molecules. J. Chem. Phys., 92, pp. 508-517. 1990.
(Eaglesham et al., 1994)	Eaglesham, D.J., P.A. Stolk, H. -J. Gossmann, J.M. Poate. Implantation and transient B diffusion in Si: The source of the interstitials. Appl. Phys. Lett., 65, pp. 2305-2307. 1994.
(Echenique et al. 1981)	Echenique, P.M., R.M. Nieminen and R.H. Ritchie. Density functional calculation of stopping power of an electron gas for slow ions. Solid State Comm., 37, pp. 779-781. 1981.
(Eckstein, 1991)	Eckstein, W. Computer simulation of ion-solid interactions. Berlin: Springer Press. 1991.
(Erginsoy et al., 1964)	Erginsoy, C., G.H. Vineyard and A. Englert. Dynamics of radiation damage in a body-centered cubic lattice. Phys. Rev., 133, pp. A595-A606. 1964.
(Fano, 1956)	Fano, U. Atomic Theory of Electromagnetic Interactions in Dense Materials. Phys. Rev., 103, pp. 1202–1218. 1956.
(Fermi, 1927)	Fermi, E. Un metodo statistico per la determinazione di alcune priorieta dell’atome’, Rend. Accad. Naz. Lincei, 6, pp. 602-607. 1927.
(Fermi, 1940)	Fermi, E. The ionization loss of energy in gases and in condensed materials. Phys. Rev., 57, pp. 485–493. 1940.
(Fermi et al., 1947)	Fermi, E and E. Teller. The capture of negative mesotrons in matter. Phys. Rev., 72, pp. 399-408. 1947.
(Ferrell et al., 1977)	Ferrell, T.L. and R.H. Ritchie. Energy losses by slow ions and atoms to electronic excitation in solids. Phys. Rev. B, 16, pp. 115–123. 1977.
(Fick, 1855)	Fick, A. Über Diffusion, Ann. Physik, Leipzig, 94, pp. 59-86. 1855.
(Firsov, 1953)	Firsov, O.B. Determination of forces acting between atoms with the used of the differential cross section of elastic scattering. Zh. Eksp. Teor. Fiz., 24, pp. 279-283. 1953.

(Firsov, 1959)	Firsov, O.B. A qualitative interpretation of the mean electron excitation energy in atomic collsions, Zh. Eksp. Teor. Fiz., 36, pp. 1517–1523. 1959.
(Furukawa et al., 1972)	Furukawa, S., H. Matsumura and H. Ishiwara. Theoretical considerations on lateral spread of implanted ions. Jap. J. Appl. Phys., 11, pp.134-142. 1972.
(Gades et al., 1992)	Gades, H. and H.M. Urbassek. Pair versus many-body potentials in atomic emission processes from a Cu surface. Nucl. Instrum. Meth. B, 69, pp. 232-241. 1992.
(Gartner et al., 1993)	Gartner, K., M. Nitschke and W. Eckstein. Computer simulation studies of low energy B implantation into amorphous and crystalline silicon. Nucl. Instrum. Meth. B, 83, pp. 87-94. 1993.
(Gartner et al., 1995)	Gartner, K., D. Stock , B. Weber, G. Betz, M. Hautala, G. Hobler, M. Hou, S. Sarite, W. Eckstein, J.J. Jimknez-Rodriguez, A.M.C. Perez-Martin, E.P. Andribet, V. Konoplev, A. Gras-Marti, M. Posselt, M.H. Shapiro, T.A. Tombrello, H.M. Urbassek, H. Hensel, Y. Yamamura and W. Takeuchi. Round robin computer simulation of ion transmission through crystalline layers. Nucl. Instrum. Meth. B, 102, pp. 183-197. 1995.
(Gay et al., 1964)	Gay, W.L. and D.E. Harrison. Machine simulations of collisions between a copper atom and a copper lattice. Phys. Rev., 135, pp. A1780-A1790. 1964.
(Gibson et al., 1960)	Gibson, J.B., A.N. Goland, M. Milgram and G.H. Vineyard. Dynamics of radiation damage. Phys. Rev., 120, pp. 1229-1253. 1960.
(Gibbons et al., 1973)	Gibbons, J.F. and S. Mylroie. Estimation of impurity profiles in ion-implanted amorphous targets using joined half-Gaussian distributions. Appl. Phys. Lett., 22, pp. 568-569. 1973.
(Gibbons et al., 1975)	Gibbons, J.F., W.S. Johnson and S.W. Mylroie. Projected range statistics: Semiconductors and related materials. New York: Halsted Press. 1975.
(Giles, 1991)	Giles, M.D. Transient phosphorus diffusion below the amorphization threshold. J. Electrochem. Soc., 138, pp. 1160-1165. 1991.

(Grande et al., 1998) Grande, P.L. and G. Schiwietz. Impact-parameter dependence of the electronic energy loss of fast ions. Phys. Rev. A, 58, pp. 3796–3801. 1998.

(Grande et al., 2002) Grande, P.L. and G. Schiwietz. The unitary convolution approximation for heavy ions. Nucl. Instrum. Meth. B, 195, pp. 55–63. 2002.

(Hane et al., 1990) Hane, M. and M. Fukuma. Ion implantation model considering crystal structure effects. IEEE Trans. Electron Dev., 37, pp. 1959-1963. 1990.

(Hansen et al., 1978) Hansen, N.K. and C. P. Coppens. Testing aspherical atom refinements on small molecule data sets. Acta Cryst. A, 34, pp. 909-921. 1978.

(Harrison et al., 1969) Harrison, D.E., W.L. Gay and H.M. Effron. Algorithm for the calculation of the classical equations of motion of an N-body system. J. Math. Phys., 10, pp. 1179-1184. 1969.

(Harrison et al., 1976) Harrison, D.E. and C.B. Delaplain. Computer simulation of the sputtering of clusters. J. Appl. Phys., 47, pp. 2252-2259. 1976.

(Harrison et al., 1978) Harrison, D.E., P.W. Kelly, B.J. Garrison and N. Winograd. Low energy ion impact phenomena on single crystal surfaces. Surf. Sci., 76, pp. 311-322. 1978.

(Harrison et al., 1982) Harrison, D.E. and R.P. Webb. A molecular dynamics simulation study of the influences of the lattice atom potential function upon atom ejection processes. J. Appl. Phys., 53, pp. 4193-4201. 1982.

(Hautala, 1986) Hautala, M. Channeling of B and As near the silicon (001) axis. Nucl. Instrum. Meth. B, 15, pp. 75-77. 1986.

(Hobler et al., 1987) Hobler, G., E. Langer and S. Selberherr. Two-dimensional modeling of ion implantation with spatial moments. Solid State Elec., 30, pp. 445-455. 1987.

(Hobler, 1995) Hobler, G. Monte Carlo simulation of two-dimensional dopant distributions at mask edges. Nucl. Instrum. Meth. B, 96, pp. 155-162. 1995.

(Hobler et al., 2000a) Hobler, G. and C.S. Murthy. Towards a comprehensive model of electronic stopping in amorphous and crystalline silicon. Proc. Intl. Conf. Ion Implantation Technology (IIT 2000), pp. 209-211. 2000.

(Hobler et al., 2000b) Hobler, G., L. Pelaz, C.S. Rafferty. Dose, energy and ion species dependence of the effective plus factor for transient enhanced diffusion. J. Electrochem. Soc., 147, pp. 3494-3501. 2000.

(Hobler et al., 2001) Hobler, G. and G. Betz. On the useful range of application of molecular dynamics simulations in the recoil interaction approximation. Nucl. Instrum. Meth. B, 180, pp. 203-208. 2001.

(Hofker et al., 1975) Hofker, W.K., D.P. Oosthoek, N.J. Koeman and H.A.M. De Grefte. Implantation of boron in silicon. Radiat. Eff., 24, pp. 223-317. 1975.

(Hohenberg et al., 1964) Hohenberg, P. and W. Kohn. Inhomogeneous electron gas. Phys. Rev., 136, B864-B871. 1964.

(Hubert et al., 1980) Hubert, F., A. Fleury, R. Bimbot and D. Gardes. Range and stopping power tables for 2.5-100 MeV nucleon heavy ions in solids. Ann. de Phys., 5S, pp. 3–213. 1980.

(Hubert et al., 1990) Hubert, F., R. Bimbot and H. Gauvin. Range and stopping power tables for 2.5-500 MeV nucleon heavy ions in solids. At. Data and Nucl. Data Tab., 46, pp. 1–213. 1990.

(Jahnel et al., 1981) Jahnel, F., H. Ryssel, G. Prinke, K. Hoffmann, K. Mueller, J.P. Biersack and R. Henkelmann. Description of arsenic and boron profiles implanted in SiO_2, Si_3N_4 and Si using Pearson distributions with four moments. Nucl. Instrum. Meth., 182-183, pp. 223-229. 1981.

(Jaraiz et al., 1996) Jaraiz, M, G.H. Gilmer, J.M. Poate, T. Diaz de la Rubia. Atomistic calculations of ion implantation in Si: Point defect and transient enhanced diffusion phenomena. Appl. Phys. Lett., 68, pp. 409-411. 1996.

(Jensen, 1932) Jensen, H. Die Ladungsverteilung in Ionen und die Gitterkonstante des Rubidiumbromids nach der Statistischen Methode. Z. f. Physik, 77, pp. 722-745. 1932.

(Jones et al., 1989) Jones, R.O. and O. Gunnarsson. The density functional formalism, its applications and prospects. Rev. Mod. Phys., 61, pp. 689-746. 1989.

(Karetta et al., 1992) Karetta, F. and H.M. Urbassek. Molecular dynamics simulations of bulk and surface damage production in low-energy Cu-Cu bombardment. J. Appl. Phys., 71, pp. 5410-5418. 1992.

(Keinonen et al., 1991) Keinonen, J., A. Kuronen, P. Tikkanen, H.G. Borner, J. Jolie, S. Ulbig, E.G. Kessler, R.M. Nieminen, M.J. Puska and A.P. Seitsonen. First-principles simulation of intrinsic collision cascades in KCl and NaCl to test interatomic potentials at energies between 5 and 350eV. Phys. Rev. Lett., 67, pp. 3692-3695. 1991.

(Keinonen et al., 1994) Keinonen, J., A. Kuronen, K. Nordlund, R.M. Nieminen and A.P. Seitsonen. First-principles simulation of collision cascades in Si to test pair-potentials for Si-Si interaction at 10 eV-5 keV. Nucl. Instrum. Meth. B, 88, pp. 382-386. 1994.

(Kinchin et al., 1955) Kinchin, G.H. and R.S. Pease. The displacement of atoms in solids by radiation. Rep. Prog. Phys., 18, pp. 1-51. 1955.

(Klein et al., 1990) Klein, K.M., C. Park and A. F. Tasch. Local electron concentration-dependent stopping power for Monte Carlo simulation of low-energy ion implantation in silicon. Appl. Phys. Lett., 57, pp. 2701-2703. 1990.

(Klein et al., 1992) Klein, K.M., C. Park and A. F. Tasch. Monte Carlo simulation of boron implantation into single-crystal silicon. IEEE Trans. Electron Dev., 39, pp. 1614-1621. 1992.

(Knipp et al., 1941) Knipp, J. and E. Teller. On the energy loss of heavy ions. Phys. Rev., 59, pp. 659–669. 1941.

(Kohn et al., 1965) Kohn, W. and L. J. Sham. Self-consistent equations including exchange and correlation effects. Phys. Rev., 140, pp. A1133–A1138. 1965.

(Kopaleishvili, 1995) Kopaleishvili, T. Collision Theory (A Short Course). Singapore: World Scientific. 1995.

(Kornich et al., 1998) Kornich, G.V. and G. Betz. MD simulation of atomic displacements in pure metals and metallic bilayers during low energy ion bombardment at 0 K. Nucl. Instrum. Meth. B, 143, pp. 455-472. 1998.

(Kreussler et al., 1981) Kreussler, S., C. Varelas and W. Brandt. Target dependence of effective projectile charge in stopping powers. Phys. Rev. B, 23, pp. 82-84. 1981.

(Lamb, 1940) Lamb, W.E. Passage of Uranium fission fragments through matter. Phys. Rev., 58, pp. 696–702. 1940.

(Law et al., 1988) Law, M.E., C.S. Rafferty and R. Dutton. SUPREM-IV Users Manual. Stanford University. 1988.

(Law, 1993) Law, M.E., FLOODS/FLOOPS Users Manual. University of Florida. 1993.

(Lenoble et al., 2002) Lenoble, D, P. Prod'homme, D. Beutier, C. Julien. Impact of energy contamination of ultra-low energy implants on sub-0.1-/spl mu/m CMOS device performance. Proc. Intl. Conf. Ion Implantation Technology (IIT 2002), pp. 40-43. 2002.

(Lenz, 1932) Lenz, W. Uber die Anwendbarkeit der statistischen Methode auf Ionengitter. Z. f. Physik, 77, pp. 713-721. 1932.

(Li et al., 2002) Li, D., G. Shrivastav, G. Wang, Y. Chen, L. Lin, S. Oak, A.F. Tasch and S. Banerjee. Accurate and computationally efficient analytical 1-D and 2-D ion implantation models based on Legendre polynomials. IEEE Trans. Elect. Dev., 49, pp. 1172-1182. 2002.

(Lifschitz et al., 1998) Lifschitz, A.F. and N. Arista. Velocity-dependent screening in metals. Phys. Rev. A, 57, pp. 200–207. 1998.

(Lindhard, 1954) Lindhard, J. On the properties of a gas of charged particles. Mat. Fys. Medd. Dan. Vid. Selsk., 28, pp. 1–57. 1954.

(Lindhard et al., 1961) Lindhard, J. and M. Scharff. Energy dissipation by ions in the keV region. Phys. Rev., 124, pp. 128–130. 1961.

(Lindhard et al., 1963) Lindhard, J., M. Scharff and H.E. Schiott. Range concepts and heavy ion ranges. Mat. Fys. Medd. Dan. Vid. Selsk., 33, pp. 1-42. 1963.

(Lindhard et al., 1964) Lindhard, J. and A. Winther. Stopping power of electron gas and equipartition rule. Mat. Fys. Medd. Dan. Vid. Selsk., 34, pp. 1-21. 1964.

(Lindhard et al., 1996) Lindhard, J. and A.H. Sørensen. On the relativistic theory of stopping of heavy ions. Phys. Rev. A, 53, pp. 2443–2456. 1996.

(Lorenz et al., 1995) Lorenz, J., R.J. Wierzbicki and H. Ryssel. Analytical modeling of lateral implantation profiles. Nucl. Instrum. Meth. B, 96, pp. 168-172. 1995.

(Ma et al., 1992)	Ma, T.C., Y. N. Wang and T. Cui. Numerical evaluation of the stopping power for a proton in a strongly coupled electron gas. J. Appl. Phys., 72, pp. 3838-3840. 1992.
(Mann et al., 1981)	Mann, A. and W. Brandt. Material dependence of low-velocity stopping powers. Phys. Rev. B, 24, pp. 4999-5003. 1981.
(Marques et al., 1995)	Marques, L.A., J.E. Rubio, M. Jaraiz, L. Enriquez and J. Barbolla. An improved molecular dynamics scheme for ion bombardment simulations. Nucl. Instrum. Meth. B, 102, pp. 7-11. 1995.
(Mathar et al., 1995)	Mathar, R.J. and M. Posselt. Effective charge theory for the electronic stopping of heavy ions in solids : Stripping criteria and target-electron models. Phys. Rev. B, 51, pp. 107-116. 1995.
(Mathiot et al., 1984)	Mathiot D, J.C. Pfister. Dopant diffusion in silicon: A consistent view involving nonequilibrium defects. J. Appl. Phys., 55, pp. 3518-3530. 1984.
(Maynard et al., 2001)	Maynard, G., G. Zwicknagel, C. Deutsch and K. Katsonis. Diffusion transport cross section and stopping power of swift heavy ions. Phys. Rev. A, 63, art. no. 052903, pp. 1–14. 2001.
(Maynard et al., 2002)	Maynard, G., M. Sarrazin, K. Katsonis, and K. Dimitriou. Quantum and classical stopping cross-sections of swift heavy ions derived from the evolution with time of the Wigner function. Nucl. Instrum. Meth. B, 193, pp. 20–25. 2002.
(Mazzone, 1991)	Mazzone, A.M. Interatomic potentials in silicon. Phys. Stat. Sol. (b), 165, pp. 395-400. 1991.
(Moliere, 1947)	Moliere, G. Z. Theorie der Streuung schneller geladener Teilchen I. Einzelstreuung am abgeschirmten Coulomb-Field, Z. Naturforsch, 2a, pp. 133 – 145. 1947.
(Morris et al., 1995)	Morris, S.J., S.-H. Yang, D.H. Lim, C. Park, K.M. Klein, M. Manassian and A.F. Tasch. An accurate and efficient model for boron implants through thin oxide layers into single-crystal silicon. IEEE Trans. Semicon. Manufacturing, 8, pp. 408-413. 1995
(Morris, 1997)	Morris, S.J. Electronic stopping in single-crystal silicon from a few keV to several MeV. Ph.D Thesis, The University of Texas at Austin. 1997.

(Mulvaney et al., 1989) Mulvaney, B.J., W.B. Richardson, T.L. Crandle. PEPPER - A process simulator for VLSI. IEEE Trans. Comp. Aid. Des., 8, pp. 336-349. 1989.

(Murthy et al., 1992) Murthy, C.S. and G.R. Srinivasan. Computer simulation studies of ion implantation in crystalline silicon. IEEE Trans. Electron Dev., 39, pp. 264-274. 1992.

(Murthy et al., 1996) Murthy, C.S., M. Posselt and Th. Frei. Three-dimensional modeling of low dose BF_2+ implantation into single-crystalline silicon. J. Vac. Sci. Technol. B, 14, pp. 278-282. 1996.

(Nakano et al., 1993) Nakano, A., P. Vashishta and R.K. Kalia. Parallel multiple-time-step molecular dynamics with three-body interaction. Comp. Phys. Comm., 77. pp. 303-312. 1993.

(Neufeld et al., 1955) Neufeld, J. and R.H. Ritchie. Passage of Charged Particles through Plasma. Phys. Rev., 98, pp. 1632–1642. 1955.

(Ngau et al., 2001) Ngau, J.L., P.B. Griffin and J.D. Plummer. Modeling the suppression of boron transient enhanced diffusion in silicon by substitutional carbon incorporation. J. Appl. Phys., 90, pp. 1768-1778. 2001.

(Nord et al., 2002) Nord, J., K. Nordlund and J. Keinonen. Amorphization mechanism and defect structures in ion-beam-amorphized Si, Ge and GaAs. Phys. Rev. B, 65, pp. 165329-165343. 2002.

(Nordlund 1995) Nordlund, K., Molecular dynamics simulation of ion ranges in the l-100 keV energy range. Comp. Mat. Sci., 3, pp. 448-456. 1995.

(Nordlund et al., 1997) Nordlund, K., N. Runeberg and D. Sundholm. Repulsive interatomic potentials calculated using Hartree-Fock and density functional theory methods. Nucl. Instrum. Meth., 132, pp. 45-54. 1997.

(Northcliffe, 1963) Northcliffe, L.C. Passage of heavy ions through matter. Ann. Rev. Nucl. Sci., 13, pp. 67–102. 1963.

(Northcliffe et al., 1970)Northcliffe, L.C. and R.F. Schilling. Range and stopping power tables for heavy ions. Nucl. Data Tab. A, 7, pp. 233–463. 1970

(Obradovic et al., 1999) Obradovic, B., G. Wang, Y. Chen, D. Li, C. Snell and A. F. Tasch. UT-MARLOWE Version 5.0 Manual. 1999.

(Oen et al., 1963)	Oen, O.S., D.K. Holmes and M.T. Robinson. Ranges of energetic atoms in solids. J. Appl. Phys., 34, pp. 302-312. 1963.
(Oen et al., 1976)	Oen, O.S. and M.T. Robinson. Computer simulation of the reflection of light ions from solids. Nucl. Instrum. Meth., 132, pp. 647-653. 1976.
(Packan et al., 1990)	Packan, P.A. and D. Plummer. Transient diffusion of low-concentration B in Si due to ^{29}Si implantation damage. Appl. Phys. Lett., 56, pp. 1787-1789. 1990.
(Park et al., 1990)	Park, C., K. M. Klein and A. F. Tasch. A comprehensive and computationally efficient modeling strategy for simulation of boron ion implantation into single-crystal silicon with explicit dose and implant angle dependence. Int. J. Comput. Math. Electron. Eng., 10, pp. 331–340. 1990.
(Pelaz et al., 1997)	Pelaz, L., M. Jaraiz, G.H. Gilmer, H-J. Gossmann, C.S. Rafferty, D.J. Eaglesham, J.M. Poate. B diffusion and clustering in ion implanted Si: The role of B cluster precursors. Appl. Phys. Lett., 70, pp. 2285-87. 1997.
(Pelaz et al., 1998)	Pelaz, L., G.H. Gilmer, M. Jaraiz, S.B. Herner, H.-J. Gossmann, D.J. Eaglesham, G. Hobler, C.S. Rafferty, J. Barbolla. Modeling of the ion mass effect on transient enhanced diffusion: Deviation from the "+1" model. Appl. Phys. Lett., 73, pp. 1421-1423. 1998.
(Peltola et al., 2002)	Peltola, J., K. Nordlund and J. Keinonen. Effects of damage build-up in range profiles in crystalline silicon: molecular dynamics simulations. Nucl. Instrum. Meth. B, 195, pp. 269-280. 2002.
(Peltola et al., 2003)	Peltola, J., K. Nordlund and J. Keinonen. Molecular dynamics simulation method for calculating fluence-dependent range profiles. Nucl. Instrum. Meth. B, 202, pp. 132-137. 2003.
(Posselt et al., 1992)	Posselt, M. and J.P. Biersack. Computer simulation of ion implantation into crystalline silicon. Nucl. Instrum. Meth. B, 64, pp. 706-710. 1992.
(Posselt, 1994)	Posselt, M. Crystal-TRIM and is applications to investigations on channeling effects during ion implantation. Rad. Eff. Def. Sol., 130-131, pp. 87-119. 1994.

(Posselt et al., 1995)	Posselt, M. and K.-H. Heinig. Comparison of BC and MD simulations of low-energy ion implantation. Nucl. Instrum. Meth. B, 102, pp. 236-241. 1995.
(Posselt et al., 1997)	Posselt, M., B. Schmidt, C.S. Murthy, T. Feudel and K. Suzuki. Modeling of damage accumulation during ion implantation into single-crystalline silicon. J. Electrochem. Soc., 144, pp. 1495-1504. 1997.
(Posselt et al., 2000)	Posselt, M., B. Schmidt, T. Feudal and N. Strecker. Atomistic simulation of ion implantation and its application in Si technology. Mat. Sci. Eng. B, 71, pp. 128-36. 2000.
(Potter, 1972)	Potter, D. Computational Physics. New York: Wiley. 1972.
(Privitera et al., 1996)	Privitera, V., S. Coffa, F. Priolo, K.K. Larsen, G. Mannino. Room-temperature migration and interaction of ion beam generated defects in crystalline silicon. Appl. Phys. Lett., 68, pp. 3422-3424. 1996.
(Prussin et al., 1985)	Prusssin, S., D.I. Margolese and R.N. Tauber. Formation of amorphous layers by ion implantation. J. App. Phys., 57, pp. 180-185. 1985.
(Puska et al., 1983)	Puska, M.J. and R.M. Nieminen. Atoms embedded in an electron gas: Phase shifts and cross sections. Phys. Rev. B, 27, pp. 6121-6128. 1983.
(Rapaport, 1995)	Rappaport, D.C. The art of molecular dynamics simulations. U.K.: Cambridge University Press. 1995.
(Robinson et al. 1963)	Robinson, M.T. and O.S. Oen. The channeling of energetic atoms in crystal lattices. Appl. Phys. Lett., 2, pp. 30-32. 1963.
(Robinson, 1970)	Robinson, M.T. Nuclear fission reactors. London: The British Nuclear Energy Society. 1970.
(Robinson et al., 1974)	Robinson, M.T. and I.M. Torrens. Computer simulation of atomic-displacement cascades in solids in the binary-collision approximation. Phys. Rev. B., 9, pp. 5008-5024. 1974.
(Rousseau et al., 1971)	Rousseau, C.C., W.K. Chu and D. Powers. Calculations of Stopping Cross Sections for 0.8- to 2.0-MeV Alpha Particles. Phys. Rev. A, 4, pp. 1066–1070. 1971.

(Rutherford, 1911)	Rutherford, E. The scattering of alpha and beta particles by matter and the structure of the atom. Phil. Mag., 21, pp. 669-688. 1911.
(Ryssel et al., 1980)	Ryssel, H., K. Haberger, K. Hoffmann, G. Prinke, R. Duemcke and A. Sachs. Simulation of doping processes. IEEE J. Solid State Circ., 15, pp. 549-557. 1980.
(Scheiblin et al., 2001)	Scheiblin, P., F. Roger, D. Poncet, C. Laviron, P. Holligerm F. Laugier, E. Guichard and J.P Caire. Predictive and calibrated simulation of doping profiles: Low energy As, B and BF_2 ion implantation. Model. Sim. Microsyst., pp. 390-393. 2001.
(Shapiro et al., 1985)	Shapiro, M.H., P.K. Haff, T.A. Tombrello and D.E. Harrison. Simulation of isotropic mass effects in sputtering. Nucl. Instrum. Meth. B, 12, pp. 137-145. 1985.
(Shapiro et al., 1988)	Shapiro, M.H., T.A. Tombrello and D.E. Harrison. Simulation of isotropic mass effects in sputtering II. Nucl. Instrum. Meth. B, 30, pp. 152-158. 1988.
(Shapiro et al., 1994)	Shapiro, M.H. and T.A. Tombrello. A molecular dynamics study of Cu dimer sputtering mechanisms. Nucl. Instrum. Meth. B, 84, pp. 453-464. 1994.
(Sigmund et al., 1989)	Sigmund, P., M.T. Robinson, M.I. Baskes, M. Hautala, F.Z. Cui, W. Eckstein, Y. Yamamura, S. Hosaka, T. Ishitani, V.I. Shulga, D.E. Harrison, I.R. Chakarov, D.S. Karpuzov, E. Kawatoh, R. Shimizu, S. Valkealahti, R.M. Nieminen, G. Betz, W. Husinsky, M.H. Shapiro, M. Vicanek and H.M. Urbassek. Round robin computer simulation of ejection probability in sputtering. Nucl. Instrum. Meth. B, 36, pp. 110-123. 1989.
(Sigmund et al., 2000)	Sigmund, P. and A. Schinner. Binary stopping theory for swift heavy ions. Europ. Phys. J. D, 12, pp. 425–434. 2000.
(Sigmund et al., 2002)	Sigmund, P. and A. Schinner. Binary theory of electronic stopping. Nucl. Instrum. Meth. B, 195, pp. 64-90. 2002.
(Sigmund et al., 2004)	Sigmund, P. Stopping of heavy ions. Springer Tracts in Modern Physics SMTP, 204, pp. 1–157. 2004.
(Sillanpaa et al., 1999)	Sillanpaa, J., K. Nordlund and J. Keinonen. Channeling in manufacturing sharp junctions: a molecular dynamics study. Phys. Scripta, T79, pp. 272-274. 1999.

(Sillanpaa, 2000)	Sillanpaa, J. Phenomenological model for electronic stopping of low-velocity ions in crystalline solids. Ph.D Thesis. University of Heksinki. 2000.
(Sillanpaa et al., 2000)	Sillanpaa, J., K. Nordlund and J. Keinonen. Electronic stopping of Si from a three-dimensional charge distibution. Phys. Rev. B, 62, pp. 3109-3116. 2000.
(Sillanpaa et al., 2001)	Sillanpaa, J., J. Peltola, K. Nordlund and J. Keinonen. Electronic stopping calculated using explicit phase shift factors. Phys. Rev. B, 63, pp. 134113-134117. 2001.
(Simionescu et al., 1995)	Simionescu, A., S. Herzog, G. Hobler, R. Schork, J. Lorenz, C. Tian and G. Stingeder. Modeling of electronic stopping and damage accumulation during arsenic implantation in silicon. Nucl. Instrum. Meth. B, 100, pp. 483-489. 1995.
(Steward et al., 1966)	Steward, P.G. and R. Wallace. Calculation of stopping power and range energy values for any heavy ion in nongaseous media. Technical report UCRL No. 17314, Univ. California, Berkeley. 1966.
(Stewart, 1973)	Stewart, R.F. Electron population analysis with generalized X-ray scattering factors: higher multipoles. J. Chem. Phys. 58, pp. 1668-1676, 1973.
(Stolk et al., 1997)	Stolk, P.A., H-J. Gossmann, D.J. Eaglesham, D.C. Jacobson, C.S. Rafferty, G.H. Gilmer, M. Jaraiz, J.M. Poate, H.S Luftman, T.E. Haynes. Physical mechanism of transient enhanced dopant diffusion in ion-implanted silicon. J Appl Phys., 81, pp. 6031-6050. 1997.
(Smith, 1977)	Smith, B., Ion implantations range data for silicon and germanium device technologies. U.K.: Cotswold Press Ltd. 1977.
(Smith et al., 1989)	Smith, R., D.E. Harrison and B.J. Garrison. KeV particle bombardment of semiconductors: A molecular dynamics simulation. Phys. Rev. B., 40, pp. 93-101. 1989.
(Sommerfeld, 1932)	Sommerfeld, A. Asymptotische Integration der Differentialgleichung des Thomas-Fermi'schen Atoms. Z. f. Physik, 78, pp. 238-308. 1932.
(Street et al., 1978)	Street, W.B., D. J. Tildesley and G. Saville. Multiple time step methods in molecular dynamics. Mol. Phys., 35, pp. 639-648. 1978.

(Tang et al., 1997) Tang, M., L. Colombo, J. Zhu, T. Diaz de la Rubia. Intrinsic point defects in crystalline silicon: Tight-binding molecular dynamics studies of self-diffusion, interstitial-vacancy recombination, and formation volumes. Phys. Rev. B, 55, pp. 14279-14289. 1997.

(Tasch et al., 1989) Tasch, A.F., H. Shin, C. Park, J. Alvis and S. Novak. An Improved Approach to Accurately Model Shallow B and BF_2 Implants in Silicon. J. Elec. Soc., 136, pp. 810-815. 1989.

(Thomas, 1927) Thomas, L.H. The calculation of atomic fields. Proc. Camb. Phil. Soc., 23, pp. 542-548. 1927.

(Tian, 1997) Tian, S. Monte Carlo simulation of ion implantation damage process in silicon: arsenic, phosphorous, silicon, BF_2 and boron implants. Ph.D Thesis. The University of Texas at Austin. 1997.

(Tian, 2003) Tian, S. Predictive Monte Carlo ion implantation simulator from sub-keV to above 10MeV. J. Appl. Phys., 93, pp. 5893-5904. 2003.

(Utsumi et al., 1982) Utsumi, K. and S. Ichimaru. Dielectric formulation of strongly coupled electron liquids at metallic densities. VI. Analytic expression for the local-field correction. Phys. Rev. A, 26, pp. 603–610. 1982.

(Verlet, 1967) Verlet, L. Computer “experiments” on classical fluids: Thermodynamical properties of Lennard-Jones Molecules. Phys. Rev., 159, pp. 93-103. 1967.

(Waite, 1957) Waite, T.R. Theoretical treatment of the kinetics of diffusion-limited reactions. Phy. Rev., 107, pp. 463-470. 1957.

(Wang at el., 1990) Wang, Y.N. and T.C. Ma. Stopping power and energy-loss straggling of slow protons in a strongly coupled degenerate electron gas. Nucl. Instrum. Meth. B, 51, pp. 216-218. 1990.

(Wilson et al., 1977) Wilson, W.D., L.G. Haggmark and J.P. Biersack. Calculations of nuclear stopping, ranges, and straggling in the low-energy region. Phys. Rev. B, 15, pp. 2458–2468. 1977.

(Wilson et al., 1989) Wilson, R.G., F.A. Stevie and C.W. Magee, Secondary Ion Mass Spectrometry. New York: Wiley. 1989.

(Wilson, 1995) Wilson, R.G. SIMS quantification in Si, GaAs, and diamond – an update. Int. J. Mass Spec. Ion Proc., 143, pp. 43-49. 1995.

(Wolf et al., 1990) Wolf, S. and R.N. Tauber. Silicon Processing for the VLSI Era, Vol. 2. pp. 299. California: Lattice Press. 1990.

(Wolf et al., 2000) Wolf, S. and R.N. Tauber. Silicon Processing for the VLSI Era, Vol. 1. pp. 399. California: Lattice Press. 2000.

(Yamamura et al., 1987) Yamamura, Y. and W. Takeuchi. Monocrystal sputtering by the computer simulation code ACOST. Nucl. Instrum. Meth. B, 29, pp. 461-470. 1987.

(Yang et al., 1992) Yang, S.H., S. Morris, S. Tian, K. Parab and A.F. Tasch. Monte Carlo simulation of arsenic ion implantation in (100) single-crystal silicon. IEEE Trans. Semicond. Man., 9, pp. 1-10. 1992.

(Yang et al., 1994) Yang, S.-H., S. Moms, D. Lim, and A.F. Tasch. An accurate and computationally efficient semi-empirical model for arsenic implants into single-crystal (100) silicon. J. Elec. Mater., 23, pp. 801-808. 1994.

(Yang et al., 1996) Yang, S.-H., S. Morris, S. Tian, M. Morris, K. Parab, B. Obradovic, A. Tasch and C. Snell. An accurate Monte Carlo binary collision model for BF_2 implants into (100) single-crystal silicon. Elec. Soc. Proc., 96, pp. 481-495. 1996.

(Zhu et al., 1993) Zhu, H. and R.S. Averback. An optimization scheme for molecular dynamics simulations of radiation effects. Nucl. Instrum. Meth. B, 83, pp. 334-338. 1993.

(Ziegler, 1978) Ziegler, J.F. The calculation of low energy He ion stopping powers. Nucl. Instrum. Meth. A, 149, pp. 129-135. 1978.

(Ziegler, 1980) Ziegler, J.F. The stopping and ranges of ions in matter. Handbook of stopping cross-sections for energetic ions in all elements, Vol. 5 of The Stopping and Ranges of Ions in Matter, pp. 1–432. New York: Pergamon. 1980.

(Ziegler et al., 1985) Ziegler, J.F., J.P. Biersack and U. Littmark. The Stopping and Range of Ions in Solids. pp. 109-140, New York: Pergamon Press. 1985.

(Ziegler, 1992) Zieglar JF. Handbook of Ion Implantation Technology. pp. 1-700. Amsterdam: Elsevier Science Ltd. 1992.

APPENDIX A MATHEMATICAL FORMULATION OF OTHER ELECTRONIC STOPPING MODELS

The mathematical representation of the stopping model of Ma et al. (1992) will be shown here, followed by the model presented by Tian (2003). The graphical representations of both models can be found in Chapter 3, Fig. 3.8.

In Lindhard's linear-response theory (Lindhard, 1954), the stopping power (-dE/dx) and energy-loss straggling of a proton with velocity ν moving in a spatial homogeneous electron gas is given by

$$\frac{-\mathrm{dE}}{\mathrm{dx}} = \frac{2e^2}{\left(\pi\nu^2\right)}\int_0^\infty \frac{\mathrm{dk}}{\mathrm{k}}\int_0^{\mathrm{k}\nu}\mathrm{d}\omega\,\omega\,\mathrm{Im}\left[\frac{-1}{\in\left(\mathrm{k},\omega\right)}\right] \tag{A.1}$$

where $\in$(k, ω) is the longitudinal dielectric function of the electron gas. Taking into account the strong coupling effect of exchange and correlation interaction of electron gas, $\in$(k, ω) can be expressed as (Utsumi et al., 1982)

$$\in\left(\mathrm{k},\omega\right) = \frac{1-\mathrm{P}\left(\mathrm{k},\omega\right)}{\left[1+\mathrm{G}\left(\mathrm{k}\right)\mathrm{P}\left(\mathrm{k},\omega\right)\right]} \tag{A.2}$$

where P(k, ω) is Lindhard's polarizability (Lindhard, 1954) and G(k) is the local-field correction (LFC) function to the random-phase approximation (RPA) dielectric function (in which G(k)=0), which includes the exchange-correlation interactions of electrons. A parameterized expression for G(k) has been given by Utsumi et al. (1982). Dimensionless variables had been defined:

$$\mathrm{z} = \mathrm{k}/2\mathrm{k}_\mathrm{F} \tag{A.3}$$

$$\mathrm{u} = \omega/\mathrm{k}\nu_\mathrm{F} \tag{A.4}$$

where k_F is the Fermi wave number and ν_F is the Fermi velocity given by Eqs. (A.5) and (A.6) respectively. ν_0 is the Bohr velocity with the value 2.18×10^8 cm/s.

$$\mathrm{k}_\mathrm{F} = \left(3\pi^2\mathrm{n}_0\right)^{1/3} \tag{A.5}$$

$$n_F = (k_F a_0) n_0 \tag{A.6}$$

With the dimensionless parameterization, the polarizability can be written as

$$P(k, w) = -(c^2/z^2)[f_1(z,u) + if_2(z,u)] \tag{A.7}$$

where $\chi^2 = 0.166\ r_S$. r_S is the one-electron radius and the dimensionless functions f_1 and f_2 are

$$f_1(q,u) = \frac{1}{2} + \frac{1}{8q}\left(1 - A_1^2\right)\ln\left|\frac{(A_1 + 1)}{(A_1 - 1)}\right| + \frac{1}{8q}\left(1 - B_1^2\right)\ln\left|\frac{(B_1 + 1)}{(B_1 - 1)}\right| \tag{A.8}$$

$$\begin{aligned} &f_2(q,u) = pu/2 && B_1 < 1 \\ &f_2(q,u) = p(1 - A_1)/8q && |A_1| < 1 < B_1 \\ &f_2(q,u) = 0 && |A_1| > 1 \end{aligned} \tag{A.9}$$

where $A_1 = q - u$ and $B_1 = q + u$. The stopping power in Eq. (A.1) can be reduced so that

$$\frac{-dE}{dx} = \frac{4pe^4}{mn^2} n_0 L \tag{A.10}$$

where L is the stopping number given by

$$L = \frac{6}{pc^2}\int_0^{\infty} z^3 dz \int_0^{n/n_F} uF(z,u)du \tag{A.11}$$

in terms of function F(z,u) given by

$$F(z,u) = \frac{c^2 f_2(z,u)}{\left\{z^2 + c^2[1 + G(z)]f_1(z,u)\right\}^2 + \left[c^2 G(z) f_2(z,u)\right]^2} \tag{A.12}$$

The integral shown in Eq. (A.11) can only extend over the regions in which $f_2(z,u) \neq 0$. The contributions to stopping power can be factored into two parts: the single-particle excitation (SPE) in which $f_2(z,u) \neq 0$ and the collective excitation (CE) in the electron gas in which $f_2(z,u) = 0$. For the contributions due to SPE, the stopping number can be calculated by integrating Eq. (A.11) over the SPE region. For the contributions due to CE, however, the double integral in Eq. (A.11) can be reduced to a line integral and the stopping number can be expressed by Eq. (A.13).

$$L = \frac{6}{c^2}\int_{u_c}^{n/n_F} du \left(\frac{zu}{\partial \mathrm{Re} \in (z,u)/\partial z}\right) z = z_r(u) \tag{A.13}$$

where $z_r(u)$ can be found from the dispersion equation for a given value of u

$$z^2 + c^2\left[1+G\left(u_c-1\right)\right]f\left(u_c\right)=0 \tag{A.14}$$

The lower limit u_c of the integral in Eq. (A.13) is the critical point where the CE curve merges into the SPE region in z-u plane and can be determined by

$$\left(u_c-1\right)^2 + c^2\left[1+G\left(u_c-1\right)\right]f\left(u_c\right)=0 \tag{A.15}$$

where $f\left(u_c\right)=0.5\left[1+u_c\ln\left(1-1/u_c\right)\right]$ (A.16)

For a low velocity proton ($v<v_F$), the contributions to the stopping power arise only from SPE. In this case, the polarizability P(z,u) and LFC function G(z) can be approximately written

$$P\left(z,u\right)=-\frac{c^2}{z^2}\left[\left(1-\frac{z^2}{3}\right)+\frac{ipu}{2}\right] \tag{A.17}$$

$$G\left(z\right)=4g_0z^2 \tag{A.18}$$

where parameters γ_0 is connected to the correlation energy of the electron gas. Substituting Eq.a (A.17) and (A.18) into (A.11), the stopping number for a slow proton can be obtained as (Wang et al., 1990)

$$L_{slow}=\left(\frac{n}{n_F}\right)^3\times\left\{\frac{1}{2}\left(1-\frac{bc^2}{3}\right)^{-2}\left[\ln\left(1+\frac{1}{t}\right)-\frac{1}{1+t}\right]\right\}\text{ for }1-\frac{bc^2}{3}\neq 0$$

$$=\left(\frac{n}{n_F}\right)^3\times\left\{\frac{1}{4c^4}\right\}\text{, otherwise} \tag{A.19}$$

where $\beta=1+12\gamma_0$ and $t=\chi^2/(1-\beta\chi^2/3)$. Assuming $\beta=1$ in Eq. (A.19), the expression will reduce to the results of Lindhard and Winther (Lindhard et al., 1964). For the high velocity proton ($v>v_F$), the effect of exchange-correlation interaction of the electron gas in the dielectric function can be neglected and the RPA dielectric theory is accurate enough in calculating the stopping power. In this case, the stopping number L, is given by

$$L_{high}=\ln\left(\frac{2mn^2}{\hbar w_p}\right)-\frac{3}{5}\left(\frac{n_F}{n}\right)^2-\left(\frac{3}{14}+\frac{c^2}{3}\right)\left(\frac{n_F}{n}\right)^4 \tag{A.20}$$

where ħ is the Plank constant and ω is the plasma oscillation frequency given by

$$\omega = \sqrt{\frac{4\pi e^2 n_0}{m}} \tag{A.21}$$

Ma et al. (1992) concluded that for low projectile energies, the effect of the exchange-correlation interaction of the electron gas enhanced the stopping power. This was attributed to the fact that for a slow proton, it can interact with many electrons in the electron gas along its path, so that the exchange-correlation interaction of the electron gas plays an important role. At high energies, results showed that the effect of exchange-correlation can be neglected.

In the work of Tian (2003), the electronic stopping is modeled by a combination of the local part of the Oen-Robinson model (Oen et al., 1976), ΔE_{el}^{NL} and the non-local part of the Lindhard-Scharff (LS) model (Lindhard et al., 1961) ΔE_{el}^{L}. For each collision, the energy loss due to electronic stopping is given by Eq. (A.22)

$$\Delta E_{el} = \Delta E_{el}^{NL} + \Delta E_{el}^{L}$$

$$\Delta E_{el}^{NL} = NLS_{el}\left[x^{NL} + x^{L}\left(1 + \frac{P_{Max}}{a}\right)\exp\left(-\frac{P_{Max}}{a}\right)\right]$$

$$\Delta E_{el}^{L} = x^{L}\,\frac{S_{el}}{2\pi a^2}\exp\left(-\frac{P}{a}\right) \tag{A.22}$$

where N and L are the atomic density of the target and the flight path length of the projectile respectively. S_{el} is the electronic stopping power in an amorphous target which will be defined later. P_{Max} is the maximum impact parameter (as defined previously in Chapter 3) which is chosen to be half of the lattice constant. In addition, the following conditions hold:

$$x^{NL} + x^{L} = 1 \text{ and } 0 \le x^{NL} \le 1,\, 0 \le x^{L} \le 1 \tag{A.23}$$

In order to obtain the best fit to the experimental data, x^{NL} is assumed to be a function of energy, which takes the form

$$x^{NL} = \beta \varepsilon^{q} \tag{A.24}$$

A dimensionless reduced energy ε is used in Eq. (A.24) thus rendering both parameters β and q dimensionless. The parameter a in Eq. (A.22) is given by Eq. (A.25) where f is a parameter that depends on implant species. It has been suggested (Hobler et al., 2000) that Eq. (A.26) is a good approximation for f. However, Tian (2003) found that Eq. (A.27) gave the best fit to the extensive set of simulation data for different implant species instead.

$$a = \frac{f a_U}{0.3} \tag{A.25}$$

$$f = \frac{1.37}{Z_1^{1/3}} \tag{A.26}$$

$$f = \frac{1.45}{Z_1^{2/5}} \tag{A.27}$$

Tian (2003) attempted to extend the LS formula by empirically “damping” the high energy stopping power with special attention paid to the transition regime. The goal is to achieve the high accuracy in the technologically important region by sacrificing the extremely high energy regime (> 100MeV for boron). Hence, the extended LS formula is given by

$$S_{el} = a k_{LS} \sqrt{E_m} \left\{ \frac{1}{\left[\frac{E/E_m}{\ln\left(E/E_m + E_m/E + e - 2\right)} \right] + \left(\frac{E_m}{E} \right)^{d/2}} \right\}^{1/d} \tag{A.28}$$

where e is the base of natural logarithms and δ=1.425 is a fitting parameter. It should be noted that when $E << E_m$ and α = 1, the equation reduces to the LS formula given in Eq. (3.48).

$$S_{el}^{LS} = k_{LS} \sqrt{E_0} = \frac{1.212 Z_1^{7/6} Z_2}{\left(Z_1^{2/3} + Z_2^{2/3} \right)^{3/2} m_1^{1/2}} \sqrt{E_0} \tag{3.48}$$

However, when $E >> E_m$, $S_{el} \approx \sqrt{\ln E/E}$ which does not have the same asymptotic behavior as the Bethe-Bloch formula (Bethe, 1928) (Bloch, 1928) which approaches ln(CE)/E with C being a constant. Extensive simulations suggest that in Tian’s formulation over the energy range of interest, q can be approximated by 0.075 for all species, hence reducing the original four free parameters to only two free parameters, α and β for each different species.

APPENDIX B TABULATED DATA OF SCALP COEFFICIENTS FOR B, P, GE, AS, IN and SB

The SCALP coefficients are tabulated for the following six species over the energy range 1keV to 100keV for three different tilt/rotation angles (7°/22°, 0°/0° and 45°/45°): Boron (Atomic number 5 Atomic Mass 10.81), Phosphorous (Atomic number 15 Atomic Mass 30.97), Germanium (Atomic number 32 Atomic Mass 72.59), Arsenic (Atomic number 33 Atomic Mass 74.92), Indium (Atomic number 49 Atomic Mass 114.8) and Antimony (Atomic number 51 Atomic Mass 121.8). For this work, only one implant dose is included, 1×10^{13} atoms/cm^2. Prussin et al. (1985) derived the critical dose for amorphization by assuming that if enough energy is applied to the crystal to cause melting, an amorphous layer will be produced. The dose D_{crit} beyond which amorphization occurs is given by

$$D_{crit} = \frac{\left[10^{21}\,\mathrm{keV}/\mathrm{cm}^3\right] R_p}{E_0} \tag{B.1}$$

where E_0 is the beam energy in keV and R_p is the mean projected range in cm.

Based on Eq. (B.1), D_{crit} for the six species can be calculated, and shown in Table B.1. E_0 is taken to 100keV since this is the largest energy investigated in this study. R_p can be found easily from the simulated profiles obtained from Crystal-TRIM. To provide an over-estimate of D_{crit}, impurity profiles of 45°/45° are used since these profiles have the largest R_p compared to those of 7°/22° and 0°/0°.

Table B.1 Amorphization threshold for six different species (B, P, Ge, As, In and Sb)

Species	**D_{crit} (atoms/cm^2)**
Boron (B)	1.075×10^{15}
Phosphorous (P)	2.026×10^{14}
Germanium (Ge)	9.000×10^{13}
Arsenic (As)	6.600×10^{13}
Indium (In)	5.500×10^{13}
Antimony (Sb)	5.000×10^{13}

Hence, the coefficients given in the SCALP tables can be used for any dose as long as the amorphization threshold calculated in Table B.1 is not exceeded since below D_{crit}, the profile shape remains constant and the profiles can be linearly scaled with dose.

(a) Impurity **Table B.2 BORON** **TILT 7° ROTATION 22°**

Energy	Tdepth	C0%	C5%	C10%	C20%	C30%	C40%	C50%	C60%	C70%	C80%	C90%	C95%
1	0.03518	3.072E+18	6.591E+18	8.439E+18	8.319E+18	5.123E+18	1.612E+18	7.759E+17	2.270E+17	8.367E+16	5.571E+16	1.435E+16	7.741E+15
5	0.09957	6.904E+17	1.524E+18	2.168E+18	3.015E+18	2.139E+18	9.416E+17	4.191E+17	1.935E+17	7.585E+16	3.817E+16	8.357E+15	1.132E+16
10	0.16456	3.242E+17	7.931E+17	1.213E+18	1.912E+18	1.376E+18	6.824E+17	2.340E+17	1.010E+17	3.023E+16	1.806E+16	5.543E+15	1.848E+15
20	0.22759	1.416E+17	2.838E+17	4.308E+17	8.674E+17	1.150E+18	9.405E+17	4.006E+17	1.648E+17	5.861E+16	1.248E+16	1.354E+16	7.068E+15
40	0.35659	4.945E+16	8.763E+16	1.543E+17	3.167E+17	6.073E+17	7.972E+17	5.668E+17	1.998E+17	6.073E+16	2.473E+16	7.821E+15	2.829E+15
60	0.46191	1.808E+16	3.566E+16	5.235E+16	1.530E+17	3.109E+17	5.682E+17	6.503E+17	2.593E+17	6.407E+16	2.166E+16	8.583E+15	2.155E+15
80	0.55566	7.638E+15	1.892E+16	3.187E+16	8.663E+16	2.191E+17	3.694E+17	5.676E+17	3.336E+17	7.981E+16	1.892E+16	6.971E+15	2.320E+15
100	0.64120	6.231E+15	1.077E+16	2.044E+16	5.034E+16	1.186E+17	2.682E+17	4.914E+17	4.018E+17	9.800E+16	2.243E+16	7.975E+15	1.745E+15

(b) Interstitial

Energy	Tdepth	C0%	C5%	C10%	C20%	C30%	C40%	C50%	C60%	C70%	C80%	C90%	C95%
1	0.03874	9.235E+19	1.444E+20	1.317E+20	6.494E+19	2.233E+19	5.916E+18	1.862E+18	6.582E+17	1.523E+17	8.555E+16	1.340E+16	1.331E+16
5	0.11383	9.617E+19	1.809E+20	1.896E+20	1.066E+20	3.228E+19	1.147E+19	4.238E+18	1.390E+18	4.756E+17	8.705E+16	3.115E+16	4.222E+16
10	0.18582	1.213E+20	1.903E+20	1.878E+20	1.213E+20	4.330E+19	1.010E+19	3.184E+18	1.175E+18	2.330E+17	3.194E+16	5.543E+15	1.252E+16
20	0.26187	1.299E+20	1.602E+20	1.631E+20	1.514E+20	8.869E+19	2.647E+19	6.965E+18	1.992E+18	5.357E+17	1.416E+17	3.302E+16	1.888E+16
40	0.38581	9.317E+19	1.098E+20	1.187E+20	1.341E+20	1.266E+20	8.022E+19	2.206E+19	4.133E+18	1.137E+18	3.571E+17	6.716E+16	1.197E+16
60	0.50489	6.477E+19	7.888E+19	8.772E+19	1.053E+20	1.242E+20	9.715E+19	3.991E+19	6.735E+18	9.755E+17	3.527E+17	5.106E+16	1.540E+16
80	0.59950	5.148E+19	6.167E+19	6.841E+19	8.474E+19	1.066E+20	1.032E+20	5.210E+19	9.043E+18	1.244E+18	2.172E+17	4.659E+16	1.247E+16
100	0.68000	4.177E+19	5.034E+19	5.613E+19	6.819E+19	9.092E+19	1.077E+20	6.720E+19	1.774E+19	2.672E+18	5.304E+17	4.765E+16	9.969E+15

(c) Vacancy

Energy	Tdepth	C0%	C5%	C10%	C20%	C30%	C40%	C50%	C60%	C70%	C80%	C90%	C95%
1	0.03874	1.072E+20	1.491E+20	1.267E+20	6.288E+19	2.129E+19	5.643E+18	1.779E+18	5.969E+17	1.660E+17	7.958E+16	1.437E+16	1.227E+16
5	0.11378	9.918E+19	1.848E+20	1.877E+20	1.063E+20	3.189E+19	1.147E+19	4.213E+18	1.374E+18	4.743E+17	8.371E+16	3.203E+16	4.062E+16
10	0.18579	1.252E+20	1.903E+20	1.877E+20	1.213E+20	4.291E+19	1.010E+19	3.136E+18	1.136E+18	2.417E+17	2.912E+16	5.543E+15	1.252E+16
20	0.26188	1.338E+20	1.602E+20	1.641E+20	1.514E+20	8.840E+19	2.618E+19	6.847E+18	2.000E+18	5.407E+17	1.328E+17	3.175E+16	1.921E+16
40	0.38581	9.396E+19	1.088E+20	1.197E+20	1.341E+20	1.266E+20	8.025E+19	2.196E+19	4.104E+18	1.118E+18	3.610E+17	6.568E+16	1.197E+16
60	0.50489	6.517E+19	7.898E+19	8.782E+19	1.053E+20	1.242E+20	9.706E+19	3.971E+19	6.725E+18	9.686E+17	3.546E+17	5.195E+16	1.540E+16
80	0.59940	5.178E+19	6.170E+19	6.841E+19	8.474E+19	1.066E+20	1.033E+20	5.242E+19	9.195E+18	1.266E+18	2.221E+17	4.805E+16	1.295E+16
100	0.68000	4.197E+19	5.034E+19	5.613E+19	6.819E+19	9.092E+19	1.077E+20	6.710E+19	1.774E+19	2.672E+18	5.284E+17	4.815E+16	9.471E+15

(a) Impurity **Table B.3 BORON** **TILT 0° ROTATION 0°**

Energy	Tdepth	C0%	C5%	C10%	C20%	C30%	C40%	C50%	C60%	C70%	C80%	C90%	C95%
1	0.04694	2.159E+18	4.573E+18	5.868E+18	4.893E+18	3.036E+18	2.015E+18	1.302E+18	6.510E+17	4.136E+17	1.715E+17	4.704E+16	1.609E+16
5	0.16553	2.502E+17	6.369E+17	8.445E+17	9.988E+17	9.859E+17	8.762E+17	7.773E+17	6.260E+17	3.569E+17	1.755E+17	3.253E+16	1.041E+16
10	0.24619	6.749E+16	1.473E+17	3.275E+17	5.048E+17	5.554E+17	5.950E+17	6.600E+17	5.584E+17	4.071E+17	2.568E+17	6.370E+16	2.658E+16
20	0.35900	1.097E+16	3.092E+16	8.318E+16	2.244E+17	3.231E+17	3.551E+17	3.780E+17	4.404E+17	4.330E+17	3.211E+17	1.466E+17	3.989E+16
40	0.51976	2.497E+15	8.112E+15	2.378E+16	7.121E+16	1.778E+17	1.966E+17	2.178E+17	3.229E+17	3.786E+17	3.397E+17	2.068E+17	7.992E+16
60	0.64743	4.167E+14	2.498E+15	4.167E+15	3.708E+16	9.115E+16	1.519E+17	1.616E+17	2.289E+17	3.328E+17	3.328E+17	2.089E+17	6.706E+16
80	0.75274	3.129E+14	2.499E+15	2.809E+15	1.690E+16	5.495E+16	1.210E+17	1.330E+17	1.670E+17	2.532E+17	3.559E+17	2.060E+17	1.020E+17
100	0.86054	7.140E+14	4.760E+14	5.000E+15	1.100E+16	3.140E+16	9.600E+16	1.160E+17	1.500E+17	2.390E+17	3.390E+17	1.910E+17	7.652E+16

(b) Interstitial

Energy	Tdepth	C0%	C5%	C10%	C20%	C30%	C40%	C50%	C60%	C70%	C80%	C90%	C95%
1	0.04577	8.162E+19	9.484E+19	7.678E+19	4.691E+19	2.488E+19	1.453E+19	7.952E+18	4.203E+18	1.794E+18	6.497E+17	1.775E+17	8.482E+16
5	0.16443	4.480E+19	5.123E+19	4.905E+19	3.679E+19	2.828E+19	2.255E+19	1.394E+19	8.762E+18	4.327E+18	1.493E+18	1.857E+17	4.330E+16
10	0.24272	2.777E+19	3.225E+19	3.882E+19	3.583E+19	2.897E+19	2.459E+19	1.961E+19	1.297E+19	8.122E+18	3.205E+18	5.813E+17	1.105E+17
20	0.34995	1.636E+19	1.845E+19	2.394E+19	3.124E+19	2.729E+19	2.344E+19	2.127E+19	1.626E+19	1.129E+19	5.829E+18	2.022E+18	6.064E+17
40	0.51824	8.392E+18	9.191E+18	1.249E+19	2.135E+19	2.557E+19	2.113E+19	1.838E+19	1.729E+19	1.319E+19	7.393E+18	2.358E+18	5.954E+17
60	0.64659	5.737E+18	5.697E+18	8.915E+18	1.569E+19	2.279E+19	2.139E+19	1.710E+19	1.629E+19	1.449E+19	7.396E+18	2.618E+18	4.747E+17
80	0.75207	3.959E+18	4.449E+18	5.789E+18	1.210E+19	1.992E+19	2.220E+19	1.720E+19	1.560E+19	1.352E+19	8.968E+18	2.849E+18	9.178E+17
100	0.84216	2.930E+18	3.002E+18	4.718E+18	8.470E+18	1.580E+19	1.990E+19	1.690E+19	1.480E+19	1.400E+19	8.459E+18	3.120E+18	7.420E+17

(c) Vacancy

Energy	Tdepth	C0%	C5%	C10%	C20%	C30%	C40%	C50%	C60%	C70%	C80%	C90%	C95%
1	0.04577	1.041E+20	9.136E+19	7.435E+19	4.760E+19	2.517E+19	1.395E+19	7.864E+18	3.841E+18	1.774E+18	6.860E+17	1.563E+17	8.482E+16
5	0.16443	4.618E+19	5.142E+19	4.865E+19	3.669E+19	2.808E+19	2.215E+19	1.394E+19	8.732E+18	4.283E+18	1.473E+18	1.758E+17	3.578E+16
10	0.24243	2.827E+19	3.215E+19	3.892E+19	3.564E+19	2.887E+19	2.469E+19	1.973E+19	1.293E+19	8.053E+18	3.126E+18	5.734E+17	1.085E+17
20	0.34995	1.646E+19	1.845E+19	2.374E+19	3.133E+19	2.734E+19	2.334E+19	2.122E+19	1.626E+19	1.124E+19	5.839E+18	2.006E+18	5.924E+17
40	0.51195	8.442E+18	9.191E+18	1.249E+19	2.053E+19	2.559E+19	2.058E+19	1.830E+19	1.658E+19	1.409E+19	7.582E+18	3.207E+18	1.008E+18
60	0.64652	5.747E+18	5.707E+18	8.905E+18	1.569E+19	2.279E+19	2.139E+19	1.710E+19	1.639E+19	1.449E+19	7.366E+18	2.598E+18	4.647E+17
80	0.75205	3.969E+18	4.449E+18	5.779E+18	1.210E+19	1.991E+19	2.220E+19	1.720E+19	1.560E+19	1.353E+19	8.958E+18	2.829E+18	9.148E+17
100	0.84215	2.940E+18	2.994E+18	4.718E+18	8.482E+18	1.580E+19	1.990E+19	1.690E+19	1.480E+19	1.400E+19	8.449E+18	3.123E+18	7.350E+17

Table B.4 BORON

TILT 45° ROTATION 45°

(a) Impurity

Energy	Tdepth	C0%	C5%	C10%	C20%	C30%	C40%	C50%	C60%	C70%	C80%	C90%	C95%
1	0.05396	1.752E+18	2.791E+18	2.780E+18	1.804E+18	1.567E+18	1.640E+18	1.814E+18	1.629E+18	1.613E+18	1.803E+18	8.715E+17	3.017E+17
5	0.16994	2.762E+17	4.581E+17	6.023E+17	4.995E+17	4.467E+17	4.681E+17	6.631E+17	6.504E+17	6.639E+17	7.313E+17	6.677E+17	5.047E+17
10	0.27980	7.442E+16	2.161E+17	2.917E+17	3.146E+17	2.250E+17	2.771E+17	4.289E+17	4.457E+17	5.091E+17	4.671E+17	4.267E+17	2.890E+17
20	0.44393	2.674E+16	5.756E+16	1.394E+17	1.799E+17	1.390E+17	1.710E+17	2.642E+17	3.101E+17	3.419E+17	3.359E+17	3.055E+17	2.008E+17
40	0.69401	7.871E+15	1.676E+16	4.879E+16	1.127E+17	7.737E+16	9.834E+16	1.716E+17	2.148E+17	2.444E+17	2.115E+17	1.915E+17	1.115E+17
60	0.90333	2.586E+15	1.038E+16	2.495E+16	7.768E+16	6.880E+16	7.908E+16	1.568E+17	1.797E+17	1.899E+17	2.007E+17	1.182E+17	7.319E+16
80	1.08869	2.856E+15	6.281E+15	1.675E+16	6.390E+16	5.302E+16	5.652E+16	1.228E+17	1.618E+17	1.877E+17	1.608E+17	1.018E+17	5.309E+16
100	1.26199	1.329E+15	4.667E+15	1.089E+16	5.287E+16	4.597E+16	5.907E+16	1.065E+17	1.419E+17	1.479E+17	1.349E+17	7.306E+16	3.778E+16

(b) Interstitial

Energy	Tdepth	C0%	C5%	C10%	C20%	C30%	C40%	C50%	C60%	C70%	C80%	C90%	C95%
1	0.04900	1.091E+20	6.164E+19	3.381E+19	1.525E+19	9.466E+18	7.258E+18	4.224E+18	1.897E+18	7.226E+17	2.245E+17	6.646E+16	3.446E+16
5	0.16311	4.364E+19	3.794E+19	2.971E+19	1.566E+19	1.003E+19	5.938E+18	3.420E+18	1.825E+18	6.802E+17	2.940E+17	1.001E+17	6.105E+16
10	0.26536	2.620E+19	2.665E+19	2.649E+19	1.377E+19	7.236E+18	4.583E+18	2.796E+18	1.156E+18	5.219E+17	2.151E+17	6.698E+16	3.649E+16
20	0.41998	1.700E+19	1.869E+19	2.078E+19	1.365E+19	6.283E+18	3.886E+18	1.940E+18	8.287E+17	3.723E+17	1.139E+17	5.420E+16	2.729E+16
40	0.62794	8.101E+18	1.117E+19	1.497E+19	1.417E+19	7.502E+18	3.103E+18	1.802E+18	7.452E+17	2.691E+17	1.056E+17	5.148E+16	2.511E+16
60	0.81184	5.771E+18	7.207E+18	1.027E+19	1.350E+19	6.972E+18	2.771E+18	1.492E+18	7.236E+17	2.011E+17	8.099E+16	3.774E+16	1.847E+16
80	0.94924	4.224E+18	5.232E+18	8.487E+18	1.258E+19	6.953E+18	2.806E+18	1.323E+18	7.159E+17	2.776E+17	8.587E+16	3.025E+16	1.737E+16
100	1.05772	3.068E+18	4.218E+18	6.257E+18	1.119E+19	7.832E+18	3.048E+18	1.239E+18	5.975E+17	2.519E+17	7.376E+16	3.088E+16	1.869E+16

(c) Vacancy

Energy	Tdepth	C0%	C5%	C10%	C20%	C30%	C40%	C50%	C60%	C70%	C80%	C90%	C95%
1	0.04916	1.216E+20	6.370E+19	3.299E+19	1.519E+19	9.481E+18	7.052E+18	4.176E+18	1.797E+18	6.760E+17	1.913E+17	6.184E+16	3.942E+16
5	0.16321	4.443E+19	3.794E+19	2.960E+19	1.552E+19	1.003E+19	5.935E+18	3.391E+18	1.786E+18	6.792E+17	2.912E+17	1.006E+17	5.864E+16
10	0.26536	2.649E+19	2.665E+19	2.649E+19	1.370E+19	7.226E+18	4.570E+18	2.779E+18	1.142E+18	5.172E+17	2.120E+17	6.698E+16	3.524E+16
20	0.41998	1.710E+19	1.877E+19	2.078E+19	1.365E+19	6.243E+18	3.868E+18	1.930E+18	8.263E+17	3.702E+17	1.129E+17	5.316E+16	2.682E+16
40	0.62794	8.121E+18	1.117E+19	1.497E+19	1.417E+19	7.512E+18	3.073E+18	1.794E+18	7.383E+17	2.723E+17	1.065E+17	5.098E+16	2.495E+16
60	0.81184	5.791E+18	7.217E+18	1.027E+19	1.345E+19	6.966E+18	2.771E+18	1.492E+18	7.223E+17	2.008E+17	8.130E+16	3.734E+16	1.847E+16
80	0.94924	4.234E+18	5.222E+18	8.497E+18	1.258E+19	6.943E+18	2.796E+18	1.323E+18	7.179E+17	2.766E+17	8.417E+16	3.025E+16	1.737E+16
100	1.05786	3.068E+18	4.218E+18	6.267E+18	1.119E+19	7.806E+18	3.038E+18	1.239E+18	5.953E+17	2.515E+17	7.236E+16	3.088E+16	1.869E+16

(a) Impurity **Table B.5 PHOSPHOROUS** **TILT 7° ROTATION 22°**

Energy	Tdepth	C0%	C5%	C10%	C20%	C30%	C40%	C50%	C60%	C70%	C80%	C90%	C95%
1	0.01784	7.749E+17	6.562E+18	1.235E+19	2.109E+19	1.111E+19	3.274E+18	1.468E+18	3.133E+17	1.573E+17	2.330E+16	1.215E+16	6.575E+15
5	0.06885	4.095E+17	3.586E+18	6.595E+18	5.452E+18	1.882E+18	6.101E+17	2.391E+17	9.614E+16	3.674E+16	2.177E+16	5.543E+15	9.939E+15
10	0.08829	3.016E+17	1.588E+18	3.354E+18	4.253E+18	1.733E+18	8.653E+17	3.256E+17	1.886E+17	1.040E+17	4.629E+16	2.831E+16	2.343E+16
20	0.17040	2.408E+17	1.291E+18	2.519E+18	2.139E+18	6.642E+17	1.756E+17	7.442E+16	3.320E+16	1.748E+16	1.448E+16	4.594E+15	1.249E+15
40	0.25575	2.207E+17	5.493E+17	1.215E+18	1.490E+18	6.204E+17	2.147E+17	6.651E+16	3.725E+16	1.468E+16	7.990E+15	6.662E+15	3.326E+15
60	0.35560	1.268E+17	3.506E+17	8.330E+17	1.129E+18	5.883E+17	1.476E+17	5.428E+16	1.768E+16	7.721E+15	6.011E+15	1.818E+15	4.085E+15
80	0.39200	9.662E+16	2.208E+17	4.176E+17	9.232E+17	8.143E+17	2.828E+17	5.566E+16	2.768E+16	9.991E+15	7.060E+15	4.666E+15	4.764E+15
100	0.50453	5.746E+16	1.539E+17	3.078E+17	7.585E+17	5.796E+17	1.499E+17	3.828E+16	1.499E+16	7.495E+15	4.167E+15	3.328E+15	1.669E+15

(b) Interstitial

Energy	Tdepth	C0%	C5%	C10%	C20%	C30%	C40%	C50%	C60%	C70%	C80%	C90%	C95%
1	0.01792	1.660E+20	1.966E+20	2.273E+20	2.607E+20	1.229E+20	2.046E+19	8.860E+18	1.739E+18	8.071E+17	4.579E+16	2.340E+16	1.220E+16
5	0.06919	2.577E+20	4.777E+20	5.010E+20	2.159E+20	6.364E+19	1.882E+19	6.881E+18	2.408E+18	7.965E+17	3.034E+17	6.157E+16	8.185E+16
10	0.13177	2.986E+20	6.006E+20	5.404E+20	1.155E+20	3.330E+19	1.084E+19	3.612E+18	1.075E+18	2.847E+17	5.379E+16	6.602E+16	2.979E+16
20	0.22782	4.156E+20	6.804E+20	5.346E+20	9.681E+19	1.441E+19	4.149E+18	1.509E+18	6.885E+17	1.731E+17	6.501E+16	3.891E+16	1.473E+16
40	0.32363	5.094E+20	6.632E+20	6.238E+20	2.117E+20	3.762E+19	8.000E+18	3.116E+18	1.410E+18	5.675E+17	7.860E+16	3.725E+16	5.887E+16
60	0.47584	5.014E+20	5.989E+20	5.653E+20	1.898E+20	2.299E+19	5.653E+18	1.928E+18	1.023E+18	3.196E+17	9.848E+16	5.711E+16	4.085E+15
80	0.55570	4.496E+20	5.196E+20	5.585E+20	2.458E+20	3.950E+19	7.404E+18	1.699E+18	8.813E+17	2.521E+17	2.128E+17	5.725E+16	2.747E+15
100	0.61181	3.987E+20	4.647E+20	5.187E+20	3.598E+20	6.063E+19	1.029E+19	2.666E+18	1.219E+18	6.965E+17	1.089E+17	1.369E+17	1.859E+16

(c) Vacancy

Energy	Tdepth	C0%	C5%	C10%	C20%	C30%	C40%	C50%	C60%	C70%	C80%	C90%	C95%
1	0.01400	2.190E+20	2.245E+20	2.299E+20	2.408E+20	1.872E+20	9.385E+19	2.048E+19	1.155E+19	2.620E+18	9.318E+17	4.664E+17	2.337E+17
5	0.06918	2.747E+20	4.940E+20	5.002E+20	2.090E+20	6.151E+19	1.836E+19	6.644E+18	2.290E+18	7.498E+17	2.961E+17	6.180E+16	6.388E+16
10	0.13168	3.056E+20	6.066E+20	5.388E+20	1.128E+20	3.271E+19	1.071E+19	3.584E+18	1.066E+18	2.896E+17	5.168E+16	6.226E+16	3.061E+16
20	0.22780	4.246E+20	6.843E+20	5.319E+20	9.495E+19	1.433E+19	4.130E+18	1.491E+18	6.819E+17	1.679E+17	6.496E+16	3.726E+16	1.442E+16
40	0.32357	5.164E+20	6.646E+20	6.244E+20	2.107E+20	3.732E+19	8.000E+18	3.106E+18	1.407E+18	5.685E+17	7.391E+16	3.595E+16	5.650E+16
60	0.47584	5.054E+20	5.995E+20	5.653E+20	1.888E+20	2.290E+19	5.613E+18	1.918E+18	1.023E+18	3.326E+17	9.718E+16	5.618E+16	4.545E+15
80	0.55570	4.526E+20	5.206E+20	5.595E+20	2.448E+20	3.930E+19	7.374E+18	1.689E+18	8.822E+17	2.527E+17	2.118E+17	5.725E+16	2.747E+15
100	0.61181	4.007E+20	4.657E+20	5.187E+20	3.598E+20	6.033E+19	1.029E+19	2.656E+18	1.209E+18	7.005E+17	1.099E+17	1.359E+17	1.859E+16

(a) Impurity **Table B.6 PHOSPHOROUS** **TILT 0° ROTATION 0°**

Energy	Tdepth	C0%	C5%	C10%	C20%	C30%	C40%	C50%	C60%	C70%	C80%	C90%	C95%
1	0.02440	6.119E+17	6.171E+18	1.173E+19	1.109E+19	4.989E+18	2.486E+18	1.503E+18	8.099E+17	4.671E+17	2.190E+17	2.813E+16	1.763E+16
5	0.10000	5.296E+17	2.568E+18	2.878E+18	1.954E+18	1.619E+18	1.224E+18	8.024E+17	4.627E+17	3.096E+17	1.619E+17	4.396E+16	3.229E+16
10	0.19465	2.168E+17	1.237E+18	1.301E+18	9.732E+17	8.476E+17	6.816E+17	4.413E+17	2.893E+17	1.671E+17	8.655E+16	3.894E+16	2.168E+16
20	0.33360	9.594E+16	4.395E+17	6.001E+17	4.987E+17	4.729E+17	4.059E+17	3.331E+17	2.579E+17	1.573E+17	8.415E+16	3.598E+16	2.099E+16
40	0.53964	3.110E+16	1.532E+17	2.945E+17	2.670E+17	2.801E+17	2.800E+17	2.301E+17	1.910E+17	1.333E+17	8.389E+16	3.872E+16	3.033E+16
60	0.72644	1.540E+16	6.229E+16	2.100E+17	2.100E+17	1.940E+17	2.000E+17	1.874E+17	1.670E+17	1.070E+17	6.619E+16	3.120E+16	2.110E+16
80	0.88131	5.560E+15	4.690E+16	1.220E+17	1.700E+17	1.510E+17	1.660E+17	1.640E+17	1.390E+17	9.810E+16	5.580E+16	3.431E+16	1.970E+16
100	1.01463	3.180E+15	3.800E+16	8.769E+16	1.440E+17	1.444E+17	1.400E+17	1.314E+17	1.210E+17	9.819E+16	6.589E+16	3.500E+16	2.890E+16

(b) Interstitial

Energy	Tdepth	C0%	C5%	C10%	C20%	C30%	C40%	C50%	C60%	C70%	C80%	C90%	C95%
1	0.02564	1.680E+20	1.811E+20	1.942E+20	1.237E+20	4.583E+19	2.040E+19	1.040E+19	4.264E+18	1.406E+18	5.718E+17	8.180E+16	4.590E+16
5	0.11400	1.869E+20	2.256E+20	1.618E+20	9.365E+19	6.190E+19	3.429E+19	1.737E+19	8.716E+18	3.668E+18	8.786E+17	1.036E+17	4.744E+16
10	0.21281	1.529E+20	1.788E+20	1.271E+20	8.777E+19	5.826E+19	3.404E+19	2.025E+19	1.005E+19	4.239E+18	1.203E+18	2.332E+17	8.394E+16
20	0.37033	1.129E+20	1.396E+20	1.161E+20	7.865E+19	5.964E+19	3.932E+19	2.200E+19	1.209E+19	5.457E+18	1.697E+18	3.028E+17	2.005E+17
40	0.63639	7.545E+19	1.169E+20	1.013E+20	6.989E+19	5.487E+19	3.658E+19	2.219E+19	1.199E+19	5.657E+18	1.539E+18	2.319E+17	8.385E+16
60	0.80601	5.449E+19	8.692E+19	9.549E+19	6.509E+19	5.489E+19	4.260E+19	2.590E+19	1.381E+19	7.939E+18	2.680E+18	5.082E+17	1.542E+17
80	0.97535	4.380E+19	7.170E+19	9.190E+19	6.720E+19	5.000E+19	4.010E+19	2.508E+19	1.410E+19	7.860E+18	2.640E+18	5.650E+17	1.280E+17
100	1.12396	3.490E+19	5.919E+19	8.169E+19	5.949E+19	5.109E+19	3.820E+19	2.680E+19	1.550E+19	7.619E+18	3.220E+18	8.589E+17	1.310E+17

(c) Vacancy

Energy	Tdepth	C0%	C5%	C10%	C20%	C30%	C40%	C50%	C60%	C70%	C80%	C90%	C95%
1	0.02560	2.210E+20	2.041E+20	1.872E+20	1.102E+20	4.285E+19	2.006E+19	1.001E+19	3.905E+18	1.282E+18	5.180E+17	7.399E+16	4.199E+16
5	0.11400	2.008E+20	2.253E+20	1.598E+20	9.295E+19	6.171E+19	3.393E+19	1.739E+19	8.608E+18	3.653E+18	8.781E+17	1.007E+17	3.821E+16
10	0.21281	1.579E+20	1.787E+20	1.261E+20	8.768E+19	5.816E+19	3.378E+19	2.019E+19	9.945E+18	4.231E+18	1.208E+18	2.146E+17	7.758E+16
20	0.37054	1.139E+20	1.396E+20	1.161E+20	7.863E+19	5.951E+19	3.901E+19	2.196E+19	1.209E+19	5.407E+18	1.682E+18	3.005E+17	1.942E+17
40	0.63622	7.615E+19	1.169E+20	1.012E+20	6.984E+19	5.495E+19	3.648E+19	2.209E+19	1.189E+19	5.627E+18	1.549E+18	2.309E+17	8.495E+16
60	0.80587	5.469E+19	8.704E+19	9.561E+19	6.509E+19	5.489E+19	4.250E+19	2.593E+19	1.385E+19	7.929E+18	2.680E+18	5.053E+17	1.528E+17
80	0.97535	4.390E+19	7.180E+19	9.190E+19	6.720E+19	5.000E+19	4.020E+19	2.508E+19	1.410E+19	7.840E+18	2.620E+18	5.640E+17	1.280E+17
100	1.12396	3.500E+19	5.929E+19	8.179E+19	5.949E+19	5.109E+19	3.810E+19	2.680E+19	1.550E+19	7.589E+18	3.210E+18	8.569E+17	1.330E+17

Table B.7 PHOSPHOROUS

TILT 45° ROTATION 45°

(a) Impurity

Energy	Tdepth	C0%	C5%	C10%	C20%	C30%	C40%	C50%	C60%	C70%	C80%	C90%	C95%
1	0.03798	6.465E+18	5.846E+18	5.116E+18	3.500E+18	3.207E+18	2.444E+18	1.918E+18	1.707E+18	1.719E+18	1.226E+18	2.231E+17	1.121E+17
5	0.14729	1.190E+18	1.763E+18	1.104E+18	6.596E+17	7.517E+17	7.398E+17	5.910E+17	5.844E+17	5.571E+17	5.119E+17	4.756E+17	2.336E+17
10	0.24999	4.904E+17	8.296E+17	5.371E+17	4.408E+17	4.161E+17	4.567E+17	3.986E+17	3.509E+17	3.537E+17	3.475E+17	3.044E+17	1.187E+17
20	0.41386	1.913E+17	4.214E+17	3.188E+17	2.232E+17	2.361E+17	2.799E+17	2.521E+17	2.355E+17	2.401E+17	2.461E+17	1.953E+17	8.717E+16
40	0.67504	6.738E+16	1.747E+17	1.956E+17	1.297E+17	1.328E+17	1.896E+17	1.717E+17	1.674E+17	1.577E+17	1.437E+17	1.138E+17	6.448E+16
60	0.88729	2.465E+16	1.247E+17	1.568E+17	1.068E+17	9.980E+16	1.387E+17	1.417E+17	1.307E+17	1.307E+17	1.138E+17	8.054E+16	4.645E+16
80	1.07877	1.899E+16	7.444E+16	1.279E+17	7.664E+16	7.455E+16	1.199E+17	1.154E+17	1.149E+17	1.159E+17	9.992E+16	6.745E+16	3.347E+16
100	1.25098	1.219E+16	5.697E+16	9.998E+16	6.809E+16	6.908E+16	1.026E+17	1.115E+17	1.075E+17	9.744E+16	8.505E+16	5.071E+16	2.758E+16

(b) Interstitial

Energy	Tdepth	C0%	C5%	C10%	C20%	C30%	C40%	C50%	C60%	C70%	C80%	C90%	C95%
1	0.03735	2.714E+20	1.624E+20	7.203E+19	3.357E+19	1.786E+19	7.343E+18	2.658E+18	1.328E+18	5.846E+17	1.634E+17	1.996E+16	3.880E+15
5	0.14391	1.953E+20	1.354E+20	6.459E+19	2.866E+19	2.021E+19	9.441E+18	4.714E+18	2.138E+18	1.052E+18	5.255E+17	2.216E+17	5.999E+16
10	0.24666	1.588E+20	1.117E+20	5.053E+19	2.909E+19	1.750E+19	9.799E+18	4.488E+18	1.976E+18	9.718E+17	4.934E+17	1.569E+17	4.964E+16
20	0.40380	1.156E+20	9.215E+19	5.252E+19	2.442E+19	1.594E+19	9.417E+18	4.030E+18	1.674E+18	9.136E+17	4.826E+17	1.634E+17	6.983E+16
40	0.65920	8.075E+19	8.065E+19	5.250E+19	2.406E+19	1.308E+19	7.070E+18	3.044E+18	1.607E+18	7.965E+17	4.372E+17	1.258E+17	4.537E+16
60	0.88600	5.818E+19	7.198E+19	5.527E+19	2.226E+19	1.108E+19	6.108E+18	2.345E+18	1.118E+18	4.820E+17	2.036E+17	6.886E+16	3.330E+16
80	1.06343	4.487E+19	6.145E+19	5.026E+19	2.008E+19	1.039E+19	6.065E+18	2.598E+18	1.079E+18	4.417E+17	2.178E+17	7.564E+16	3.627E+16
100	1.22803	3.728E+19	5.717E+19	5.507E+19	2.119E+19	9.974E+18	5.717E+18	2.329E+18	9.105E+17	3.708E+17	1.569E+17	5.117E+16	2.279E+16

(c) Vacancy

Energy	Tdepth	C0%	C5%	C10%	C20%	C30%	C40%	C50%	C60%	C70%	C80%	C90%	C95%
1	0.03735	3.109E+20	1.758E+20	6.577E+19	3.335E+19	1.744E+19	7.300E+18	2.568E+18	1.240E+18	5.837E+17	1.394E+17	1.759E+16	3.880E+15
5	0.14390	2.023E+20	1.334E+20	6.369E+19	2.850E+19	2.008E+19	9.372E+18	4.637E+18	2.112E+18	1.048E+18	5.244E+17	2.165E+17	6.088E+16
10	0.24000	1.618E+20	1.137E+20	5.168E+19	2.909E+19	1.882E+19	9.803E+18	4.775E+18	2.144E+18	1.033E+18	4.469E+17	2.631E+17	1.320E+17
20	0.40380	1.166E+20	9.185E+19	5.238E+19	2.452E+19	1.584E+19	9.402E+18	4.009E+18	1.664E+18	9.136E+17	4.804E+17	1.614E+17	6.928E+16
40	0.65913	8.115E+19	8.065E+19	5.250E+19	2.396E+19	1.308E+19	7.057E+18	3.024E+18	1.597E+18	7.915E+17	4.312E+17	1.248E+17	4.528E+16
60	0.88600	5.828E+19	7.198E+19	5.517E+19	2.226E+19	1.108E+19	6.078E+18	2.345E+18	1.118E+18	4.830E+17	2.036E+17	6.786E+16	3.375E+16
80	1.06343	4.497E+19	6.155E+19	5.016E+19	2.008E+19	1.039E+19	6.045E+18	2.588E+18	1.079E+18	4.407E+17	2.168E+17	7.594E+16	3.627E+16
100	1.22803	3.728E+19	5.727E+19	5.517E+19	2.109E+19	9.954E+18	5.717E+18	2.329E+18	9.085E+17	3.688E+17	1.559E+17	5.077E+16	2.239E+16

Table B.8 GERMANIUM

TILT 7° ROTATION 22°

(a) Impurity

Energy	Tdepth	C0%	C5%	C10%	C20%	C30%	C40%	C50%	C60%	C70%	C80%	C90%	C95%
1	0.01000	1.000E+05	4.213E+18	8.427E+18	1.685E+19	2.528E+19	2.267E+19	1.450E+19	6.339E+18	7.882E+17	5.258E+17	2.634E+17	1.322E+17
5	0.05308	1.000E+05	3.161E+18	7.660E+18	7.472E+18	2.983E+18	1.099E+18	2.419E+17	1.346E+17	2.664E+16	9.423E+15	5.000E+15	4.450E+15
10	0.08431	2.500E+15	1.531E+18	6.002E+18	4.554E+18	1.183E+18	5.374E+17	2.402E+17	1.108E+17	4.312E+16	2.366E+16	8.180E+15	1.162E+16
20	0.14880	1.750E+16	1.285E+18	4.732E+18	1.602E+18	4.424E+17	1.710E+17	7.421E+16	4.579E+16	1.620E+16	1.380E+16	6.250E+15	2.900E+15
40	0.21120	3.140E+16	8.860E+17	2.850E+18	1.837E+18	3.756E+17	1.017E+17	5.184E+16	2.850E+16	1.476E+16	1.363E+16	4.659E+15	3.202E+15
60	0.30747	7.230E+16	9.780E+17	2.083E+18	8.970E+17	1.670E+17	5.493E+16	2.141E+16	1.085E+16	5.000E+15	5.000E+15	3.640E+15	1.360E+15
80	0.35920	7.100E+16	9.076E+17	1.700E+18	1.040E+18	1.694E+17	5.530E+16	2.730E+16	1.070E+16	6.000E+15	2.811E+15	2.330E+15	2.000E+15
100	0.39920	6.780E+16	3.918E+17	1.370E+18	9.270E+17	2.450E+17	8.000E+16	1.941E+16	1.170E+16	4.720E+15	3.060E+15	3.010E+15	2.833E+15

(b) Interstitial

Energy	Tdepth	C0%	C5%	C10%	C20%	C30%	C40%	C50%	C60%	C70%	C80%	C90%	C95%
1	0.01000	2.210E+20	2.357E+20	2.504E+20	2.798E+20	3.092E+20	2.557E+20	1.608E+20	6.584E+19	2.206E+18	1.471E+18	7.359E+17	3.684E+17
5	0.06908	4.510E+20	8.615E+20	7.174E+20	1.813E+20	3.771E+19	5.996E+18	1.617E+18	2.904E+17	1.015E+17	4.396E+16	1.246E+16	2.345E+16
10	0.14782	5.500E+20	1.031E+21	5.541E+20	6.417E+19	1.102E+19	2.606E+18	7.604E+17	2.501E+17	3.914E+16	7.153E+16	2.730E+16	2.696E+16
20	0.18380	7.150E+20	1.238E+21	8.062E+20	1.246E+20	3.361E+19	1.220E+19	5.165E+18	2.011E+18	7.722E+17	1.793E+17	4.023E+17	1.500E+17
40	0.39986	9.320E+20	1.260E+21	4.900E+20	3.925E+19	8.666E+18	3.260E+18	1.020E+18	5.555E+17	2.195E+17	1.210E+17	6.829E+16	3.499E+15
60	0.53177	1.100E+21	1.330E+21	5.660E+20	3.270E+19	7.330E+18	2.010E+18	1.280E+18	4.675E+17	2.239E+17	1.620E+17	8.640E+16	1.829E+16
80	0.57196	1.140E+21	1.460E+21	8.150E+20	6.100E+19	1.090E+19	3.420E+18	1.270E+18	1.050E+18	1.670E+17	1.120E+17	1.010E+17	1.050E+17
100	0.65198	1.140E+21	1.380E+21	8.170E+20	6.000E+19	1.310E+19	3.590E+18	1.830E+18	1.090E+18	7.530E+17	1.371E+17	3.060E+16	4.390E+16

(c) Vacancy

Energy	Tdepth	C0%	C5%	C10%	C20%	C30%	C40%	C50%	C60%	C70%	C80%	C90%	C95%
1	0.01000	3.370E+20	3.223E+20	3.076E+20	2.782E+20	2.488E+20	1.916E+20	1.205E+20	4.930E+19	1.603E+18	1.069E+18	5.349E+17	2.680E+17
5	0.06885	4.910E+20	8.872E+20	6.936E+20	1.779E+20	3.632E+19	5.767E+18	1.582E+18	2.740E+17	1.181E+17	4.040E+16	1.445E+16	9.950E+15
10	0.14782	5.770E+20	1.029E+21	5.374E+20	6.230E+19	1.079E+19	2.541E+18	7.389E+17	2.531E+17	3.513E+16	7.057E+16	2.545E+16	2.696E+16
20	0.18371	7.360E+20	1.251E+21	7.938E+20	1.225E+20	3.326E+19	1.212E+19	5.119E+18	2.012E+18	7.722E+17	1.757E+17	4.024E+17	1.490E+17
40	0.39986	9.500E+20	1.255E+21	4.840E+20	3.883E+19	8.655E+18	3.260E+18	1.020E+18	5.535E+17	2.216E+17	1.240E+17	6.704E+16	3.499E+15
60	0.53177	1.110E+21	1.330E+21	5.610E+20	3.240E+19	7.300E+18	2.010E+18	1.280E+18	4.692E+17	2.292E+17	1.620E+17	8.730E+16	1.829E+16
80	0.57196	1.150E+21	1.460E+21	8.110E+20	6.060E+19	1.080E+19	3.440E+18	1.260E+18	1.050E+18	1.650E+17	1.080E+17	9.830E+16	1.050E+17
100	0.65198	1.140E+21	1.390E+21	8.140E+20	5.960E+19	1.300E+19	3.560E+18	1.830E+18	1.090E+18	7.540E+17	1.369E+17	2.920E+16	4.390E+16

Table B.9 GERMANIUM

TILT 0° ROTATION 0°

(a) Impurity

Energy	Tdepth	C0%	C5%	C10%	C20%	C30%	C40%	C50%	C60%	C70%	C80%	C90%	C95%
1	0.00999	1.000E+05	3.207E+18	6.415E+18	1.283E+19	1.924E+19	1.792E+19	1.267E+19	7.427E+18	3.517E+18	2.348E+18	1.179E+18	5.945E+17
5	0.08578	2.940E+15	2.579E+18	4.692E+18	2.640E+18	1.889E+18	1.083E+18	5.750E+17	2.726E+17	1.403E+17	7.037E+16	3.734E+16	2.372E+16
10	0.17460	9.260E+15	2.545E+18	1.710E+18	1.235E+18	8.611E+17	4.718E+17	3.403E+17	1.897E+17	1.106E+17	7.601E+16	2.009E+16	2.072E+16
20	0.32680	4.710E+16	1.189E+18	8.140E+17	6.403E+17	4.538E+17	3.010E+17	1.910E+17	1.180E+17	6.785E+16	4.178E+16	2.120E+16	2.120E+16
40	0.60522	4.410E+16	5.200E+17	3.810E+17	3.132E+17	2.540E+17	1.869E+17	1.370E+17	8.047E+16	4.640E+16	2.578E+16	1.860E+16	1.197E+16
60	0.79521	2.310E+16	3.590E+17	2.840E+17	2.560E+17	1.934E+17	1.300E+17	9.530E+16	7.530E+16	4.310E+16	2.980E+16	1.840E+16	1.530E+16
80	0.97439	1.860E+16	2.460E+17	2.340E+17	1.890E+17	1.500E+17	1.360E+17	9.185E+16	6.170E+16	4.440E+16	2.860E+16	1.860E+16	1.060E+16
100	1.11878	8.600E+15	1.750E+17	1.860E+17	1.560E+17	1.470E+17	1.150E+17	7.699E+16	5.440E+16	4.120E+16	2.720E+16	1.740E+16	1.330E+16

(b) Interstitial

Energy	Tdepth	C0%	C5%	C10%	C20%	C30%	C40%	C50%	C60%	C70%	C80%	C90%	C95%
1	0.01000	1.700E+20	1.895E+20	2.090E+20	2.480E+20	2.870E+20	2.437E+20	1.591E+20	7.457E+19	1.630E+19	1.087E+19	5.439E+18	2.725E+18
5	0.09899	3.850E+20	5.044E+20	3.295E+20	1.599E+20	7.539E+19	3.593E+19	1.507E+19	6.411E+18	2.347E+18	7.583E+17	7.903E+16	3.502E+16
10	0.25056	3.560E+20	3.350E+20	2.135E+20	1.097E+20	4.679E+19	1.978E+19	7.956E+18	2.360E+18	1.009E+18	2.856E+17	1.901E+16	5.119E+16
20	0.47280	3.090E+20	2.541E+20	1.944E+20	1.076E+20	5.488E+19	2.540E+19	1.127E+19	4.528E+18	1.950E+18	8.216E+17	1.553E+17	1.640E+17
40	0.94673	2.390E+20	2.120E+20	1.650E+20	9.420E+19	4.929E+19	2.010E+19	9.055E+18	3.330E+18	1.140E+18	2.366E+17	6.000E+16	1.450E+16
60	1.25915	2.040E+20	2.040E+20	1.570E+20	9.920E+19	4.890E+19	2.590E+19	1.143E+19	4.820E+18	1.860E+18	3.179E+17	6.200E+16	2.595E+16
80	1.49589	1.690E+20	1.930E+20	1.520E+20	1.030E+20	5.930E+19	2.700E+19	1.310E+19	5.406E+18	2.320E+18	4.200E+17	1.240E+17	9.164E+16
100	1.69954	1.460E+20	2.001E+20	1.480E+20	1.100E+20	6.270E+19	3.110E+19	1.520E+19	6.340E+18	2.510E+18	7.520E+17	3.840E+17	2.869E+16

(c) Vacancy

Energy	Tdepth	C0%	C5%	C10%	C20%	C30%	C40%	C50%	C60%	C70%	C80%	C90%	C95%
1	0.01000	2.960E+20	2.867E+20	2.774E+20	2.588E+20	2.402E+20	1.901E+20	1.242E+20	5.825E+19	1.279E+19	8.528E+18	4.269E+18	2.140E+18
5	0.09738	4.200E+20	5.162E+20	3.324E+20	1.587E+20	7.831E+19	3.705E+19	1.544E+19	7.111E+18	2.523E+18	8.901E+17	1.405E+17	3.145E+16
10	0.25056	3.730E+20	3.313E+20	2.122E+20	1.087E+20	4.641E+19	1.986E+19	7.842E+18	2.343E+18	9.883E+17	2.800E+17	1.901E+16	5.119E+16
20	0.47280	3.160E+20	2.525E+20	1.937E+20	1.070E+20	5.474E+19	2.530E+19	1.118E+19	4.512E+18	1.930E+18	8.277E+17	1.522E+17	1.630E+17
40	0.94667	2.420E+20	2.110E+20	1.650E+20	9.400E+19	4.920E+19	2.000E+19	9.070E+18	3.320E+18	1.130E+18	2.387E+17	5.910E+16	1.450E+16
60	1.25915	2.050E+20	2.040E+20	1.570E+20	9.920E+19	4.880E+19	2.590E+19	1.142E+19	4.840E+18	1.860E+18	3.150E+17	6.270E+16	2.439E+16
80	1.49589	1.700E+20	1.920E+20	1.520E+20	1.030E+20	5.920E+19	2.690E+19	1.300E+19	5.400E+18	2.320E+18	4.200E+17	1.230E+17	9.104E+16
100	1.69931	1.470E+20	2.002E+20	1.480E+20	1.100E+20	6.270E+19	3.100E+19	1.520E+19	6.340E+18	2.500E+18	7.500E+17	3.830E+17	2.952E+16

Table B.10 GERMANIUM

TILT 45° ROTATION 45°

(a) Impurity

Energy	Tdepth	C0%	C5%	C10%	C20%	C30%	C40%	C50%	C60%	C70%	C80%	C90%	C95%
1	0.04976	2.170E+17	6.258E+18	6.955E+18	3.204E+18	1.595E+18	1.256E+18	9.866E+17	6.587E+17	3.949E+17	2.125E+17	6.238E+16	1.139E+16
5	0.29930	1.540E+18	1.320E+18	8.769E+17	4.954E+17	3.001E+17	1.781E+17	1.607E+17	1.209E+17	1.102E+17	5.831E+16	3.107E+16	1.370E+16
10	0.57028	9.237E+17	5.818E+17	4.468E+17	2.839E+17	1.402E+17	1.120E+17	9.075E+16	8.917E+16	5.339E+16	3.379E+16	1.674E+16	2.309E+15
20	0.97470	4.838E+17	3.014E+17	2.179E+17	1.727E+17	1.030E+17	7.747E+16	5.868E+16	5.498E+16	4.538E+16	3.495E+16	1.819E+16	7.403E+15
40	1.59555	2.280E+17	1.890E+17	1.360E+17	9.889E+16	7.409E+16	5.189E+16	3.810E+16	3.220E+16	2.920E+16	2.970E+16	1.240E+16	5.867E+15
60	2.06900	1.120E+17	1.470E+17	9.468E+16	7.328E+16	5.979E+16	3.719E+16	2.795E+16	3.119E+16	2.329E+16	2.427E+16	9.997E+15	5.809E+15
80	2.48801	8.329E+16	1.140E+17	6.929E+16	5.979E+16	4.909E+16	3.372E+16	2.454E+16	2.910E+16	2.240E+16	2.056E+16	9.998E+15	6.479E+15
100	2.87498	4.620E+16	9.730E+16	6.220E+16	5.180E+16	5.270E+16	2.850E+16	2.800E+16	2.550E+16	2.255E+16	1.700E+16	8.000E+15	3.500E+15

(b) Interstitial

Energy	Tdepth	C0%	C5%	C10%	C20%	C30%	C40%	C50%	C60%	C70%	C80%	C90%	C95%
1	0.04590	4.380E+20	2.397E+20	1.141E+20	3.097E+19	1.170E+19	6.484E+18	3.855E+18	2.296E+18	1.103E+18	2.871E+17	5.462E+16	2.493E+16
5	0.30260	3.940E+20	1.135E+20	5.980E+19	1.984E+19	9.879E+18	5.585E+18	3.715E+18	2.066E+18	1.233E+18	4.598E+17	1.038E+17	3.355E+16
10	0.57162	3.519E+20	8.717E+19	5.688E+19	2.259E+19	9.690E+18	5.538E+18	3.864E+18	2.649E+18	1.113E+18	5.018E+17	9.328E+16	9.227E+15
20	0.97457	2.779E+20	8.112E+19	5.008E+19	2.591E+19	1.180E+19	6.478E+18	4.069E+18	2.709E+18	1.639E+18	7.217E+17	2.233E+17	6.364E+16
40	1.62533	2.360E+20	8.119E+19	4.870E+19	2.410E+19	1.170E+19	6.139E+18	3.910E+18	2.390E+18	1.540E+18	7.949E+17	2.036E+17	5.949E+16
60	2.10693	2.049E+20	8.316E+19	4.709E+19	2.399E+19	1.340E+19	6.078E+18	3.701E+18	2.732E+18	1.610E+18	9.248E+17	2.529E+17	2.823E+16
80	2.56662	1.750E+20	8.059E+19	4.239E+19	2.319E+19	1.250E+19	6.401E+18	3.519E+18	2.371E+18	1.460E+18	8.150E+17	1.840E+17	4.389E+16
100	2.93891	1.540E+20	8.160E+19	4.110E+19	2.350E+19	1.240E+19	5.410E+18	3.767E+18	2.350E+18	1.340E+18	7.550E+17	1.830E+17	4.490E+16

(c) Vacancy

Energy	Tdepth	C0%	C5%	C10%	C20%	C30%	C40%	C50%	C60%	C70%	C80%	C90%	C95%
1	0.04590	5.090E+20	2.542E+20	1.067E+20	3.037E+19	1.149E+19	6.483E+18	3.729E+18	2.185E+18	1.108E+18	2.728E+17	5.028E+16	2.493E+16
5	0.30260	4.100E+20	1.127E+20	5.980E+19	1.986E+19	9.839E+18	5.565E+18	3.676E+18	2.058E+18	1.232E+18	4.620E+17	9.601E+16	3.355E+16
10	0.57162	3.579E+20	8.667E+19	5.678E+19	2.259E+19	9.699E+18	5.558E+18	3.850E+18	2.629E+18	1.104E+18	5.058E+17	9.133E+16	9.996E+15
20	0.97454	2.799E+20	8.103E+19	5.008E+19	2.589E+19	1.180E+19	6.478E+18	4.049E+18	2.709E+18	1.639E+18	7.202E+17	2.256E+17	6.261E+16
40	1.62533	2.380E+20	8.109E+19	4.860E+19	2.410E+19	1.170E+19	6.129E+18	3.910E+18	2.390E+18	1.540E+18	7.969E+17	2.019E+17	5.949E+16
60	2.10693	2.059E+20	8.309E+19	4.699E+19	2.399E+19	1.330E+19	6.068E+18	3.701E+18	2.723E+18	1.610E+18	9.268E+17	2.529E+17	2.769E+16
80	2.56662	1.760E+20	8.059E+19	4.239E+19	2.319E+19	1.250E+19	6.405E+18	3.529E+18	2.365E+18	1.460E+18	8.174E+17	1.830E+17	4.389E+16
100	2.93891	1.540E+20	8.150E+19	4.110E+19	2.350E+19	1.240E+19	5.420E+18	3.760E+18	2.350E+18	1.340E+18	7.540E+17	1.820E+17	4.492E+16

(a) Impurity **Table B.11 ARSENIC** **TILT 7° ROTATION 22°**

Energy	Tdepth	C0%	C5%	C10%	C20%	C30%	C40%	C50%	C60%	C70%	C80%	C90%	C95%
1	0.01000	1.000E+05	4.199E+18	8.397E+18	1.679E+19	2.519E+19	2.260E+19	1.448E+19	6.364E+18	8.404E+17	5.606E+17	2.808E+17	1.409E+17
5	0.04920	1.000E+05	2.893E+18	6.957E+18	8.444E+18	3.476E+18	1.424E+18	4.828E+17	1.046E+17	6.115E+16	2.490E+16	9.300E+15	4.075E+15
10	0.09538	1.000E+05	2.401E+18	6.905E+18	3.243E+18	8.237E+17	3.004E+17	1.212E+17	4.240E+16	2.410E+16	7.500E+15	5.900E+15	3.900E+15
20	0.16880	2.500E+16	2.054E+18	4.695E+18	1.038E+18	2.985E+17	1.289E+17	4.676E+16	2.062E+16	1.620E+16	5.600E+15	3.775E+15	2.388E+15
40	0.23760	6.380E+16	1.190E+18	2.863E+18	1.063E+18	2.198E+17	6.630E+16	3.380E+16	2.000E+16	1.190E+16	5.630E+15	1.880E+15	1.963E+15
60	0.23600	1.000E+05	2.711E+17	1.954E+18	1.610E+18	5.472E+17	1.409E+17	5.200E+16	3.600E+16	2.060E+16	6.800E+15	1.020E+16	6.100E+15
80	0.33040	2.140E+15	4.129E+17	1.610E+18	1.010E+18	2.515E+17	6.253E+16	2.500E+16	9.290E+15	7.731E+15	4.232E+15	2.860E+15	2.897E+15
100	0.33540	2.500E+15	3.219E+17	1.203E+18	1.250E+18	4.191E+17	1.160E+17	3.130E+16	2.031E+16	3.130E+15	4.370E+15	3.793E+15	1.880E+15

(b) Interstitial

Energy	Tdepth	C0%	C5%	C10%	C20%	C30%	C40%	C50%	C60%	C70%	C80%	C90%	C95%
1	0.01000	3.990E+20	3.671E+20	3.351E+20	2.712E+20	2.073E+20	1.491E+20	9.377E+19	3.840E+19	1.261E+18	8.408E+17	4.209E+17	2.109E+17
5	0.06135	4.990E+20	8.662E+20	7.425E+20	2.518E+20	5.521E+19	1.197E+19	2.379E+18	7.408E+17	2.423E+17	7.769E+16	1.355E+16	1.695E+16
10	0.14386	5.920E+20	1.043E+21	5.441E+20	5.957E+19	1.331E+19	2.083E+18	5.177E+17	1.795E+17	6.100E+16	4.359E+16	5.918E+15	1.498E+16
20	0.18396	7.490E+20	1.271E+21	7.606E+20	1.143E+20	3.240E+19	1.157E+19	3.488E+18	1.939E+18	1.091E+18	3.854E+17	1.113E+17	8.120E+16
40	0.35554	1.000E+21	1.326E+21	5.580E+20	5.440E+19	1.160E+19	4.710E+18	1.675E+18	3.930E+17	2.209E+17	1.802E+17	8.120E+16	1.290E+17
60	0.43100	8.930E+20	1.476E+21	7.040E+20	7.211E+19	1.371E+19	5.409E+18	2.911E+18	1.230E+18	3.870E+17	1.294E+17	2.485E+16	1.904E+17
80	0.61060	9.920E+20	1.390E+21	5.860E+20	3.440E+19	7.464E+18	2.549E+18	9.196E+17	3.430E+17	9.555E+16	1.440E+16	2.140E+15	3.627E+16
100	0.68736	1.000E+21	1.390E+21	6.570E+20	4.669E+19	7.270E+18	2.909E+18	1.100E+18	4.410E+17	1.083E+17	1.480E+17	6.825E+16	1.310E+16

(c) Vacancy

Energy	Tdepth	C0%	C5%	C10%	C20%	C30%	C40%	C50%	C60%	C70%	C80%	C90%	C95%
1	0.01000	2.350E+20	2.423E+20	2.497E+20	2.644E+20	2.791E+20	2.277E+20	1.432E+20	5.866E+19	2.008E+18	1.339E+18	6.699E+17	3.355E+17
5	0.06128	4.580E+20	8.376E+20	7.612E+20	2.668E+20	5.900E+19	1.274E+19	2.584E+18	7.589E+17	2.874E+17	9.083E+16	1.170E+16	1.295E+16
10	0.14640	5.640E+20	1.040E+21	5.434E+20	5.910E+19	1.213E+19	1.933E+18	4.302E+17	1.536E+17	7.360E+16	2.820E+16	7.350E+15	2.405E+16
20	0.18396	7.270E+20	1.256E+21	7.745E+20	1.166E+20	3.273E+19	1.160E+19	3.510E+18	1.965E+18	1.083E+18	3.730E+17	1.122E+17	8.120E+16
40	0.35560	9.850E+20	1.326E+21	5.650E+20	5.489E+19	1.170E+19	4.750E+18	1.673E+18	3.980E+17	2.280E+17	1.823E+17	8.214E+16	1.310E+17
60	0.43143	8.800E+20	1.474E+21	7.087E+20	7.248E+19	1.368E+19	5.437E+18	2.896E+18	1.230E+18	3.850E+17	1.320E+17	2.850E+16	1.902E+17
80	0.61060	9.790E+20	1.390E+21	5.900E+20	3.460E+19	7.478E+18	2.559E+18	9.211E+17	3.490E+17	9.909E+16	1.678E+16	2.140E+15	3.419E+16
100	0.68754	9.930E+20	1.390E+21	6.610E+20	4.700E+19	7.295E+18	2.910E+18	1.109E+18	4.486E+17	1.105E+17	1.450E+17	7.001E+16	1.440E+16

(a) Impurity   Table B.12 ARSENIC   TILT 0° ROTATION 0°

Energy	Tdepth	C0%	C5%	C10%	C20%	C30%	C40%	C50%	C60%	C70%	C80%	C90%	C95%
1	0.00897	1.000E+05	1.000E+05	1.000E+05	2.579E+19	2.609E+19	1.828E+19	1.041E+19	7.459E+18	6.925E+18	2.983E+18	6.432E+17	3.572E+17
5	0.07988	1.000E+05	4.380E+18	4.430E+18	2.900E+18	2.020E+18	1.187E+18	6.570E+17	3.770E+17	1.785E+17	7.670E+16	4.000E+16	3.330E+16
10	0.16988	1.400E+16	2.730E+18	1.720E+18	1.240E+18	8.600E+17	5.160E+17	2.990E+17	2.040E+17	8.000E+16	6.600E+16	3.110E+16	2.000E+16
20	0.32967	2.600E+16	1.230E+18	8.420E+17	6.400E+17	4.800E+17	2.780E+17	2.037E+17	1.120E+17	7.600E+16	4.300E+16	1.900E+16	1.800E+16
40	0.58111	3.900E+16	5.650E+17	4.180E+17	3.520E+17	2.680E+17	1.860E+17	1.310E+17	7.883E+16	5.200E+16	3.100E+16	1.550E+16	1.200E+16
60	0.73800	1.560E+16	3.260E+17	3.000E+17	2.530E+17	2.160E+17	1.580E+17	1.200E+17	8.080E+16	5.880E+16	2.760E+16	1.880E+16	1.526E+16
80	0.89191	1.390E+16	2.450E+17	2.380E+17	1.840E+17	1.860E+17	1.370E+17	1.058E+17	8.270E+16	5.450E+16	3.270E+16	2.240E+16	1.390E+16
100	1.03006	1.050E+16	2.060E+17	2.150E+17	1.720E+17	1.570E+17	1.160E+17	1.020E+17	6.620E+16	4.670E+16	3.050E+16	1.740E+16	1.480E+16

(b) Interstitial

Energy	Tdepth	C0%	C5%	C10%	C20%	C30%	C40%	C50%	C60%	C70%	C80%	C90%	C95%
1	0.01000	1.680E+20	1.875E+20	2.070E+20	2.460E+20	2.850E+20	2.412E+20	1.560E+20	7.068E+19	1.234E+19	8.228E+18	4.119E+18	2.064E+18
5	0.09154	3.900E+20	5.228E+20	3.397E+20	1.743E+20	8.709E+19	4.235E+19	2.003E+19	8.839E+18	2.653E+18	9.779E+17	2.190E+17	7.067E+16
10	0.21875	3.550E+20	3.975E+20	2.406E+20	1.287E+20	6.328E+19	2.798E+19	1.189E+19	5.773E+18	2.185E+18	7.345E+17	1.544E+17	7.522E+16
20	0.45534	3.050E+20	2.762E+20	1.919E+20	1.116E+20	5.390E+19	2.792E+19	1.242E+19	4.548E+18	2.030E+18	5.110E+17	1.344E+17	6.371E+16
40	0.85936	2.450E+20	2.180E+20	1.690E+20	1.042E+20	5.300E+19	2.410E+19	1.196E+19	5.070E+18	1.438E+18	6.520E+17	1.830E+17	1.020E+17
60	1.02798	2.020E+20	2.378E+20	1.724E+20	1.200E+20	7.070E+19	3.860E+19	2.076E+19	9.130E+18	4.080E+18	1.530E+18	3.547E+17	2.920E+17
80	1.32086	1.730E+20	2.217E+20	1.629E+20	1.120E+20	6.852E+19	3.833E+19	1.590E+19	8.003E+18	3.097E+18	9.922E+17	2.760E+17	1.486E+17
100	1.61925	1.570E+20	2.090E+20	1.550E+20	1.020E+20	6.200E+19	2.920E+19	1.410E+19	5.230E+18	2.453E+18	4.750E+17	6.640E+16	2.330E+16

(c) Vacancy

Energy	Tdepth	C0%	C5%	C10%	C20%	C30%	C40%	C50%	C60%	C70%	C80%	C90%	C95%
1	0.01000	3.010E+20	2.901E+20	2.791E+20	2.572E+20	2.353E+20	1.847E+20	1.196E+20	5.460E+19	9.997E+18	6.668E+18	3.339E+18	1.674E+18
5	0.09154	4.300E+20	5.192E+20	3.327E+20	1.705E+20	8.613E+19	4.162E+19	1.954E+19	8.803E+18	2.571E+18	9.867E+17	2.206E+17	6.299E+16
10	0.21882	3.740E+20	3.918E+20	2.387E+20	1.282E+20	6.327E+19	2.766E+19	1.181E+19	5.684E+18	2.196E+18	7.182E+17	1.480E+17	6.870E+16
20	0.45530	3.130E+20	2.753E+20	1.919E+20	1.113E+20	5.390E+19	2.774E+19	1.234E+19	4.556E+18	2.020E+18	5.070E+17	1.330E+17	6.327E+16
40	0.85931	2.480E+20	2.180E+20	1.690E+20	1.042E+20	5.300E+19	2.410E+19	1.196E+19	5.070E+18	1.435E+18	6.510E+17	1.780E+17	1.020E+17
60	1.02800	2.040E+20	2.368E+20	1.724E+20	1.200E+20	7.070E+19	3.850E+19	2.075E+19	9.110E+18	4.060E+18	1.530E+18	3.496E+17	2.950E+17
80	1.32083	1.740E+20	2.218E+20	1.629E+20	1.120E+20	6.853E+19	3.834E+19	1.590E+19	8.010E+18	3.106E+18	9.832E+17	2.780E+17	1.502E+17
100	1.61923	1.570E+20	2.091E+20	1.550E+20	1.020E+20	6.200E+19	2.920E+19	1.410E+19	5.220E+18	2.450E+18	4.760E+17	6.640E+16	2.210E+16

Table B.13 ARSENIC

TILT 45° ROTATION 45°

(a) Impurity

Energy	Tdepth	C0%	C5%	C10%	C20%	C30%	C40%	C50%	C60%	C70%	C80%	C90%	C95%
1	0.04590	1.920E+17	5.830E+18	7.516E+18	4.038E+18	2.012E+18	1.353E+18	1.100E+18	8.289E+17	6.704E+17	3.001E+17	6.594E+16	2.493E+16
5	0.26561	1.250E+18	1.394E+18	9.907E+17	5.921E+17	3.434E+17	2.284E+17	2.140E+17	1.750E+17	1.327E+17	9.589E+16	2.698E+16	1.749E+16
10	0.48360	9.620E+17	6.742E+17	4.773E+17	3.340E+17	1.839E+17	1.429E+17	1.160E+17	1.080E+17	8.830E+16	6.330E+16	3.435E+16	1.512E+16
20	0.83988	4.388E+17	3.619E+17	2.542E+17	2.179E+17	1.280E+17	8.566E+16	7.827E+16	6.998E+16	6.558E+16	3.939E+16	2.315E+16	7.777E+15
40	1.37948	2.049E+17	2.169E+17	1.460E+17	1.020E+17	8.697E+16	6.128E+16	4.810E+16	4.069E+16	4.229E+16	3.129E+16	1.530E+16	6.998E+15
60	1.79809	1.080E+17	1.610E+17	9.858E+16	8.078E+16	7.173E+16	5.235E+16	4.091E+16	3.743E+16	3.480E+16	3.359E+16	1.358E+16	6.506E+15
80	2.15520	6.519E+16	1.280E+17	8.179E+16	6.449E+16	5.639E+16	4.319E+16	3.836E+16	3.050E+16	2.730E+16	2.250E+16	1.323E+16	8.685E+15
100	2.44980	4.690E+16	1.130E+17	7.420E+16	6.120E+16	4.900E+16	4.000E+16	3.235E+16	2.980E+16	2.366E+16	2.210E+16	1.270E+16	9.230E+15

(b) Interstitial

Energy	Tdepth	C0%	C5%	C10%	C20%	C30%	C40%	C50%	C60%	C70%	C80%	C90%	C95%
1	0.04552	4.350E+20	2.411E+20	1.152E+20	3.026E+19	1.074E+19	5.643E+18	3.333E+18	1.519E+18	6.761E+17	1.854E+17	1.908E+16	5.740E+15
5	0.26280	4.040E+20	1.174E+20	7.045E+19	2.610E+19	1.075E+19	6.174E+18	4.356E+18	2.635E+18	1.285E+18	6.374E+17	1.427E+17	4.727E+16
10	0.48366	3.580E+20	1.023E+20	6.162E+19	2.610E+19	1.234E+19	6.901E+18	4.270E+18	3.000E+18	1.690E+18	8.330E+17	2.417E+17	6.959E+16
20	0.86388	3.039E+20	9.451E+19	5.698E+19	2.679E+19	1.140E+19	5.828E+18	3.929E+18	2.399E+18	1.648E+18	7.717E+17	1.979E+17	5.180E+16
40	1.39193	2.479E+20	9.227E+19	5.118E+19	2.669E+19	1.410E+19	6.768E+18	4.059E+18	3.009E+18	1.638E+18	8.288E+17	2.729E+17	5.918E+16
60	1.80042	2.120E+20	9.261E+19	5.186E+19	2.569E+19	1.383E+19	6.945E+18	4.229E+18	2.726E+18	1.678E+18	1.058E+18	3.028E+17	8.039E+16
80	2.17600	1.790E+20	9.061E+19	4.811E+19	2.600E+19	1.330E+19	7.019E+18	4.129E+18	2.680E+18	1.390E+18	8.539E+17	2.719E+17	7.207E+16
100	2.52740	1.600E+20	8.710E+19	4.800E+19	2.520E+19	1.331E+19	6.387E+18	3.640E+18	2.290E+18	1.480E+18	6.676E+17	2.570E+17	6.580E+16

(c) Vacancy

Energy	Tdepth	C0%	C5%	C10%	C20%	C30%	C40%	C50%	C60%	C70%	C80%	C90%	C95%
1	0.04552	5.040E+20	2.548E+20	1.069E+20	2.953E+19	1.071E+19	5.562E+18	3.248E+18	1.522E+18	7.028E+17	1.854E+17	1.908E+16	5.740E+15
5	0.26280	4.230E+20	1.169E+20	7.015E+19	2.607E+19	1.080E+19	6.168E+18	4.317E+18	2.635E+18	1.285E+18	6.360E+17	1.429E+17	4.563E+16
10	0.48368	3.650E+20	1.016E+20	6.159E+19	2.610E+19	1.238E+19	6.889E+18	4.270E+18	3.010E+18	1.690E+18	8.330E+17	2.433E+17	6.782E+16
20	0.86388	3.079E+20	9.435E+19	5.678E+19	2.669E+19	1.140E+19	5.828E+18	3.919E+18	2.389E+18	1.645E+18	7.707E+17	1.979E+17	5.100E+16
40	1.39193	2.489E+20	9.207E+19	5.118E+19	2.669E+19	1.410E+19	6.778E+18	4.059E+18	3.019E+18	1.644E+18	8.308E+17	2.749E+17	5.918E+16
60	1.80042	2.130E+20	9.250E+19	5.186E+19	2.569E+19	1.383E+19	6.950E+18	4.223E+18	2.721E+18	1.678E+18	1.051E+18	3.034E+17	8.009E+16
80	2.17600	1.800E+20	9.051E+19	4.811E+19	2.590E+19	1.330E+19	7.019E+18	4.129E+18	2.680E+18	1.380E+18	8.559E+17	2.719E+17	7.222E+16
100	2.52740	1.600E+20	8.700E+19	4.800E+19	2.520E+19	1.331E+19	6.381E+18	3.640E+18	2.290E+18	1.480E+18	6.648E+17	2.570E+17	6.480E+16

Table B.14 INDIUM

TILT 7° ROTATION 22°

(a) Impurity

Energy	Tdepth	C0%	C5%	C10%	C20%	C30%	C40%	C50%	C60%	C70%	C80%	C90%	C95%
1	0.00667	1.000E+05	4.210E+18	8.420E+18	1.684E+19	2.526E+19	3.368E+19	4.210E+19	3.368E+19	2.526E+19	1.684E+19	8.421E+18	4.211E+18
5	0.03720	1.000E+05	3.962E+17	2.008E+18	1.148E+19	8.578E+18	4.080E+18	1.173E+18	1.576E+17	1.495E+16	1.030E+16	5.650E+15	3.325E+15
10	0.06808	1.000E+05	1.314E+17	4.394E+18	6.220E+18	2.729E+18	9.223E+17	3.183E+17	8.934E+16	3.231E+16	6.136E+15	3.330E+15	3.330E+15
20	0.11500	1.000E+05	2.114E+17	3.538E+18	3.143E+18	8.770E+17	3.360E+17	1.537E+17	6.568E+16	2.698E+16	1.200E+16	4.000E+15	8.125E+15
40	0.18310	1.000E+05	6.548E+17	3.121E+18	1.607E+18	4.500E+17	1.300E+17	6.373E+16	4.851E+16	1.771E+16	1.026E+16	4.221E+15	3.299E+15
60	0.24360	1.000E+05	7.386E+17	3.131E+18	1.080E+18	2.280E+17	7.847E+16	3.977E+16	2.080E+16	1.280E+16	8.583E+15	3.080E+15	1.540E+15
80	0.30659	1.000E+05	5.669E+17	2.590E+18	6.906E+17	1.770E+17	4.650E+16	2.219E+16	9.410E+15	4.547E+15	4.165E+15	2.950E+15	1.612E+15
100	0.34319	1.000E+05	2.580E+17	2.350E+18	7.877E+17	1.320E+17	4.640E+16	2.680E+16	1.050E+16	5.557E+15	3.017E+15	4.550E+15	2.270E+15

(b) Interstitial

Energy	Tdepth	C0%	C5%	C10%	C20%	C30%	C40%	C50%	C60%	C70%	C80%	C90%	C95%
1	0.00667	2.620E+20	2.557E+20	2.494E+20	2.368E+20	2.242E+20	2.116E+20	1.990E+20	1.592E+20	1.194E+20	7.960E+19	3.980E+19	1.990E+19
5	0.04191	5.450E+20	8.750E+20	1.002E+21	5.755E+20	1.927E+20	4.402E+19	7.038E+18	8.000E+17	1.590E+17	3.854E+16	4.360E+16	2.458E+16
10	0.06914	6.610E+20	1.154E+21	1.247E+21	4.535E+20	1.531E+20	4.240E+19	1.056E+19	3.104E+18	7.081E+17	3.436E+17	7.342E+16	3.992E+16
20	0.14792	7.950E+20	1.498E+21	1.121E+21	2.050E+20	4.939E+19	1.397E+19	3.628E+18	1.143E+18	5.418E+17	6.752E+16	7.456E+16	5.348E+16
40	0.27986	1.010E+21	1.810E+21	8.937E+20	9.536E+19	2.421E+19	8.526E+18	2.094E+18	7.951E+17	5.844E+17	1.597E+17	1.012E+17	3.350E+16
60	0.39992	1.200E+21	1.920E+21	7.262E+20	5.320E+19	1.431E+19	6.234E+18	1.880E+18	6.810E+17	2.108E+17	1.481E+17	7.717E+16	1.338E+16
80	0.56383	1.330E+21	1.750E+21	4.450E+20	2.450E+19	7.059E+18	2.090E+18	1.139E+18	1.136E+17	1.960E+17	7.468E+16	1.000E+16	2.649E+16
100	0.46395	1.420E+21	1.996E+21	9.860E+20	1.030E+20	2.230E+19	7.893E+18	3.342E+18	1.350E+18	1.170E+18	6.480E+17	3.094E+17	2.480E+17

(c) Vacancy

Energy	Tdepth	C0%	C5%	C10%	C20%	C30%	C40%	C50%	C60%	C70%	C80%	C90%	C95%
1	0.00667	3.120E+20	2.884E+20	2.648E+20	2.177E+20	1.705E+20	1.234E+20	7.620E+19	6.096E+19	4.572E+19	3.048E+19	1.524E+19	7.621E+18
5	0.04193	6.140E+20	9.197E+20	1.010E+21	5.322E+20	1.768E+20	4.008E+19	6.157E+18	7.454E+17	1.712E+17	3.974E+16	5.773E+16	3.245E+16
10	0.06913	7.120E+20	1.203E+21	1.244E+21	4.313E+20	1.466E+20	4.065E+19	1.027E+19	2.938E+18	6.850E+17	3.514E+17	7.561E+16	3.695E+16
20	0.14792	8.230E+20	1.523E+21	1.093E+21	1.989E+20	4.854E+19	1.376E+19	3.536E+18	1.131E+18	5.515E+17	6.686E+16	7.887E+16	5.026E+16
40	0.27981	1.040E+21	1.810E+21	8.826E+20	9.382E+19	2.397E+19	8.542E+18	2.066E+18	8.008E+17	5.972E+17	1.583E+17	9.675E+16	3.345E+16
60	0.39991	1.220E+21	1.920E+21	7.162E+20	5.258E+19	1.421E+19	6.204E+18	1.840E+18	6.680E+17	2.156E+17	1.461E+17	8.087E+16	1.412E+16
80	0.56383	1.350E+21	1.740E+21	4.390E+20	2.420E+19	7.042E+18	2.070E+18	1.129E+18	1.139E+17	1.980E+17	7.476E+16	1.060E+16	2.813E+16
100	0.46394	1.440E+21	2.003E+21	9.770E+20	1.020E+20	2.210E+19	7.882E+18	3.342E+18	1.340E+18	1.160E+18	6.450E+17	3.108E+17	2.500E+17

(a) Impurity **Table B.15 INDIUM** **TILT 0° ROTATION 0°**

Energy	Tdepth	C0%	C5%	C10%	C20%	C30%	C40%	C50%	C60%	C70%	C80%	C90%	C95%
1	0.00667	1.000E+05	4.690E+18	9.379E+18	1.876E+19	2.814E+19	3.752E+19	4.690E+19	3.753E+19	2.815E+19	1.877E+19	9.389E+18	4.699E+18
5	0.05385	1.000E+05	2.908E+17	4.385E+18	4.942E+18	3.808E+18	2.441E+18	1.157E+18	9.088E+17	3.500E+17	2.454E+17	3.615E+16	1.350E+16
10	0.11511	1.000E+05	2.274E+18	2.995E+18	1.992E+18	1.613E+18	9.812E+17	5.900E+17	4.059E+17	2.156E+17	9.330E+16	5.825E+16	4.073E+16
20	0.24499	1.000E+05	1.483E+18	1.130E+18	8.395E+17	6.306E+17	4.294E+17	2.701E+17	1.705E+17	1.039E+17	5.112E+16	2.344E+16	2.165E+16
40	0.45028	1.880E+15	7.950E+17	5.230E+17	4.310E+17	3.450E+17	2.499E+17	1.632E+17	1.090E+17	6.810E+16	3.870E+16	2.321E+16	1.568E+16
60	0.60355	6.250E+15	5.320E+17	3.883E+17	3.161E+17	2.676E+17	1.890E+17	1.340E+17	9.540E+16	5.515E+16	4.385E+16	2.290E+16	1.960E+16
80	0.77543	7.740E+15	4.130E+17	3.013E+17	2.433E+17	1.932E+17	1.501E+17	1.123E+17	8.069E+16	4.638E+16	3.652E+16	1.758E+16	1.420E+16
100	0.92080	1.170E+16	3.000E+17	2.260E+17	1.990E+17	1.781E+17	1.360E+17	8.970E+16	6.430E+16	4.830E+16	2.800E+16	1.520E+16	1.380E+16

(b) Interstitial

Energy	Tdepth	C0%	C5%	C10%	C20%	C30%	C40%	C50%	C60%	C70%	C80%	C90%	C95%
1	0.00667	1.460E+20	1.575E+20	1.690E+20	1.920E+20	2.150E+20	2.380E+20	2.610E+20	2.088E+20	1.566E+20	1.044E+20	5.221E+19	2.611E+19
5	0.05727	4.710E+20	7.141E+20	6.269E+20	3.455E+20	1.853E+20	9.260E+19	4.545E+19	2.209E+19	8.369E+18	1.360E+18	1.610E+17	4.350E+16
10	0.15055	4.670E+20	6.133E+20	4.081E+20	2.200E+20	9.795E+19	4.974E+19	2.179E+19	8.261E+18	2.840E+18	7.539E+17	2.246E+17	7.750E+16
20	0.35975	4.560E+20	4.510E+20	2.881E+20	1.494E+20	7.210E+19	3.300E+19	1.230E+19	4.190E+18	1.755E+18	3.510E+17	4.000E+16	5.828E+16
40	0.65957	3.840E+20	3.425E+20	2.550E+20	1.483E+20	7.720E+19	3.367E+19	1.530E+19	7.250E+18	2.987E+18	1.090E+18	2.938E+17	1.303E+17
60	0.99964	3.380E+20	2.922E+20	2.230E+20	1.320E+20	6.375E+19	3.038E+19	1.310E+19	4.650E+18	1.384E+18	3.890E+17	1.132E+17	5.223E+16
80	1.25494	2.990E+20	2.974E+20	2.155E+20	1.278E+20	6.890E+19	3.070E+19	1.510E+19	5.790E+18	1.580E+18	3.430E+17	4.747E+16	1.014E+17
100	1.44329	2.670E+20	2.630E+20	2.040E+20	1.340E+20	7.350E+19	3.810E+19	1.588E+19	6.610E+18	2.130E+18	5.530E+17	1.458E+17	9.300E+16

(c) Vacancy

Energy	Tdepth	C0%	C5%	C10%	C20%	C30%	C40%	C50%	C60%	C70%	C80%	C90%	C95%
1	0.00667	4.020E+20	3.793E+20	3.566E+20	3.112E+20	2.658E+20	2.204E+20	1.750E+20	1.400E+20	1.050E+20	7.001E+19	3.501E+19	1.751E+19
5	0.05673	5.360E+20	7.283E+20	6.118E+20	3.406E+20	1.847E+20	9.473E+19	4.532E+19	2.220E+19	8.774E+18	1.847E+18	1.778E+17	3.950E+16
10	0.15040	4.940E+20	6.000E+20	4.066E+20	2.174E+20	9.826E+19	4.951E+19	2.194E+19	8.186E+18	2.762E+18	7.240E+17	2.167E+17	7.610E+16
20	0.35952	4.710E+20	4.470E+20	2.878E+20	1.486E+20	7.160E+19	3.300E+19	1.230E+19	4.230E+18	1.735E+18	3.561E+17	4.330E+16	6.034E+16
40	0.65956	3.900E+20	3.408E+20	2.550E+20	1.483E+20	7.690E+19	3.358E+19	1.530E+19	7.230E+18	2.974E+18	1.100E+18	2.938E+17	1.282E+17
60	0.99961	3.410E+20	2.912E+20	2.230E+20	1.320E+20	6.376E+19	3.029E+19	1.310E+19	4.640E+18	1.384E+18	3.890E+17	1.139E+17	5.235E+16
80	1.25489	3.010E+20	2.968E+20	2.152E+20	1.278E+20	6.880E+19	3.070E+19	1.500E+19	5.760E+18	1.570E+18	3.400E+17	4.831E+16	1.011E+17
100	1.44326	2.690E+20	2.620E+20	2.040E+20	1.330E+20	7.350E+19	3.810E+19	1.579E+19	6.600E+18	2.130E+18	5.560E+17	1.463E+17	9.650E+16

Table B.16 INDIUM

TILT 45° ROTATION 45°

(a) Impurity

Energy	Tdepth	C0%	C5%	C10%	C20%	C30%	C40%	C50%	C60%	C70%	C80%	C90%	C95%
1	0.03352	1.000E+05	6.034E+18	1.197E+19	5.918E+18	3.061E+18	1.913E+18	1.496E+18	1.171E+18	7.137E+17	2.206E+17	7.981E+15	4.490E+15
5	0.22961	4.850E+17	2.049E+18	1.325E+18	5.522E+17	3.282E+17	2.606E+17	2.014E+17	1.558E+17	1.453E+17	8.791E+16	2.724E+16	6.561E+15
10	0.45920	6.440E+17	8.936E+17	6.656E+17	2.876E+17	1.787E+17	1.208E+17	1.210E+17	8.329E+16	6.330E+16	4.590E+16	1.920E+16	7.248E+15
20	0.85578	4.570E+17	3.865E+17	2.960E+17	1.893E+17	1.090E+17	7.344E+16	5.940E+16	5.347E+16	4.780E+16	2.790E+16	8.330E+15	4.440E+15
40	1.45533	2.470E+17	2.410E+17	1.530E+17	1.090E+17	6.000E+16	5.730E+16	4.230E+16	3.427E+16	2.600E+16	2.070E+16	1.100E+16	2.670E+15
60	1.93897	1.810E+17	1.580E+17	1.110E+17	8.290E+16	5.760E+16	3.290E+16	3.214E+16	2.880E+16	2.380E+16	1.640E+16	9.312E+15	3.100E+15
80	2.35286	1.220E+17	1.360E+17	9.060E+16	7.480E+16	4.520E+16	3.340E+16	2.512E+16	2.120E+16	1.950E+16	1.810E+16	7.200E+15	3.000E+15
100	2.65914	9.000E+16	1.140E+17	7.200E+16	5.856E+16	4.960E+16	2.827E+16	2.270E+16	1.995E+16	2.020E+16	1.396E+16	8.750E+15	5.880E+15

(b) Interstitial

Energy	Tdepth	C0%	C5%	C10%	C20%	C30%	C40%	C50%	C60%	C70%	C80%	C90%	C95%
1	0.02995	4.880E+20	3.452E+20	2.023E+20	6.275E+19	2.108E+19	1.017E+19	4.815E+18	2.891E+18	1.392E+18	4.835E+17	5.715E+16	2.907E+16
5	0.22680	5.120E+20	1.653E+20	8.480E+19	2.544E+19	1.245E+19	7.099E+18	4.414E+18	2.457E+18	1.668E+18	5.767E+17	1.272E+17	1.876E+16
10	0.45920	4.660E+20	1.430E+20	7.977E+19	2.503E+19	1.258E+19	7.290E+18	4.220E+18	3.057E+18	1.590E+18	6.142E+17	1.663E+17	2.154E+16
20	0.85921	4.360E+20	1.124E+20	6.850E+19	2.740E+19	1.370E+19	7.425E+18	3.850E+18	2.762E+18	1.450E+18	7.249E+17	1.498E+17	4.220E+16
40	1.45949	3.690E+20	1.140E+20	6.630E+19	2.930E+19	1.270E+19	7.900E+18	4.710E+18	2.860E+18	1.560E+18	9.680E+17	2.620E+17	5.230E+16
60	1.97596	3.300E+20	1.080E+20	5.930E+19	3.010E+19	1.280E+19	7.050E+18	4.683E+18	3.020E+18	1.647E+18	7.613E+17	2.060E+17	3.500E+16
80	2.39989	2.930E+20	1.080E+20	5.970E+19	2.840E+19	1.350E+19	6.780E+18	4.436E+18	2.650E+18	1.700E+18	8.980E+17	1.788E+17	5.413E+16
100	2.79867	2.630E+20	1.050E+20	5.590E+19	2.768E+19	1.352E+19	7.023E+18	3.954E+18	2.350E+18	1.536E+18	7.608E+17	2.110E+17	2.581E+16

(c) Vacancy

Energy	Tdepth	C0%	C5%	C10%	C20%	C30%	C40%	C50%	C60%	C70%	C80%	C90%	C95%
1	0.02995	5.810E+20	3.941E+20	2.072E+20	6.090E+19	2.070E+19	1.010E+19	4.754E+18	2.710E+18	1.301E+18	4.572E+17	6.337E+16	3.219E+16
5	0.22680	5.370E+20	1.633E+20	8.430E+19	2.534E+19	1.245E+19	7.064E+18	4.403E+18	2.466E+18	1.684E+18	5.744E+17	1.273E+17	1.830E+16
10	0.45920	4.750E+20	1.422E+20	7.977E+19	2.500E+19	1.258E+19	7.292E+18	4.230E+18	3.045E+18	1.600E+18	6.106E+17	1.703E+17	2.224E+16
20	0.85921	4.420E+20	1.116E+20	6.830E+19	2.730E+19	1.370E+19	7.426E+18	3.860E+18	2.755E+18	1.450E+18	7.236E+17	1.480E+17	4.330E+16
40	1.45949	3.710E+20	1.140E+20	6.640E+19	2.930E+19	1.270E+19	7.900E+18	4.700E+18	2.870E+18	1.550E+18	9.684E+17	2.610E+17	5.270E+16
60	1.97596	3.310E+20	1.080E+20	5.940E+19	3.010E+19	1.280E+19	7.040E+18	4.688E+18	3.020E+18	1.637E+18	7.623E+17	2.070E+17	3.500E+16
80	2.39989	2.940E+20	1.080E+20	5.970E+19	2.840E+19	1.350E+19	6.770E+18	4.430E+18	2.650E+18	1.710E+18	8.970E+17	1.788E+17	5.373E+16
100	2.79867	2.630E+20	1.050E+20	5.580E+19	2.768E+19	1.352E+19	7.030E+18	3.949E+18	2.360E+18	1.536E+18	7.597E+17	2.110E+17	2.581E+16

(a) Impurity **Table B.17 ANTIMONY** **TILT 7° ROTATION 22°**

Energy	Tdepth	C0%	C5%	C10%	C20%	C30%	C40%	C50%	C60%	C70%	C80%	C90%	C95%
1	0.00667	1.000E+05	5.200E+18	1.040E+19	2.080E+19	3.120E+19	4.160E+19	5.200E+19	4.160E+19	3.120E+19	2.080E+19	1.040E+19	5.201E+18
5	0.02980	1.000E+05	2.257E+17	4.515E+17	9.484E+18	1.088E+19	7.683E+18	3.921E+18	1.209E+18	4.386E+17	1.037E+17	1.590E+16	8.450E+15
10	0.06423	1.000E+05	4.172E+16	3.720E+18	6.640E+18	3.340E+18	1.265E+18	4.811E+17	1.350E+17	5.369E+16	7.868E+15	3.330E+15	3.330E+15
20	0.10600	1.000E+05	1.283E+17	2.439E+18	3.802E+18	1.303E+18	4.594E+17	2.432E+17	8.506E+16	4.391E+16	1.390E+16	1.043E+16	3.650E+15
40	0.16310	1.000E+05	3.570E+17	2.970E+18	2.271E+18	4.803E+17	2.096E+17	1.085E+17	5.165E+16	3.505E+16	1.982E+16	7.780E+15	4.798E+15
60	0.26370	1.000E+05	9.631E+17	3.410E+18	7.529E+17	1.714E+17	5.540E+16	2.620E+16	1.537E+16	5.380E+15	6.920E+15	1.540E+15	1.540E+15
80	0.26330	5.880E+14	1.500E+17	2.730E+18	1.303E+18	2.370E+17	8.590E+16	3.760E+16	1.710E+16	1.342E+16	8.240E+15	3.387E+15	4.710E+15
100	0.29984	4.550E+14	2.570E+17	1.550E+18	1.220E+18	2.000E+17	8.730E+16	3.450E+16	1.333E+16	1.209E+16	3.640E+15	2.730E+15	3.180E+15

(b) Interstitial

Energy	Tdepth	C0%	C5%	C10%	C20%	C30%	C40%	C50%	C60%	C70%	C80%	C90%	C95%
1	0.00667	2.600E+20	2.528E+20	2.456E+20	2.312E+20	2.168E+20	2.024E+20	1.880E+20	1.504E+20	1.128E+20	7.520E+19	3.760E+19	1.880E+19
5	0.03784	5.550E+20	8.643E+20	1.061E+21	6.847E+20	2.633E+20	6.785E+19	1.038E+19	1.350E+18	1.654E+17	5.762E+16	2.465E+16	1.283E+16
10	0.07683	6.730E+20	1.188E+21	1.189E+21	3.645E+20	9.317E+19	2.284E+19	4.251E+18	8.797E+17	3.352E+17	7.630E+16	2.383E+16	3.960E+16
20	0.16378	8.170E+20	1.557E+21	8.906E+20	1.390E+20	3.429E+19	5.982E+18	1.372E+18	1.940E+17	5.458E+16	1.502E+16	2.830E+16	2.908E+16
40	0.27549	1.040E+21	1.835E+21	9.245E+20	9.710E+19	2.536E+19	8.558E+18	1.985E+18	6.907E+17	2.741E+17	7.916E+16	1.689E+16	8.240E+16
60	0.43513	1.220E+21	1.864E+21	4.584E+20	3.660E+19	1.024E+19	3.359E+18	1.040E+18	4.494E+17	1.001E+17	7.316E+16	2.935E+16	1.386E+17
80	0.43594	1.360E+21	2.110E+21	1.009E+21	7.487E+19	1.590E+19	7.120E+18	2.600E+18	6.882E+17	6.529E+17	2.934E+17	1.590E+16	3.060E+16
100	0.65032	1.460E+21	1.752E+21	5.440E+20	2.720E+19	7.240E+18	1.980E+18	7.180E+17	2.380E+17	4.270E+16	2.410E+16	9.990E+15	8.399E+15

(c) Vacancy

Energy	Tdepth	C0%	C5%	C10%	C20%	C30%	C40%	C50%	C60%	C70%	C80%	C90%	C95%
1	0.00667	3.160E+20	2.914E+20	2.668E+20	2.177E+20	1.685E+20	1.194E+20	7.020E+19	5.616E+19	4.212E+19	2.808E+19	1.404E+19	7.021E+18
5	0.03787	6.310E+20	9.144E+20	1.079E+21	6.364E+20	2.390E+20	6.304E+19	9.085E+18	1.242E+18	1.473E+17	5.780E+16	2.940E+16	1.520E+16
10	0.07684	7.270E+20	1.231E+21	1.179E+21	3.468E+20	8.885E+19	2.218E+19	4.020E+18	8.007E+17	3.151E+17	7.245E+16	2.381E+16	4.622E+16
20	0.16371	8.480E+20	1.583E+21	8.680E+20	1.356E+20	3.385E+19	6.004E+18	1.306E+18	1.840E+17	5.440E+16	1.743E+16	3.367E+16	3.260E+16
40	0.27540	1.060E+21	1.836E+21	9.079E+20	9.549E+19	2.515E+19	8.568E+18	1.957E+18	6.923E+17	2.760E+17	8.152E+16	1.799E+16	8.444E+16
60	0.43199	1.240E+21	1.865E+21	4.667E+20	3.640E+19	1.039E+19	3.607E+18	1.021E+18	4.950E+17	9.690E+16	1.022E+17	2.417E+16	1.041E+17
80	0.43594	1.380E+21	2.110E+21	9.988E+20	7.411E+19	1.570E+19	7.110E+18	2.600E+18	6.802E+17	6.554E+17	2.931E+17	1.530E+16	2.760E+16
100	0.64005	1.480E+21	1.810E+21	5.370E+20	2.700E+19	7.230E+18	1.980E+18	7.290E+17	3.134E+17	1.540E+17	5.500E+16	1.000E+16	4.550E+15

Table B.18 ANTIMONY

TILT 0° ROTATION 0°

(a) Impurity

Energy	Tdepth	C0%	C5%	C10%	C20%	C30%	C40%	C50%	C60%	C70%	C80%	C90%	C95%
1	0.00667	1.000E+05	5.840E+18	1.168E+19	2.336E+19	3.504E+19	4.672E+19	5.840E+19	4.673E+19	3.505E+19	2.337E+19	1.169E+19	5.849E+18
5	0.04989	1.000E+05	1.871E+16	3.374E+18	5.866E+18	4.484E+18	2.766E+18	1.569E+18	9.410E+17	4.673E+17	2.707E+17	9.656E+16	4.640E+16
10	0.11930	1.000E+05	2.646E+18	2.658E+18	2.122E+18	1.556E+18	8.928E+17	4.836E+17	2.967E+17	1.726E+17	7.520E+16	3.287E+16	2.047E+16
20	0.23946	1.000E+05	1.173E+18	1.151E+18	9.381E+17	7.042E+17	4.663E+17	2.884E+17	1.545E+17	9.864E+16	7.247E+16	2.113E+16	1.105E+16
40	0.42800	6.250E+14	8.240E+17	5.640E+17	4.863E+17	3.826E+17	2.738E+17	1.630E+17	1.200E+17	8.060E+16	4.314E+16	2.190E+16	1.926E+16
60	0.62718	1.530E+15	5.270E+17	3.660E+17	3.118E+17	2.400E+17	1.860E+17	1.216E+17	7.910E+16	5.150E+16	3.270E+16	1.890E+16	1.220E+16
80	0.79337	1.540E+15	3.781E+17	2.898E+17	2.470E+17	2.090E+17	1.380E+17	1.030E+17	7.080E+16	3.920E+16	2.770E+16	1.176E+16	1.189E+16
100	0.83167	3.440E+15	2.910E+17	2.640E+17	2.080E+17	1.750E+17	1.375E+17	1.121E+17	8.015E+16	5.000E+16	3.470E+16	2.880E+16	2.000E+16

(b) Interstitial

Energy	Tdepth	C0%	C5%	C10%	C20%	C30%	C40%	C50%	C60%	C70%	C80%	C90%	C95%
1	0.00667	1.210E+20	1.389E+20	1.568E+20	1.926E+20	2.284E+20	2.642E+20	3.000E+20	2.400E+20	1.800E+20	1.200E+20	6.001E+19	3.001E+19
5	0.05269	4.380E+20	7.051E+20	6.564E+20	3.724E+20	2.044E+20	1.058E+20	5.441E+19	2.666E+19	1.012E+19	3.295E+18	4.307E+17	3.281E+16
10	0.14274	4.890E+20	6.129E+20	4.070E+20	2.345E+20	1.055E+20	5.133E+19	2.415E+19	9.593E+18	3.399E+18	1.105E+18	1.883E+17	7.806E+16
20	0.33887	4.490E+20	4.290E+20	3.155E+20	1.633E+20	7.624E+19	3.581E+19	1.470E+19	5.711E+18	1.334E+18	6.349E+17	1.853E+17	4.260E+16
40	0.67600	4.060E+20	3.442E+20	2.670E+20	1.490E+20	6.766E+19	3.490E+19	1.390E+19	4.918E+18	1.845E+18	5.410E+17	3.573E+16	1.659E+16
60	0.98361	3.370E+20	3.042E+20	2.350E+20	1.340E+20	6.871E+19	3.100E+19	1.325E+19	5.120E+18	1.610E+18	4.370E+17	9.490E+16	5.510E+16
80	1.17083	3.040E+20	3.040E+20	2.348E+20	1.480E+20	7.400E+19	4.246E+19	1.692E+19	6.337E+18	3.217E+18	6.329E+17	1.125E+17	1.640E+17
100	1.39179	2.700E+20	2.850E+20	2.230E+20	1.410E+20	7.390E+19	4.000E+19	1.800E+19	5.990E+18	2.850E+18	8.100E+17	8.160E+16	1.020E+17

(c) Vacancy

Energy	Tdepth	C0%	C5%	C10%	C20%	C30%	C40%	C50%	C60%	C70%	C80%	C90%	C95%
1	0.00667	1.990E+20	2.033E+20	2.076E+20	2.162E+20	2.248E+20	2.334E+20	2.420E+20	1.936E+20	1.452E+20	9.681E+19	4.841E+19	2.421E+19
5	0.05292	5.250E+20	7.219E+20	6.443E+20	3.752E+20	1.983E+20	9.739E+19	5.151E+19	2.508E+19	9.172E+18	2.965E+18	3.972E+17	3.869E+16
10	0.14264	5.200E+20	6.019E+20	4.023E+20	2.324E+20	1.053E+20	5.110E+19	2.398E+19	9.661E+18	3.291E+18	1.123E+18	1.882E+17	7.750E+16
20	0.33887	4.660E+20	4.265E+20	3.145E+20	1.633E+20	7.576E+19	3.553E+19	1.463E+19	5.690E+18	1.321E+18	6.462E+17	1.871E+17	4.187E+16
40	0.67600	4.120E+20	3.432E+20	2.670E+20	1.490E+20	6.760E+19	3.480E+19	1.380E+19	4.890E+18	1.852E+18	5.440E+17	3.561E+16	1.692E+16
60	0.98361	3.410E+20	3.040E+20	2.356E+20	1.340E+20	6.856E+19	3.100E+19	1.315E+19	5.130E+18	1.640E+18	4.370E+17	9.290E+16	5.560E+16
80	1.17084	3.060E+20	3.030E+20	2.348E+20	1.480E+20	7.406E+19	4.245E+19	1.692E+19	6.342E+18	3.207E+18	6.373E+17	1.116E+17	1.660E+17
100	1.39179	2.710E+20	2.850E+20	2.230E+20	1.410E+20	7.380E+19	4.000E+19	1.800E+19	6.000E+18	2.836E+18	8.080E+17	8.190E+16	1.020E+17

Table B.19 ANTIMONY

TILT 45° ROTATION 45°

(a) Impurity

Energy	Tdepth	C0%	C5%	C10%	C20%	C30%	C40%	C50%	C60%	C70%	C80%	C90%	C95%
1	0.02998	1.000E+05	5.667E+18	1.133E+19	7.239E+18	4.235E+18	2.693E+18	1.729E+18	1.331E+18	1.040E+18	5.860E+17	1.697E+17	8.533E+16
5	0.22680	3.830E+17	2.099E+18	1.358E+18	6.514E+17	3.537E+17	2.497E+17	2.183E+17	1.628E+17	1.314E+17	7.648E+16	2.330E+16	1.079E+16
10	0.45920	6.440E+17	9.396E+17	6.174E+17	3.284E+17	1.694E+17	1.220E+17	9.920E+16	8.780E+16	7.580E+16	3.775E+16	1.465E+16	8.027E+15
20	0.85674	4.070E+17	4.318E+17	3.160E+17	1.722E+17	1.030E+17	6.892E+16	7.110E+16	5.028E+16	4.110E+16	2.597E+16	1.110E+16	3.890E+15
40	1.47876	2.780E+17	2.090E+17	1.690E+17	1.110E+17	7.051E+16	4.380E+16	3.500E+16	3.080E+16	2.380E+16	2.440E+16	7.650E+15	2.650E+15
60	1.97380	1.800E+17	1.550E+17	1.120E+17	8.640E+16	5.050E+16	3.500E+16	2.879E+16	2.640E+16	2.380E+16	1.616E+16	7.140E+15	4.050E+15
80	2.35700	1.270E+17	1.390E+17	8.920E+16	7.040E+16	5.140E+16	3.260E+16	2.260E+16	1.860E+16	2.118E+16	1.140E+16	8.564E+15	3.800E+15
100	2.79750	9.950E+16	1.120E+17	7.380E+16	5.680E+16	3.878E+16	2.970E+16	2.270E+16	2.030E+16	1.680E+16	1.130E+16	5.830E+15	3.330E+15

(b) Interstitial

Energy	Tdepth	C0%	C5%	C10%	C20%	C30%	C40%	C50%	C60%	C70%	C80%	C90%	C95%
1	0.02984	4.860E+20	3.450E+20	2.040E+20	6.398E+19	2.059E+19	9.359E+18	4.254E+18	2.710E+18	1.260E+18	3.953E+17	1.965E+16	1.033E+16
5	0.22720	5.260E+20	1.694E+20	8.408E+19	2.547E+19	1.222E+19	7.168E+18	4.366E+18	2.795E+18	1.516E+18	4.855E+17	1.250E+17	1.033E+16
10	0.46280	4.910E+20	1.406E+20	7.601E+19	2.485E+19	1.216E+19	6.870E+18	4.310E+18	2.820E+18	1.780E+18	4.970E+17	1.190E+17	1.905E+16
20	0.85926	4.570E+20	1.217E+20	7.320E+19	2.541E+19	1.270E+19	6.931E+18	4.920E+18	3.087E+18	1.670E+18	6.660E+17	1.724E+17	2.610E+16
40	1.51324	3.730E+20	1.070E+20	6.790E+19	3.020E+19	1.300E+19	7.170E+18	4.210E+18	2.910E+18	1.560E+18	7.380E+17	1.060E+17	3.020E+16
60	2.03869	3.440E+20	1.060E+20	6.070E+19	2.920E+19	1.330E+19	6.720E+18	4.160E+18	2.870E+18	1.636E+18	7.590E+17	1.370E+17	3.617E+16
80	2.47828	3.050E+20	1.100E+20	6.060E+19	2.990E+19	1.350E+19	7.450E+18	4.600E+18	2.470E+18	1.670E+18	6.600E+17	1.090E+17	3.619E+16
100	2.87857	2.750E+20	1.040E+20	5.810E+19	2.840E+19	1.260E+19	6.200E+18	3.892E+18	2.770E+18	1.530E+18	7.090E+17	1.910E+17	2.500E+16

(c) Vacancy

Energy	Tdepth	C0%	C5%	C10%	C20%	C30%	C40%	C50%	C60%	C70%	C80%	C90%	C95%
1	0.02984	5.850E+20	3.988E+20	2.126E+20	6.238E+19	1.991E+19	9.180E+18	4.172E+18	2.523E+18	1.160E+18	3.602E+17	1.965E+16	1.033E+16
5	0.22720	5.520E+20	1.671E+20	8.358E+19	2.537E+19	1.212E+19	7.120E+18	4.340E+18	2.748E+18	1.488E+18	4.814E+17	1.274E+17	1.033E+16
10	0.46280	5.010E+20	1.403E+20	7.600E+19	2.475E+19	1.216E+19	6.840E+18	4.340E+18	2.820E+18	1.780E+18	4.880E+17	1.200E+17	1.985E+16
20	0.85926	4.630E+20	1.217E+20	7.310E+19	2.541E+19	1.270E+19	6.957E+18	4.900E+18	3.086E+18	1.660E+18	6.738E+17	1.725E+17	2.610E+16
40	1.51324	3.750E+20	1.060E+20	6.780E+19	3.010E+19	1.300E+19	7.160E+18	4.200E+18	2.910E+18	1.560E+18	7.410E+17	1.060E+17	2.960E+16
60	2.03864	3.450E+20	1.060E+20	6.070E+19	2.920E+19	1.330E+19	6.720E+18	4.150E+18	2.880E+18	1.636E+18	7.580E+17	1.370E+17	3.614E+16
80	2.47821	3.070E+20	1.100E+20	6.060E+19	2.990E+19	1.350E+19	7.460E+18	4.600E+18	2.470E+18	1.660E+18	6.570E+17	1.090E+17	3.635E+16
100	2.87857	2.760E+20	1.040E+20	5.810E+19	2.840E+19	1.260E+19	6.190E+18	3.892E+18	2.770E+18	1.530E+18	7.090E+17	1.920E+17	2.500E+16

APPENDIX C C++ PROGRAM CODES FOR EXTRACTION OF SCALP COEFFICIENTS

The following C++ program *scalpextract.cc* generates the SCALP tables automatically given the simulated impurity and damage profiles (*readinfile*), and arranges the SCALP coefficients in tabular form, given in the output file (*scalpcoeff*)

```
/***************************************************************************
**Extracting SCALP coefficients from Crystal TRIM ion, interstitial and vacancy profiles
***************************************************************************/
#include <stdio.h>
#include <stdlib.h>
#include <math.h>

void main(void)
{
        float energy, depth[2000], conc[2000], limit, tdepth, tdepth00, tdepth01, tdepth02,
tdepth05, tdepth10, tdepth15, tdepth20, tdepth25, tdepth30, tdepth35, tdepth40, tdepth45,
tdepth50, tdepth55, tdepth60, tdepth65, tdepth70, tdepth75, tdepth80, tdepth85, tdepth90,
tdepth95, c00, c01, c02, c05, c10, c15, c20, c25, c30, c35, c40, c45, c50, c55, c60, c65, c70,
c75, c80, c85, c90, c95;

        int i,N;

        limit = 1.00000000e15;
        energy= 10;

FILE *CTfile1,*Scoeff;

        CTfile1=fopen("readinfile","r");
        Scoeff=fopen("scalpcoeff","a");

i=0;
while(fscanf(CTfile1,"%f %f", &depth[i], &conc[i]) !=EOF) i++;
N=i;

for(i=0; i<=N; i++)
                {
                fscanf(CTfile1,"%f %f", &depth[i], &conc[i]);
                }

                {
                for(i=N; i>=1; i--)
                                {
                                if ((limit < conc[i-1]) && (limit > conc[i]))

                                tdepth = (limit-conc[i])/(conc[i-1]-conc[i])*(depth[i-1]-
depth[i])+depth[i-1];
                                }
                }
```

```
tdepth00  = tdepth * 0.00;
tdepth01  = tdepth * 0.01;
tdepth02  = tdepth * 0.025;
tdepth05  = tdepth * 0.05;
tdepth10  = tdepth * 0.10;
tdepth15  = tdepth * 0.15;
tdepth20  = tdepth * 0.20;
tdepth25  = tdepth * 0.25;
tdepth30  = tdepth * 0.30;
tdepth35  = tdepth * 0.35;
tdepth40  = tdepth * 0.40;
tdepth45  = tdepth * 0.45;
tdepth50  = tdepth * 0.50;
tdepth55  = tdepth * 0.55;
tdepth60  = tdepth * 0.60;
tdepth65  = tdepth * 0.65;
tdepth70  = tdepth * 0.70;
tdepth75  = tdepth * 0.75;
tdepth80  = tdepth * 0.80;
tdepth85  = tdepth * 0.85;
tdepth90  = tdepth * 0.90;
tdepth95  = tdepth * 0.95;

for(i=0; i<=N; i++)
        {
        fscanf(CTfile1,"%f %f", &depth[i], &conc[i]);
        }
        {
        for(i=0; i<=N; i++)
                        {
                        if ((tdepth01 > depth[i]) && (tdepth01 < depth[i+1]) )
                                c01 = (tdepth01-depth[i])/(depth[i+1]-depth[i])*(conc[i+1]-
conc[i])+conc[i];
                        if (tdepth01 == depth[i])
                                c01 = conc[i];

                        if ((tdepth02 > depth[i]) && (tdepth02 < depth[i+1]) )
                                c02 = (tdepth02-depth[i])/(depth[i+1]-depth[i])*(conc[i+1]-
conc[i])+conc[i];
                        if (tdepth02 == depth[i])
                                c02 = conc[i];

                        if ((tdepth05 > depth[i]) && (tdepth05 < depth[i+1]) )
                                c05 = (tdepth05-depth[i])/(depth[i+1]-depth[i])*(conc[i+1]-
conc[i])+conc[i];
                        if (tdepth05 == depth[i])
                                c05 = conc[i];

                        if ((tdepth10 > depth[i]) && (tdepth10 < depth[i+1]) )
                                c10 = (tdepth10-depth[i])/(depth[i+1]-depth[i])*(conc[i+1]-
conc[i])+conc[i];
                        if (tdepth10 == depth[i])
                                c10 = conc[i];
```

```
                    if ((tdepth15 > depth[i]) && (tdepth15 < depth[i+1]) )
                            c15 = (tdepth15-depth[i])/(depth[i+1]-depth[i])*(conc[i+1]-
conc[i])+conc[i];
                    if (tdepth15 == depth[i])
                            c15 = conc[i];

                    if ((tdepth20 > depth[i]) && (tdepth20 < depth[i+1]) )
                            c20 = (tdepth20-depth[i])/(depth[i+1]-depth[i])*(conc[i+1]-
conc[i])+conc[i];
                    if (tdepth20 == depth[i])
                            c20 = conc[i];

                    if ((tdepth25 > depth[i]) && (tdepth25 < depth[i+1]) )
                            c25 = (tdepth25-depth[i])/(depth[i+1]-depth[i])*(conc[i+1]-
conc[i])+conc[i];
                    if (tdepth25 == depth[i])
                            c25 = conc[i];

                    if ((tdepth30 > depth[i]) && (tdepth30 < depth[i+1]) )
                            c30 = (tdepth30-depth[i])/(depth[i+1]-depth[i])*(conc[i+1]-
conc[i])+conc[i];
                    if (tdepth30 == depth[i])
                            c30 = conc[i];

                    if ((tdepth35 > depth[i]) && (tdepth35 < depth[i+1]) )
                            c35 = (tdepth35-depth[i])/(depth[i+1]-depth[i])*(conc[i+1]-
conc[i])+conc[i];
                    if (tdepth35 == depth[i])
                            c35 = conc[i];

                    if ((tdepth40 > depth[i]) && (tdepth40 < depth[i+1]) )
                            c40 = (tdepth40-depth[i])/(depth[i+1]-depth[i])*(conc[i+1]-
conc[i])+conc[i];
                    if (tdepth40 == depth[i])
                            c40 = conc[i];

                    if ((tdepth45 > depth[i]) && (tdepth45 < depth[i+1]) )
                            c45 = (tdepth45-depth[i])/(depth[i+1]-depth[i])*(conc[i+1]-
conc[i])+conc[i];
                    if (tdepth45 == depth[i])
                            c45 = conc[i];

                    if ((tdepth50 > depth[i]) && (tdepth50 < depth[i+1]) )
                            c50 = (tdepth50-depth[i])/(depth[i+1]-depth[i])*(conc[i+1]-
conc[i])+conc[i];
                    if (tdepth50 == depth[i])
                            c50 = conc[i];

                    if ((tdepth55 > depth[i]) && (tdepth55 < depth[i+1]) )
                            c55 = (tdepth55-depth[i])/(depth[i+1]-depth[i])*(conc[i+1]-
conc[i])+conc[i];
                    if (tdepth55 == depth[i])
                            c55 = conc[i];
                    if ((tdepth60 > depth[i]) && (tdepth60 < depth[i+1]) )
```

```
                                        c60 = (tdepth60-depth[i])/(depth[i+1]-depth[i])*(conc[i+1]-
conc[i])+conc[i];
                              if (tdepth60 == depth[i])
                                        c60 = conc[i];

                              if ((tdepth65 > depth[i]) && (tdepth65 < depth[i+1]) )
                                        c65 = (tdepth65-depth[i])/(depth[i+1]-depth[i])*(conc[i+1]-
conc[i])+conc[i];
                              if (tdepth65 == depth[i])
                                        c65 = conc[i];

                              if ((tdepth70 > depth[i]) && (tdepth70 < depth[i+1]) )
                                        c70 = (tdepth70-depth[i])/(depth[i+1]-depth[i])*(conc[i+1]-
conc[i])+conc[i];
                              if (tdepth70 == depth[i])
                                        c70 = conc[i];

                              if ((tdepth75 > depth[i]) && (tdepth75 < depth[i+1]) )
                                        c75 = (tdepth75-depth[i])/(depth[i+1]-depth[i])*(conc[i+1]-
conc[i])+conc[i];
                              if (tdepth75 == depth[i])
                                        c75 = conc[i];

                              if ((tdepth80 > depth[i]) && (tdepth80 < depth[i+1]) )
                                        c80 = (tdepth80-depth[i])/(depth[i+1]-depth[i])*(conc[i+1]-
conc[i])+conc[i];
                              if (tdepth80 == depth[i])
                                        c80 = conc[i];

                              if ((tdepth85 > depth[i]) && (tdepth85 < depth[i+1]) )
                                        c85 = (tdepth85-depth[i])/(depth[i+1]-depth[i])*(conc[i+1]-
conc[i])+conc[i];
                              if (tdepth85 == depth[i])
                                        c85 = conc[i];

                              if ((tdepth90 > depth[i]) && (tdepth90 < depth[i+1]) )
                                        c90 = (tdepth90-depth[i])/(depth[i+1]-depth[i])*(conc[i+1]-
conc[i])+conc[i];
                              if (tdepth90 == depth[i])
                                        c90 = conc[i];

                              if ((tdepth95 > depth[i]) && (tdepth95 < depth[i+1]) )
                                        c95 = (tdepth95-depth[i])/(depth[i+1]-depth[i])*(conc[i+1]-
conc[i])+conc[i];
                              if (tdepth95 == depth[i])
                                        c95 = conc[i];
                              }
          c00 = conc[0];
          }

fprintf(Scoeff,"\n%f\t%f\t%e\t%e\t%e\t%e\t%e\t%e\t%e\t%e\t%e\t%e\t%e\t%e\t%e\t%e\t%e\t
%e\t%e\t%e\t%e\t%e\t%e\t%e",energy, tdepth, c00, c01, c02, c05, c10, c15, c20, c25, c30, c35,
c40, c45, c50, c55, c60, c65, c70, c75, c80, c85, c90, c95);
}
```

The next C++ program *interpolate.cc* basically performs the reverse SCALP procedure by generating a new profile given the implant conditions. It first reads in the SCALP tables (*scalptable*) and performs interpolation between two energy entries if the user-input energy is not found in the tables. The output file (*profile*) is a depth (µm) versus concentration (atoms/cm^3). A UNIX script then links the C++ code to the DIOS input file, which imports the profile for subsequent diffusion simulations.

```
/***************************************************************************
** Interpolation of values in scalp table
***************************************************************************/

#include <stdio.h>
#include <stdlib.h>
#include <math.h>

#define N 10
void main(void)
{
        float energy[N], tdepth[N], c0[N], c5[N], c10[N], c20[N], c30[N], c40[N], c50[N],
c60[N], c70[N], c80[N], c90[N], c95[N], penergy, ptdepth, pc0, pc5, pc10,
        pc20, pc30, pc40, pc50, pc60, pc70, pc80, pc90, pc95, tdepth00, tdepth05, tdepth10,
tdepth20, tdepth30, tdepth40, tdepth50, tdepth60, tdepth70, tdepth80,
        tdepth90, tdepth95, lastvalue;
        int i;

penergy = 50;

FILE *bint722, *bint722out;

        bint722=fopen("scalptable","r");
        bint722out=fopen("profile","w");

for(i=1; i<=N; i++)
        {
        fscanf(bint722,"%f %f %e %e %e %e %e %e %e %e %e %e %e %e", &energy[i],
&tdepth[i], &c0[i], &c5[i], &c10[i], &c20[i], &c30[i], &c40[i], &c50[i], &c60[i],
        &c70[i], &c80[i], &c90[i], &c95[i]);
        }

        {
        if (penergy > energy[N] || penergy < energy[1])
                {
                printf("You have entered a value beyond interpolatable range!\n");
                }

        else for(i=1; i<=N; i++)
                {
                if ((penergy - energy[i]) == 0)
                        {
```

```
                ptdepth = tdepth[i];
                pc0 = c0[i];
                pc5 = c5[i];
                pc10 = c10[i];
                pc20 = c20[i];
                pc30 = c30[i];
                pc40 = c40[i];
                pc50 = c50[i];
                pc60 = c60[i];
                pc70 = c70[i];
                pc80 = c80[i];
                pc90 = c90[i];
                pc95 = c95[i];

printf("For an implant energy of %f keV,\ntdepth is %f and C0, C5, C10, C20, C30, C40, C50,
C60, C70, C80, C90 and C95 are %e %e %e %e %e %e %e %e %e %e %e %e\n",penergy,
ptdepth, pc0, pc5, pc10, pc20, pc30, pc40, pc50, pc60, pc70, pc80, pc90, pc95);
                }

            if ((penergy > energy[i]) && (penergy < energy[i+1]) )
                {
                ptdepth = (penergy-energy[i])/(energy[i+1]-
energy[i])*(tdepth[i+1]-tdepth[i])+tdepth[i];
                pc0 = (penergy-energy[i])/(energy[i+1]-energy[i])*(c0[i+1]-
c0[i])+c0[i];
                pc5 = (penergy-energy[i])/(energy[i+1]-energy[i])*(c5[i+1]-
c5[i])+c5[i];
                pc10 = (penergy-energy[i])/(energy[i+1]-
energy[i])*(c10[i+1]-c10[i])+c10[i];
                pc20 = (penergy-energy[i])/(energy[i+1]-
energy[i])*(c20[i+1]-c20[i])+c20[i];
                pc30 = (penergy-energy[i])/(energy[i+1]-
energy[i])*(c30[i+1]-c30[i])+c30[i];
                pc40 = (penergy-energy[i])/(energy[i+1]-
energy[i])*(c40[i+1]-c40[i])+c40[i];
                pc50 = (penergy-energy[i])/(energy[i+1]-
energy[i])*(c50[i+1]-c50[i])+c50[i];
                pc60 = (penergy-energy[i])/(energy[i+1]-
energy[i])*(c60[i+1]-c60[i])+c60[i];
                pc70 = (penergy-energy[i])/(energy[i+1]-
energy[i])*(c70[i+1]-c70[i])+c70[i];
                pc80 = (penergy-energy[i])/(energy[i+1]-
energy[i])*(c80[i+1]-c80[i])+c80[i];
                pc90 = (penergy-energy[i])/(energy[i+1]-
energy[i])*(c90[i+1]-c90[i])+c90[i];
                pc95 = (penergy-energy[i])/(energy[i+1]-
energy[i])*(c95[i+1]-c95[i])+c95[i];

printf("For an implant energy of %f keV,\ntdepth is %f and C0, C5, C10, C20, C30, C40, C50,
C60, C70, C80, C90 and C95 are %e %e %e %e %e %e %e %e %e %e %e %e\n",penergy,
ptdepth, pc0, pc5, pc10, pc20, pc30, pc40, pc50, pc60, pc70, pc80, pc90, pc95);
                }
            }
    }
```

```
lastvalue = 1.000e15;
tdepth00  = ptdepth * 0.00;
tdepth05  = ptdepth * 0.05;
tdepth10  = ptdepth * 0.10;
tdepth20  = ptdepth * 0.20;
tdepth30  = ptdepth * 0.30;
tdepth40  = ptdepth * 0.40;
tdepth50  = ptdepth * 0.50;
tdepth60  = ptdepth * 0.60;
tdepth70  = ptdepth * 0.70;
tdepth80  = ptdepth * 0.80;
tdepth90  = ptdepth * 0.90;
tdepth95  = ptdepth * 0.95;

fprintf(bint722out,"  XUnitText: um\n  YUnitText: /cm3\n  XLowLimit:   0.\n XHighLimit:
10.00000\n LogY: true\n  YLowLimit:     12.0000\n YHighLimit:     21.0000\n TitleText:
dios\nITotal\n%f     %e\n%f     %e\n%f     %e\n%f     %e\n%f     %e\n%f     %e\n%f     %e\n%f
%e\n%f     %e\n%f     %e\n%f     %e\n%f     %e\n%f     %e\n",tdepth00, pc0, tdepth05, pc5,
tdepth10, pc10, tdepth20, pc20, tdepth30, pc30, tdepth40, pc40, tdepth50, pc50, tdepth60,
pc60, tdepth70, pc70, tdepth80, pc80, tdepth90, pc90, tdepth95, pc95, ptdepth, lastvalue);
}
```

UNIX script for linking C++ code to DIOS input file (*link*)

```
set energy=”user-defined”
echo $energy
sed s/penergy=50/penergy=$energy/g  interpolate.cc > interpolate2.cc
c++ interpolate2.cc
a.out
```

DIOS input file

```
TITLE("simple nmos example")

!     ************* Set up user-grid and substrate *************

! Define a user-grid to start (simulate half of the symmetric structure):
grid( x=(0.0, 0.4)  y=(-1.0, 0.0), nx=6)

! silicon substrate definition:
substrate (orientation=100, elem=B, conc=5.0E14, ysubs=0.0)

! start the graphical output, set to update each step & every 10 time steps:
replace(control(ngra=10))
graph(triangle=on, plot)

!     ************* Start simulation of Process Steps *************
comment('poly gate deposition')
deposit(material=po, thickness=180nm)

comment('poly gate pattern')
mask(material=re, thickness=800nm, xleft=0, xright=0.09)

comment('poly gate etch')
```

```
etching(material=po, stop=sigas, rate(aniso=200))
etch(material=re)
replace(control(refineall=2,refineboundary=4))

comment('attempting to load profile')
set energy=50
set species=I
sh link
implantation(si(file='int.plx', stdvl=2.56e-3), Fit1dprofiletodose=on, factor=1, function=1dmc,
element=$species, damage=no, amorphization=no, energy=$energy, t=-7, rot=22)

1d(file=output, xsection(0.2), spe(Itotal), fac=-1, append=off, format=plx)

save(file=ninit,type=dfise)

exit
```

APPENDIX D DMOL INPUT FILES USED IN POTENTIAL CALCULATIONS

The following described the procedure for calculating the total energy in DMOL (version 960)

1. Three files are necessary for the simulation to proceed.

   (a) ***.car*** file describing the geometry of the system in angstroms, which is automatically updated during calculation. For example, for the calculation of the total energy of a system consisting of two B atoms separated 10Å apart, the ***.car*** file will be given as

```
!BIOSYM archive 3
PBC=OFF
!DATE Tue Mar  2 10:45:08 2004
B       0.000000000    0.000000000    0.000000000 XXX  ND    ?      B   0.000
B      10.000000000    0.000000000    0.000000000 XXX  ND    ?      B   0.000
end
end
```

   (b) ***.input*** file consisting of keywords and their associated options which direct the calculation and provide options for various aspects of the calculation

```
DMOL input file for the TRY molecule.  Fri Nov 7 17:11:13 2003
Product DMol
Version 960

#    ==  Primary Job Keywords  ==
Calculate  energy
Basis      dn
Geometry   car  angs
Symmetry   C1
Spin       restricted
Charge     0.000000
Occupation default

#    ==  DFT Specifications  ==
Functionals      vwn
Integration_Grid fine

#    ==  Environment  ==
Point_Charges  off
Electric_Field off

#    ==  Molecular Properties  ==
Electrostatic_Moments off
Mulliken_analysis 0
Hirshfeld_analysis 0
Plot                off
```

```
#    ==  Additional Job Control  ==
Ndiff       1
Vibdif      0.010000
Project     on
FrqRestart  0
Lmax        2 2
Frozen      none
Fixoc       1000
Print       off
Partial_DOS off

#    ==  SCF Tolerances, Limits & Convergence Criteria  ==
SCF_Density_Convergence 0.0000010000
SCF_Energy_Convergence  off
SCF_Iterations          100
Mixing_Alpha            0.250000
Mixing_Beta             0.250000
SCF_Restart             off
Smear                   0.100000
Number_Bad_Steps        13
Direct_SCF              on
```

(c) a script file, ***.csh*** for background running of job

```
dmol “filename”
set e_status = $status
exit $e_status
```

2. The simulation is first started with the default double numerical (DN) basis set. The basis set files (***.inatom*** and ***.basis***) based on the default DN basis sets as well as the output files (***.occup***, ***.outmol*** and ***.outatom***) will be generated. The ***.inatom*** file needs to be modified for addition of hydrogenic orbitals.

3. The addition of orbitals to the basis set is achieved by constructing a new basis set, with the *DATOM* utility supplied with the DMOL program package and changing the basis option in the ***.input*** file to “user-defined” option. For Z_1<11 (B, C, N and F), the standard basis sets are automatically augmented with hydrogenic orbitals. For Z_1>11 (P, Ge, As, In and Sb), hydrogenic orbitals have been added for two nuclear charges, Z_1 and Z_1-1. For the special case of Si, hydrogenic orbitals 1s, 2p, 3d and 4f are added for four nuclear charges, Z_1=14, 13, 11 and 15. The format of the ***.inatom*** and the modified ***.input*** files for a B-B pair energy calculation are given below:

```
! Atomic basis set for Boron (Z1 = 5), hydrogenic orbitals includes automatically
vwn  none none            ! local correlation functional with no gradient correction
```

```
5.,0,0,0,0,          ! za, ncha, nspin, istart, ithrow
5.,0,0,1,2,          ! za = nuclear charge of atom,
5.,2,0,1,-1,         ! ncha = number of orbital occupations to be changed from
2,0,-1.,0.,          that of neutral atom to specify occupations in ions
2,1,-1.,0.,          ! nspin = spin-restricted calculation (0 or 1)
5.,4,0,-1,-1,        ! istart = starting potential for atomic DFT calculation
4,3,0.,0.,           ! ithrow = option for handling orbitals after each calculation
3,2,0.,0.,
2,1,0.,0.,           ! nprinc, Lorb, oup, odown
1,0,0.,0.,           ! ncha lines of this type is required
7.,4,0,-1,-1,        ! nprinc = principle quantum number of orbital whose
4,3,0.,0.,           occupation is to be changed
3,2,0.,0.,           ! Lorb = angular momentum quantum number of orbital
2,1,0.,0.,           whose occupation is to be changed
1,0,0.,0.,           ! oup = occupation charge for spin up
-1                   ! odown = occupation charge for spin down
```

```
! Modified DMOL input file for the TRY molecule.  Fri Nov 7 17:11:13 2003
Product DMol
Version 960

#    ==  Primary Job Keywords  ==
Calculate  energy
Basis      user
13 0 0 0 0 0 0 0 0 0 0 0 0 0
13 0 0 0 0 0 0 0 0 0 0 0 0 0
```

(Note: When **user** is specified, the exact orbitals in the .basis file to be retained, dropped, or treated as frozen core can be specified. Starting from the line immediately after the keyword **Basis**, the data for each unique atom type (i.e., for each different atomic number) in the same order that the atoms appear in the **Geometry** specification is entered. The data have the format:

nfrz   *nnls(i), i=1,nfrz*

nfrz = number of atomic basis functions on the atom
nnls(*i*) tells DMol how to treat the *ith* basis function of that atom.

nnls(*i*) = 0 means include basis function #*i* in the calculation.
nnls(*i*) = 1 means treat basis function #*i* as a frozen core.
nnls(*i*) = 2 means delete this basis function entirely.

nfrz and *nnls* are repeated for each atom type, the list is terminated with a blank line, all the rest of the parameters in the input file remain unchanged)

```
Geometry   car  angs
Symmetry   C1
Spin       restricted
Charge     0.000000
Occupation default

#    ==  DFT Specifications  ==
Functionals     vwn
```

```
Integration_Grid fine

#    ==  Environment  ==
Point_Charges  off
Electric_Field off

#    ==  Molecular Properties  ==
Electrostatic_Moments off
Mulliken_analysis 0
Hirshfeld_analysis 0
Plot                off

#    ==  Additional Job Control  ==
Ndiff      1
Vibdif     0.010000
Project    on
FrqRestart  0
Lmax       2 2
Frozen     none
Fixoc      1000
Print      off
Partial_DOS off

#    ==  SCF Tolerances, Limits & Convergence Criteria  ==
SCF_Density_Convergence 0.0000010000
SCF_Energy_Convergence  off
SCF_Iterations         100
Mixing_Alpha           0.250000
Mixing_Beta            0.250000
SCF_Restart            off
Smear                  0.100000
Number_Bad_Steps       13
Direct_SCF             on
```

4. The calculations are then repeated with the modified ***.inatom*** and ***.input*** file. When *DATOM* utility is run, formatted output appears in the ***.outatom*** file, containing a summary of each atomic calculation. The basis sets themselves are written to a binary file ***.basis***. This file consists of the value of each atomic orbital over a spherical mesh consisting of about 300 radial points. When these data are read by DMOL, the value of each basis function at each molecular mesh point is determined by a spline fit on the atomic mesh. An example of an ***.outatom*** file for a B-B potential energy run is shown below:

```
----------------------------------------------------
 Basis set generated using Datom program
----------------------------------------------------
datom psi/biosym version 1/95
input as read:
vwn  none none
```

```
interpreted as:
vosko wilk nusair local correlation

input as read:
5.,0,0,0,0,            ! B
interpreted as:
5.0  Boron        0  0  0  0
dist   1  9.47E-01  1  0   0.55   0.95
dist   2 -1.47E-01  1  0   0.55  -0.15
dist   3 -2.25E-02  1  0   0.55   0.15
dist   4 -5.54E-03  1  0   0.55   0.25
dist   5 -1.69E-03  1  0   0.55   0.30
dist   6 -5.97E-04  1  0   0.55   0.35
dist   7 -2.23E-04  1  0   0.55   0.37
dist   8 -8.44E-05  1  0   0.55   0.38
dist   9 -3.21E-05  1  0   0.55   0.38
dist  10 -1.22E-05  1  0   0.60   0.38
dist  11 -5.07E-06  1  0   0.65   0.42
dist  12 -1.79E-06  1  0   0.70   0.35
dist  13 -5.18E-07  1  0   0.75   0.29
dist  14 -1.18E-07  1  0   0.80   0.23
dist  15 -1.98E-08  1  0   0.85   0.17
dist  16  3.49E-09  2  0   1.00  -0.18
dist vrs  4.60E-08  9.54  6.63E-09  1.67 -2.73E-09  1.67
5.0   B
1s  2.00      -6.564347 -1.02E-10Ha      -178.625eV
2s  2.00      -0.344701  5.79E-10Ha        -9.380eV
2p  1.00      -0.136603  5.68E-10Ha        -3.717eV

ion charge             2.664535E-15
sumei,eee,eze (ha)       -13.954698      23.006005     -56.484589
kinetic energy           24.161048ha       657.456ev
exchange:    local       -3.229170ha        -87.870ev
nlsd          0.000000ha         0.000ev
correlation: local       -0.294490ha        -8.013ev
nlsd          0.000000ha         0.000ev
exchange+correlation      -3.523660ha        -95.884ev

total energy: local      -24.344198ha       -662.440ev
nlsd       -24.344198ha       -662.440ev

input as read:
5.,0,0,1,2,
 interpreted as:
5.0  Boron        0  1  1  2
dist   1  2.18E-02 -2  0   0.55   0.02
dist   2  5.99E-03 -1  0   0.55   0.28
dist   3  9.41E-04 -1  0   0.55   0.16
dist   4  2.78E-04 -2  0   0.55   0.30
dist   5  1.29E-04 -2  0   0.60   0.46
dist   6  7.07E-05 -2  0   0.60   0.55
dist   7  3.31E-05 -2  0   0.65   0.47
dist   8  1.69E-05 -2  0   0.65   0.51
dist   9  7.30E-06 -2  0   0.65   0.43
```

```
dist  10  3.15E-06 -2  0   0.65   0.43
dist  11  1.38E-06 -1  0   0.65   0.44
dist  12  6.16E-07 -1  0   0.65   0.45
dist  13  2.75E-07 -1  0   0.65   0.45
dist  14  1.22E-07 -1  0   0.65   0.44
dist  15  5.43E-08 -1  0   0.65   0.44
dist  16  2.41E-08 -1  0   0.65   0.44
dist  17  1.07E-08 -1  0   0.65   0.44
dist  18  4.75E-09 -1  0   1.00   0.44
dist vrs  1.29E-08  6.58  5.19E-09  1.24  5.96E-08  1.24

5.0   B
1s  1.00      -6.563384  1.01E-09Ha      -178.599eV
1s  1.00      -6.550876  3.18E-09Ha      -178.258eV
2s  1.00      -0.360441  4.50E-11Ha        -9.808eV
2s  1.00      -0.318624  2.83E-09Ha        -8.670eV
2p  1.00      -0.150853  3.31E-10Ha        -4.105eV
2p  0.00      -0.113184  2.10E-09Ha        -3.080eV

spin polarization. energy:
local                  -0.009416ha         -0.256ev
local + nlsd           -0.009416ha         -0.256ev
sumei,eee,eze (ha)       -13.944179      23.056468     -56.516741
kinetic energy           24.172453ha       657.766ev
exchange:    local       -3.246916ha       -88.353ev
nlsd          0.000000ha          0.000ev
correlation: local       -0.290643ha        -7.909ev
nlsd          0.000000ha          0.000ev
exchange+correlation      -3.537559ha       -96.262ev

total energy: local      -24.353614ha       -662.696ev
nlsd       -24.353614ha       -662.696ev

input as read:
5.,2,0,1,-1,
interpreted as:
5.0  Boron         2  0  1 -1
n, l, delta occ  2  0  -1.000   0.000
n, l, delta occ  2  1  -1.000   0.000
dist   1  1.91E-02  2  0   0.55   0.02
dist   2 -6.83E-01  1  0   0.55 -35.72
dist   3 -2.64E-01  1  0   0.60   0.39
dist   4 -1.16E-01  1  0   0.65   0.44
dist   5 -4.42E-02  1  0   0.70   0.38
dist   6 -1.40E-02  1  0   0.75   0.32
dist   7 -3.80E-03  2  1   0.80   0.27
dist   8 -8.81E-04  2  0   0.85   0.23
dist   9 -1.56E-04  2  0   0.90   0.18
dist  10 -1.77E-05  2  0   0.95   0.11
dist  11  2.51E-06  1  0   0.95  -0.14
dist  12  3.33E-07  1  0   0.95   0.13
dist  13  2.75E-08  1  0   1.00   0.08
dist  14  2.10E-09  1  0   1.00   0.08
dist vrs  5.94E-06 17.90  3.03E-10  1.61 -3.02E-10  1.61
```

```
5.0   B
orthogonalized against n = 1  0.999990
orthogonalized against n = 2  0.002935
1s  2.00      -7.683693  4.77E-11Ha      -209.084eV     1.09E-05 residual
rejected as basisfunction, norm after orthogonalization too small
orthogonalized against n = 1 -0.003376
orthogonalized against n = 2  0.977810
2s  1.00      -1.151191  2.92E-11Ha       -31.326eV     4.39E-02 residual
orthogonalized against n = 2  0.934919
2p  0.00      -0.937633  3.30E-11Ha       -25.514eV     1.26E-01 residual

ion charge            2.000000E+00
sumei,eee,eze (ha)       -16.518577      15.043699     -50.675635
kinetic energy           22.974345ha       625.164ev
exchange:    local       -2.723530ha       -74.111ev
nlsd          0.000000ha          0.000ev
correlation: local       -0.205822ha        -5.601ev
nlsd          0.000000ha          0.000ev
exchange+correlation      -2.929352ha       -79.712ev

total energy: local      -23.108793ha      -628.823ev
nlsd       -23.108793ha       -628.823ev

input as read:
5.,4,0,-1,-1,
interpreted as:
5.0  Boron        4  0 -1 -1  hydrogenic atom calculation
n, l, delta occ  4  3   0.000   0.000
n, l, delta occ  3  2   0.000   0.000
n, l, delta occ  2  1   0.000   0.000
n, l, delta occ  1  0   0.000   0.000
5.0   B
4f  0.00      -0.781250 -4.26E-07Ha       -21.259eV     1.00E+00 residual
3d  0.00      -1.388889 -1.15E-07Ha       -37.794eV     1.00E+00 residual
orthogonalized against n = 2  0.715453
orthogonalized against n = 2  0.597460
2p  0.00      -3.125000  2.83E-07Ha       -85.036eV     1.31E-01 residual
orthogonalized against n = 1  0.996005
orthogonalized against n = 2  0.044829
orthogonalized against n = 2  0.043130
1s  0.00     -12.500000 -8.40E-08Ha      -340.142eV     4.10E-03 residual

ion charge            5.000000E+00

input as read:
7.,4,0,-1,-1,
interpreted as:
7.0  Nitrogen      4  0 -1 -1  hydrogenic atom calculation
n, l, delta occ  4  3   0.000   0.000
n, l, delta occ  3  2   0.000   0.000
n, l, delta occ  2  1   0.000   0.000
n, l, delta occ  1  0   0.000   0.000
7.0   N
```

```
orthogonalized against n = 4  0.880937
4f  0.00      -1.531251 -8.32E-07Ha       -41.667eV     2.24E-01 residual
orthogonalized against n = 3  0.906107
3d  0.00      -2.722222 -2.29E-07Ha       -74.075eV     1.79E-01 residual
orthogonalized against n = 2  0.525056
orthogonalized against n = 2  0.564997
orthogonalized against n = 2  0.604076
2p  0.00      -6.124999  5.53E-07Ha      -166.670eV     4.02E-02 residual
orthogonalized against n = 1  0.933262
orthogonalized against n = 2  0.117092
orthogonalized against n = 2  0.125250
orthogonalized against n = 1  0.287820
1s  0.00     -24.500000 -1.58E-07Ha      -666.679eV     1.68E-02 residual

ion charge            7.000000E+00

input as read:
 -1
interpreted as:
z<0 : all done
```

5. The results of each simulation can be found in the ***.outmol*** file. The example shown below is obtained with the input files shown above, a B-B pair single-point calculation using VWN functional with DN basis sets with additional hydrogenic orbitals. By changing the separation in the ***.car*** file, total energy values can be obtained at different r and the potential energy curve can be obtained by subtracting the total energy at r=8 from that at r=r. The ***.outmol*** file starts with a header that gives the version number of the program and copyright information. Following this is a summary of all the input flags in the input file.

```
DMol Version 960
Density Functional Theory electronic structure program.
Copyright (c) 1996 by Molecular Simulations, Inc.

INPUT FLAGS:
______________________________________________________________________
Calculate  energy
Basis    USER
Geometry   car   angs
Symmetry C1
Spin       restricted
Charge   0.000000
Occupation DEFAULT

Integration_Grid FINE
Nonlocal          energy
Functionals       vwn
Electric_Field  off
Point_Charges   off
```

```
Solvate        off
Electrostatic_Moments off
Mulliken_analysis  0
Bond_Order off
Hirshfeld_analysis 0
ESP_Charges off
Nuclear_EFG off
Optical_Absorption off

Plot  off

Ndiff   1
Vibdif     0.010000
Project on
FrqRestart 1
Frozen  none
Lmax  2 2
Fixoc   1000
Print off

Smear           0.100000
SCF_Density_Convergence  1e-06
Number_Bad_Steps 13
SCF_Energy_Convergence   Off
SCF_Iterations   100
Direct_SCF  on
Mixing_Alpha     0.250000
Partial_DOS off
DIIS     4
Mixing_Beta      0.250000
SCF_Restart off
```

Following this come several lines that reflect the input options that are indicated above.

```
nat=   2 nspin=0 nfroz= 1 ihirsh=0 imull=0 iplot=0 idip=0 nitpri=  0
iscf=100 iuwav=0 iupot=0 itask=0 idrct=1 nbstep=13 idofld=0 idos=0

Molecule Rotation Matrix:
0.00000   1.00000   0.00000
0.00000   0.00000   1.00000
1.00000   0.00000   0.00000

Molecule Center Of Mass Offset:
499.50000   0.00000   0.00000
```

The next section is headed by the string "specifications for basis sets". Following this appears the basis set data which are read from the ***.inmol*** file or generated internally if the .input file is used. These lines appear in a format such as:

```
specifications for basis sets:
nfile=  5  nbas= 1  nfroz=13   0 0 0 0 0 0 0 0 0 0 0 0 0
```

Here nfile refers to the basis set number in the ***.basis*** file (which equals the atomic number), nbas counts the total number of basis sets that have been read in. These indicate whether an atomic basis function is ignored completely (=2), included as a valence orbital (=0), or included as a frozen core (=1). Following these lines appears a summary of the basis set information extracted from the ***.basis*** file.

```
Boron      nbas= 1  z= 5. 13 radial functions,  spin energy= -0.009
n=1  L=0  occ= 2.00 e=     -6.564347     -178.6250
n=2  L=0  occ= 2.00 e=     -0.344701       -9.3798
n=2  L=1  occ= 1.00 e=     -0.136603       -3.7172
n=2  L=0  occ= 0.00 e=     -1.151191      -31.3255
n=2  L=1  occ= 0.00 e=     -0.937633      -25.5143
n=4  L=3  occ= 0.00 e=     -0.781250      -21.2589
n=3  L=2  occ= 0.00 e=     -1.388889      -37.7936
n=2  L=1  occ= 0.00 e=     -3.125000      -85.0356
n=1  L=0  occ= 0.00 e=    -12.500000     -340.1425
n=4  L=3  occ= 0.00 e=     -1.531251      -41.6675
n=3  L=2  occ= 0.00 e=     -2.722222      -74.0755
n=2  L=1  occ= 0.00 e=     -6.124999     -166.6698
n=1  L=0  occ= 0.00 e=    -24.500000     -666.6792
```

This includes the atom name, nuclear charge, total number of basis functions (referred to as radial functions), atomic spin energy, and total atomic energy (spin-restricted). Spin energy is the difference in the atomic energies between spin-restricted and spin-unrestricted calculations. Next comes a list of each atomic orbital, or radial function, specifying the principal quantum number, angular momentum, occupation in the atomic calculation, and orbital eigenvalue in Hartrees and in eV. Lastly, a flag telling how the basis function is used in the calculation is shown. This can be frozen, meaning frozen core; blank, meaning active; or eliminated, meaning dropped from the calculation completely. The next two lines show the density functional methods used:

```
vwn  none none
Vosko Wilk Nusair local correlation
```

The next section summarizes the symmetry information. In this case, no global symmetry is used for the system.

```
no SYMDEC file present
no global symmetry used for this molecule
```

The next section summarizes the total number of orbitals, followed by a summary of the atomic coordinates.

```
n  norb   jdegn   representation
1   82      1       a
total number of valence orbitals:     82

n  norc   jdegn   representation
1    0      1       a
total number of core orbitals:      0

need: mws, mwfm,   mwvc,    mwn, mwv, mwc, mwm, coef
3403    6724       0      32   82    0   82    1
current dimensions:
3403    6724       0      32   82    0   82    1

coordinates for atoms        atom type mceq  bas file element
0.000000    0.000000    0.000000    1     1     1     1    5  Boron
1887.836263    0.000000    0.000000    2     1     2     1    5  Boron
```

The coordinates are the Cartesian coordinates of the atoms in the order in which they appeared in the input file. The column “type” reflects the different atomic numbers of atoms in the input--each different atomic number is assigned a new type. “mceq” indicates which atoms are symmetrically equivalent. The column “bas” indicates the order in which basis sets are found in the ***.basis*** file. Several sections appear that show input data, including the orbital occupations, parameters for the integration procedure, and the maximum angular momentum of the fitting functions. The occupation information looks like:

```
occup input as read:
0   0.00000 1000   0.10000
as interpreted:
iopt=   0     0.00  icfr=      1000    delte=  1.00E-01
molecule charge=   0.0   active electron number=   10.0
including core=   10.0   (without charge=          10.0)
```

Setting iopt = 0 tells the program to attempt to determine the optimal orbital occupation. Setting icfr = 1000 instructs the program to attempt this for the first 1000 iterations, which should be all iterations. Next, information for the fitting basis is read. This indicates the number of spherical harmonic functions that are used in the analytic representation of the model density and electrostatic potential:

```
prolo input as read from INMOL:
0    0    1    0    1    2
```

```
as interpreted:
npr 0 mlod  0 ipart 1 iref 0 lmaxv   2
no symmetry assumed for potential
nrf,mwf         18         18
modef      62339      500000       1269          6
```

Following this is information about the number of gradient directions to be evaluated.

```
prede1 input as read from INMOL:
0    0
as interpreted:
modes,nprder    0    0
no symmetry assumed for derivatives
```

The section controlling the numerical integration parameters appears as follows:

```
parti3 input as read:
0    0    5    6    1  0.000010 12.000000  1.200000
as interpreted:
inputs,npri,ipa,iomax,iomin,thres,rmaxp,sp
0    0    5    6    1   0.00001  12.00000   1.20000
wta dimension        4282
file type nrtb   zn   rmaxp   thres     thresh     iomax iomin lmaxv lmaxz
5    1   32   5.  12.000  0.00001  0.00000031     6     3     2     3
Integration points and checksum:       3202       9.999990
Integration points and checksum:       3202       9.999990
mwp        3202

Memory use data:
nloop=      3203     3834      237      285   157256
nloopd=      821      822      656      656       16       13
int array elements available (maxi):    500000 (  1.9 Mb)
real array elements available (maxr):   1250000 (  9.5 Mb)
minimum real array elements needed:    212272 (  1.6 Mb)
real array elements used:    708864 (  5.4 Mb)
```

Next follows a number of parameters that control the SCF (self-consistent field) calculation:

```
SCF parameter input as read:
2.500E-01 2.500E-01 1.000E-06 0.000E+00
as interpreted:
mixing parameters   0.25000   0.25000

Density tolerance for converging SCF: 1.000E-06
```

Next begin the actual self-consistent iterations for solution of the DFT equations. A summary of the self-consistent procedure appears after each iteration. This information includes the total energy, binding energy (relative to free atoms), nuclear repulsion energy, degree of convergence for the density and the total elapsed CPU time (seconds on Cray, minutes on other machines). For this example, the output is:

```
Total Energy          Binding E   Cnvgnce_Dens    Cnvgnce_E       Time
ef   -0.4868839960E+02       0.0188280    0.0000794       -           0.0
ef   -0.4868839999E+02       0.0188276    0.0000593    0.00000039        0.0
ef   -0.4868840116E+02       0.0188265    0.0000006    0.00000117        0.0

en total energy:       -48.6884012 au      -1324.87937 eV      -30552.381 Kcal/mol
en binding energy:       0.0188265 au          0.51229 eV          11.814 Kcal/mol
en nuclear repulsion energy:          0.0132427 au
```

Following the final iteration appear the molecular orbital (MO) eigenvalues in Hartrees and the orbital occupations; these appear in columns, one for each molecular orbital. Expansion coefficients, if requested, appear only for active (not frozen) orbitals. MOs are grouped first by atom, and then by angular momentum, as illustrated in the following example:

```
Eigenvalues and occupations:

Alpha orbitals, symmetry block   1    a
Degeneracy:   1  Size:  82

-0.65643E+01    -0.65643E+01    -0.34470E+00    -0.34470E+00    -0.13660E+00    -
 0.13660E+00 -0.13660E+00 -0.13660E+00 -0.13660E+00 -0.13660E+00
  2.00         2.00         2.00         2.00         0.33         0.33         0.33         0.33         0.33
 0.33


 0.17195E+00       0.17195E+00       0.17195E+00       0.17195E+00       0.17195E+00
 0.17195E+00  0.23447E+00  0.23447E+00  0.40425E+00  0.40425E+00
  0.00         0.00         0.00         0.00         0.00         0.00         0.00         0.00         0.00
 0.00


 0.40425E+00       0.40425E+00       0.40425E+00       0.40425E+00       0.40425E+00
 0.40425E+00  0.40425E+00  0.40425E+00  0.40425E+00  0.40425E+00
 0.00         0.00         0.00         0.00         0.00         0.00         0.00         0.00         0.00
 0.00

Molecular orbital spectrum:

energy of Highest Occupied Molecular Orbital     -0.136602        -3.717
number of eigenvalues listed: 82

state                     eigenvalue         occupation
(au)            (ev)

 1   +    1    a        -6.564341      -178.625    2.000
 2   +    2    a        -6.564341      -178.625    2.000
 3   +    3    a        -0.344700        -9.380    2.000
```

4	+	4	a	-0.344700	-9.380	2.000
5	+	5	a	-0.136602	-3.717	0.333
6	+	6	a	-0.136602	-3.717	0.333
7	+	7	a	-0.136602	-3.717	0.333
8	+	8	a	-0.136602	-3.717	0.333
9	+	9	a	-0.136602	-3.717	0.333
10	+	10	a	-0.136602	-3.717	0.333
11	+	11	a	0.171946	4.679	0.000
12	+	12	a	0.171946	4.679	0.000
13	+	13	a	0.171946	4.679	0.000
14	+	14	a	0.171946	4.679	0.000
15	+	15	a	0.171946	4.679	0.000
16	+	16	a	0.171946	4.679	0.000
17	+	17	a	0.234466	6.380	0.000
18	+	18	a	0.234468	6.380	0.000
19	+	19	a	0.404245	11.000	0.000
20	+	20	a	0.404245	11.000	0.000
21	+	21	a	0.404245	11.000	0.000
22	+	22	a	0.404245	11.000	0.000
23	+	23	a	0.404245	11.000	0.000
24	+	24	a	0.404245	11.000	0.000
25	+	25	a	0.404245	11.000	0.000
26	+	26	a	0.404245	11.000	0.000
27	+	27	a	0.404245	11.000	0.000
28	+	28	a	0.404245	11.000	0.000
29	+	29	a	0.404245	11.000	0.000
30	+	30	a	0.404245	11.000	0.000
31	+	31	a	0.404245	11.000	0.000
32	+	32	a	0.404245	11.000	0.000
33	+	33	a	0.481000	13.089	0.000
34	+	34	a	0.481000	13.089	0.000
35	+	35	a	0.481000	13.089	0.000
36	+	36	a	0.481000	13.089	0.000
37	+	37	a	0.481000	13.089	0.000
38	+	38	a	0.481000	13.089	0.000
39	+	39	a	0.481000	13.089	0.000
40	+	40	a	0.481000	13.089	0.000
41	+	41	a	0.481000	13.089	0.000
42	+	42	a	0.481000	13.089	0.000
43	+	43	a	1.386432	37.727	0.000
44	+	44	a	1.386432	37.727	0.000
45	+	45	a	1.386432	37.727	0.000
46	+	46	a	1.386432	37.727	0.000
47	+	48	a	1.386433	37.727	0.000
48	+	47	a	1.386433	37.727	0.000
49	+	49	a	1.624023	44.192	0.000
50	+	50	a	1.624023	44.192	0.000
51	+	51	a	1.624023	44.192	0.000
52	+	52	a	1.624023	44.192	0.000
53	+	53	a	1.624023	44.192	0.000
54	+	54	a	1.624023	44.192	0.000
55	+	55	a	1.624023	44.192	0.000
56	+	56	a	1.624023	44.192	0.000
57	+	57	a	1.624023	44.192	0.000

```
58  +  58   a      1.624023     44.192   0.000
59  +  59   a      1.624023     44.192   0.000
60  +  60   a      1.624023     44.192   0.000
61  +  61   a      1.624023     44.192   0.000
62  +  62   a      1.624023     44.192   0.000
63  +  63   a      2.580412     70.217   0.000
64  +  64   a      2.580412     70.217   0.000
65  +  65   a      2.580412     70.217   0.000
66  +  66   a      2.580412     70.217   0.000
67  +  67   a      2.580412     70.217   0.000
68  +  68   a      2.580412     70.217   0.000
69  +  69   a      2.580412     70.217   0.000
70  +  70   a      2.580412     70.217   0.000
71  +  71   a      2.580412     70.217   0.000
72  +  72   a      2.580412     70.217   0.000
73  +  73   a      4.978180    135.463   0.000
74  +  74   a      4.978185    135.463   0.000
75  +  75   a      7.598732    206.772   0.000
76  +  76   a      7.598732    206.772   0.000
77  +  77   a      7.598732    206.772   0.000
78  +  78   a      7.598732    206.772   0.000
79  +  79   a      7.598737    206.772   0.000
80  +  80   a      7.598737    206.772   0.000
81  +  81   a     47.712623   1298.328   0.000
82  +  82   a     47.712640   1298.328   0.000
```

Finally, the .outmol file concludes with the run time.

```
all done time     0.033
hostname: cougar.nus.edu.sg
platform: irix6m4
All Done: time = 1.8u 0.5s 0:02 82% 0+0k 7+52io 4pf+0w
```

The quantity we are interested in the total energy of the system (in bold), which is expressed in units of atomic units, eV or kcal/mol. For this work, all input conditions are kept constant, while the basis sets are augmented with hydrogenic orbitals. The ***.inatom*** files for all nine species (B, C, N, F, P, Ge, As, In and Sb) studied in this work are shown in Table D.1 below. As mentioned, B, C, N and F utilizes a standard basis set with automatically augmented hydrogenic orbitals. On the other hand, basis sets of P, Ge, As, In and Sb do not contain hydrogenic orbitals by default and have been added for two nuclear charges, Z_1 and Z_1-1. For the special case of Si, hydrogenic orbitals 1s, 2p, 3d and 4f are added for four nuclear charges, Z_1=14, 13, 11 and 15. Since each orbital is orthogonalized against the previous ones, the order in which the orbitals are added can affect the results. It has been found that results obtained with the hydrogenic orbitals added in this order (Z_1=14, 13, 11 and 15) agree much better with those obtained from the fully-numerical 2D Hartee-Fock-Slater (HFS) method used for providing accurate reference potentials (Nordlund et al., 1997).

Table D.1 Input parameters in ***.inatom*** file for nine species (B, C, N, F, P, Ge, As, In and Sb) and Si as target, with standard DN basis sets and additional hydrogenic orbitals

Boron	**Carbon**	**Nitrogen**	**Fluorine**	**Phosphorous**
vwn none none	vwn none none	vwn none none	vwn none none	vwn none none
5.,0,0,0,0,	6.,0,0,0,0,	7.,0,0,0,0,	9.,0,0,0,0,	15.,0,0,0,0,
5.,0,0,1,2,	6.,0,0,1,2,	7.,0,0,1,2,	9.,0,0,1,2,	15.,0,0,1,2,
5.,2,0,1,-1,	6.,1,0,1,-1,	7.,1,0,1,-1,	9.,1,0,1,-1,	15.,2,0,1,-1
2,0,-1.,0.,	2,1,-2.,0.,	2,1,-2.,0.,	2,1,-2.,0.,	3,1,-2.,0.,
2,1,-1.,0.,	5.,4,0,-1,-1,	5.,4,0,-1,-1,	5.,4,0,-1,-1,	3,2,0.,0.,
5.,4,0,-1,-1,	4,3,0.,0.,	4,3,0.,0.,	4,3,0.,0.,	***15.,4,0,-1,-1***
4,3,0.,0.,	3,2,0.,0.,	3,2,0.,0.,	3,2,0.,0.,	***4,3,0.,0.,***
3,2,0.,0.,	2,1,0.,0.,	2,1,0.,0.,	2,1,0.,0.,	***3,2,0.,0.,***
2,1,0.,0.,	1,0,0.,0.,	1,0,0.,0.,	1,0,0.,0.,	***2,1,0.,0.,***
1,0,0.,0.,	7.,4,0,-1,-1,	7.,4,0,-1,-1,	7.,4,0,-1,-1,	***1,0,0.,0.,***
7.,4,0,-1,-1,	4,3,0.,0.,	4,3,0.,0.,	4,3,0.,0.,	***14.,4,0,-1,-1***
4,3,0.,0.,	3,2,0.,0.,	3,2,0.,0.,	3,2,0.,0.,	***4,3,0.,0.,***
3,2,0.,0.,	2,1,0.,0.,	2,1,0.,0.,	2,1,0.,0.,	***3,2,0.,0.,***
2,1,0.,0.,	1,0,0.,0.,	1,0,0.,0.,	1,0,0.,0.,	***2,1,0.,0.,***
1,0,0.,0.,	-1	-1	-1	***1,0,0.,0.,***
-1				-1
Germanium	**Arsenic**	**Indium**	**Antimony**	**Silicon**
vwn none none	vwn none none	vwn none none	vwn none none	vwn none none
32.,0,0,0,0,	33.,0,0,0,0,	49.,0,0,0,0,	51.,0,0,0,0,	14.,0,0,0,0,
32,0,0,1,2,	33.,0,0,1,2,	49.,0,0,1,2,	51.,0,0,1,2,	14.,0,0,1,2,
32.,3,0,1,-1,	33.,3,0,1,-1,	49.,3,0,1,-1,	51.,3,0,1,-1,	14.,2,0,1,-1
3,2,-1.,0.,	3,2,-1.,0.,	4,2,-1.,0.,	4,2,-1.,0.,	3,1,-2.,0.,
4,1,-1.,0.,	4,1,-1.,0.,	5,1,-1.,0.,	5,1,-1.,0.,	3,2,0.,0.,
4,2,0.,0.,	4,2,0.,0.,	5,2,0.,0.,	5,2,0.,0.,	***14.,4,0,-1,-1***
32.,4,0,-1,-1	***33.,4,0,-1,-1***	***49.,4,0,-1,-1***	***51.,4,0,-1,-1***	***4,3,0.,0.,***
4,3,0.,0.,	***4,3,0.,0.,***	***4,3,0.,0.,***	***4,3,0.,0.,***	***3,2,0.,0.,***
3,2,0.,0.,	***3,2,0.,0.,***	***3,2,0.,0.,***	***3,2,0.,0.,***	***2,1,0.,0.,***
2,1,0.,0.,	***2,1,0.,0.,***	***2,1,0.,0.,***	***2,1,0.,0.,***	***1,0,0.,0.,***
1,0,0.,0.,	***1,0,0.,0.,***	***1,0,0.,0.,***	***1,0,0.,0.,***	***13.,4,0,-1,-1***
31.,4,0,-1,-1	***32.,4,0,-1,-1***	***48.,4,0,-1,-1***	***50.,4,0,-1,-1***	***4,3,0.,0.,***
4,3,0.,0.,	***4,3,0.,0.,***	***4,3,0.,0.,***	***4,3,0.,0.,***	***3,2,0.,0.,***
3,2,0.,0.,	***3,2,0.,0.,***	***3,2,0.,0.,***	***3,2,0.,0.,***	***2,1,0.,0.,***
2,1,0.,0.,	***2,1,0.,0.,***	***2,1,0.,0.,***	***2,1,0.,0.,***	***1,0,0.,0.,***
1,0,0.,0.,	***1,0,0.,0.,***	***1,0,0.,0.,***	***1,0,0.,0.,***	***11.,4,0,-1,-1***
-1	-1	-1	-1	***4,3,0.,0.,***
				3,2,0.,0.,
				2,1,0.,0.,
				1,0,0.,0.,
				15.,4,0,-1,-1
				4,3,0.,0.,
				3,2,0.,0.,
				2,1,0.,0.,
				1,0,0.,0.,
				-1

APPENDIX E MATHEMATICAL FORMULATION OF SCATTERING PHASE SHIFTS

The mathematical derivations of scattering problems will be given here (Kopaleishvili, 1995). At the initial moment there are two infinitely separated particles, which therefore do not interact with each other. It is further assumed that they have non-zero relative velocity allowing them to be drawn together. As a result, their interaction is switched on. Thus, in the initial state there are two free particles with the given momenta and the quantum numbers characterizing the internal state of particles; as for the final state, there are two or more free particles with the given observables. The main task of the collision (scattering theory) is to find the probability of transition of the system from the initial state to the final state. Experimentally, collision processes are realized in the following way: there are many particles being part of some matter. This matter is irradiated by the beam of particles (incident particles). After the interaction with the matter, the incident particles and target particles scatter in all directions. The formulation of the scattering phase shifts will be developed here. Assuming the potential V(r) is centro-symmetric and as a result, for the particle moving in such a field the angular momentum l is the integral of motion. This enables the use of their common eigenfunctions given in Eq. (E.1) to act as basis functions for the expansion of the wave function $\varphi_{\kappa}^{(+)}(G)$ which satisfies the stationary Schrodinger equation given in Eq. (E.2)

$$Y_{lm}(\theta,\varphi) \equiv Y_{lm}(\hat{G}) \text{ where } \hat{G} = \frac{G}{r} \tag{E.1}$$

$$(D + k^2)\varphi_{\kappa}^{(+)}(G) = \frac{2\mu}{\bar{h}^2} V(r)\varphi_{\kappa}^{(+)}(G) \tag{E.2}$$

The following expansion can be written

$$\varphi_{\kappa}^{(+)}(G) = \sqrt{\frac{2}{\pi}}\sum_{l=0}^{\infty} i^{l}\varphi_{kl}^{(+)}(r)\sum_{m=-l}^{+l} Y_{lm}(\hat{G})Y_{lm}^{*}(\hat{G}) \tag{E.3a}$$

$$= (2p)^{-3/2}\sum_{l=0}^{\infty} i^{l}(2l+1)j_{kl}^{(+)}(r)P_{l}(\cos q) \tag{E.3b}$$

where the well-known relation between the Legendre polynomials $P_l(\cos q)$ and the spherical angular function $Y_{lm}(q, j)$ are related by

$$P_l(\cos\theta) = \frac{4\pi}{2l+1}\sum_{m=-l}^{+1} Y_{lm}(\hat{A})Y_{lm}(\hat{B}), \cos\theta = \hat{A}\hat{B} \tag{E.4}$$

$\varphi_\kappa^{(+)}(G)$ are the radial wave functions represented in the following form

$$\varphi_\kappa^{(+)}(G) = e^{i\delta_l(k)}\frac{u_l(kr)}{kr} \tag{E.5}$$

The quantities $\delta_l(k)$ are the phase shifts, the meaning of which will be clarified below. If Eq. (E.3a) is substituted into Eq. (E.2) where the Laplacian Δ is expressed in spherical variables,

$$D = \frac{1}{r^2}\frac{\partial}{\partial r}\left(r^2\frac{\partial}{\partial r}\right) - \frac{I}{\bar{h}^2 r^2} \tag{E.6}$$

then the radial equation for the functions $u_l(kr)$ is obtained by

$$\frac{d^2u_l}{dr^2} + \left[k^2 - \frac{2m}{\bar{h}^2}V(r) - \frac{l(l+1)}{r^2}\right]u_l = 0 \tag{E.7}$$

where the equality $I^2 Y_{lm} = \bar{h}^2 l(l+1)Y_{lm}$ was used. Before Eq. (E.7) is solved, some of the results which are obtained from this equation when V(r) = 0 i.e. from the radial Schrodinger equation for free particle are listed. When V(r) = 0 in Eq. (E.7), it leads to

$$\frac{d^2u_l^0}{dr^2} + \left[k^2 - \frac{l(l+1)}{r^2}\right]u_l^0 = 0 \tag{E.8}$$

This equation, as an arbitrary second order differential equation has two linearly independent solutions. One of them is

$$u_l^0(kr) = \tilde{j}(kr) = krj_l(kr) \tag{E.9a}$$

which is regular at r = 0, and Eq. (E.9b) which is singular at r = 0.

$$u_l^0(kr) = \tilde{n}_l(kr) = krn_l(kr) \tag{E.9b}$$

Here $n_l(x)$ is the Neumann spherical function, which is related to the ordinary Neumann function $N_{l+\frac{1}{2}}(x)$ as follows

$$n_l(x) = \sqrt{\frac{p}{2x}} N_{l+\frac{1}{2}}(x) = \sqrt{\frac{p}{2x}} (-1)^{l-1} J_{-l-\frac{1}{2}}(x) \tag{E.10}$$

For the functions $j_l(x)$ and $n_l(x)$ two linear combinations can be constructed.

$$h_l^{(\pm)}(x) = -n_l(x) \pm i j_l(x) \tag{E.11}$$

which are known as the Hankel spherical functions and have the following asymptotic behavior

$$h_l^{(\pm)}(x) \xrightarrow[x\to\infty]{} \frac{\exp\left[\pm i\left(x - \frac{lp}{2}\right)\right]}{x} \tag{E.12}$$

That is, they represent the outgoing and incoming spherical functions respectively. Now looking at Eq. (E.7) and keeping in mind that the function V(r), which is the physical potential causing the scattering of the particle, must vanish at r→∝, the last two terms in square brackets in Eq. (E.7) can be neglected compared with k^2, when the value of r is sufficiently large. As a result, Eq. (E.13) is obtained large values of r.

$$\frac{d^2 u_l}{dr^2} + k^2 u_l = 0 \tag{E.13}$$

This equation is satisfied by the function

$$u_l = e^{\pm ikr} \tag{E.14}$$

If Eq. (E.12) is taken into account, then the general solution of Eq. (E.13) can be written as

$$u_l = kr\left[a_l^{(-)} h_l^{(-)}(kr) + a_l^{(+)} h_l^{(+)}(kr)\right] \tag{E.15}$$

for the large values of r. Thus we arrive at the conclusion that the general solution u_l of Eq. (E.7) at r→∝ must coincide with the solution u_l^0 of Eq. (E.8) i.e.

$$u_l(kr) \xrightarrow[r\to\infty]{} u_l^0(kr) \tag{E.16}$$

It is necessary to find the conditions where Eq. (E.16) will be held. The solution we are looking for is rewritten as

$$u_l(r) = u_l^0 F_l(r) \tag{E.17}$$

where

$$u_l^0 = krh_l^{(\pm)}(kr) \tag{E.18}$$

Substituting Eq. (E.12) into Eq. (E.7), the following expression is obtained

$$\frac{F_l''}{F_l} + 2\frac{u_l^{0\prime}}{u_l^0}\frac{F_l'}{F_l} = \frac{2m}{\bar{h}^2}V(r) \tag{E.19}$$

where the prime (′) denotes the derivative over r. According to Eq. (E.12) and Eq. (E.18), for large values of r,

$$u_l^{0\prime} \Big/ u_l^0 = \pm ik \tag{E.20}$$

From the condition given in Eq. (E.16), for arbitrary large values of r, the function $F_l(r)$ must be a smooth function. Therefore its second derivative must be much smaller than the first derivatives i.e.

$$F_l'' << kF_l' \tag{E.21}$$

In this case on the right hand side of Eq. (E.19), the first term can be neglected as compared with the second one. As a result taking into account Eq. (E.20), we obtain

$$\frac{F_l'}{F_l} = \pm \frac{m}{ik\bar{h}^2}V(r) \tag{E.22}$$

From this equation immediately follows

$$\ln F_l(r) = \pm \frac{m}{ik\bar{h}^2}\int_{r_0}^{r} V(r')dr' + \ln F_l(r_0) \tag{E.23}$$

where r_0 is an arbitrary large fixed value r. If the potential V(r) obeys the condition

$$|V(r)| \xrightarrow[r\to\infty]{} \frac{a}{r^{1+e}} \tag{E.24}$$

where α is an arbitrary finite constant and ε>0, then from Eq. (E.23) we have

$$\lim_{r\to\infty} F_l(r) = \text{cons tan t} \tag{E.25}$$

This constant which appears as the quantities $a_l^{(\pm)}$ in Eq. (E.15) depends on the potential V(r) and the energy E(k) of the particle. Consequently, if the potential V(r) obeys the condition given in Eq. (E.24), then the general solution of Eq. (E.7) u_l at r→∝ has the form which is given by Eq. (E.15). The quantities $a_l^{(\pm)}$ need to be chosen in such a way that for the case V(r) = 0 this expression is reduced to the corresponding expression for the radial wave function u_l^0 for the free particle, Eq. (E.16) i.e. according to Eq. (E.9a) the function u_l has the form

$$u_l \xrightarrow[r\to\infty]{} u_l^0 \longrightarrow \sin\left(kr-\frac{lp}{2}\right) \tag{E.26}$$

Up till now, it is enough to assume that

$$a_l^{(-)}=\frac{i}{2}e^{-id_l(k)}, a_l^{(+)}=-\frac{i}{2}e^{id_l(k)} \tag{E.27}$$

Then using Eq. (E.4), (E.11) and (E.15) for the functions $j_{kl}^{(+)}(r)$ and $u_l(r)$ the following asymptotic expressions are obtained

$$j_{kl}^{(+)}(r) \xrightarrow[r\to\infty]{} \frac{i}{2}\left[h_l^{(-)}(kr)-S_l(k)h_l^{(+)}(kr)\right] \tag{E.28a}$$

$$u_l(kr) \xrightarrow[r\to\infty]{} \cos d_l\left[j_l(kr)-tgd_l n_l(kr)\right]kr \tag{E.28b}$$

where

$$S_l(k)=e^{i2d_l(k)} \tag{E.29}$$

Finally, Eq. (E.30) is obtained.

$$u_l(kr) \xrightarrow[r\to\infty]{} \sin\left(kr-\frac{lp}{2}+d_l\right) \tag{E.30}$$

As was mentioned above, the quantities $a_l^{(\pm)}$, and consequently the quantities $d_l(k)$, depend on the interaction potential V(r) and as can be seen from Eq. (E.17), (E.23), (E.24) and (E.27), the quantities $d_l(k)$ vanish when V(r) = 0. Thus, **the quantities $d_l(k)$ are the phase shifts produced by the interaction and therefore characterize the scattering process on the potential V(r). The quantities $d_l(k)$ are called the scattering phase shifts.**

CURRICULUM VITAE

Particulars

Name: **Chan Hay Yee, Serene**
Gender: **Female**
Date of Birth: **28th October 1978**
Nationality: **Singaporean**
Address: **Blk 103 Bishan Street 12**
#18-272 Singapore 570103
Contact Information: **+65-97514678 (Mobile)**
+65-63543661 (Home)
Email: **chanhy@charteredsemi.com** **or**
engp1438@nus.edu.sg **or**
chyeehy@gmail.com

Education

1985-1990: Paya Lebar Methodist Girls' Primary School
1991-1994: Paya Lebar Methodist Girls' Secondary School
1995-1996: Nanyang Junior College (Core subjects: Chemistry, Physics and Mathematics C)
1997-2001: National University of Singapore (Department of Chemical and Biomolecular Engineering – B. Eng Second Class (Upper))
2001-2005: National University of Singapore (Department of Chemical and Biomolecular Engineering – PhD in progress)

Work Experience

Jan 2000-Jun 2000: Industrial Attachment at Novotronics Pte Ltd
Main responsibilities:
1) Learning and testing of technical software mainly
(a) CFDRC (Computational Fluid Dynamics Research Corporation), a software package for virtual prototyping of semiconductor processes and equipment.
(b) CHEMKIN (Sandia National Laboratories), a software suite used in the microelectronics, combustion, and chemical processing industries.
2) Handled project with Tech Semiconductor Singapore Pte Ltd on the simulation, modeling and design of CVD reactor.

Jun 2001-Jun 2005: Lab demonstrator for Year II Chemical and Biomolecular Engineering students (2003) and grader for module CN4119: Design I (2004 and 2005)

Jun 2001-Jun 2005: Mentored under Dr Lap Chan (Special Project Group) and Dr Francis Benistant (TD-DTD TCAD).

Other information

1) Final Year Research Project *(Jul 2000-Oct 2000)*: Modeling and simulation study of laminar and turbulent flow in tubular structures using computational fluid dynamics (CFD) package GAMBIT and FLUENT.
2) Final Year Design Project *(Jan 2001-Apr 2001)*: Handled chemical and mechanical design of continuously-stirred tank reactor for hydroformylation of propene using HYSYS and Microsoft Visio.
3) PhD Project *(Jun 2001-Jun 2005)*

Awards

Awarded A*STAR Graduate Fellowship in July 2002

Technical presentations (poster)

1) H.Y. Chan, M. P. Srinivasan, N. L. Ma, F. Benistant, K.R. Mok, Lap Chan
   "Modeling of Damage Formed after Ion Implantation and their Effect on Effective N-Plus Factor"
   Symposium on Microelectronics (SOM 2004)
   4th June 2004
   Institute of Microelectronics (IME), Singapore

2) H.Y. Chan, K. Nordlund, J. Peltola, H.-JL. Gossmann, N. L. Ma, M. P. Srinivasan, F. Benistant, Lap Chan
   "Low Energy Ion Implantation in Crystalline Silicon: Application of Binary Collision Approximation and Molecular Dynamics"
   7th International Conference on Computer Simulation of Radiation Effects in Solids (COSIRES 2004)
   28th June 2004 – 2nd July 2004
   Department of Physical Sciences, University of Helsinki
   Helsinki, Finland

3) H.Y. Chan, M. P. Srinivasan, H. M. Jin, F. Benistant, Lap Chan
   "Continuum Modeling of Post-Implantation Damage and the Effective +N Factor in Crystalline Silicon at Room Temperature"
   3rd International Conference on Materials for Advanced Technologies/International Union of Materials Research Societies: 9th International Conference on Advanced Materials ICMAT2005/IUMRS-ICAM2005)
   3rd July 2005 – 8th July 2005
   Suntec Singapore International Convention and Exhibition Centre
   Singapore

Technical presentations (oral)

1) H.Y Chan, F. Benistant, M. P Srinivasan, A. Erlebach, C. Zechner
   "New Analytical Damage Tables for Crystalline Silicon"
   7th International Workshop on Fabrication, Characterization, and Modeling of Ultra-Shallow Junctions in Semiconductors (USJ-2003)
   27th April 2003 - 1st May 2003
   Chaminade Conference Center
   Santa Cruz, California, USA

2) H.Y. Chan, N. L. Ma, K. Nordlund, M. P. Srinivasan, F. Benistant, Y.L. Tan
   "Low Energy Ion Implantation in Crystalline Silicon: A Molecular Dynamics Approach"
   International Conference on Scientific and Engineering Computation (IC-SEC 2004)
   30th June 2004 – 2nd July 2004
   Riverfront Ballroom Grand Copthorne Waterfront Hotel, Singapore

3) H.Y Chan, H.-JL. Gossmann, N. Montgomery, C. Mulcahy, S. Biswas, K. Nordlund, M. P Srinivasan, F. Benistant, C. M. Ng, Lap Chan
"Application of Molecular Dynamics for Low Energy Ion Implantation in Crystalline Silicon"
8th International Workshop on Fabrication, Characterization, and Modeling of Ultra-Shallow Junctions in Semiconductors (USJ-2005)
5th June 2005 – 8th June 2005
Plaza Resort and Spa Daytona Beach
Florida, USA

4) H.Y. Chan, M. P. Srinivasan, H. M. Jin, F. Benistant, Lap Chan
"Application of Molecular Dynamics in Low Energy Ion Implantation in Crystalline Silicon"
3rd International Conference on Materials for Advanced Technologies/International Union of Materials Research Societies: 9th International Conference on Advanced Materials (ICMAT2005/IUMRS-ICAM2005)
3rd July 2005 – 8th July 2005
Suntec Singapore International Convention and Exhibition Centre
Singapore

5) H.Y. Chan, M. P. Srinivasan, H.M. Jin, F. Benistant, Lap Chan
"Monte Carlo vs Molecular Dynamics Methods in Simulating Low Energy Ion Implantation Profiles"
Symposium on Microelectronics (SOM 2005)
5th August 2005
Institute of Microelectronics (IME)
Singapore

6) N. L. Yakovlev, C. C. Lee, H. Y. Chan, M. P. Srinivasan, C. M. Ng, D. Gui, L. Chan, R. Liu, A. T. S. Wee, A. R. Chanbasha, N. J. Montgomery, C. P. A. Mulcahy, S. Biswas, H. -J. L. Gossmann, M. Harris
"Collaborative SIMS study and simulation of implanted dopants in Si"
The 15th International Conference on Secondary Ion Mass Spectrometry (SIMS XV)
12th September 2005 -16th September 2005
Manchester, United Kingdom

Publications

1) H. Y. Chan, F. Benistant, M. P. Srinivasan, A. Erlebach and C. Zechner
"Analytical Damage Tables for Crystalline Silicon"
Journal of Vacuum Science and Technology B 22 (1), pp. 463 – 467, 2004

2) H. Y. Chan, K. Nordlund, J. Peltola, H. -J. L. Gossmann, N. L. Ma, M. P. Srinivasan, F. Benistant, Lap Chan
"The Effect of Interatomic Potential in Molecular Dynamics Simulation of Low Energy Ion Implantation"
Nuclear Instruments and Methods in Physics Research B 228 (1-4), pp. 240-244, 2005

3) H.Y. Chan, M. P. Srinivasan, F. Benistant, H. M. Jin, Lap Chan
“Sampling Calibration of Ion Implantation Profiles in Crystalline Silicon from 0.1-300keV using Monte Carlo simulations”
Solid State Electronics 49 (7), pp. 1243-1249, 2005

4) H.Y. Chan, K. Nordlund, H. -J. L. Gossmann, M. Harris, N. J. Montgomery, S. Biswas, M. P. Srinivasan, F. Benistant, C.M. Ng, Lap Chan
“Molecular Dynamics with Phase-shift-based Electronic Stopping for calibration of Ion Implantation profiles in Crystalline Silicon”
Thin Solid Films 504 (1-2), pp. 121-125, 2006

5) H.Y. Chan, K. R. Mok, M. P. Srinivasan, F. Benistant, Lap Chan, H. M. Jin
“Continuum Modeling of Post-Implantation Damage and the Effective Plus Factor in Crystalline Silicon at Room Temperature”
Thin Solid Films 504 (1-2), pp. 269-273, 2006

6) H.Y. Chan, H. -J. L. Gossmann, N. Montgomery, C. Mulcahy, S. Biswas, K. Nordlund, M. P. Srinivasan, F. Benistant, C. M. Ng, Lap Chan
“Application of Molecular Dynamics for Low Energy Ion Implantation in Crystalline Silicon”
Journal of Vacuum Science and Technology B 24 (1),
pp. 462 – 467, 2006

7) N. L. Yakovlev, C. C. Lee, H. Y. Chan, M. P. Srinivasan, C. M. Ng, D. Gui, L. Chan, R. Liu, A. T. S. Wee, A. R. Chanbasha, N. J. Montgomery, C. P. A. Mulcahy, S. Biswas, H. -J. L. Gossmann, M. Harris
“Collaborative SIMS study and simulations of implanted dopants in Silicon”
Applied Surface Science (pending publication)